



THE UNIVERSITY  
OF ADELAIDE



# **EVALUATION OF SEALS AND ASSOCIATED RESERVOIR ROCKS: TRIASSIC NAPPAMERRI GROUP AND CUDDAPAN FORMATION, COOPER BASIN, SOUTH AUSTRALIA**

**By**

**Rodica Dragomirescu**

Bachelor of Engineering (Honours)  
Bucharest University, Romania

This thesis is submitted in the fulfillment of the requirements for the  
degree of

**Master of Science in Petroleum Geology**  
at

The National Centre for Petroleum Geology and Geophysics (NCPGG)  
The University of Adelaide

July 2002

## TABLE OF CONTENTS

<b>CHAPTER ONE – INTRODUCTION.....</b>	<b>1</b>
1.1 INTRODUCTION.....	1
1.2 RESEARCH OBJECTIVES.....	1
1.3 LOCATION OF THE STUDY AREA.....	2
1.4 GEOLOGICAL SETTING.....	4
1.4.1 Stratigraphy and structural evolution of the Cooper Basin.....	4
1.4.2 Structure of the Cooper Basin.....	9
1.5 PREVIOUS INVESTIGATIONS.....	9
1.6 SEAL POTENTIAL.....	12
<b>CHAPTER TWO – SEDIMENTOLOGY AND LITHOFACIES ANALYSIS.....</b>	<b>13</b>
2.1 INTRODUCTION.....	13
2.2 DATA AVAILABILITY.....	14
2.3 IDENTIFICATION OF DEPOSITIONAL ENVIRONMENTS AND LITHOFACIES DESCRIPTION.....	14
2.4 LITHOFACIES CLASSIFICATION AND DESCRIPTION.....	19
2.4.1 RF-1 Gravels from the base of fluvial channels (Plate 2.4).....	20
2.4.2 RF-2 and RF-3 Fluvial channel and chute sands (Plate 2.5).....	21
2.4.3 RF-4 Crevasse splay sands (Plate 2.6).....	22
2.4.4 RF-5 Fine-grained sands from top of point bars (Plate 2.7).....	23
2.4.5 SF-1 Diagenetically-modified fluvial sandstones (Plate 2.8).....	24
2.4.6 SF-2 Lacustrine mudstones (Plate 2.9).....	25
2.4.7 SF-3 Palaeosols (Plate 2.10).....	26
2.4.8 SF-4 Floodplain mudstones (Plate 2.11).....	27
2.4 SUMMARY.....	28
<b>CHAPTER THREE – METHODOLOGY.....</b>	<b>29</b>
3.1 SEDIMENTOLOGICAL LOGGING.....	29
3.2 SELECTION CRITERIA.....	29
3.3 X - RAY DIFFRACTION (XRD) ANALYSIS.....	29
3.4 OPTICAL PETROGRAPHY.....	30
3.5 SCANNING ELECTRON MICROSCOPY (SEM).....	31
3.6 MERCURY INJECTION CAPILLARY PRESSURE (MICP) TECHNIQUES	32
3.7 WIRE-LINE LOG ANALYSIS AND MAPPING.....	35

<b>CHAPTER FOUR – SAMPLE PETROGRAPHY AND DIAGENETIC HISTORY</b>	<b>36</b>
4.1 INTRODUCTION.....	36
4.2 PETROGRAPHIC OBSERVATIONS.....	36
4.2.1 Texture.....	36
4.2.2 Framework grain composition.....	40
4.3 XRD RESULTS AND INTERPRETATION.....	42
4.4 DIAGENETIC EVENTS.....	49
4.4.1 Compaction.....	49
4.4.2 Alteration.....	49
4.4.3 Cementation.....	49
4.4.3.1 Quartz.....	50
4.4.3.2 Clay.....	51
4.4.3.3 Siderite.....	51
4.4.3.4 Pyrite.....	52
4.5 HYDROCARBONS.....	52
4.6 DIAGENETIC HISTORY.....	52
4.7 SUMMARY.....	53
<b>CHAPTER FIVE - RESERVOIR QUALITY .....</b>	<b>54</b>
5.1 INTRODUCTION.....	54
5.2 POROSITY TYPES.....	54
5.2.1 Primary porosity.....	54
5.2.2 Secondary porosity.....	55
5.2.3 Microporosity.....	55
5.3 FACTORS THAT CONTROL POROSITY.....	55
5.4 FACTORS THAT CONTROL THE PORE SYSTEM GEOMETRY.....	57
5.5 PERMEABILITY.....	58
5.5.1 Factors that control permeability.....	58
5.5.2 Permeability evaluation from mercury injection capillary pressure curves...	60
5.6 SUMMARY.....	63
<b>CHAPTER SIX – PETROPHYSICAL CONTROLS ON HYDROCARBON MIGRATION AND SEALING.....</b>	<b>65</b>
6.1 INTRODUCTION.....	65
6.2 CAPILLARY PRESSURE.....	65
6.2.1 Displacement pressure.....	66

6.2.2	Interfacial tension.....	67
6.2.3	Wettability.....	68
6.2.4	Radius of pore throats.....	68
6.2.5	Subsurface densities of fluids.....	69
6.3	SEAL CAPACITY CALCULATION.....	70
6.4	CONVERSION EQUATION FROM AIR/MERCURY LABORATORY DATA TO BRINE/HYDROCARBON RESERVOIR CONDITIONS.....	70
6.5	THRESHOLD PRESSURE.....	71
6.5.1	Definition.....	71
6.5.2	Methods of estimating threshold pressure from capillary pressure curves...	71
6.5.3	Determination of threshold pressure.....	72
6.6	SUBSURFACE EXTRAPOLATION OF RESERVOIR FLUIDS DENSITY, INTERFACIAL TENSION AND WETTABILITY.....	74
6.6.1	Subsurface oil density.....	74
6.6.2	Subsurface gas density.....	74
6.6.3	Subsurface brine density.....	75
6.6.4	Oil/water interfacial tension.....	76
6.6.5	Gas/water interfacial tension.....	76
6.6.6	Wettability.....	76
6.7	CALCULATION OF HYDROCARBON COLUMN HEIGHTS.....	77
6.8	SUMMARY.....	82
<b>CHAPTER SEVEN– EVALUATION OF SEAL POTENTIAL.....</b>		<b>83</b>
7.1	INTRODUCTION.....	83
7.2	SEAL GEOMETRY.....	83
7.2.1	Data availability.....	83
7.2.2	Mineral identification/lithology reconstruction from wireline logs.....	83
7.2.3	Correlation and mapping.....	84
7.2.4	Thickness and areal extent of SF-1 Diagenetically-modified sandstones	86
7.2.5	Thickness and areal extent of SF-2 Lacustrine mudstones.....	86
7.2.6	Thickness and areal extent of SF-3 and SF-4 Palaeosols and Floodplain mudstones.....	86
7.3	SEAL INTEGRITY.....	90
7.4	SEAL POTENTIAL. RISK ASSESSMENT.....	91

7.4.1 Seal capacity .....	91
7.4.2 Seal geometry.....	93
7.4.3 Seal integrity.....	95
7.5 SEAL POTENTIAL RANKING.....	95
7.6 SUMMARY.....	96
<b>CHAPTER EIGHT – CONCLUSIONS.....</b>	<b>98</b>

## REFERENCES

### LIST OF FIGURES

- Figure 1.1 Location of the studied fields within the Cooper Basin.
- Figure 1.2 Stratigraphic column of the Cooper Basin, South Australia (Alexander *et al.*, 1998).
- Figure 1.3 Major structural elements of the Cooper Basin, South Australia and approximate location of the studied fields (modified after Gravestock and Jensen-Schmidt, 1998).
- Figure 2.1 Model for lateral and vertical accretion deposits of meandering rivers (after Walker, 1984).
- Figure 2.2 Block diagram showing morphological elements of a meandering river system (after Walker, 1984).
- Figure 2.3 Generalized depositional model, vertical sequences and electric (SP) log profiles of a meander belt sand body produced by a high-sinuosity channel. (A) Complete fining-upward sequence of the mid- or downstream point bar. (B) Truncated vertical sequence of the upstream end of the point bar (from Galloway and Hobday, 1983).
- Figure 2.4 Depositional model, vertical sequences and electric log (SP) profiles of a chute-modified point bar. (A) Upstream portions of the point bar are capped by chute-channel deposits. (B) Downstream, the channel and lower point bar deposits are capped by chute-bar sediments (from Galloway and Hobday, 1983).
- Figure 3.1 The Micromeritics Autopore 9410 mercury injection porosimeter.
- Figure 3.2 A closer view of the Micromeritics Autopore 9410 mercury injection porosimeter.

- Figure 3.3 Schematic view of an assembled penetrometer and the component parts, using the nylon nut and cover (new style).
- Figure 4.1 Examples of grain size distribution. a) medium sand, moderately sorted with symmetrical, very flat curve (RF-2), b) fine sand, moderately well sorted with negatively skewed, normal distribution (RF-3), c) medium sand, moderately sorted, with very flat, positively skewed curve (RF-4).
- Figure 4.2 Grain to grain relationships. The low compaction indicators in the fine-grained sediments are in part a function of the presence of matrix.
- Figure 4.3 Constituents of the total rock composition as determined by visual estimation from thin sections of samples selected for MICP evaluation as listed in Table 3.1.
- Figure 4.4 QFR ternary diagram showing the framework grain composition of the sandstone facies (Folk, 1968). The bias away from the feldspar pole is a function of the alteration of feldspar to clay.
- Figure 4.5 Textural classification of fine-grained rocks and sediments (Picard, 1971).
- Figure 4.6.a Representative XRD peak pattern of clean quartz-rich gravel (RF-1), Teloepa 2-8188 ft.
- Figure 4.6.b Representative XRD peak pattern for a clay-rich palaeosol (SF-3), Merrimelia 29-7130 ft.
- Figure 4.6.c Representative XRD peak pattern for a crevasse splay sand (RF-4) with a high background of organic material, Merrimelia 17-7080ft.
- Figure 4.6.d Representative XRD peak pattern of siderite-cemented fine sand from the top of point bars (RF-5), Merrimellia 7- 7065 ft 11 in.
- Figure 4.7 Indication of mineral composition from raw XRD peak area data. Variation in total counts is a function of smear thickness. Quartz is low because the  $4.27\text{\AA}^0$  peak was used. Bars indicate relative proportions between samples but not relative proportions of each mineral in a sample (see Table 3.1 for sample listing).
- Figure 4.8 Cross-plots that illustrate (a) reservoir/seal quality, (b) sealing lithofacies quality, (c) reservoir lithofacies quality (values are derived from measurement of XRD peak areas).

- Figure 4.9 Cross-plots that illustrate reservoir/seal quality. (a) porosity versus kaolin + illite (b) permeability versus kaolin + illite (c) porosity versus kaolin (d) permeability versus kaolin (d) porosity versus illite (e) permeability versus illite (values are derived from measurement of XRD peak areas).
- Figure 4.10 Relative proportions of cement types as determined by visual estimation in thin sections (see Table 3.1 for listing).
- Figure 5.1 Relative proportions of porosity types as determined by visual estimation in thin sections.
- Figure 5.2 Relationship between (a) porosity and quartz overgrowth cement and (b) porosity and matrix.
- Figure 5.3 Relationship between core plug porosities and porosities measured in thin section.
- Figure 5.4 Semi-log cross plot of core porosity versus permeability.
- Figure 5.5 Relationship between core plug permeability and (a) Swanson permeability to air and brine, (b) Winland permeability (c) Pittman permeability. (d) Correlation between Pittman and Winland permeabilities.
- Figure 6.1 Mercury injection capillary pressure curve with a flat plateau (Telopea 2, 8186'3").
- Figure 6.2 Mercury injection capillary pressure curve with a steep gradient (Beanbush 1, 8723'3").
- Figure 6.3 Sensitivity of hydrocarbon column height to interfacial tension (IT = 5, 16 and 21 dynes/cm) and contact angle (CA = 0<sup>o</sup>, 15<sup>o</sup> and 20<sup>o</sup>). Variations in interfacial tension have a greater influence on column height than changes to the contact angle.
- Figure 6.4 Calculated oil column heights held by (a) diagenetically-modified fluvial sandstones (SF-1), (b) fine-grained lacustrine sediments (SF-2), (c) palaeosols (SF-3) and (d) floodplain mudstones (SF-4) versus various reservoir lithologies.
- Figure 6.5 Seal capacity results. (a) Range of maximum oil column height held by each sealing lithology (including varying interfacial tensions). (b) Range of maximum gas column height held by each sealing lithology (including varying interfacial tensions).
- Figure 7.1 Identification of kaolin-cemented sandstones from petrophysical cross-plots. Merrimelia 15.

- Figure 7.2 Lithology reconstruction from petrophysical cross-plots. Merrimelia 29.
- Figure 7.3 Separation of sands from silts and shales using a GR cut-off value of 130 API. Merrimelia 3.
- Figure 7.4 NE - SW Lithostratigraphic correlation of the Nappamerri Group-Merrimelia Field, Cooper Basin.
- Figure 7.5 NE - SW Lithostratigraphic correlation of the Nappamerri Group-Merrimelia Field, Cooper Basin.
- Figure 7.6 WNW - ESE Lithostratigraphic correlation of the Nappamerri Group - Merrimelia Field, Cooper Basin.
- Figure 7.7 WNW - ESE Lithostratigraphic correlation of the Nappamerri Group - Merrimelia Field, Cooper Basin.
- Figure 7.8 Cumulative shale thickness (m) for sealing interval 1, Merrimelia Field. The northern end of this field shows much less shale than the south and east.
- Figure 7.9 Shale/total thickness ratio (%) for sealing interval 1, Merrimelia Field. Although sealing interval 1 is thin in the northern part of the field, the shale content is very high.
- Figure 7.10 Cumulative shale thickness (m) for sealing interval 2, Merrimelia Field. The southern end of this field shows more shale than the central and northern part.
- Figure 7.11 Shale/total thickness ratio (%) of sealing interval 2, Merrimelia Field, Cooper Basin. Although sealing interval 2 is thin in the central and northern part of the field, the shale content is very high.
- Figure 7.12 Cumulative shale thickness (m) of the Nappamerri Group, Merrimelia Field. The southern end of this field shows more shale than the northern part.
- Figure 7.13 Shale/total thickness ratio (%) for the Nappamerri Group, Merrimelia Field. The shale content is very low because of two sandy units within the Nappamerri Group.
- Figure 7.14 Isopach map of the Nappamerri Group (from Alexander et al., 1998) showing the thickening of the Nappamerri Group toward adjacent troughs (Nappamerri and Patchawarra Trough).



- Figure 7.15 Merrimelia Ridge and adjacent troughs, with the C seismic horizon (Early Cretaceous as datum, near top of the Cadna-Owie Formation) (from Gravestock, and Jensen-Schmidt, 1998), showing Merrimelia Ridge dipping toward southeast; Nappamerri Group is situated above the P seismic horizon (Late Permian, near top of the Toolachee Formation). F = fault.
- Figure 7.16 Schematic palaeogeographic representation of Big Lake and Moomba areas (Stuart *et al.*, 1988).
- Figure 7.17 Sandstone body interconnection as a function of the net sand fraction of the sequence (Crane, 1982).
- Figure 7.18 Seal integrity (after Brown, in Kaldi, 2000).
- Figure 7.19 Merrimelia Field Depth Structure Top 74-9 Sand, Mid Nappamerri Formation (Siffleet, 1992).
- Figure 7.20 Schematic cross section through Merrimelia Field, showing main sealing intervals and hydrocarbon distribution, modified after Burgess, 1990. Location of cross section is marked on Fig. 7.19.
- Figure 7.21 Schematic illustration of the sealing facies geometry and their relative seal capacity (not to scale). SF-1 extent is from approximate 100m to less than 1Km. SF-2 extent is less than 1Km. SF-3 and SF-4 extent is from approximate 500m to more than 10Km.
- Figure 7.22 (a) The relative seal potential of diagenetically-modified sandstones (SF-1) and lacustrine silts and clays (SF-2). (b) The relative seal potential of palaeosols (SF-3) and floodplain mudstones (SF-4).

### LIST OF TABLES

- Table 1.1 List of the wells and cored intervals, used in this study.
- Table 2.1 Facies classification (modified from Miall, 1978c).
- Table 3.1 Sample selection and completed analyses. (a) sealing lithologies, (b) reservoir lithologies.
- Table 4.1 Descriptive terms applied to parameter values (McManus, 1988).
- Table 6.1 Range of air/mercury and brine/hydrocarbon threshold pressures for the identified sealing and reservoir facies, alternate interfacial tension (IT) 16 dynes/cm and 30 dynes/cm with a 0° contact angle (CA).

- Table 6.2 Range of maximum hydrocarbon column heights as a function of seal lithologies, considering an oil/brine and gas/brine system of reservoir (hydrocarbon column height in meters and feet).
- Table 7.1 Cumulative shale thickness and shale/total thickness ratios of Sealing Interval 1, 2 and the Nappamerri Group.

### LIST OF PLATES

- PLATE 2.1 Facies associations - Nappamerri Group, Callamurra and Paning Members. Merrimelia 29
- PLATE 2.2 Facies associations - Nappamerri Group, Tinchoo Formation. Telopea 2
- PLATE 2.3 Facies associations - Cuddapan Formation. Beanbush 1
- PLATE 2.4 Sample photographs, thin section and SEM photomicrographs, pore size distribution and mercury injection data of RF1: Gravels from the base of fluvial channels
- PLATE 2.5 Sample photographs, thin section and SEM photomicrographs, grain and pore size distribution and mercury injection data of RF-2 and RF-3: Fluvial channel and chute sands
- PLATE 2.6 Sample photographs, thin section and SEM photomicrographs, grain and pore size distribution and mercury injection data of RF-4: Crevasse splay sands
- PLATE 2.7 Sample photographs thin section and SEM photomicrographs, grain size distribution and mercury injection data of RF-5: Fine-grained sands from top of point bars
- PLATE 2.8 Sample photographs, thin section and SEM photomicrographs, grain size distribution and mercury injection data of SF-1: Diagenetically-modified fluvial sandstones
- PLATE 2.9 Sample photographs, thin section and SEM photomicrographs and mercury injection data of SF-2: Fine-grained lacustrine sediments
- PLATE 2.10 Sample photographs, thin section and SEM photomicrographs, and mercury injection data of SF-3: Palaeosols
- PLATE 2.11 Sample photographs, thin section and SEM photomicrographs, and mercury injection data of SF-4: Floodplain mudstones
- PLATE 4.1 Thin section photomicrographs of mechanical and chemical compaction
- PLATE 4.2 Thin section and SEM photomicrographs of quartz cement
- PLATE 4.3 SEM photomicrographs of kaolin cement

PLATE 4.4	Thin section photomicrographs of kaolin and illite
PLATE 4.5	Thin section and SEM photomicrographs of detrital clays
PLATE 4.6	Thin section photomicrographs of siderite cement
PLATE 4.7	SEM photomicrographs of siderite cement
PLATE 4.8	Thin section photomicrographs of hydrocarbon occurrence and pyrite cement
PLATE 5.1	SEM photomicrographs of primary porosity
PLATE 5.2	Thin section photomicrographs of primary porosity, secondary porosity and microporosity

## APPENDICES

APPENDIX 2.1	PORE SIZE STATISTICS
APPENDIX 3.1	XRD TRACES
APPENDIX 3.2	THIN SECTION DESCRIPTIONS
APPENDIX 3.3	GRAIN SIZE MEASUREMENTS IN THIN SECTIONS
APPENDIX 3.4	PORE SIZE MEASUREMENTS IN THIN SECTIONS
APPENDIX 3.5	CORRECTED VALUES OF GRAIN SIZE (PHI)
APPENDIX 3.6	MERCURY INJECTION CAPILLARY PRESSURE DATA AND CHARTS
APPENDIX 4.1	GRAIN SIZE DESCRIPTION AND STATISTICS (PHI)
APPENDIX 4.2	PROPORTION OF FRAMEWORK GRAIN COMPONENTS, POROSITY AND CEMENT OF ROCK COMPOSITION
APPENDIX 4.3	MINERALOGICAL COMPOSITION FROM XRD DATA
APPENDIX 5.1	PERMEABILITY CALCULATION
APPENDIX 6.1	SUBSURFACE OIL DENSITY
APPENDIX 6.2	AVERAGE GAS MOLECULAR WEIGHT
APPENDIX 6.3	CALCULATION OF SUBSURFACE BRINE AND GAS DENSITIES
APPENDIX 7.1	NAPPAMERRI GROUP TOPS (PEPS DATABASE)

## ABSTRACT

This study evaluates the seal potential (capacity, geometry and integrity) of four sealing lithofacies and the reservoir quality of five reservoir lithofacies from the Early-Middle Triassic Nappamerri Group and late Triassic Cuddapan Formation, Cooper Basin in South Australia.

The Nappamerri Group and Cuddapan Formation sediments are heterolithic fluvial units and comprise both sealing and reservoir lithologies. Five reservoir lithofacies: gravels from the base of fluvial channels, fluvial channel sands, chute sands, crevasse splay sands and sands from the top of point bars and four sealing lithofacies: diagenetically modified fluvial sandstones, lacustrine mudstones, palaeosols and floodplain mudstones were identified.

Reservoir quality, pore and pore throat size distributions are controlled by petrographic composition, texture and the subsequent diagenetic overprint. These are influenced by depositional environment.

Seal capacity was evaluated using mercury injection capillary pressure analyses and was calculated for both oil and gas accumulations. The highest column of hydrocarbon is associated with lacustrine mudstones (1353 m oil and 727 m gas). The next highest column of hydrocarbon can be supported by palaeosols and floodplain mudstones (1132 m oil and 609 m gas). The lowest hydrocarbon column (37 m oil and 20 m gas) is supported by diagenetically modified fluvial sandstones. The sensitivity of column height to interfacial tension, the wettability and the subsurface extrapolation of fluid densities were tested using empirical hydrocarbon fluid property data from the Cooper Basin.

Recognition of the sealing lithologies on wire-line logs was completed by calibrating the cores to petrophysical cross-plots. Seals were evaluated in terms of their geometry (thickness and areal extent). Sealing intervals were correlated and mapped for thickness and quality across the Merrimelia Field.

Seal integrity was qualitatively determined on the basis of petrographic criteria, core description and literature analogs.

The sealing potential of the four lithofacies identified in the study area was ranked. The best sealing potential exists within the palaeosols and floodplain mudstones. These lithofacies occur as two sealing intervals; they are thick, extend over the entire Merrimelia Field and have high measured seal capacities. Although of relatively higher seal capacity and homogeneity, lacustrine mudstones have a lower seal potential because they are thin and occur only locally. The poorest seal potential occurs within the diagenetically modified sandstones. This lithofacies is thin, with unpredictable distribution, poor rock mechanical properties and low seal capacity.

This study demonstrates that the Nappamerri Group contains a variety of sealing lithofacies with different seal potential; it can no longer be regarded as a simple regional seal but must be treated as a series of intraformational seals. Detailed knowledge of the seal potential will improve the assessment of the seal risk and thus help guide future exploration in the Cooper Basin.

## **STATEMENT OF AUTHENTICITY AND AVAILABILITY**

This work contains no material which has been accepted for the award of any other degree or diploma in any university or other tertiary institution and, to the best of my knowledge and belief, contains no material previously published or written by another person, except where due reference has been made in the text.

I give consent to this copy of my thesis, when deposited in the University Library, being available for loan and photocopying.

Rodica Dragomirescu

## ACKNOWLEDGEMENTS

I wish to thank the Primary Industries and Resources of South Australia (PIRSA) for supporting my project in terms of scholarship and various forms of data.

I appreciate the help provided by Mr. J. Stanley, Department of Geology and Geophysics for XRD analysis, Ian Pontifex and Associates for thin section preparation and Mr. Chris Bentley from the University of South Australia for mercury injection capillary pressure analysis. I would also like to thank B. Logan and staff from the Core Library and the staff from the Centre for Electron Microscopy and Microstructure Analysis for assistance with SEM work.

I am deeply grateful to my friend Evelina Paraschivoiu, PhD student at the NCPGG for her friendship, continuous moral support and help during the course of study.

I take this opportunity to express my appreciation to the staff and students at the National Centre for Petroleum Geology and Geophysics (NCPGG) especially to Paul Grech, Ghazi Kraishan, Tom Kivior and Takeshi Nakanishi for their help and useful discussions in various areas.

I want to record my thankfulness to Dr. Simon Lang for very constructive discussions during the study.

I would like to thank Dr. John Kaldi, Director of the NCPGG who initiated this project and provided me constant logistical help and encouragement throughout the study.

I am grateful to Dr. Nicholas Lemon, Senior Lecturer at the NCPGG for his valuable suggestions and guidance.

I would also like to acknowledge my gratefulness to Elinor Alexander from PIRSA for consistent support in data access and fruitful discussions.

Finally, the moral support, encouragement and understanding of my family could make it possible to complete this project successfully.

## **CHAPTER ONE**

### **INTRODUCTION**

#### **1.1 INTRODUCTION**

The Cooper Basin is the largest and most significant hydrocarbon-producing onshore petroleum province in Australia. The Cooper Basin contains a complete petroleum system, comprising a source rock, a path for the migration of hydrocarbons from the source rock, a reservoir rock and a seal for hydrocarbon trapping. The presence and quality of the sealing rocks, as a component part of the petroleum system is a very important factor in controlling the distribution and size of hydrocarbon accumulations.

This project is the first study to evaluate the seal properties of the various depositional facies identified in the Triassic strata of the Cooper Basin.

The diverse methodologies employed in this investigation made possible a comprehensive characterization of the various selected sealing lithologies. Mercury injection capillary pressure (MICP) measurements enabled the calculation of the maximum height of hydrocarbon column that the identified sealing lithologies can support.

As one of the major factors controlling the distribution and size of the oil and gas accumulations, detailed knowledge of the seal quality and its distribution will improve the assessment of seal risk and guide exploration and development opportunities within the study area.

#### **1.2 RESEARCH OBJECTIVES**

The focus of this investigation concerns the seal potential of the Cooper Basin Triassic sediments. Therefore, the goal of the study is subdivided into the following specific objectives:

- To separate potential seal and reservoir lithologies, according to their depositional environment;



- To characterize specific seal lithology attributes;
- To quantify seal capacities using mercury injection capillary pressure measurements;
- To combine the seal capacity results with thickness and areal extent of each lithology in order to determine overall seal potential;
- To illustrate the petrography and diagenetic history of the Triassic rocks of the Cooper Basin.
- To provide recommendations concerning seal quality and distribution for future exploration work.

### 1.3 LOCATION OF THE STUDY AREA

The Cooper Basin is located in the desert region of northeastern South Australia and southwestern Queensland and extends over an area of 130 000 km<sup>2</sup>. One third of the basin is in South Australia and covers an area of 35 000 km<sup>2</sup>. The remainder is in Queensland with a minor percentage occurring in the NW corner of New South Wales (Fig. 1.1).

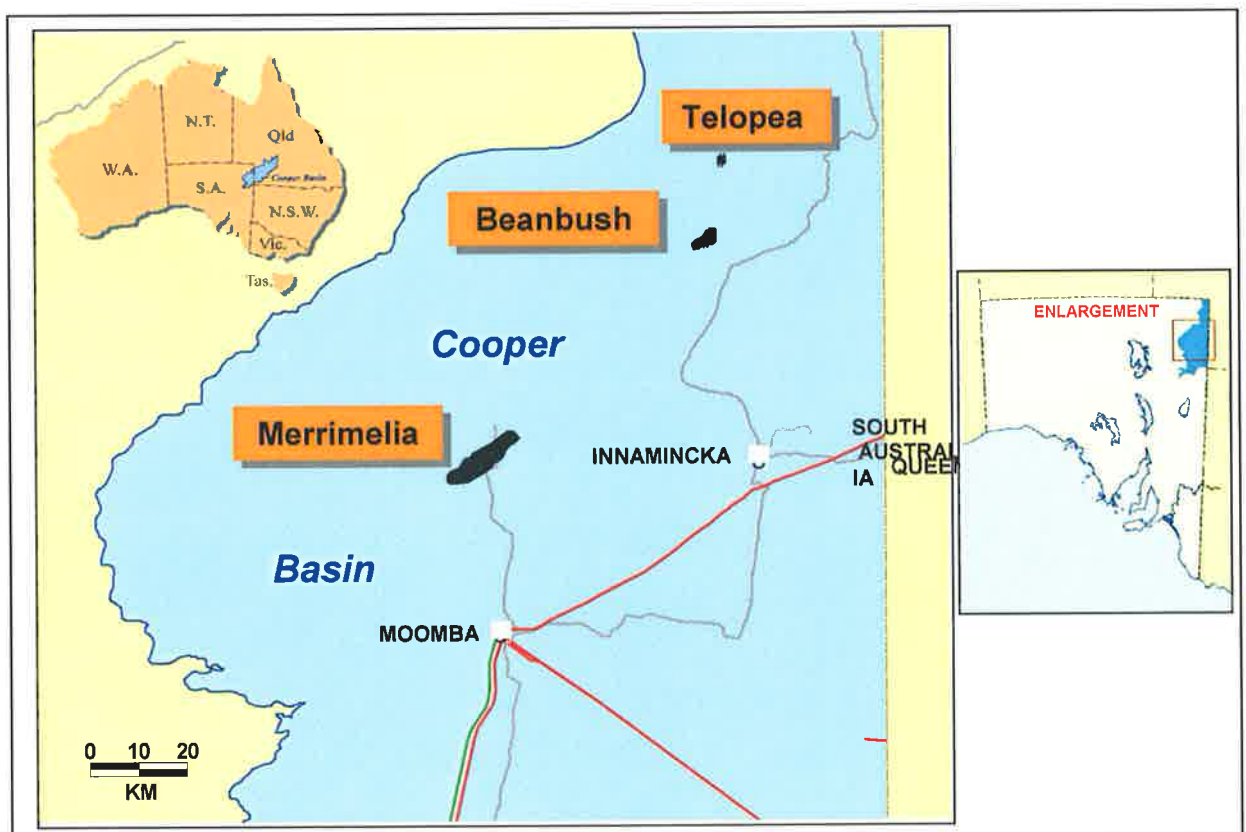


Figure 1.1 Location of the studied fields within the Cooper Basin.

The Cooper Basin contains non-marine sediments of Late Carboniferous to Triassic age (up to 2000 m). It is entirely covered by the Mesozoic Eromanga Basin and is partly underlain by the Cambro-Ordovician strata of the eastern Warburton Basin (Hollingsworth, 1989).

The focus of this study is the Triassic sedimentary succession from Telopea, Beanbush and Merrimelia Fields, located in the southeastern part of the Cooper Basin (Fig. 1.1). The Merrimelia Field occurs on the Gidgealpa-Merrimelia-Innaminka trend, while Beanbush and Telopea Fields are situated in the Patchawarra Trough (Fig.1.3).

These fields contain wells that encountered hydrocarbon accumulations and have cored intervals through all Triassic stratigraphic units. The wells used in this study comprise: eleven wells from the Merrimelia Field that penetrate the Nappamerri Group, one well from Telopea Field, representative for Tinchoo Formation and one well from Beanbush Field, representative of the Cuddapan Formation. The list of the selected wells, cored intervals and intercepted formations is presented in Table 1.1

The nomenclature is based on the classification adopted by PIRSA and Santos (Channon and Wood, 1989; Powis, 1989).

<b>Well</b>	<b>Cored intervals (ft)</b>	<b>Recovery (ft)</b>	<b>Formation/Member</b>
Beanbush 1	8715 - 8750	30	Cuddapan
Merrimelia 2	7350 - 7359	8	Callamurra
Merrimelia 3	7320 - 7830	384	Callamurra-Paning-Wimma
Merrimelia 5	7354 - 7474	44	Callamurra
Merrimelia 6	6970 - 7030	60	Paning
Merrimelia 7	6986 - 7118	80	Paning
Merrimelia 8	7054 - 7141	79	Callamurra-Paning
Merrimelia 9	7014 - 7133	115	Callamurra-Paning
Merrimelia 13	7070 - 7110	39	Paning
Merrimelia 15	7066 - 7150	75	Callamurra-Paning
Merrimelia 17	7077 - 7167	84	Paning
Merrimelia 29	7093 - 7153	52	Callamurra-Paning
Telopea 2	8165 - 8224	59	Tinchoo

Table 1.1 List of the wells and cored intervals, used in this study

## 1.4 GEOLOGICAL SETTING

The Cooper Basin is a northeast-trending structural depression. The succession in the basin comprises rocks deposited from the Late Carboniferous to Late Triassic, in glacial, fluvial, lacustrine and deltaic environments. The Cooper Basin unconformably overlies the Cambrian-Devonian rocks of the Warburton Basin and is unconformably overlain by the Jurassic-Cretaceous sediments of the Eromanga Basin.

### 1.4.1 Stratigraphy and structural evolution of the Cooper Basin

The stratigraphy of the Cooper Basin is presented in Fig. 1.2. Formations succession and major orogenesis phases are addressed in the following paragraphs:

The orogenesis at the end of Warburton Basin sedimentation probably triggered the glaciation (Powell and Veevers, 1987). Cooper Basin sedimentation began with the glacial deposits of the Merrimelia Formation (Grund, 1966; Martin, 1967; Battersby, 1976; Williams *et al.*, 1985) and Tirrawarra Sandstone. These deposits formed during the waning stages of the Permo-Carboniferous Gondwanan glaciation (Powell and Veevers, 1987). At that time, the major basement ridges were part of a pre-existing landscape (Gravestock and Jensen-Schmidt, 1998).

The Merrimelia Formation comprises the lowest formation of the Gidgealpa Group (Williams and Wild, 1984), which unconformably overlies the Warburton Basin. It is a complex unit of conglomerate, diamictite, sandstone, conglomeratic mudstone, siltstone and shale that was deposited in various glacial settings (Alexander *et al.*, 1998).

The Tirrawarra Formation is composed of fine to coarse sandstones with intercalations of shales and thin coal beds. Seggie *et al.* (1994) and Hamlin *et al.* (1996) recognized four major facies in the Tirrawarra Formation. These include: (1) delta front to glaciolacustrine clastics, (2) distributary channel, mouth bar and interdistributary deposits, (3) sandy braid-delta plain deposits and (4) sandstone to mudrock and coal deposits of fluvial system origin (Alexander *et al.*, 1998).

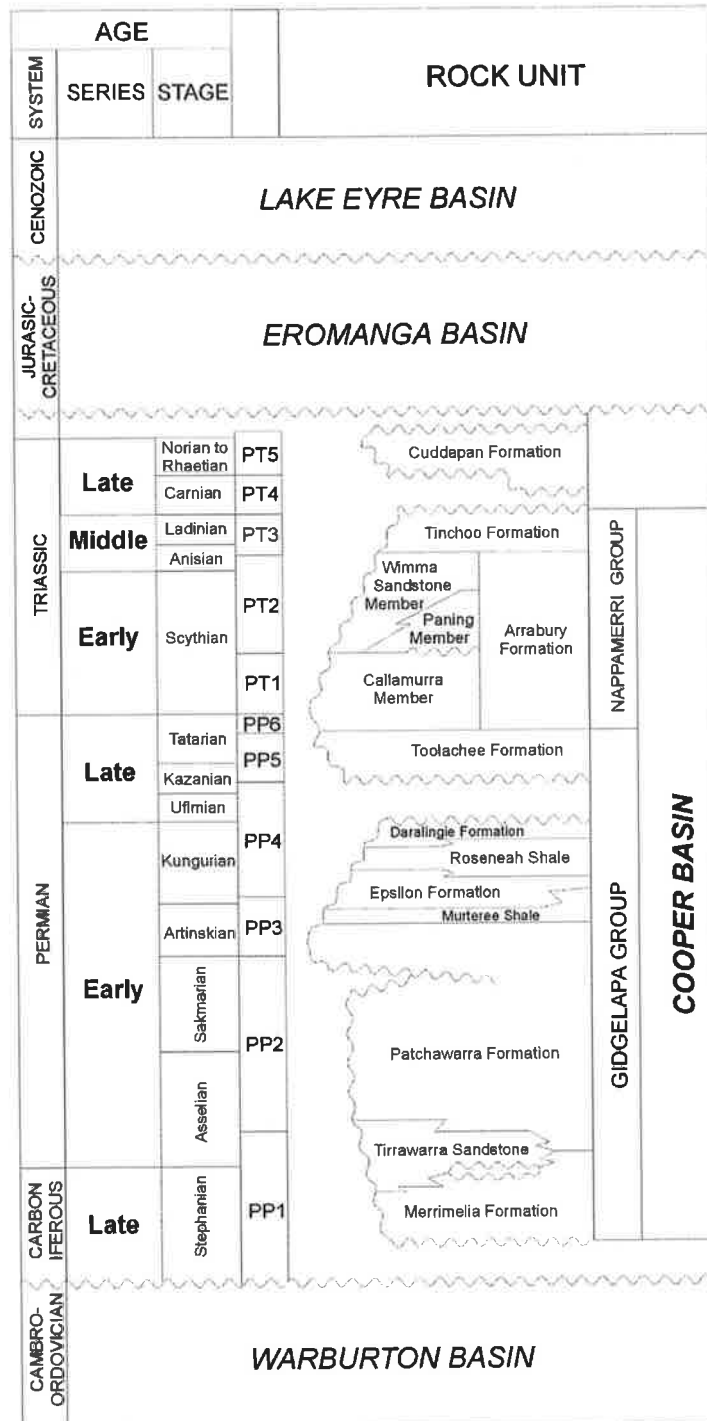


Figure 1.2 Stratigraphic column of the Cooper Basin, South Australia (Alexander *et al.*, 1998).

Sedimentation continued with a post-glacial epoch of peat swamp deposits, the Patchawarra Formation. In this time, during the Sakmarian, two episodes of tectonic uplift were recorded (Apak *et al.*, 1993, 1997).

The thickest and most widespread unit in the Cooper Basin, the Patchawarra Formation, was deposited in a fluvial meandering system. It consists of sandstones, siltstones, shale and thick and extensive coal seams (Alexander *et al.*, 1998).

Two transgressive phases covered the Cooper Basin with lakes, resulting in the Murteree and Roseneath Shale deposition (Stuart, 1976; Thornton, 1979). Between them, the retreat of lakes led to the deposition of shoreline sandstones, the Epsilon Formation (Stuart, 1976). Structural growth recommenced in Early Permian, during deposition of the Epsilon Formation and culminated in the Daralingie unconformity from late Early Permian to Late Permian (Gravestock and Jensen-Schmidt, 1998).

The Murteree Shale is composed of horizontally laminated siltstones, which were deposited in a deep lake environment (Williams, 1995).

The deposition of the Epsilon Formation followed the retreat of the Murteree lake. The Epsilon Formation was deposited in a deltaic environment and consists of sandstones, shales and coal seams.

The Roseneath Shale comprises siltstones, mudstones and minor sandstones deposited in a lacustrine environment (Stuart, 1976; Thornton, 1979). Regional transgressions and regressions influenced the deposition of the Murteree-Epsilon-Roseneath formations. An open basin setting with restricted access to the sea was proposed by Thornton (1979) and Stuart (1976).

The Daralingie Formation is dominated by carbonaceous and micaceous siltstones and mudstones with interbedded sandstones (Alexander *et al.*, 1998). The lower part is transitional from the underlying Roseneath Shale, while the top of the formation is marked by an unconformity. The lower part of Daralingie Formation was deposited in a deltaic environment (Williams, 1995), while a floodplain environment with high sinuosity fluvial channels was interpreted for middle to upper part.

A hiatus of about 12 Ma is recorded palynologically at the end of Early Permian (Thornton, 1979). This hiatus is known as the Daralingie unconformity and represents a tectonic episode that caused uplift and erosion of the Permian section of the Cooper Basin. The differential uplift formed several anticlines and closures (Battersby, 1976; Thornton, 1979; Heath, 1989) that were eroded, resulting in a

hiatus between Daralingie and Toolachee Formation (Thornton, 1979; Heath, 1989). After Daralingie Formation sedimentation, the tectonic activity caused fault reactivation that resulted in an angular contact between Daralingie and Toolachee Formation (Gray and Roberts, 1984).

From the Late Permian to Late Triassic, sedimentation continued with the deposition of meandering fluvial deposits of the Toolachee and Nappamerri Group (Thornton, 1979). During the time of deposition of Nappamerri Group, a change in the climate at the onset of Triassic is shown by the occurrence of red beds (Papalia, 1969, Thornton, 1979).

The Toolachee Formation consists of interbedded sandstones, siltstones and carbonaceous shales, with thin coal seams and conglomerates. It was deposited in a meandering fluvial system. Williams (1982, 1984) recognized three facies associations within the Toolachee Formation: point bars sandstones, mudstones and coal seams, and locally developed alluvial channels. The Toolachee Formation disconformably overlies the Daralingie Formation and unconformably overlies older rocks down to the level of the Warburton Basin on ridges (Gravestock and Morton, 1994).

Since natural gas was discovered in 1963 at Gidgealpa and Tirrawarra Fields, many authors have contributed to the better understanding of the Cooper Basin Triassic stratigraphy. Papalia (1969), defined the "Nappamerri Formation as the Triassic sediments with "redbed characteristics" conformably overlying the Gidgealpa Group (Toolachee Formation) and unconformably overlain by the Eromanga Basin. Papalia described four informal rock units in the Nappamerri Formation. Youngs and Boothby (1982, 1985) interpreted the depositional environments of four different informal lithological units within the formation. In 1989, Channon and Wood (Santos, South Australia) and Powis (Esso Australia, Queensland), conducted separate reviews of Triassic stratigraphy and delineated two formations: the Arrabury Formation (Late Permian to Early Triassic) and Tinchoo Formation (Middle to Late Triassic). The Arrabury Formation was subdivided into members: Callamurra Member (defined by Channon and Wood, 1989) and Paning and Wimma Sandstone Members (defined by Powis, 1989). Channon and Wood based their subdivision on the work of Youngs and Boothby (1985). The Nappamerri Formation is unconformably overlain by eroded

remnants of the Late Triassic Cuddapan Formation (Powis, 1989). Foster (1982) recognised the age of (*P. microcorpus*) zone as being middle Late Permian.

The Arrabury Formation consists of mudstones, siltstones and sandstones. It was deposited in a vegetated floodplain with ephemeral lakes and soil horizons developed on exposed areas around low-sinuosity meandering rivers (Alexander *et al.*, 1998). The base of the formation overlies the Toolachee Formation and unconformably overlies sedimentary rocks and volcanics of the Warburton Basin towards the Cooper Basin margins and in places on the Gidgealpa-Merrimelia-Innaminka Ridge (Alexander *et al.*, 1998). The Arrabury Formation contains no coals; it was formed during the 'Early Triassic coal gap' (Veevers *et al.*, 1994). The floodplain sedimentation evident in the Toolachee Formation continued into the Triassic but a climate change at this time is suggested by the change to soil formation rather than coal deposition on the floodplains. The change from gray to red beds further supports such a climate change.

In the northern part of Cooper Basin, South Australia, the Tinchoo Formation consists of sandstones, intraclast conglomerates and siltstone interbeds deposited in a low-sinuosity fluvial environment (Alexander *et al.*, 1998).

The Nappamerri Group is widespread in South Australia and is more than 500 m thick in the Nappamerri and Patchawarra Troughs. It onlaps structural ridges and was eroded around the margins of the Cooper Basin.

The Cuddapan Formation disconformably overlies the Tinchoo Formation and is disconformably overlain by the Eromanga Basin sediments, Poolowanna Formation and Hutton Sandstone. The Cuddapan Formation comprising interbedded siltstone and sandstone with minor mudstone, was deposited in a high-sinuosity fluvial system. However, only eroded remnants exist in South Australia (Wiltshire, 1982).

The Late Triassic Cuddapan Formation has a limited extent and was disconformably deposited over the Nappamerri Group (Wiltshire, 1982; Veevers, 1984 and Wopfner, 1985).

A major phase of uplift during the Late Triassic to Early Jurassic terminated the deposition of the Cooper Basin sediments and resulted in erosion of the sediments in the southeastern part of Cooper Basin (Kantsler *et al.*, 1983; Heath *et al.*, 1989).

### 1.4.2 Structure of the Cooper Basin

As early as 1958, Sprigg suggested that Cooper Basin structural evolution is associated with rejuvenation of the pre-existent basement structures (Sprigg, 1958). The mechanisms of the Cooper Basin deformation were interpreted as being dominantly extension (Stanmore, 1989), compression (Sun, 1997; Apak *et al.*, 1997) or mixed: extension, strike slip and compression (Kuang, 1985). It was concluded that the structural style of the Cooper Basin is the result of various deformation mechanisms (Gravestock and Jensen-Schmidt, 1998).

The main structural elements of the Cooper Basin consist of two intrabasin highs, the Gidgealpa-Merrimelia-Packsaddle-Innamincka Trend and the Murteree-Della-Nappacoongee Trend that separate three major depocentres, the Patchawarra, Nappamerri and Tenappera troughs (Fig. 1.3). The ridges are asymmetric and have the northern margins bounded by major faults, while the southern margins are bounded by minor faults.

### 1.5 PREVIOUS INVESTIGATIONS

Cooper Basin seals have not been rigorously studied even though they are a vital component of petroleum system risk analysis (Gravestock *et al.* 1998). Only limited evaluation of these seals has been done to date.

Bowering (1982) proposed a model that follows the Gussow theory of secondary hydrocarbon migration. This model concerns the Eromanga oil entrapment and shows that oil, after filling a trap beyond its spill-point, is forced into successively higher traps by gas displacement. The conclusion is that each anticlinal trap along the migration path is capable of sealing the entire hydrocarbon column.

Heath *et al.* (1989) noted the strong relationship between the oil discoveries from the Eromanga Basin and associated thin Permo-Triassic seals. They also generalized that the largest oil accumulation occurs below the deepest, most competent top seal, estimated from shale thickness.



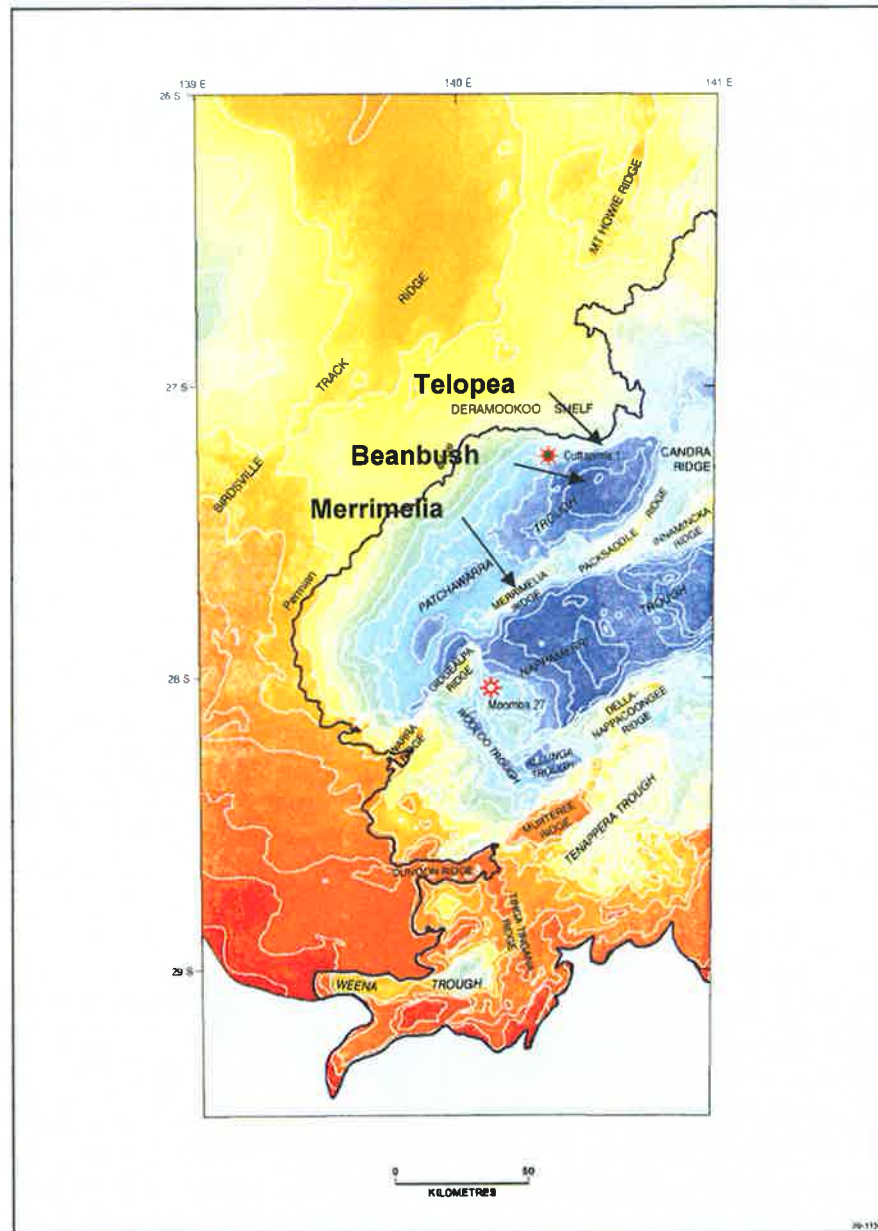


Figure 1.3 Major structural elements of the Cooper Basin, South Australia and approximate location of the studied fields (modified after Gravestock and Jensen-Schmidt, 1998).

Dunlop *et al.* (1992) proposed a model to explain the lack of Cooper Basin gas accumulations on the eastern and southern flanks of the Murteree Ridge. This model suggests that fresh artesian water enhanced gas solubility leading to depletion of gas reservoirs by diffusion.

Solomon (1992) used capillary pressure techniques to determine the capacity of several sealing intervals within the Eromanga Basin. Her results showed that there is

a discrepancy between the excellent seal capacity derived from the capillary pressure results and some of the observed heights of oil columns. This is thought to be due to the poor lateral continuity of mudstone beds (facies changes), as well as fractures and faults.

Boult (1996) and Boult *et al.* (1997) showed that the Birkead Formation in the Eromanga Basin is a capillary seal and traps may be incapable of retaining hydrocarbons to structural spill.

Historically, the Arrabury Formation was regarded as a regional seal above the Permian formations (Gravestock *et al.*, 1998), even though the rocks are heterolithic and comprise both fine-grained sealing lithologies as well as sandy lithologies that form oil and gas reservoirs. Five wells, situated 15 km basinward of the Arrabury Formation zero edge, have been examined in order to test the quality of the Arrabury seal (Gravestock *et al.*, 1998). The source rocks for Eromanga oil occurrences have been queried as being in the Permian, Jurassic or Cretaceous rocks, or from more than one source (Heath *et al.*, 1989, Michaelsen and McKirdy, 1989). Also, the possibility that hydrocarbons migrated through beds of low capillary seal efficiency or through faults and fractures was discussed by Gravestock *et al.* (1998). The lithology of the Arrabury Formation was examined in cuttings and wireline logs (Alexander *et al.*, 1998). It was concluded that the Arrabury Formation contains some poor seal facies and some moderately good reservoirs. Therefore, much of the oil generated in Toolachee, Epsilon and Daralingie Formation has migrated to higher traps through the poor quality Arrabury seal (Gravestock *et al.*, 1998).

Seals were defined on gamma ray logs as >160 API. The thickness of rock meeting this cut-off was divided by total seal interval thickness and recorded as a percent to represent the 'seal efficiency' value. Seal efficiency was calculated in the five examined wells. The results show only 8-18% of the Arrabury Formation has >160 API, regardless of the unit thickness. It was concluded that the Arrabury Formation contains more 'weak links', independent of thickness than was suspected (Gravestock *et al.*, 1998).

There is little published material on the composition and diagenetic history of Triassic rocks in the Cooper Basin.

## 1.6 SEAL POTENTIAL

This project aims to evaluate the reservoir quality and seal potential of the Triassic strata in the Cooper Basin. The seal potential of cap rocks is defined as seal capacity, seal geometry and seal integrity (Kaldi and Atkinson, 1993, 1997).

Any lithology can form a seal in the subsurface, if the threshold pressure of the potential seal rock is greater than the buoyancy pressure of the hydrocarbons within the accumulation (Schowalter, 1979; Sneider, 1987; Vavra *et al.*, 1992). The capillary properties of the potential sealing lithology, exemplified by the size of the largest interconnected continuous pore throat, together with the relative densities of the hydrocarbon and formation water control the capacity of a seal to hold back hydrocarbons (Kaldi and Atkinson, 1993, 1997).

Seal capacity refers to the calculated hydrocarbon column height that a lithology can support. Mercury injection capillary pressure analyses were obtained by measuring the pressure needed to inject mercury into the rock pore throats. A Micromeritics Autopore 9410 mercury injection porosimeter was used. The threshold pressure, the most important factor in seal capacity calculation was determined from mercury injection capillary pressure curves.

Seal geometry comprises thickness and areal extent of the seal. A relatively thick lithology, whose sealing properties are laterally consistent over the entire structure, is needed for a seal to be effective. Seal geometry was determined from lithostratigraphic correlation of identified lithofacies and by comparison with depositional analogs from the literature.

Seal integrity refers to rock mechanical properties such as ductility and likelihood of fluid conduct microfractures and faults. It was evaluated from rock mechanics studies from literature analogs, petrographic analysis and review of region stresses.

The sealing potential of each of the sealing lithologies was derived as a product of the three individual components. The various seals were ranked in relation to each other, using a semiquantitative seal potential model developed by Kaldi and Atkinson (1993, 1997).

## CHAPTER TWO

### SEDIMENTOLOGY AND LITHOFACIES ANALYSIS

#### 2.1 INTRODUCTION

Papalia (1969) described the Nappamerri Formation as interbedded varicoloured shales, sandstones and siltstones deposited in a continental fluvial to lacustrine environment. Later work on lithostratigraphy and environments of deposition of the Triassic strata was carried out by Youngs and Boothby (1985), Powis (1989), Channon and Wood (1989) and Alexander *et al.* (1998). They concluded that the Triassic sediments, both Nappamerri Group and Cuddapan Formation were deposited in a floodplain environment with meandering channels, localized lakes and soils developed on exposed areas.

“There are no significant differences in the environment of deposition of each of the formations and members identified within the Nappamerri Group. In fact, without palynology, it is virtually impossible to discriminate between the formations on visual appearance and sedimentological logging alone” (Pers. Comm. N. Lemon, 1999). Therefore, the Triassic sediments were interpreted for their depositional environment irrespective of their stratigraphic classification.

Many factors contribute to the architecture of pores and pore throats. Understanding these is critical in predicting sealing or reservoir properties. The capacity of a rock to hold back hydrocarbons or to permit the flow of fluids depends on its capillary pressure properties. The capillary properties, in turn, are controlled by the rock's pore system. The size of pores and pore throats and their distribution control the porosity and permeability of a rock. Depositional facies control the original texture and composition of a rock. The diagenetic transformations that occur after deposition are determined by chemical composition, nature of fluids that circulate through the rock pore system, burial and temperature (Wilson, 1993). Processes such as cementation, dissolution and compaction commonly result in modifications to pore and pore throat sizes and their interconnectivity.

## **2.2 DATA AVAILABILITY**

This chapter utilizes the core logs from wells of the Cooper Basin fields, completed by Alexander, 1999. Cores from thirteen wells of Merrimelia, Telopea and Beanbush fields were examined at the State Core Library of South Australia. Core log descriptions and interpretations of Alexander, 1999 were utilized. Some of the core was relogged and some previously unlogged core intervals were logged.

This chapter documents techniques used to characterize the pore geometry of the identified sealing and reservoir lithologies. Porosities and pore diameters were evaluated with petrographic image analysis. All pore measurements in thin sections are presented in Appendix 3.4. The size of pores and their distribution are illustrated by histograms of pore diameter (microns) versus frequency (%) in Plates 2.4, 2.5 and 2.6. Statistical parameters were calculated to characterize the pore distribution (Appendix 2.1). Threshold pressures and pore throat size distributions were evaluated from mercury injection capillary pressure curves (Appendix 3.6). Sizes of pores and pore throats were also measured under the scanning electron microscope, wherever possible.

## **2.3 IDENTIFICATION OF THE DEPOSITIONAL ENVIRONMENTS AND LITHOFACIES DESCRIPTION**

The logged lithofacies were interpreted and grouped into depositional facies based on the depositional models described in detail by Galloway and Hobday (1983), Miall (1996) and Walker and Douglas (1984). The model for lateral and vertical accretion of meandering rivers deposits, together with the morphological elements of a meandering river system (Walker and Douglas, 1984), are presented in Fig. 2.1 and Fig. 2.2, respectively. A depositional model of a meanderbelt sand body and of a chute-modified point bar, together with characteristic vertical sequences and electrical logs (Galloway and Hobday, 1983) are illustrated in Fig. 2.3 and Fig. 2.4, respectively.

Each lithofacies represents a rock unit with distinctive features, including composition, grain size, bedding characteristics and sedimentary structures. The interpretation of depositional facies was based equally on both lithofacies

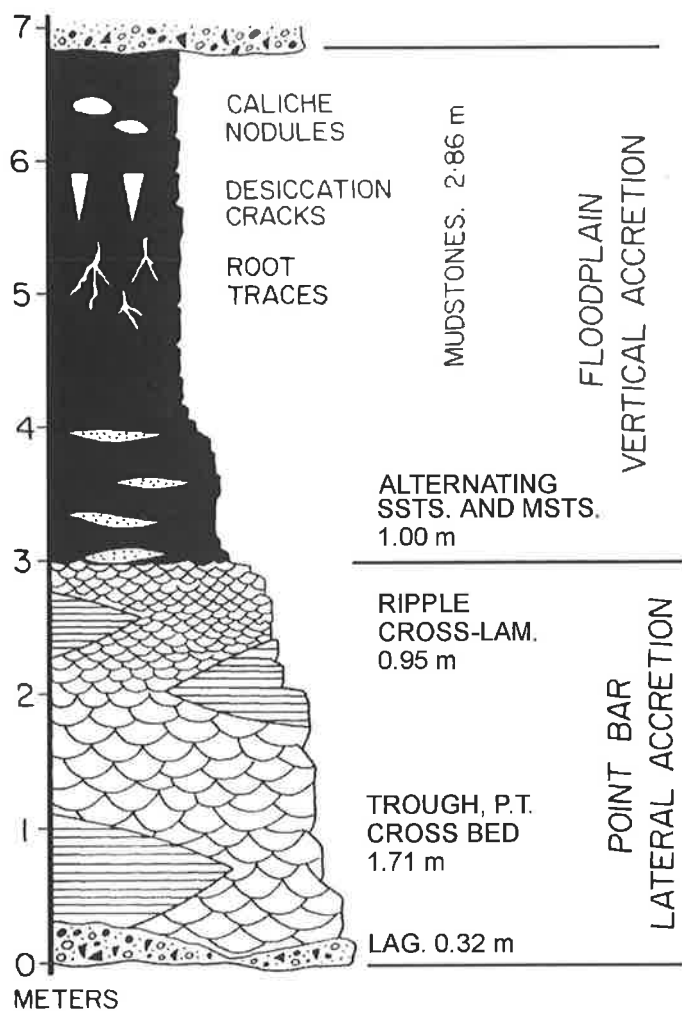


Figure 2.1 Model for lateral and vertical accretion deposits of meandering rivers (after Walker and Douglas, 1984).

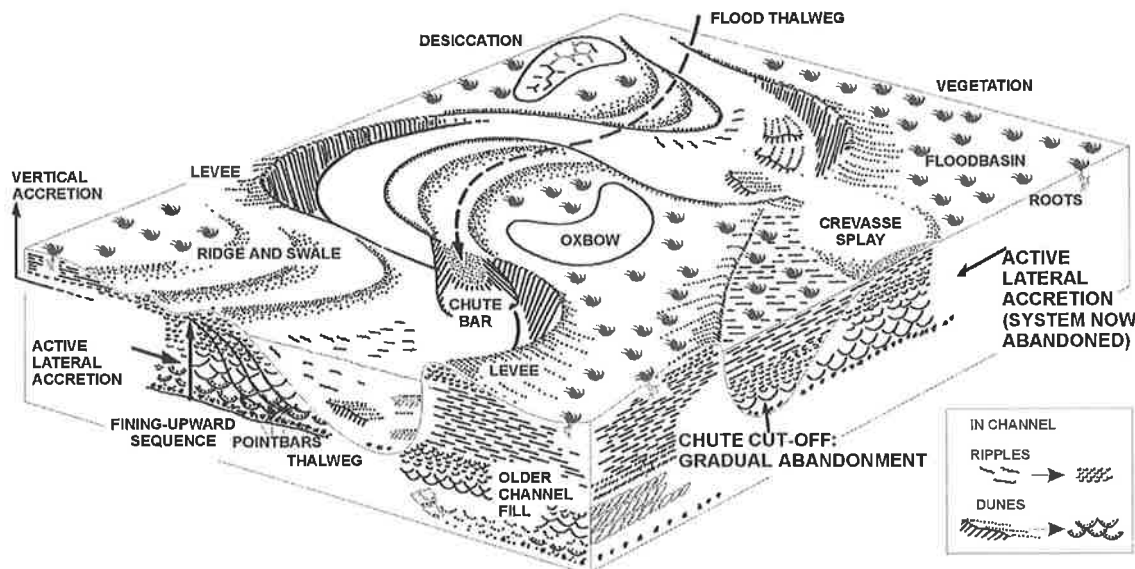


Figure 2.2 Block diagram showing morphological elements of a meandering river system (after Walker and Douglas, 1984).

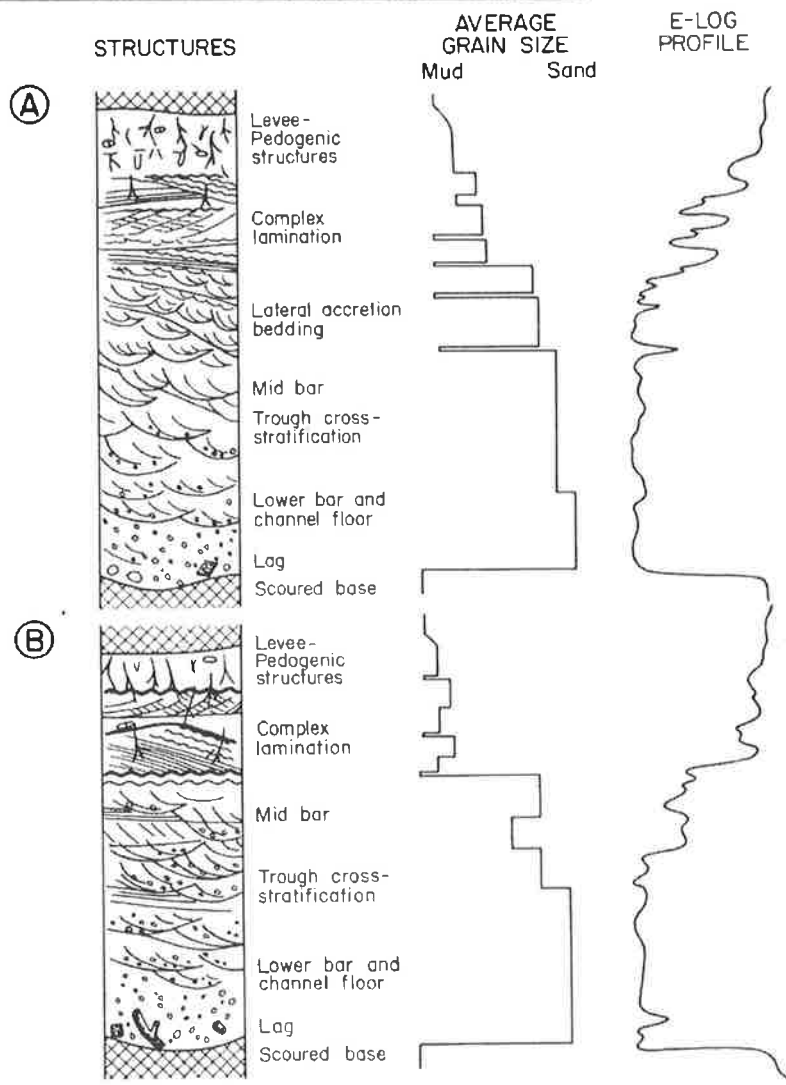
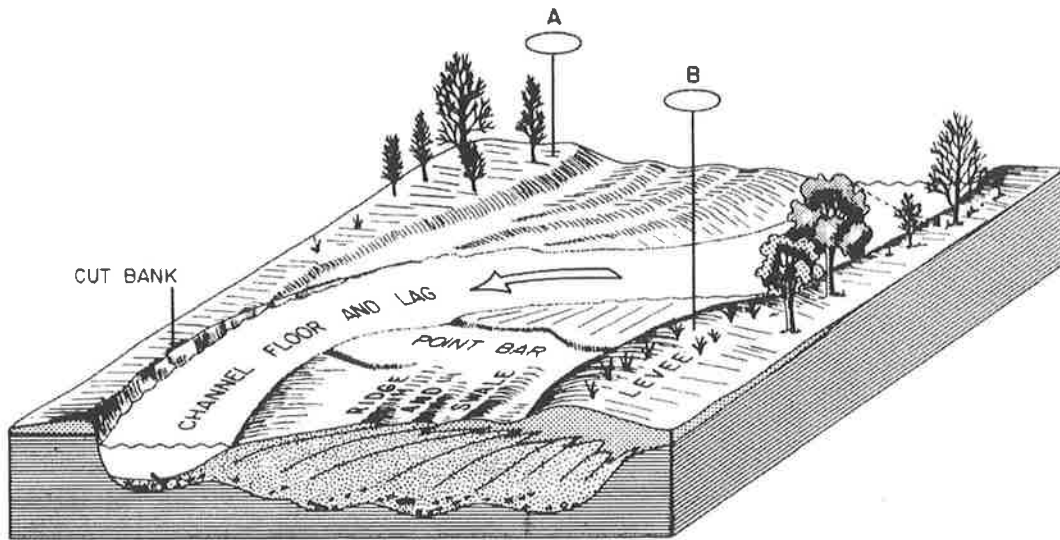


Figure 2.3 Generalized depositional model, vertical sequences and electric (SP) log profiles of a meanderbelt sand body produced by a high-sinuosity channel. (A) Complete fining-upward sequence of the mid- or downstream point bar. (B) Truncated vertical sequence of the upstream end of the point bar (from Galloway and Hobday, 1983).

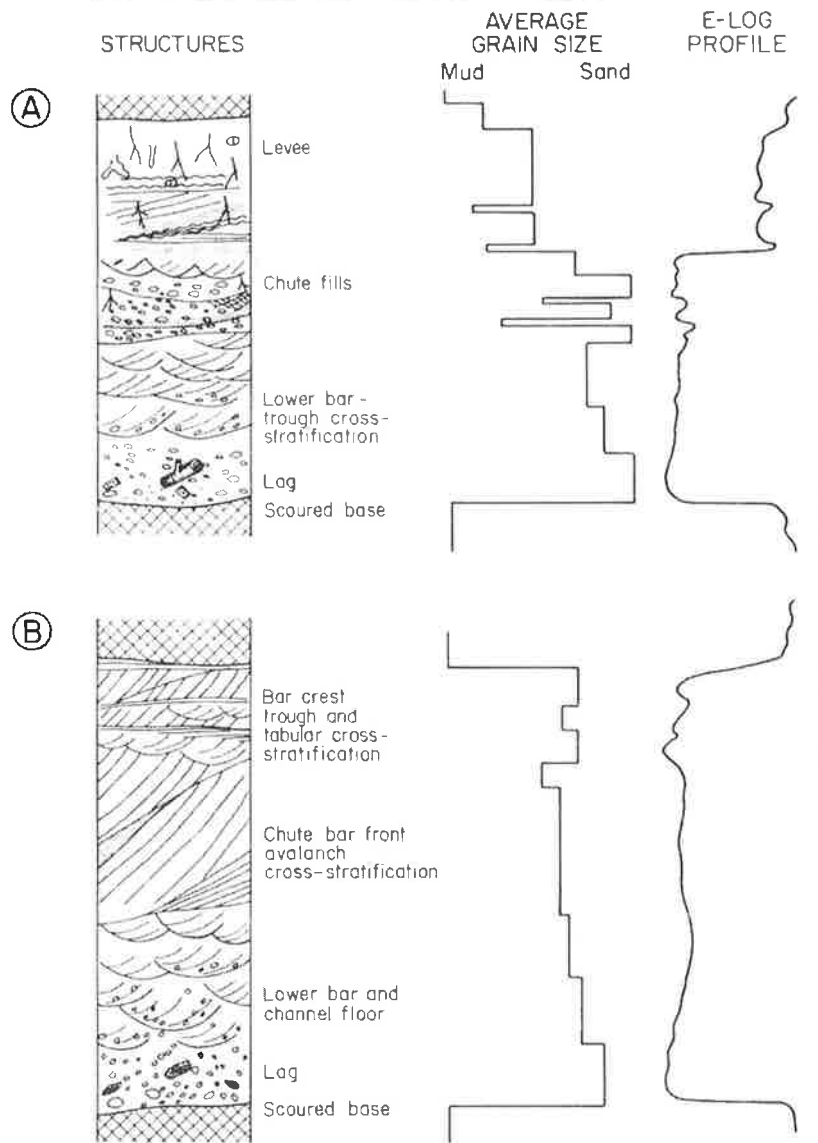
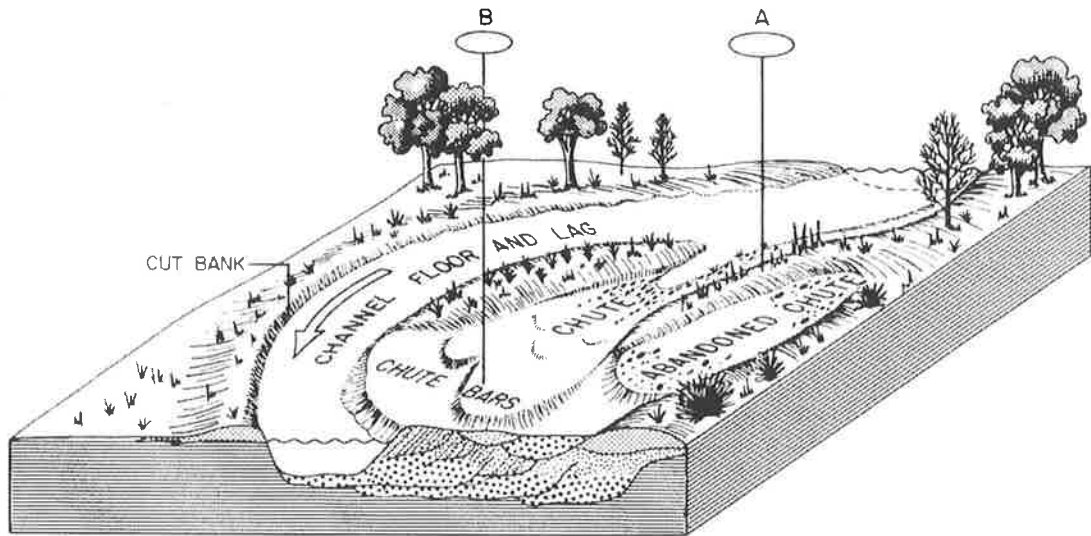


Figure 2.4 Depositional model, vertical sequences and electric log (SP) profiles of a chute-modified point bar. (A) Upstream portions of the point bar are capped by chute-channel deposits. (B) Downstream, the channel and lower point bar deposits are capped by chute-bar sediments (from Galloway and Hobday, 1983)



identification and position in the sequence. The interpreted depositional facies were matched to wireline log signatures in examples taken from the studied cores (Plates 2.1, 2.2 and 2.3).

The depositional facies identified in the Triassic strata correspond to two major components of the fluvial meandering system: channel sediments (RF-1 to RF-5, SF-1) and the fine components that form the inter-channel sediments and floodplains (SF-2 to SF-4). In the description of depositional environments, references regarding the component lithofacies are made. The lithofacies are named accordingly to the lithofacies scheme (Table 2.1) proposed by Miall (1978).

Facies code	Lithofacies	Sedimentary structures	Interpretation
Gcm	Clast-supported, massive gravel	-	Pseudoplastic debris flow (Inertial bedload, turbulent flow)
Gmm	Matrix-supported, massive gravel	Weak grading	Plastic debris flow (High-strength, viscous)
Sp	Sand, fine to very coarse, may be pebbly	Solitary or grouped planar cross-beds	Transverse or linguoid bedforms (2-D dunes)
Sr	Sand, very fine to coarse	Ripple cross-lamination	Ripples (lower flow regime)
St	Sand, fine to very coarse, may be pebbly	Solitary or grouped trough cross-beds	Sinuuous-crested and linguoid (3-D dunes)
Sh	Sand, fine to very coarse, may be pebbly	Horizontal lamination parting or streaming lineation	Planar-bed flow (critical flow)
Fl	Sand, silt, mud	Fine laminations, very small ripples	Overbank, abandoned channel, or waning flood deposits
Fm	Mud, silt	Massive, desiccation cracks	Overbank, abandoned channel, or drape deposits
P	Palaeosol carbonate (calcite, siderite)	Pedogenic features: nodules, filaments	Soil with chemical precipitation

Table 2.1 Facies classification (modified after Miall, 1978).

The depositional environment of various lithofacies associations interpreted in cores and their wireline logs signature are shown in Plates 2.1 –2.3. Crevasse splay deposits and palaeosols are characteristic of the lower Nappamerri Group (Merrimelia 29, Plate 2.1). Point bar lateral accretion deposits preferentially developed in the upper part of Nappamerri Group (Telopea 2, Plate 2.2) and in Cuddapan Formation (Beanbush 1, Plate 2.3). Lacustrine muds/silts, overbank floodplain deposits and more distal crevasse splays occur in Cuddapan Formation (Beanbush 1, Plate 2.3).

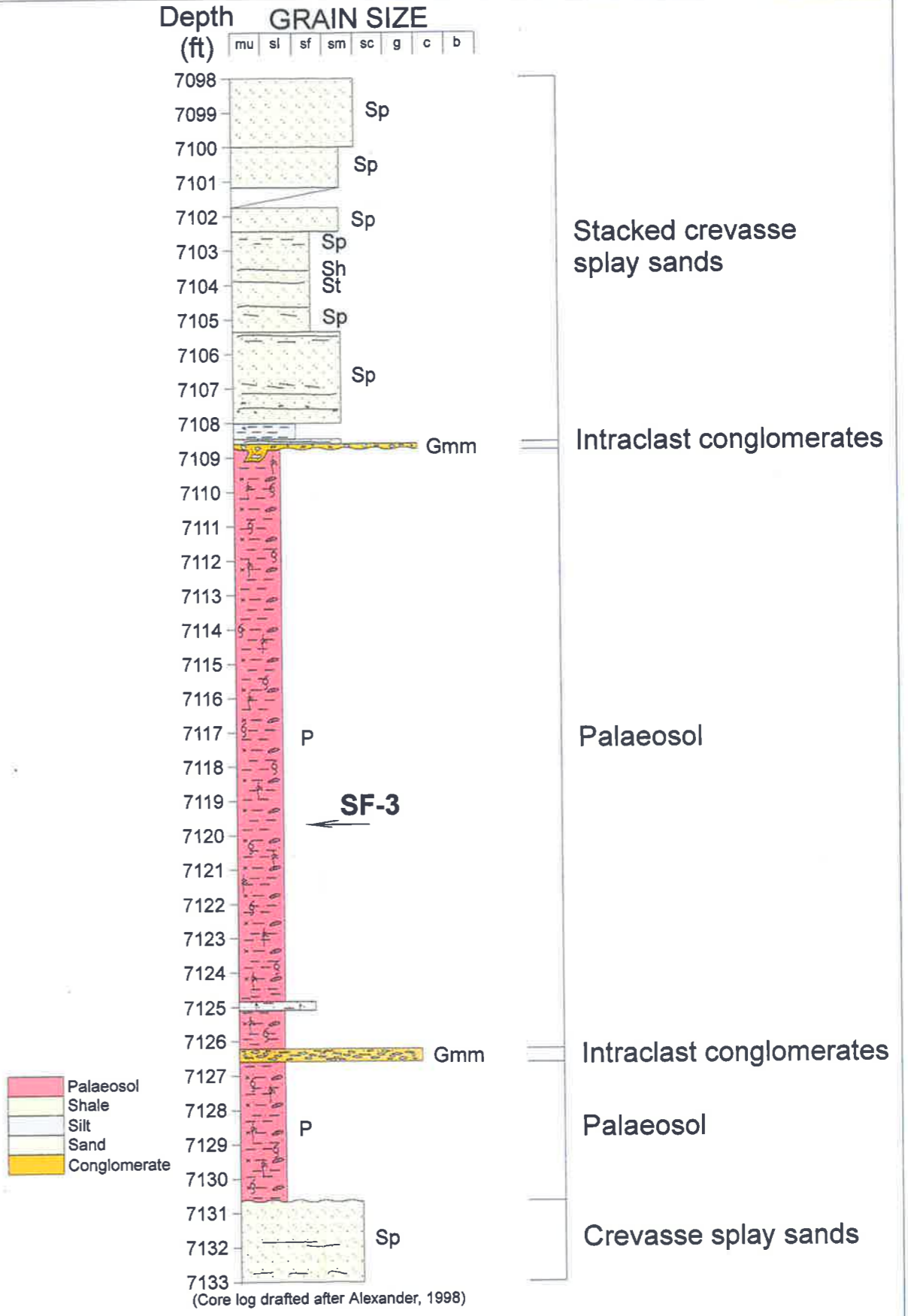
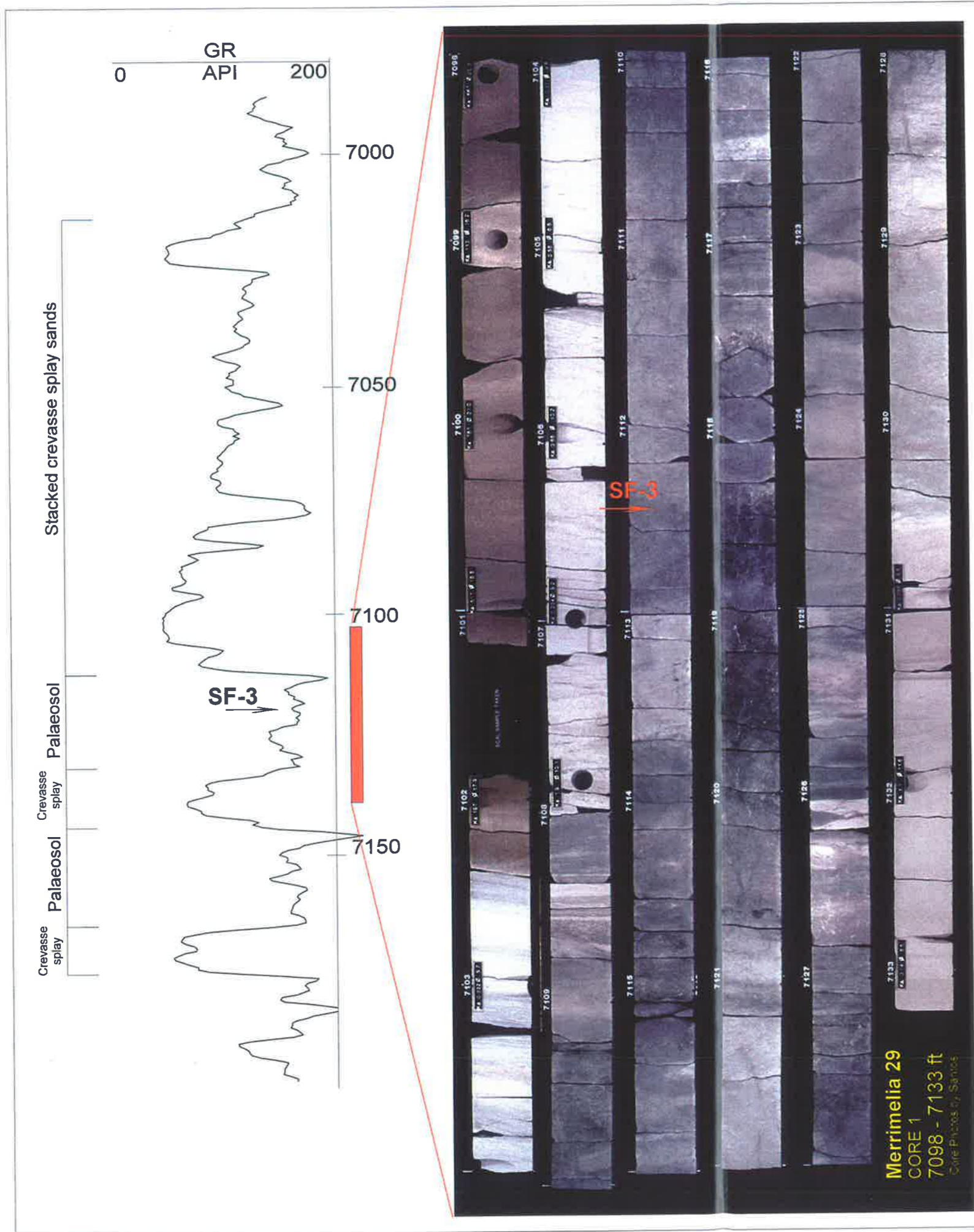
## 2.4 LITHOFACIES CLASSIFICATION AND DESCRIPTION

Five reservoir lithofacies (rock types RF-1 to RF- 5) and four sealing lithofacies (rock types SF-1 to SF-4) were identified according to their depositional environment:

- RF-1 gravels from the base of fluvial channels;
- RF-2 fluvial channel sands;
- RF-3 chute sands;
- RF-4 crevasse splay sands;
- RF-5 sands at the top of point bars;
- SF-1 diagenetically-modified fluvial sandstones;
- SF-2 lacustrine mudstones;
- SF-3 palaeosols;
- SF-4 floodplain mudstones.

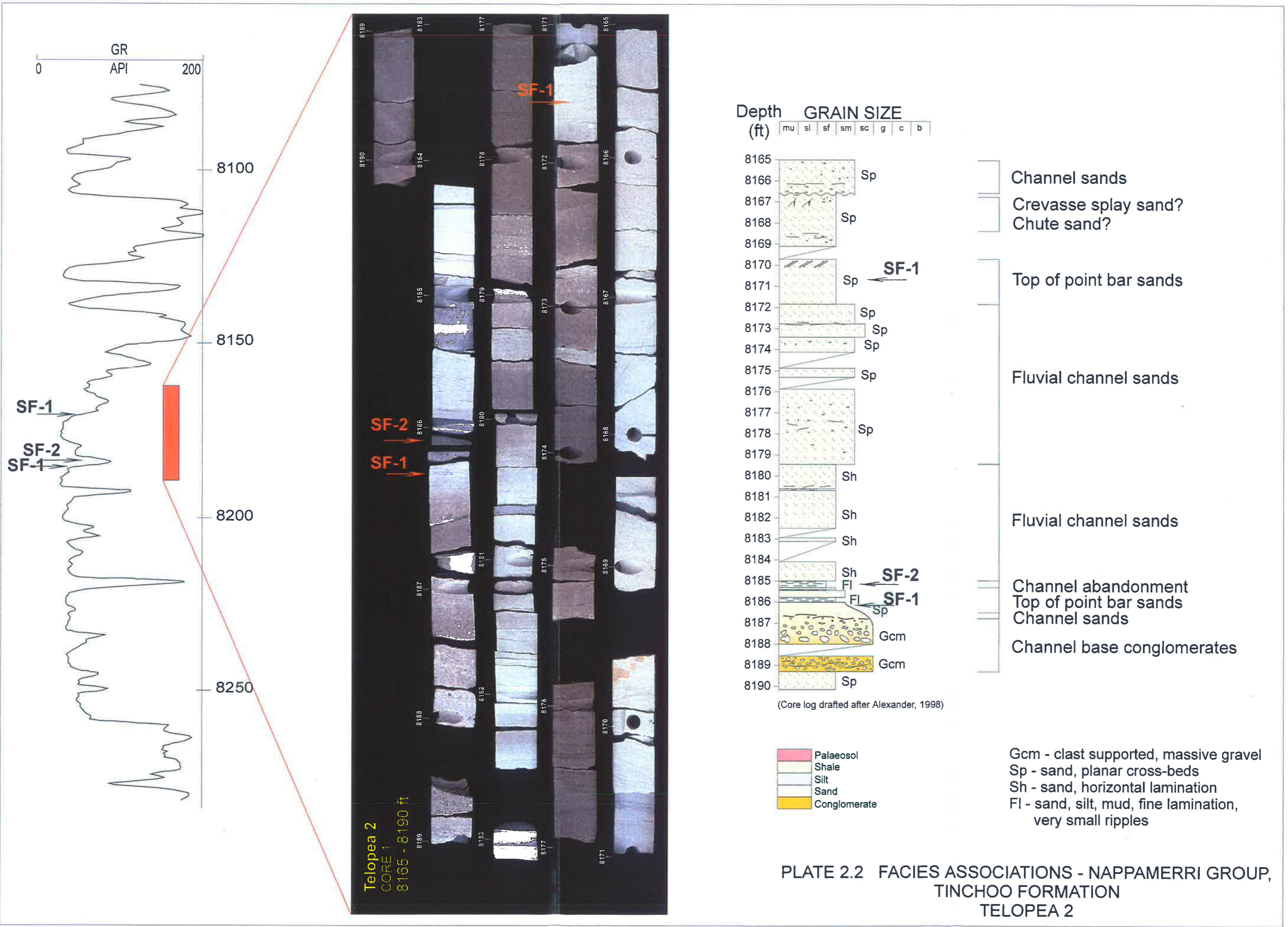
The following are discussed for each lithology:

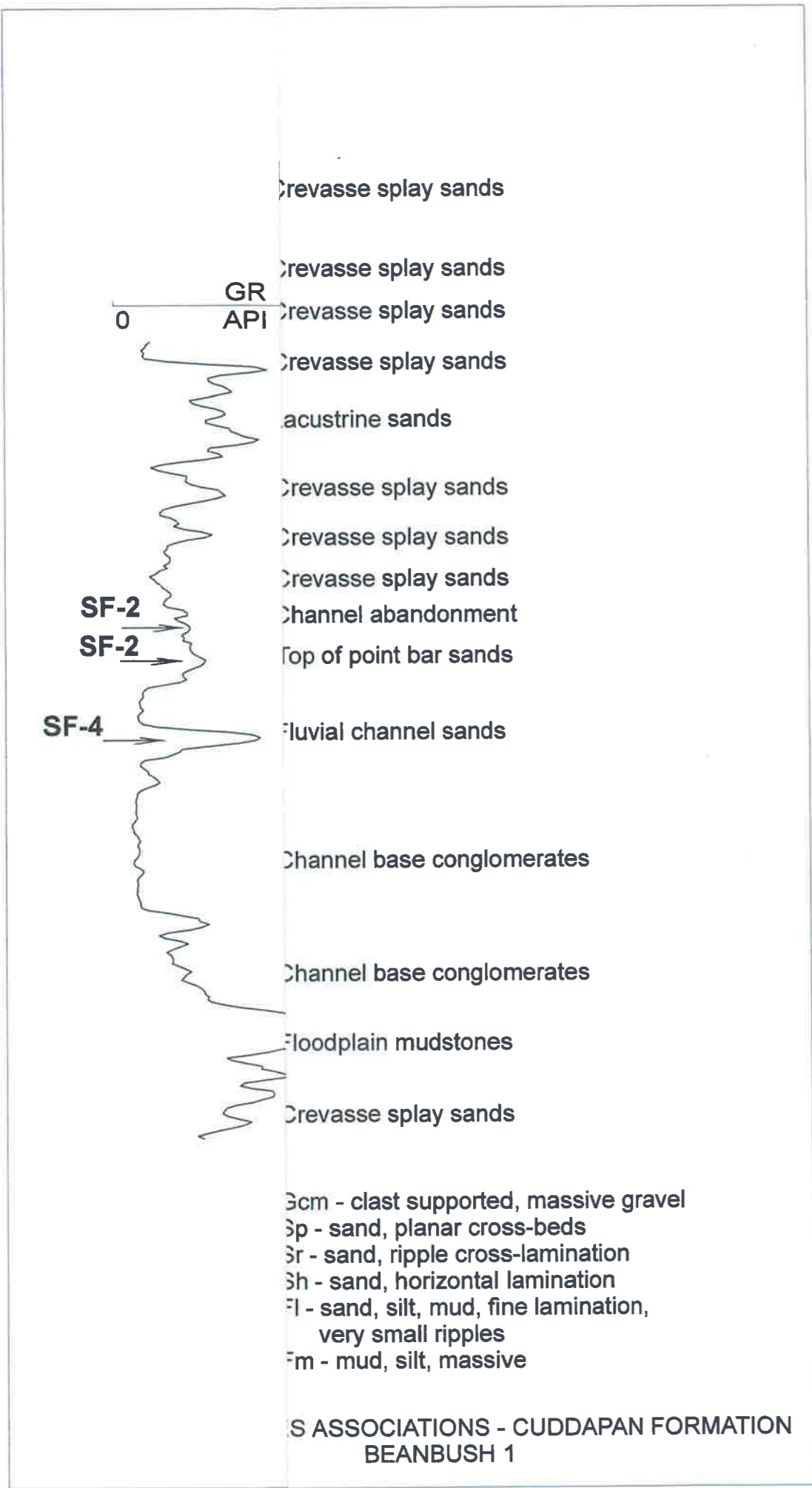
- Lithofacies;
- Position in sedimentary sequence;
- Sedimentary structures;
- Textural characteristics;
- Petrographic composition;
- Diagenetic processes;
- Porosity types;
- Pore size distribution;
- Pore throat size distribution;
- Core porosity and permeability.



Gmm - matrix supported, massive gravel    Sh - sand, horizontal lamination  
 Sp - sand, planar cross-beds                      P - palaeosol  
 St - sand, trough cross-beds

**PLATE 2.1 FACIES ASSOCIATIONS - NAPPAMERRI GROUP, CALLAMURRA AND PANING MEMBERS, MERRIMELIA 29**





Framework grain composition together with porosity, cement and matrix proportions were grouped for each environment of deposition and illustrated in Fig. 4.3. The relative proportions of various types of cements and porosities identified in the studied samples are shown in Figs. 4.9 and 5.1, respectively.

#### **2.4.1 RF-1 Gravels from the base of fluvial channels (Plate 2.4)**

These rocks are conglomerates deposited at the base of point bars, above a basal erosion surface (Plates 2.2 and 2.3). They consist of clast-supported pebble gravels with a massive structure (Gcm). This facies is interpreted to be deposited by low strength; pseudo-plastic debris flows (Miall, 1996). Deposits are quartzitic and poorly sorted. Thickness of conglomerates varies from 0.7 m in Telopea 2 to 1.3 m in Beanbush 1. Another type of conglomerate is the intraclast conglomerate (Gmm). The rocks constitute of granule and cobble sized reworked grey-brown mudstone and siltstone and quartz pebbles in a muddy sandstone matrix (Alexander *et al.*, 1998). Thickness of intraclast conglomerates in Merrimelia 29, is less than 15 cm (Plate 2.1)

Many intersections at the base of channels show poorly sorted massive pebble gravels (Plate 2.4.a and 2.4.e), with subangular to subrounded grains. The compaction is illustrated by straight-line contacts of quartz overgrowths to stylolites. Quartz is the dominant framework grain with small amounts of lithics and matrix. Quartz cementation (Plate 2.4.c, 2.4.g and 2.4.k) and grain dissolution (Plate 2.4.f) are the characteristic diagenetic events.

Total porosity in gravels, mainly intergranular porosity (Plate 2.4.k) varies from 12.7% to 30% by the rock volume. Secondary porosity from dissolution (Plate 2.4.f) and microporosity occur in equal amounts: 3% - 4%. The primary pores are clean and well interconnected. Clay minerals, mainly kaolin, fill some pore spaces creating microporosity that can form up to 44% of the total kaolin filled area. Average pore diameter, measured in thin sections ranges from 186 to 569 microns and standard deviations of pore distribution from 114 to 531 microns (Appendix 2.1) suggest a wide spread of sizes about the average (Plate 2.4.d and 2.4.h).

Scanning electron microscopy reveals pore sizes of 50 - 500 microns (Plate 2.4.c and g) and micropores of up to 10 microns. The pore throat size curves display a trimodal distribution. The first class of pore throats corresponds with the micropores between kaolin booklets (throat sizes between 0.7 and 1.3 microns). The second class illustrates the throats of the primary pores (throat sizes from 3 to 5 microns).

The third class is associated with oversized pores (throats sizes between 7 and 40 microns) and formed by dissolution (Plate 2.4.l). In Telopea 2, the average pore throat size from class three is smaller than in Beanbush 1 due to a higher content of quartz overgrowth cement that diminishes some of the pore throats (Plate 2.4.f). RF-1 samples present the largest throat sizes and therefore the highest permeability. Mercury/air threshold pressures are 2 - 5.4 psi (Plate 2.4.j). Ambient core porosity varies from 2.7% to 12.8% and horizontal plug permeability ranges from 36 mD to 1880 mD.

#### **2.4.2 RF-2 and RF-3 Fluvial channel and chute sands (Plate 2.5)**

This facies comprises moderately sorted, fine to medium-grained sands with planar cross-beds (Sp), trough cross-beds (St) and planar bedding (Sh) at the base. These sandstones were deposited by sand transport across the lower and mid point bar. This facies displays a fining-upward trend from basal conglomerates to fine-grained sands at the top of point bars. Thickness of point bar deposits varies from 1 m in Telopea 2 (Plate 2.2) to 3 m in Beanbush 1 (Plate 2.3).

During floods, small channels or chutes cut directly across the surface of the point bar (Galloway and Hobday, 1983). This facies interrupts the normal fining-upward succession of the point bar comprising an ungraded, clean sand deposit (Fig. 2.4). These rocks are moderately well sorted, fine to medium grained cross-bedded sandstones (Sp).

The sands from the mid section of the point bar units are moderately sorted (fluvial channel) to moderately well sorted (chute sands), fine to medium grained (Plate 2.5.g and 2.5.h), cross-bedded sands (Plate 2.5.a and 2.5.d). The grains are subangular to subrounded, and present straight line to concave-convex grain contacts. Compositionally, the samples are litharenites (Plate 2.5.b and 2.5.e) or sublitharenites. Quartz, mainly monocrystalline, is the main component, comprising 42% - 60% by the rock constitution. Matrix is absent or occasionally present and rock fragments constitute 6% - 25% of the rock composition. Quartz overgrowth cement (Plate 2.5.c, 2.5.f and 2.5.m) is more abundant in fluvial channel sands (7%-10%) than chute sands (5%). Kaolin cementation (Plate 2.5.c, 2.5.f and 2.5.m) comprises 5% - 7% of the rock volume in both cases. Small amounts of illite and siderite are present in chute sands.

Total porosity, estimated from thin sections, varies between 13% and 21% by total rock volume, and is mainly interconnected primary pores. Secondary porosity, from dissolution, is 3% to 5% and microporosity is 5% of the rock constitution. The average pore size, measured in thin sections is 126 - 219 microns. The pore size histograms illustrate tight distributions, with St. Dev. = 71 – 167 microns, suggesting good packing (Plate 2.5.i and 2.5.j). Scanning electron microscopy reveals pore sizes of 125 - 250 microns (Plate 2.5.c and 2.5.f) and micropores of 30 to 35 microns. Note that scanning electron microscopy measures the pore sizes while mercury injection capillary pressure analysis gives a measure of the pore throat sizes.

The pore throat size distribution shows three pore throat classes. The first, around 1.3 microns, is the microporosity between kaolin booklets. The second class of pore throats, between 2 and 5 microns, represents the primary, intergranular porosity. The third class has the biggest pore throats, between 10 and 22 microns and illustrates throats of secondary pores from rock fragment dissolution (Plate 2.5.k). The better sorting of pore throat distribution in comparison to RF-1 samples, gives these rocks better permeability. Mercury/air threshold pressures have values between 3.5-6.1 psi (Plate 2.5.l). The horizontal plug permeability (ambient) varies from 0.27 mD to 1360 mD and core porosity ranges from 9.2% to 21%.

### **2.4.3 RF-4 Crevasse splay sands (Plate 2.6)**

Crevasse splay sands are deposited during flood events, when the increased flow velocity of the river produces local breaches in the levees and results in the deposition of sand lobes on the floodplain. Crevasse splay deposits thin away from the channel and interfinger with floodplain shales. This facies has a heterogeneous internal structure that reflects the multiple shallow flood events (Galloway and Hobday, 1983). These rocks occur in cores as cross-bedded (Sp) and ripple cross laminated (Sr), moderately to moderately well sorted fine or medium sands. Crevasse splays can develop on the floodplain (Merrimelia 29, Plate 2.1) or into lakes (Beanbush 1, Plate 2.3). Crevasse splays present a coarsening-upward profile and can be seen as multiple events or stacked crevasse splay deposits within the floodplain sediments (Plate 2.2). The thickness of individual crevasse splay deposits ranges from 20 cm in Beanbush 1 (Plate 2.1) to 3.5 m in Merrimelia 29 (Plate 2.1).

Crevasse splay sandstones are cross-bedded (Plate 2.6.a) or ripple crossed laminated (Plate 2.5.d), moderately to moderately well sorted, fine or medium sands



(Plate 2.6.g), with subangular to subrounded grain shapes. The quartz grains and rock fragments are surrounded by siderite (Plate 2.6.b, 2.6.c, 2.6.f and 2.6.l) or clayey matrix (Plate 2.6.e) or present mainly straight-line grain to grain contacts. Samples are litharenites (Plate 2.6.b) or sublithic wackes (Plate 2.6.e). Kaolin, quartz overgrowth and siderite act as cements.

Average porosity, estimated from thin section is 9.55%. The total porosity is mainly remnant primary porosity (Plate 2.6.b, 2.6.f and 2.6.l) and minor secondary and microporosity. Samples can be totally clay cemented in which case the only porosity is microporosity, common in a distal crevasse splay, or have pore spaces with average mean pore diameters of 141 - 244 microns and St. Dev. = 90 – 200 microns, similar to a proximal crevasse splay (Plate 2.6.h and 2.6.i). Measurements of pore sizes under SEM show values of 70 to 200 microns.

The differences in the pore throat distribution are related to proximity to the main fluvial channel, thus illustrating the role of sedimentary control. Beanbush 1, 8716' sample was probably deposited as a distributary mouth developed from a crevasse splay. The sample is a clay-cemented sandstone. Pore throat sizes are poorly sorted, with the majority of pore throats lying within a large range, from 0.0065 to 0.03 microns (Plate 2.6.j). The small size of pore throats suggests a very tightly packed rock where the original porosity was lost due to compaction, facilitated by the high matrix content. The small population of pore throats with radius between 0.2 - 0.4 microns represents microporosity between the kaolin booklets. Merrimellia 7, 7108'4" sample is a proximal crevasse splay developed on a floodplain. The pore throat size distribution (Plate 2.6.j) is dispersed and presents two populations. The first population corresponds to microporosity between compacted kaolin booklets, and varies between 0.2 - 1.2 microns. The second population represents pore throat sizes of 2.5 to 5.5 microns. Siderite cementation reduces the size of pore throats. The threshold pressure varies between 8.6 psi (sample deposited in proximal environment) and 1142 psi (sample deposited in distal environment) (Plate 2.6.k). Core plug porosity varies between 8.2% - 18.8% and horizontal permeability ranges from 0.16 mD to 105 mD.

#### **2.4.4 RF-5 Fine-grained sands from the top of point bars (Plate 2.7)**

Towards the point bar top (Plates 2.2 and 2.3), the sands fine upward, become rippled and contain interbedded mud lamination. This facies is deposited under declining channel flow rates (Galloway and Hobday, 1983).

Examples in this study illustrate planar cross bedding (Sp) (Plate 2.3), horizontal bedding (Sh) (Plate 2.2) and silty wisps. The rocks are moderately to poorly sorted, fine-grained sands.

The samples from the top of point bars show planar cross bedding and silty wisps (Plate 2.7.a and 2.7.e); are moderately well sorted, fine-grained sands (Plate 2.7.d and 2.7.h), with subangular to subrounded grains and tangential to straight-line grain contacts. Petrographically, the rocks are litharenites (Plate 2.7.b and 2.7.f) or lithic wackes. Detrital clay proportions up to 17%, is important in favouring compaction and therefore obstructing the pore system. Kaolin (Plate 2.7. b and 2.7.c) precipitates in higher proportions than quartz overgrowth cement in this group. Siderite precipitation (Plate 2.7.f, 2.7.g and 2.7.k) is present from trace amounts up to 45% by the total rock composition.

The pores in these sands are filled with kaolin, siderite (Plate 2.7.b, 2.7.f and 2.7.k) and minor illite obstructs the pore throats. The remnant pores are very small, with little interconnectivity. The average total porosity estimated from thin section is 8.2% and is dominated by microporosity. A pore size distribution could not be defined as majority of pores are filled with kaolin (Plate 2.7.b) and too small to measure easily. Measurements of pore sizes under SEM show pores of up to 50 microns, mainly modified primary pores (Plate 2.7.c).

The pore throat curve displays good sorting and the throat sizes vary between 0.3 and 0.5 microns (Plate 2.7.i). These sizes correspond to the kaolin framework microporosity and the small size of throats suggests that kaolin has been compacted, a process favoured by organic matter and matrix. The threshold pressures have values between 136 and 156 psi (Plate 2.7.j). Core plug porosity is 9.6% and permeability is 0.37 mD.

#### **2.4.5 SF-1 Diagenetically-modified fluvial sandstones (Plate 2.8)**

This lithofacies is situated at the top of a point bar succession and was identified in cores (Telopea 2) as sealing oil accumulations (Plate 2.2 and 2.8.a). The rocks contain planar cross bedding (Sp) and silty wisps. The samples are moderately well sorted fine to very fine sands.

Essentially, facies SF-1 is the same as RF-5 in terms of deposition but in core this rock type is devoid of oil staining despite occurring immediately above oil-saturated intervals. As such, it is a seal.

The rocks illustrate planar cross-bedding and silty wisps (Plates 2.8.a and 2.8.e). The samples are moderately well sorted, fine to very fine sands (Plate 2.8.g), with subangular to sub-rounded grains and straight-line to concave-convex grain contacts (Plate 2.8.b). Petrographically, the samples are sublitharenites (Plate 2.8.b) and lithic wackes (Plate 2.8.f). Kaolin is the main cement (up to 10% of the rock volume) followed by quartz overgrowth (up to 7% of the rock volume) and trace amounts of illite and siderite. Kaolin (Plate 2.8.c, 2.8.d and 2.8.h) completely surrounds or partially fills the pores, obstructing the pore throats. The remnant primary pores are very small, with little to no interconnectivity (Plate 2.8.b and 2.8.c) and are thus ineffective for hydrocarbon migration.

The average total porosity estimated from thin section is 8% and is dominated by microporosity between kaolin booklets.

The Scanning Electron Microscope reveals remnant pores with sizes of 5 to 80 microns (Plate 2.8.h). The threshold pressure varies between 167 - 251 psi (Plate 2.8.j). The pore throat size ranges between 0.2 - 0.5 microns (Plate 2.8.i); this corresponds with the microporosity between kaolin booklets. Core plug average porosity is 8.5% and air permeability (ambient) is 0.39 mD.

#### **2.4.6 SF-2 Lacustrine mudstones (Plate 2.9)**

Lacustrine mudstones form in the lower floodplain environment within abandoned channel depressions (eg. ox bow lakes) as well as in broad shallow lakes on the floodplain. Both environments comprise mud and silt.

The channel abandonment deposits occur as narrow and elongate channel plugs at the top of point bars and within the channel-fill deposits (Galloway and Hobday, 1983). They consist of silt or clay deposited from the main stream during floods (Walker, 1984). The sediments are deposited from suspension and from weak traction currents. This facies shows alternating laminations of clayey siltstones and silty claystones (FI), whose thickness varies from few centimeters to 1.5 m (Plates 2.2 and 2.3).

Shallow lake deposits comprise finely laminated siltstones with local very fine-grained sandstones. Sedimentary structures include synaeresis cracks, dewatering structures, swaley bedding and small scale ripples that were probably reworked by wind generated waves (Alexander *et al.*, 1998, Youngs and Boothby, 1985).

In the Nappamerri Group, lacustrine deposits are exemplified by moderately well sorted, fine-grained muddy sands with horizontal, even lamination (Sh) or small scale

ripples (Sr) in Beanbush 1 (Plate 2.3). Sand was introduced into these environments during floods as crevasse splay deposits.

This facies occurs as moderately well sorted fine-grained muddy sands (Plate 2.9.a and 2.9.b) with horizontal, even lamination and small scale ripples (Plate 2.9.a) or as alternating laminations of clayey siltstones and silty claystones (Plate 2.9.e and 2.9.f). Grains are mainly subangular to sub-rounded, floating in the clay-rich matrix (Plate 2.9.b, 2.9.c and 2.9.d). Local cementation comprises kaolin, siderite and pyrite (Plate 2.9.g).

In thin sections, the samples lack apparent porosity (Plate 2.9.b and 2.9.c). One sample has alternating laminae with authigenic kaolin resulting in minor microporosity.

The mercury injection capillary curves show high threshold pressures: 2743 - 9231 psi (Plate 2.9.i) and small pore throat sizes: 0.0012-0.01 microns (Plate 2.9.h). The sample Beanbush 1, 8712'3" illustrates a small population of pore throats of 0.15 microns that corresponds to compacted kaolin framework microporosity (Plate 2.9.h). The variability shown by this facies is a function of variable grain size. Some lacustrine sediments are silty and some are muddy. Core plug measurements of lacustrine facies give porosity ranging from 0.78 –3.4% and ambient/air permeability of 0.025mD.

#### **2.4.7 SF-3 Palaeosols (Plate 2.10)**

This facies represents distal floodplain deposits that formed on exposed areas, in arid or seasonal climates. Palaeosols are exposed to surface weathering processes for extended periods. Evaporation and capillary groundwater flow near the surface during arid periods concentrate the ions that were dissolved by rain infiltration. One result of these processes is the precipitation of carbonate cement (Miall, 1996). These deposits are characterized by an obliteration of the primary sedimentary structures by bioturbation and pedogenesis and the development of a strong, vertical fabric. The sub-vertical structure develops by water movement up and down along root traces and burrows. Diffuse mineral segregation leads to mottling. Mottling is also induced by oxidation or reduction caused by the flux of meteoric water through sediments containing some organic material. Palaeosols are typified by extensive colour banding from gray to orange, red and purple. Palaeosols commonly consist of several layers that vary in color, texture and mineralogy. The variation of palaeosol

maturity depends on many factors. The pedofacies model (Brown and Kraus, 1987 and Kraus, 1987, 1992) relates the palaeosol stage to distance from the alluvial channel. Other factors that influence the palaeosol maturity are related to regional changes in fluvial style and sedimentation rate, that are controlled by tectonic subsidence (Atkinson, 1986), variation in substrate lithology (Theriault and Desrochers, 1993) or variation in biogenic activity and calcium ion supply (Wright, 1990).

Palaeosols (P), well developed in Merrimelia Field are typified by root molds (Plate 2.10.a, 2.10.k), siderite nodules (Plate 2.10.e), sub-vertical structures and breccias associated with collapse structures (Alexander *et al.*, 1998).

These rocks are mottled grey siltstones, claystones or moderately to moderately well sorted very fine argillaceous litharenite (Plate 2.1, 2.10.b and 2.10.f). Quartz, rock fragments and some organic matter comprise the larger grain components. Grains are subangular to subrounded and float in the clay matrix, the main rock component (Plate 2.10.c, 2.10.d, 2.10.g and 2.10.h), which is compacted and practically lacking porosity (Plate 2.10.c and 2.10.h). Siderite occurs as reddish to brown micritic patches (Plate 2.10.b and 2.10.e) or as sparry crystals, replacing rootlets (Plate 2.10.k).

Based on thin section observations, the rocks have no visible porosity. The pore throat distribution displays throat sizes between 0.002 and 0.01 microns (Plate 2.10.i) and the threshold pressures vary between 5484 and 7727 psi (Plate 2.10.j). Porosity ranges from 1.4% - 3.9% and ambient/air permeability is less than 0.001 mD.

#### **2.4.8 SF-4 Floodplain mudstones (Plate 2.11)**

Floodplain deposits form when the stream overflows its river banks and spills across the interchannel areas. Sediments are sand and silt near the channel margin, grading to silt and clay farther away (Galloway and Hobday, 1983). This depositional facies occurs as sheet-like units with considerable areal extent from hundreds of meters to several kilometers (Miall, 1996).

In the studied area, these rocks occur as dark grey to black silty claystones locally including clayey siltstone lenses (Plate 2.3). Generally, the samples are homogenous (Fm). Facies SF-4 originated in similar settings as SF-3, but these rocks represent areas where the water table was high enough to prevent soil development.

Mudstones from floodplain environments are dark grey to black silty claystones (Plate 2.11.e and 2.11.f), locally including clay-rich siltstone lenses (Plate 2.11.a and 2.11.b). Generally, the samples are homogenous. Quartz grains (Plate 2.11.c and 2.11.g) are subangular to subrounded and float within the clay matrix. The matrix consists of detrital clays (Plate 2.11.c, 2.11.d and 2.11.g) and is the main component of the rock, followed by quartz and subordinate rock fragments. The high percentage of clays and organic matter (Plate 2.11.c) has resulted in compaction and complete loss of porosity. Cementation is sporadic, comprising some kaolin, siderite and pyrite. Porosity of samples can be considered negligible. The threshold pressures range between 3921 to 7725 psi (Plate 2.11.i) and pore throat sizes vary from 0.0013 to 0.01 microns (Plate 2.11.h). Core plug porosity ranges between 0.5% to 3.1% and ambient/air permeability between 0.014 to 0.047 mD.

## 2.5 SUMMARY

Based on lithofacies identification, position in sedimentary sequence and using different models from literature, five depositional facies of reservoir rocks (RF-1 to RF-5) and four depositional facies of sealing rocks (SF-1 to SF-4) have been identified. They are: gravels from the base of fluvial channels (RF-1), fluvial channel sands (RF-2), chute sands (RF-3), crevasse splay sands (RF-4), sands from the top of point bars (RF-5), diagenetically-modified fluvial sandstones (SF-1), lacustrine mudstones (SF-2), palaeosols (SF-3) and floodplain mudstones (SF-4). The depositional facies were described in terms of lithofacies, sedimentary structures, textural characteristics, petrographic composition, diagenetic processes, porosity types, pore size distribution, pore throat size distribution, core porosity and permeability.

Nearly all the Triassic sediments in the Cooper Basin were deposited in a meandering fluvial environment. The stratigraphic subdivision of the Nappamerri Group shown in Fig. 1.2 was not particularly evident in the cored intervals logged. In light of this, sampling for seal and reservoir evaluation was based on depositional facies without regard to the exact stratigraphic location.

## PLATE 2.4

### **Sample photographs, thin section and SEM photomicrographs, pore size distribution and mercury injection data of RF-1: Gravels from the base of fluvial channels**

- a. Whitish-light grey, granule to small pebble gravel with grain size of up to 6 mm and massive structure, Beanbush 1, 8735 ft 2 in ( $\Phi = 12.8\%$ ,  $K = 1880$  mD). Each scale bar subdivision represents 1cm.
- b. Porosity distribution in gravel. Large, tabular, interconnected primary pores, protected by euhedral quartz overgrowths. Beanbush 1, 8735 ft 2 in, plane polarized light. Scale bar = 1 mm.
- c. Tabular open pores preserved between quartz overgrowths in gravel. Note the excellent pore interconnectivity. Pore sizes are about 500 microns. Beanbush 1, 8735 ft 2 in. Scale bar = 500 microns.
- d. Pore size distribution (microns) in gravel, Beanbush 1. 8735 ft 2 in. Poor sorting of pores. Average pore size = 569, Standard deviation = 531.
- e. Whitish-light grey pebble gravel, with grain size of up to 8 mm and massive structure ( $\Phi = 9.1\%$ ,  $K = 66$  mD). Teloepa 2, 8188 ft. Scale bar subdivision represents 1cm.
- f. Porosity distribution in gravel. Primary pores preserved between quartz overgrowth cement associated with oversized pores resulted from dissolution. Teloepa 2, 8188 ft, plane polarized light. Scale bar = 1 mm.
- g. Low magnification SEM image of quartz-rich gravel. Open pores of almost 400 microns diameter are protected by quartz overgrowths. Clear pore throats. Kaolin covers some of the framework grains. Teloepa 2, 8188 feet. Scale bar = 200 microns.

- h. Pore size distribution (microns) in gravel, Telopea 2, 8188 ft. Average pore size = 278, Standard deviation = 198.
- i. Pore throat distribution determined from MICP shows three classes of pore throats: 1) associated with micropores (0.7 - 1.3 microns), 2) associated with primary pores (3 - 5 microns) and 3) associated with oversized pores from dissolution (7 - 40 microns).
- j. Mercury injection capillary pressure curves show Hg/air threshold pressures of 2 - 5.4 psi.
- k. Well developed quartz overgrowths, identified by the presence of dust rims and euhedral faces, protecting primary porosity in a gravel. Beanbush 1, 8735 ft 2 in, plane polarized light. Scale bar = 1 mm.



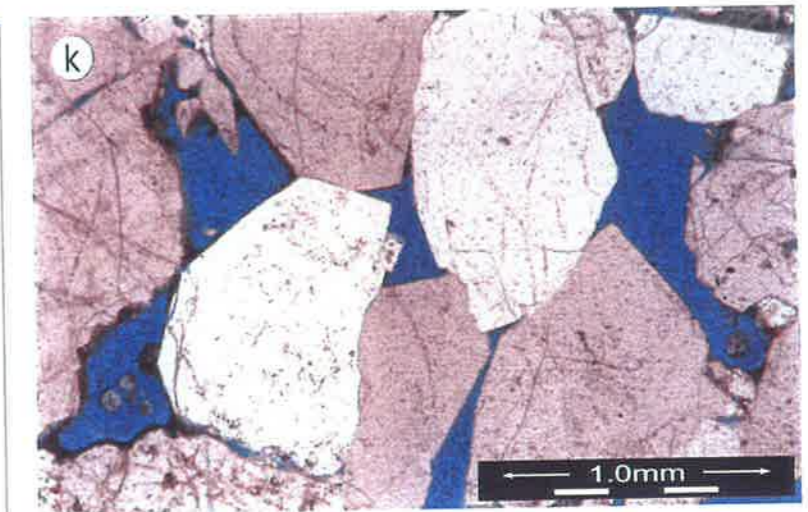
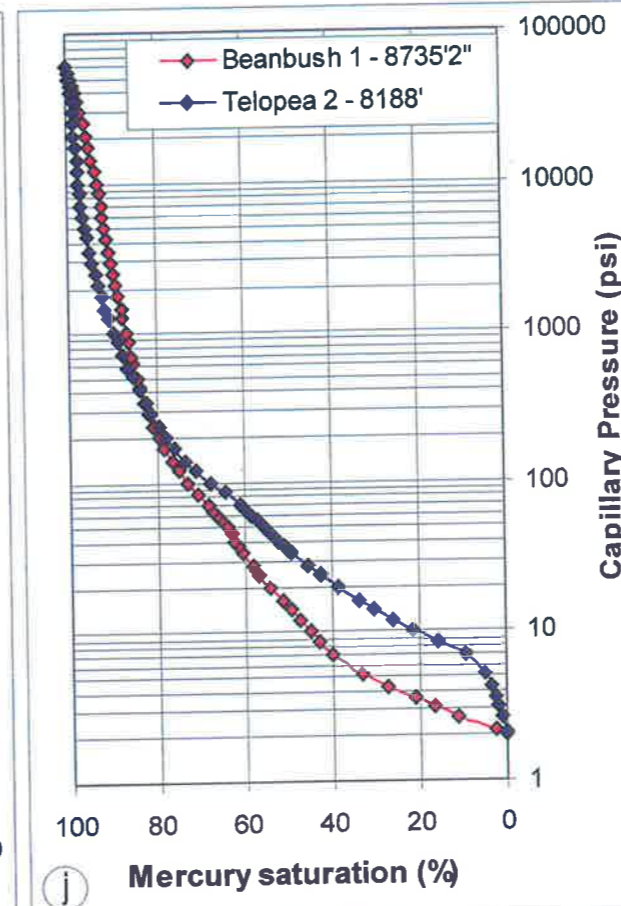
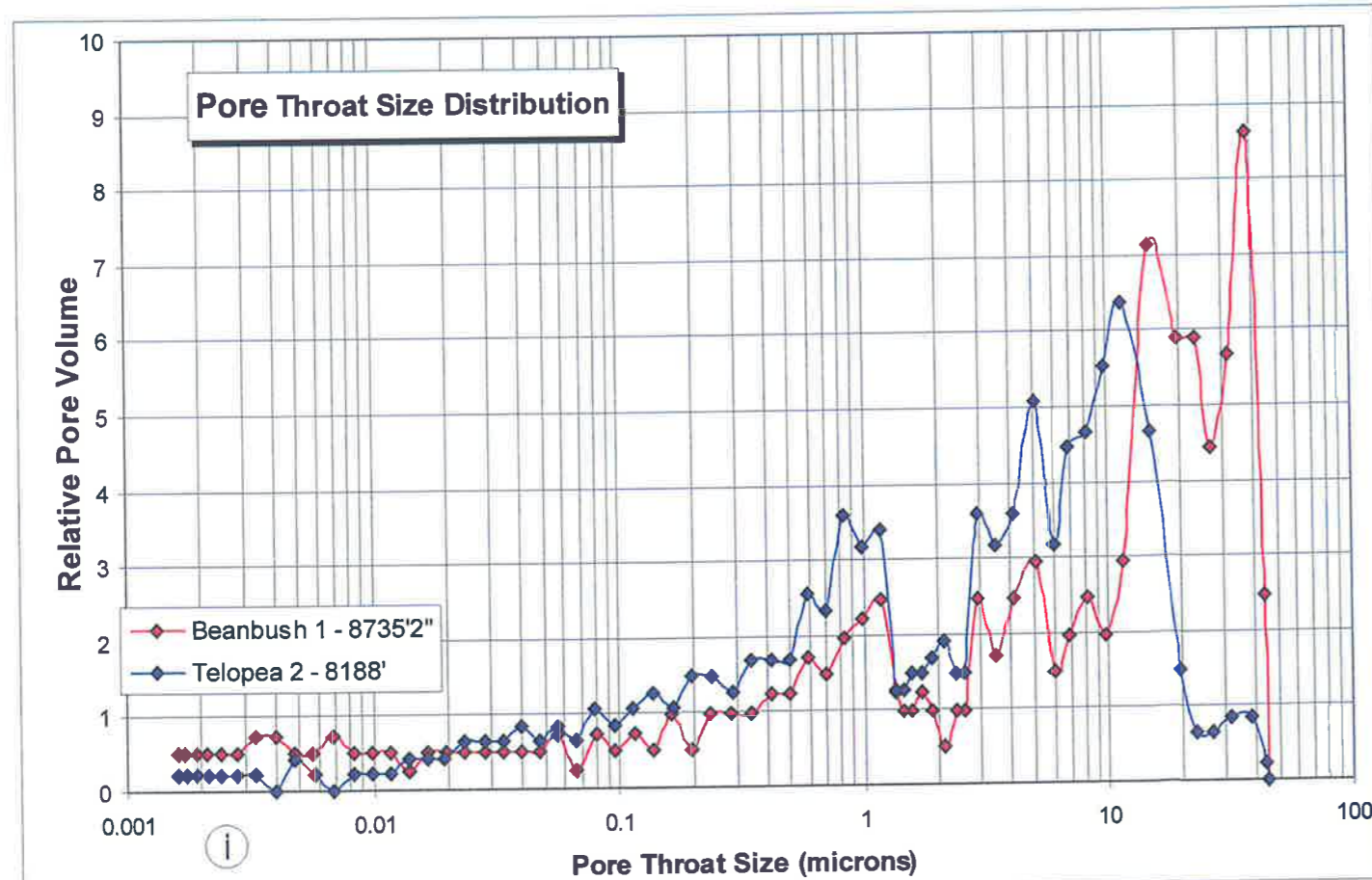
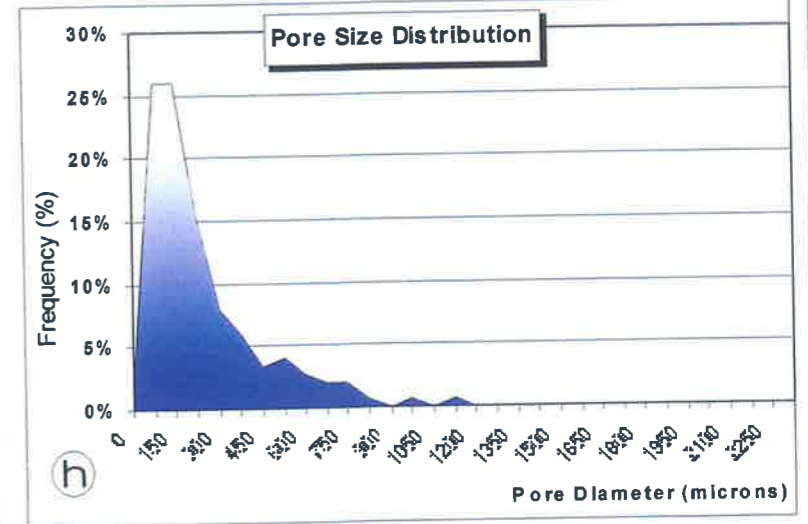
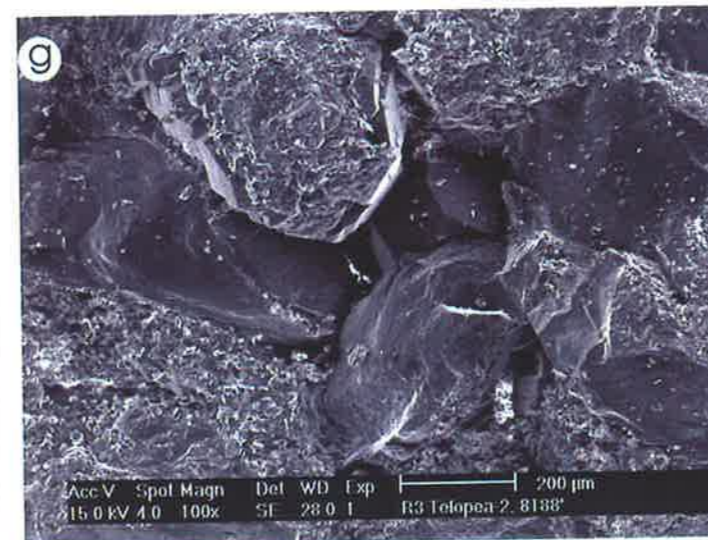
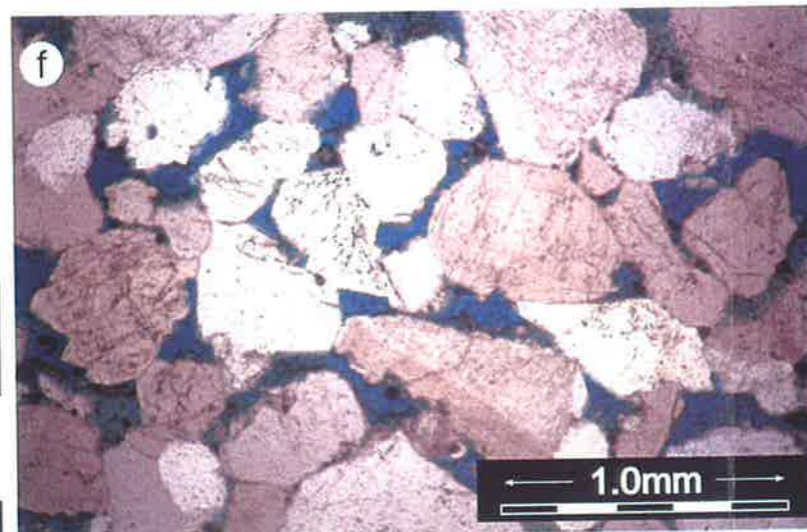
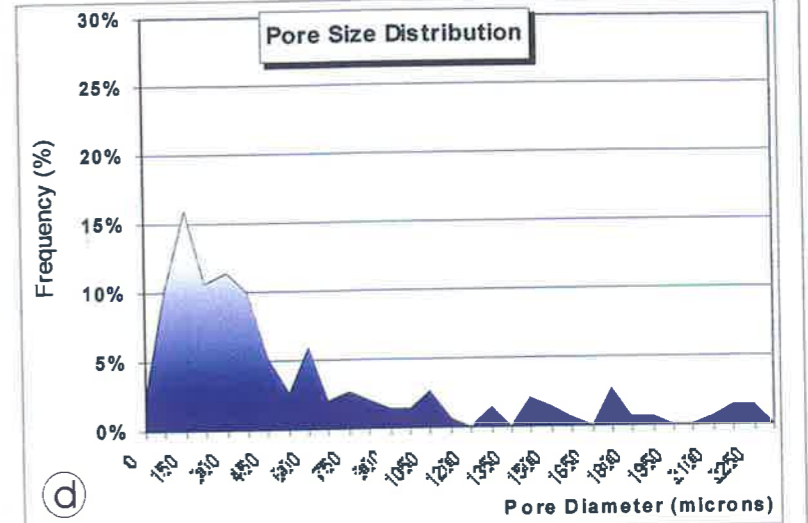
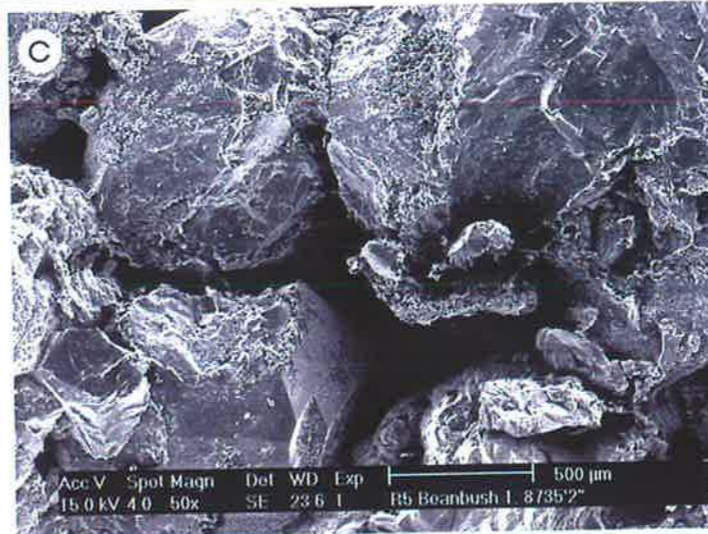
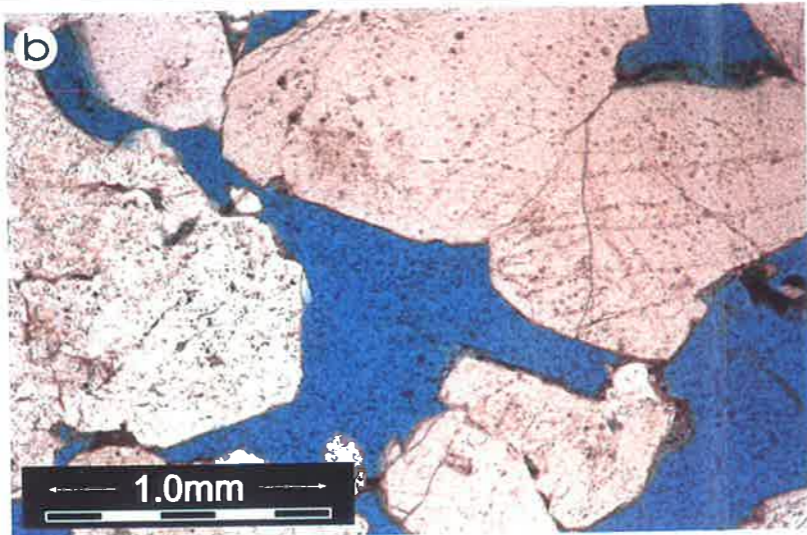


PLATE 2.4  
RF-1: GRAVELS FROM THE BASE OF  
FLUVIAL CHANNELS

## PLATE 2.5

### **Sample photographs, thin section and SEM photomicrographs, grain and pore size distribution and mercury injection data of RF-2 and RF-3: Fluvial channel and chute sands**

- a. Buff, oil stained, moderately sorted, medium grained sandstone with planar cross bedding deposited in a fluvial channel, Merrimelia 29, 7100 ft ( $\Phi = 21\%$ ,  $K = 787$  mD). Each subdivision of scale bar represents 1cm.
- b. Porosity distribution in fluvial channel sand (litharenite). The excellent porosity and high degree of interconnectivity resulted from the combination of partially preserved primary porosity, illustrated by pores with angular contours preserved between euhedral quartz overgrowths and secondary porosity, illustrated by incompletely leached grains or oversized pores. Ductile rock fragments are deformed during compaction, blocking pore throats. Kaolin precipitates in pore or throats spaces, reducing porosity and permeability. Merrimelia 29, 7100 ft, plane polarized light. Scale bar = 1 mm.
- c. Porosity distribution in fluvial channel sand. The intergranular porosity is protected by quartz overgrowth cement, shown by euhedral terminations. Kaolin covers the framework grains. Pores have sizes of up to 200 microns. Merrimelia 29, 7100 ft. Scale bar = 200 microns.
- d. Pale grey to off white, cross-bedded, moderately well sorted, medium grained chute sand, Merrimelia 17, 7078 ft 2 1/2 in ( $\Phi = 16.2\%$ ,  $K = 126$  mD). Each subdivision of scale bar represents 1cm.
- e. Porosity distribution in chute sand (litharenite). Oversized pores, the result of dissolution, and primary pores join together to create good porosity with high interconnectivity. Rock fragments and quartz overgrowths are affected by dissolution. Clay minerals line the pores. Merrimelia 17, 7078 ft 2 1/2 in, plane polarized light. Scale bar = 1 mm.

- f. SEM photomicrograph of chute sand. Pores of up to 150 microns diameter are protected by quartz overgrowths with euhedral terminations and show good interconnectivity. Light dusting of kaolin. Merrimelia 17, 7078 ft 2 ½ in, scale bar = 200 microns.
- g. Grain size distribution in fluvial channel sand suggests fine-grained (PHI = 2 - 3), moderately sorted (St. Dev. = 0.73) sand. Merrimelia 29, 7100 ft.
- h. Grain size distribution in a chute sand illustrates a medium grained (PHI = 1 - 2), moderately well sorted (St. Dev. = 0.65) sand. Merrimelia 17, 7078 ft 2 ½ in.
- i. Good sorting of pore size distribution in fluvial sands, Merrimelia 29, 7100 ft. Average pore size = 165, Standard deviation = 119.
- j. Pore size distribution (microns) in chute sand,. Average pore size = 183, Standard deviation = 167.
- k. Pore throats from MICP analysis display a trimodal distribution. The sizes of pore throats can be associated with the microporosity between kaolin booklets (1.3 microns), with the primary porosity (2 - 5 microns) and with primary coupled with secondary porosity (10 - 25 microns).
- l. Mercury injection capillary pressure curves illustrate Hg/air threshold pressures of 3.5 - 6.1 psi.
- m. SEM micrograph of kaolin booklets interfered with euhedral quartz overgrowth cement. Patches of authigenic kaolin reduces porosity and permeability of sample. Merrimelia 17, 7078 ft 2 in. Scale bar = 20 microns.

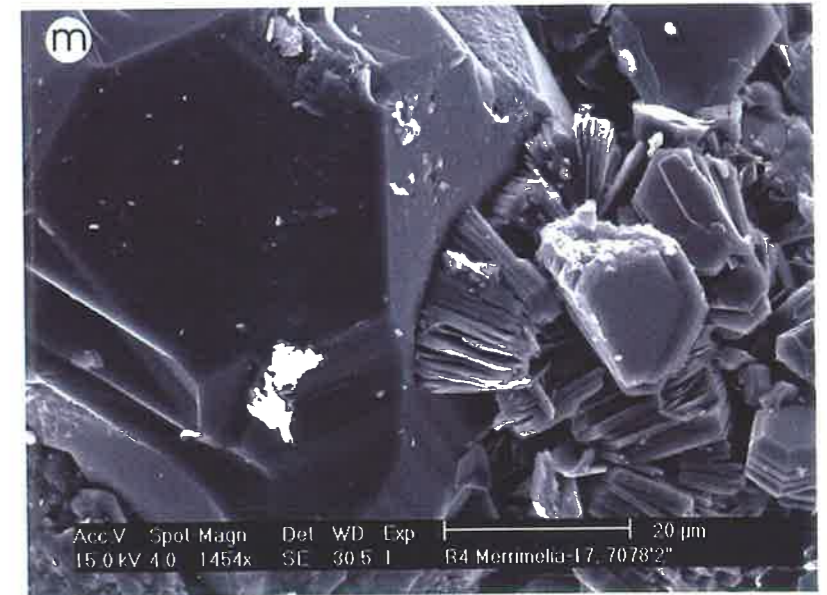
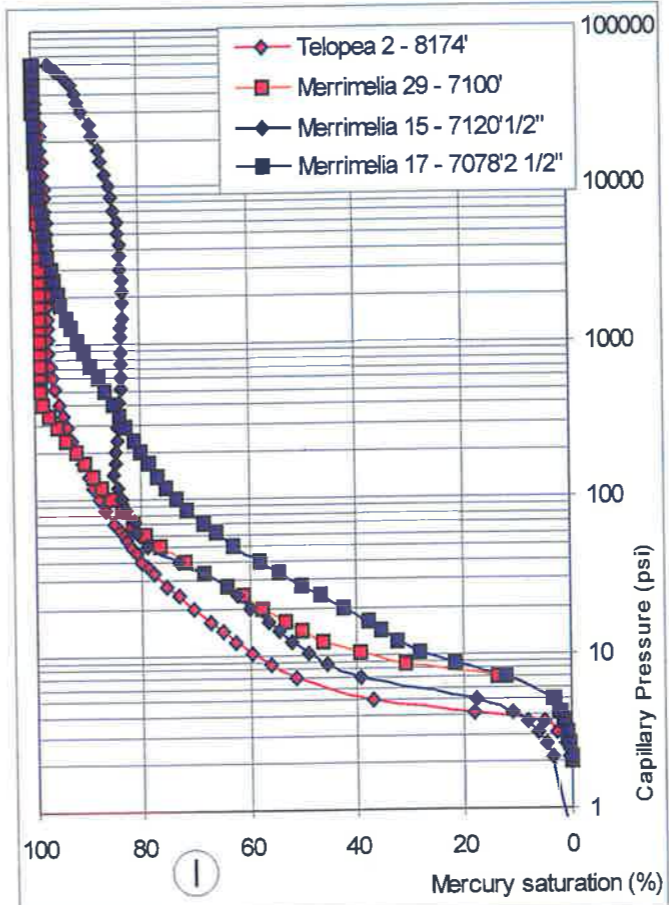
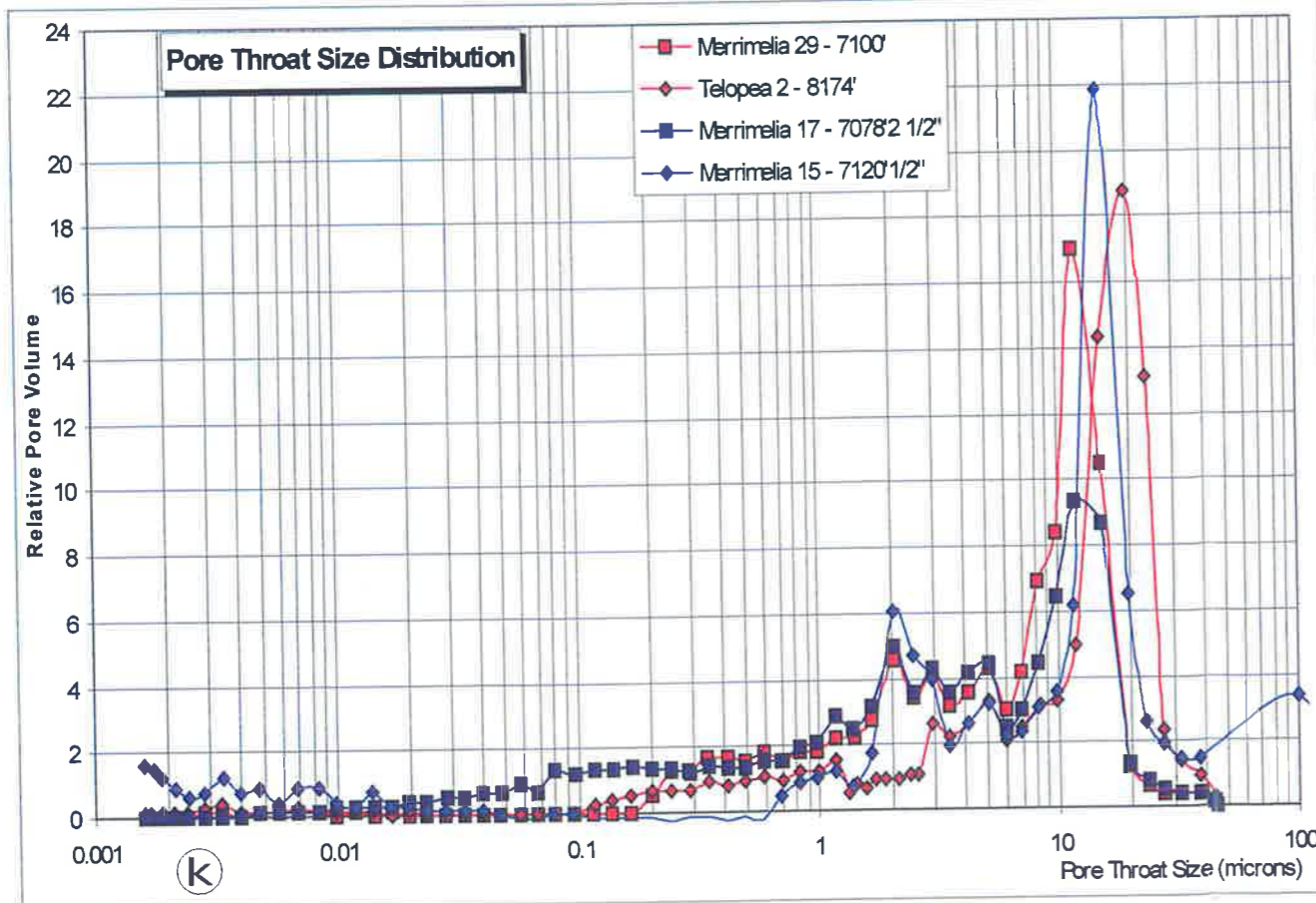
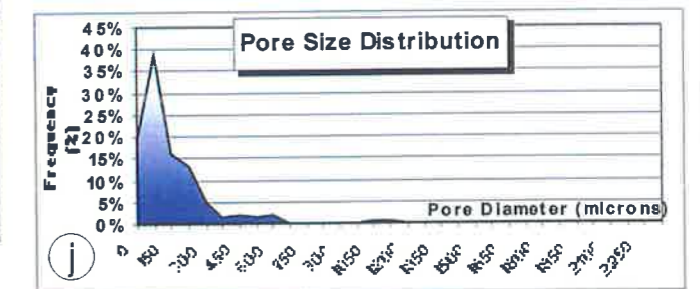
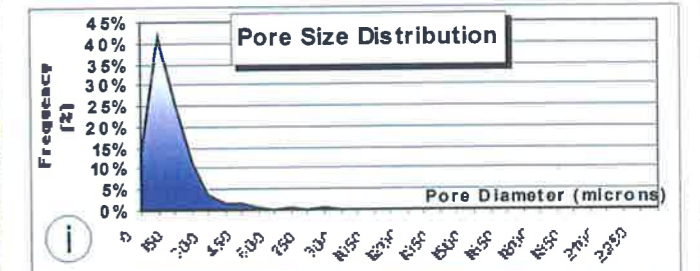
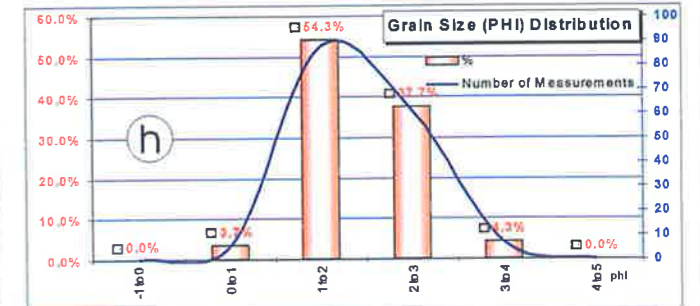
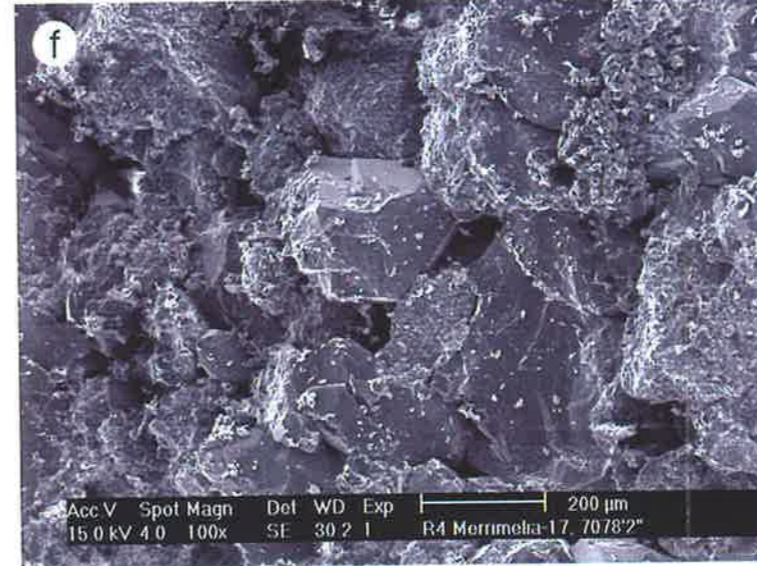
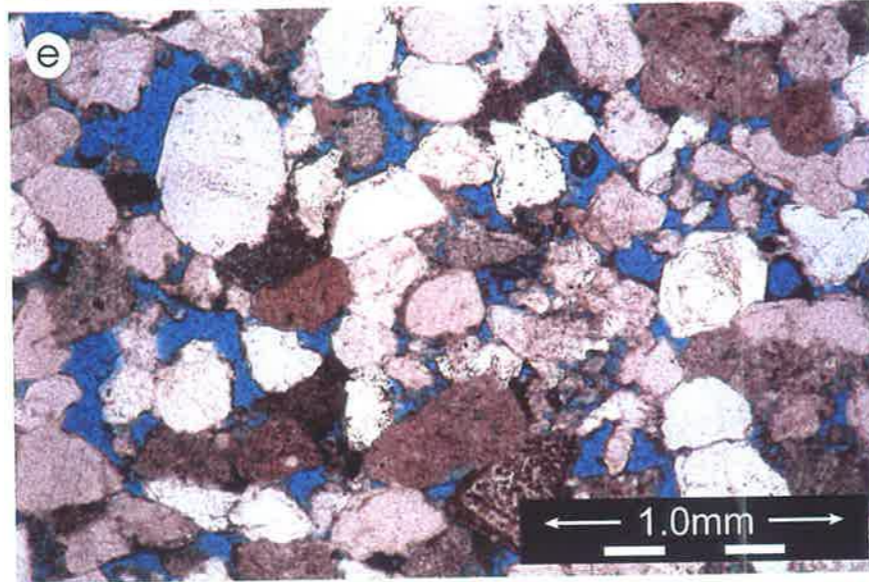
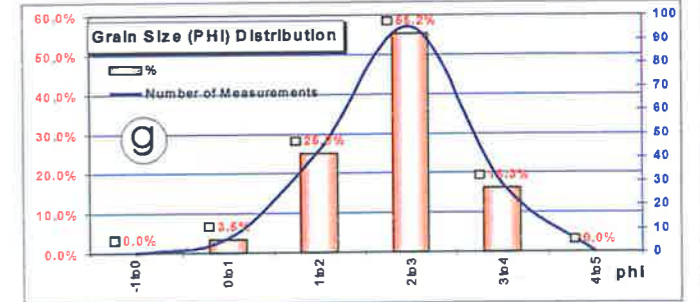
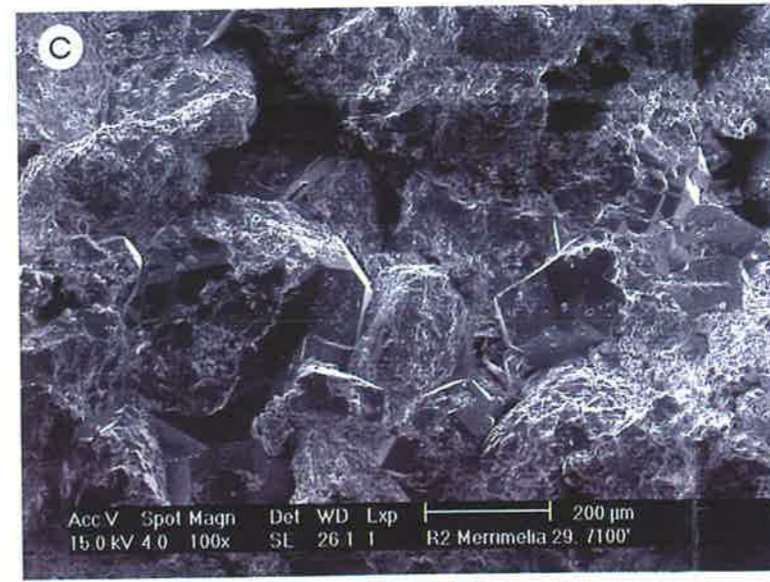
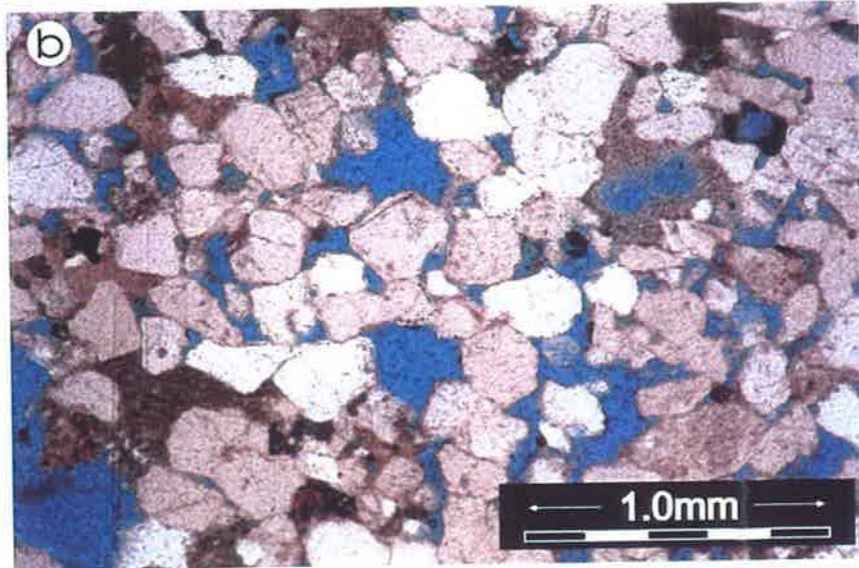
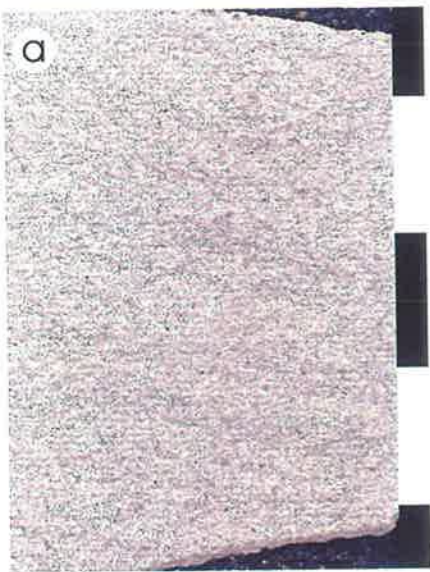


PLATE 2.5  
RF-2 and RF-3: FLUVIAL CHANNEL  
and CHUTE SANDS

## PLATE 2.6

### **Sample photographs, thin section and SEM photomicrographs, grain size distribution and mercury injection data of RF-4: Crevasse splay sands**

- a. Cross-bedded, off white-grey-orange, medium grained sandstone deposited as a proximal crevasse splay. The rock contains grey clay and orange-brown reworked intraclasts, Merrimelia 7, 7108 ft 4 in ( $\Phi = 14.2\%$ ,  $K = 7.5$  mD,  $S_o = 39.9\%$ ). Each scale bar subdivision is 1cm.
- b. Siderite-cemented litharenite in thin section. Porosity reduction in this sample is caused mainly by the siderite and kaolin cementation. Quartz overgrowth cement and kaolin precipitation is favored by feldspar dissolution which predates the sparry siderite cement. Merrimelia 7, 7108 ft 4 in, plane polarized light. Scale bar = 1 mm.
- c. SEM micrograph of crevasse splay sand. Siderite covers the framework grain components, and partially fills the pore spaces. Open pores with 100 microns diameter are still preserved in this sample. Merrimelia 7, 7108 ft 4 in. Scale bar = 200 microns.
- d. Fine grained, ripple cross-laminated sandstone deposited as a distal crevasse splay. Beanbush 1, 8716 ft. ( $\Phi = 9.6\%$ ,  $K = 2.2$  mD). Each scale bar subdivision is 1cm.
- e. Thin section photomicrograph of a sublithic wacke deposited in a distal crevasse splay environment. The high proportion of detrital clays in the rock favors porosity reduction by compaction. Beanbush 1, 8716 ft, plane polarized light. Scale bar = 1 mm.
- f. SEM photomicrograph of rhombic siderite crystals intergrown with prismatic quartz overgrowth cement. Note the conservation of interconnected, large pores up to 100 microns diameter. Merrimelia 7, 7108 ft 4 in. Scale bar = 50 microns.

- g. Grain size distribution in a proximal crevasse splay suggests medium grained sandstones (PHI = 1-2) moderately well sorted (St. Dev. = 0.68), Merrimelia 7, 7108 ft 4 in.
- h. Pore size (microns) distribution in proximal crevasse splay sand. Average pore size = 185, Standard deviation = 143, Merrimelia 7, 7108 ft 4 in.
- i. Pore size (microns) distribution in proximal crevasse splay sand. Average pore size = 244, Standard deviation = 200, Merrimelia 29, 7136 ft.
- j. Pore throat distribution from MICP analysis differs as a function of the proximity to the fluvial channel. Beanbush 1, 8716' shows pore throats less than 0.03 microns, while Merrimelia 7, 7108'4" shows two populations of pore throats that correspond to compacted kaolin (0.2 - 1.2 microns) and to remnant primary pores after siderite cementation (2.5 - 7 microns).
- k. Mercury injection capillary pressure curves illustrate Hg/air threshold pressures of 8.6 to 1142 psi.
- l. Detail of siderite spar that coats the quartz grains and partially fills pore spaces. Pore throats are still preserved. Merrimelia 7, 7108 ft 4 in, plane polarised light. Scale bar = 0.25 mm.

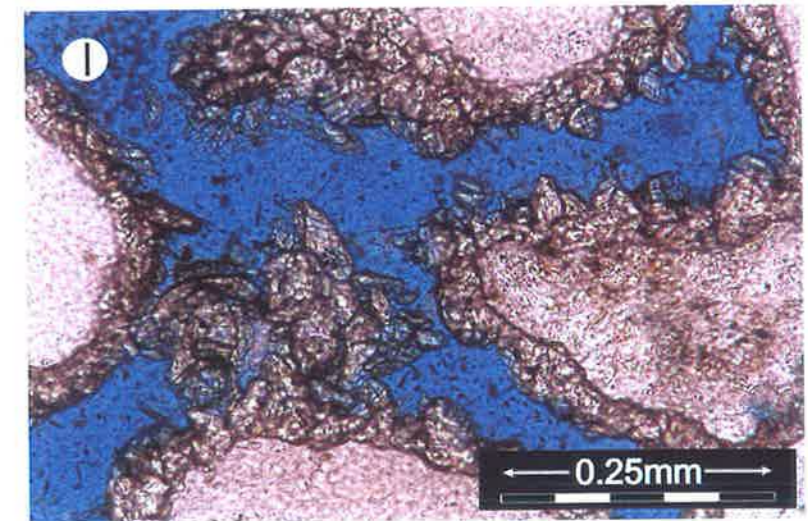
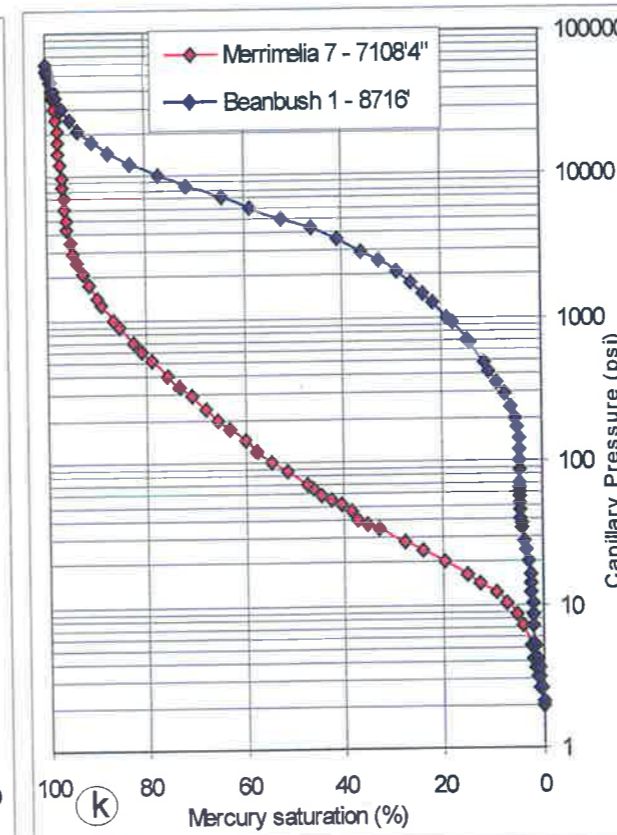
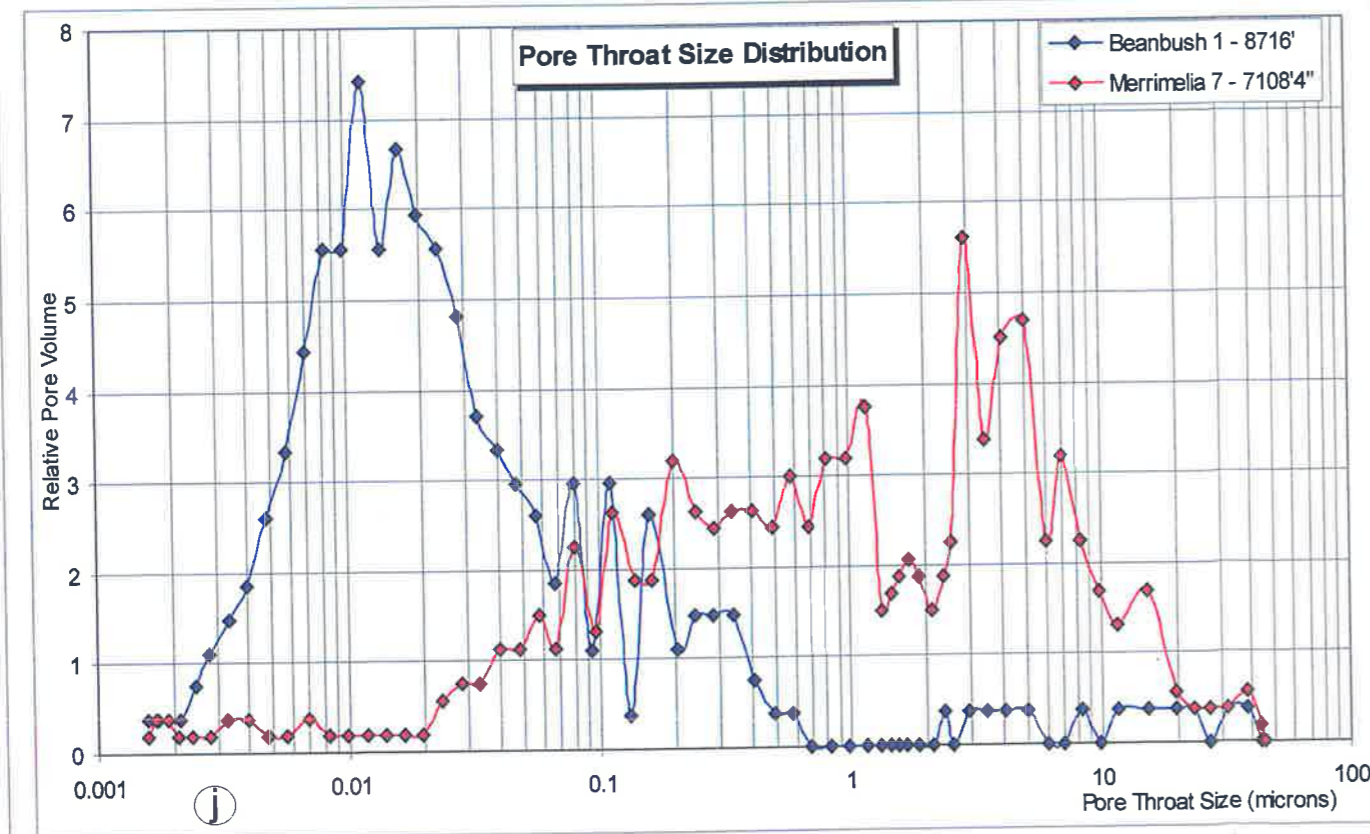
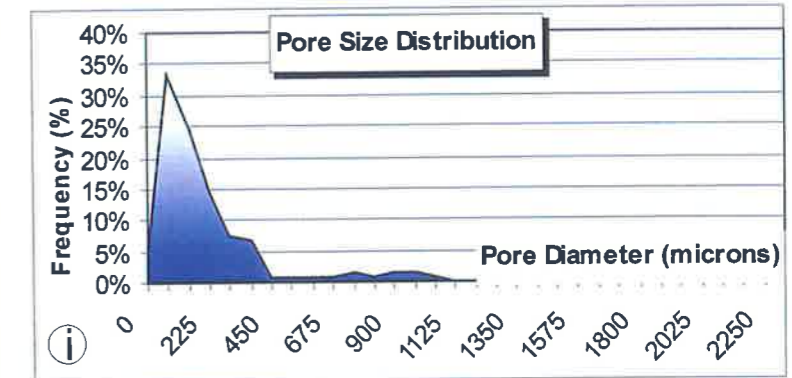
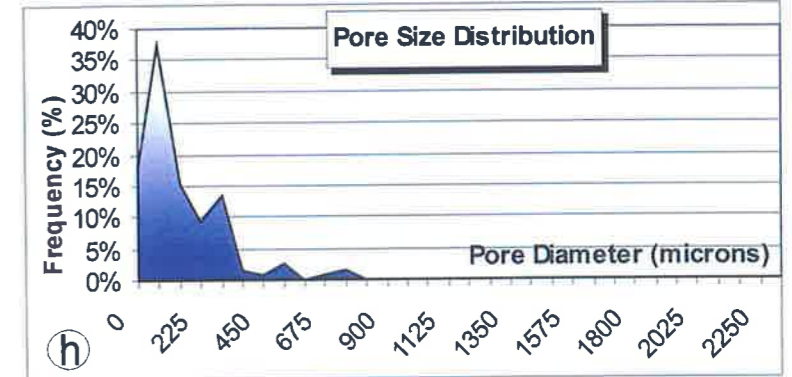
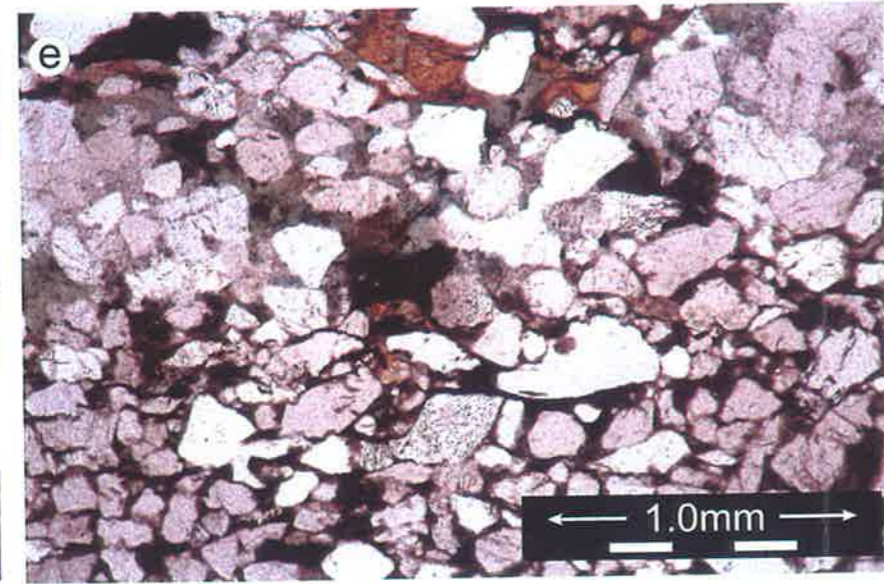
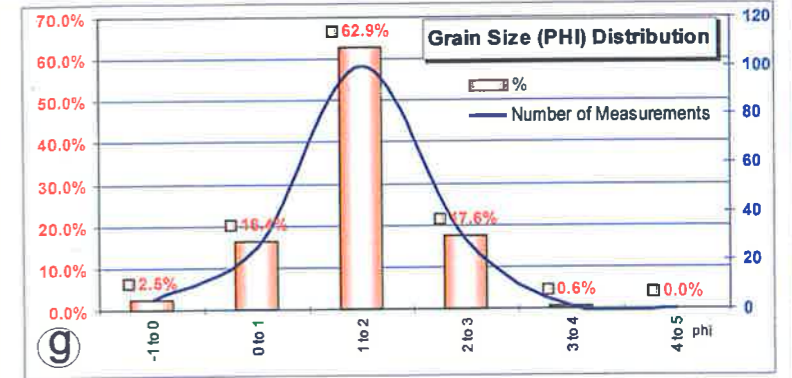
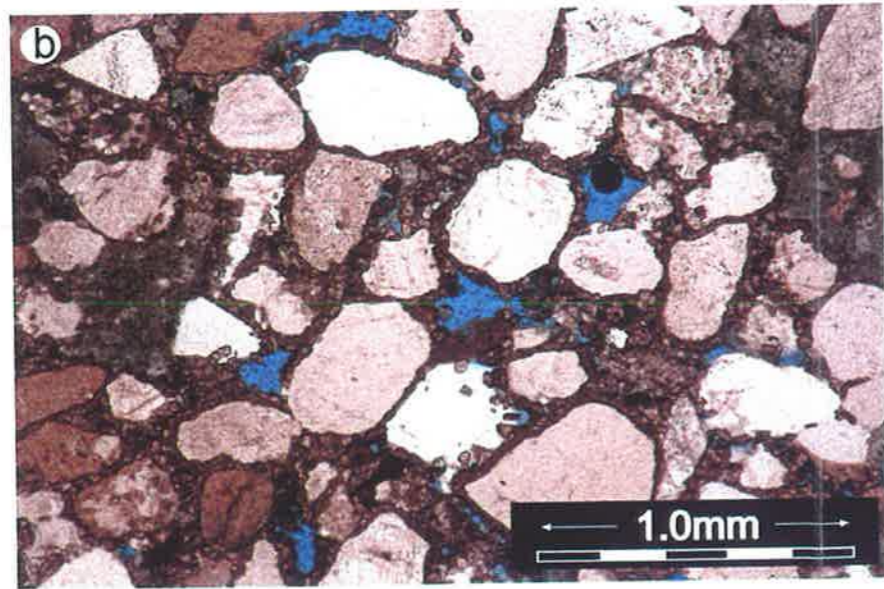
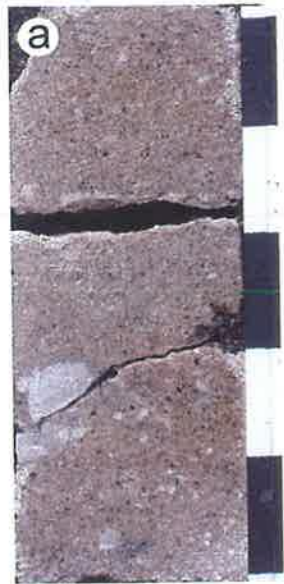


PLATE 2.6  
RF-3: CREVASSE SPLAY SANDS

## PLATE 2.7

### **Sample photographs, thin section and SEM photomicrographs, grain size distribution and mercury injection data of RF-5: Fine-grained sands from top of point bars**

- a. Off white, fine-grained, cross-bedded sandstone. The sample shows silty wisps, siderite spots and no porosity. Merrimelia 3, 7542 ft 6 in. Each scale bar subdivision represents 1cm.
- b. Porosity distribution in a fine-grained litharenite deposited at the top of point bar. Primary pores are completely occupied by kaolin that creates microporosity. Minor matrix and siderite contributes to the porosity occlusion. Merrimelia 3, 7542 ft 6 in, plane polarized light. Scale bar = 1 mm.
- c. Low magnification under SEM of a fine-grained sandstone shows the framework components covered by kaolin cement. Merrimelia 3, 7542ft 6 in. Scale bar = 200 microns.
- d. Grain size distribution of a sample from Merrimelia 3, 7542 ft illustrates a fine-grained sand ( $PHI = 2 - 3$ ) which is moderately well sorted ( $St. Dev. = 0.53$ ).
- e. Off white to light grey fine-grained sandstone. The sample is cross-bedded with dark grey, siltier toesets. The rock has an orange shade from siderite impregnation. Merrimelia 7, 7065 ft 11 in. Each scale bar subdivision represents 1cm.
- f. Porosity distribution in point bar sand (litharenite). Siderite, aggressively etches quartz and kaolin to fill the pore spaces. Merrimelia 7, 7065 ft 11 in, plane polarised light. Scale bar = 1 mm.
- g. SEM micrograph of platy clays and siderite that fill the available pore spaces. Merrimelia 7, 7065 ft 11 in. Scale bar = 10 microns.



- h. Grain size distribution in Merrimelia 7, 7065 ft 11 in suggests fine-grained sand (PHI = 2-3), moderately well sorted (St. Dev. = 0.58).
- i. Pore throat distribution from MICP analysis displays excellent sorting. Pore throat sizes of 0.17 to 0.5 microns correspond to compacted kaolin microporosity.
- j. Mercury injection capillary pressure curves shows Hg/air threshold pressures of 136 to 156 psi.
- k. Detail of fine-grained sandstone that lost its primary porosity by intense cementation of kaolin (centre) and siderite. Merrimelia 7, 7065 ft 11 in, crossed polarized light. Scale bar = 0.25 mm.

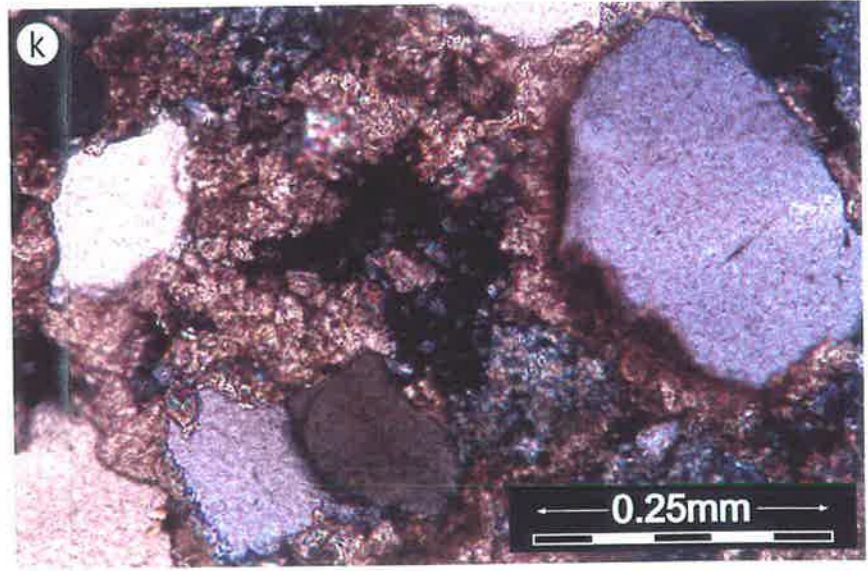
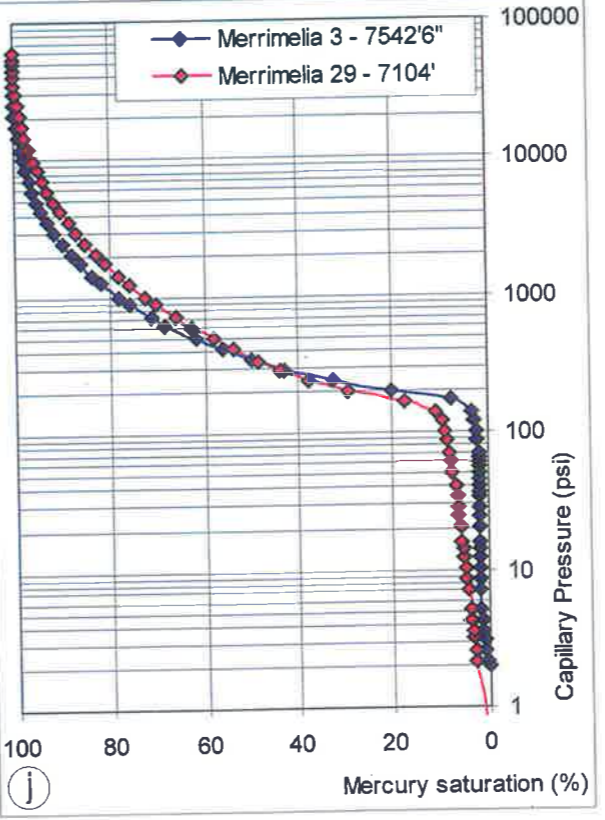
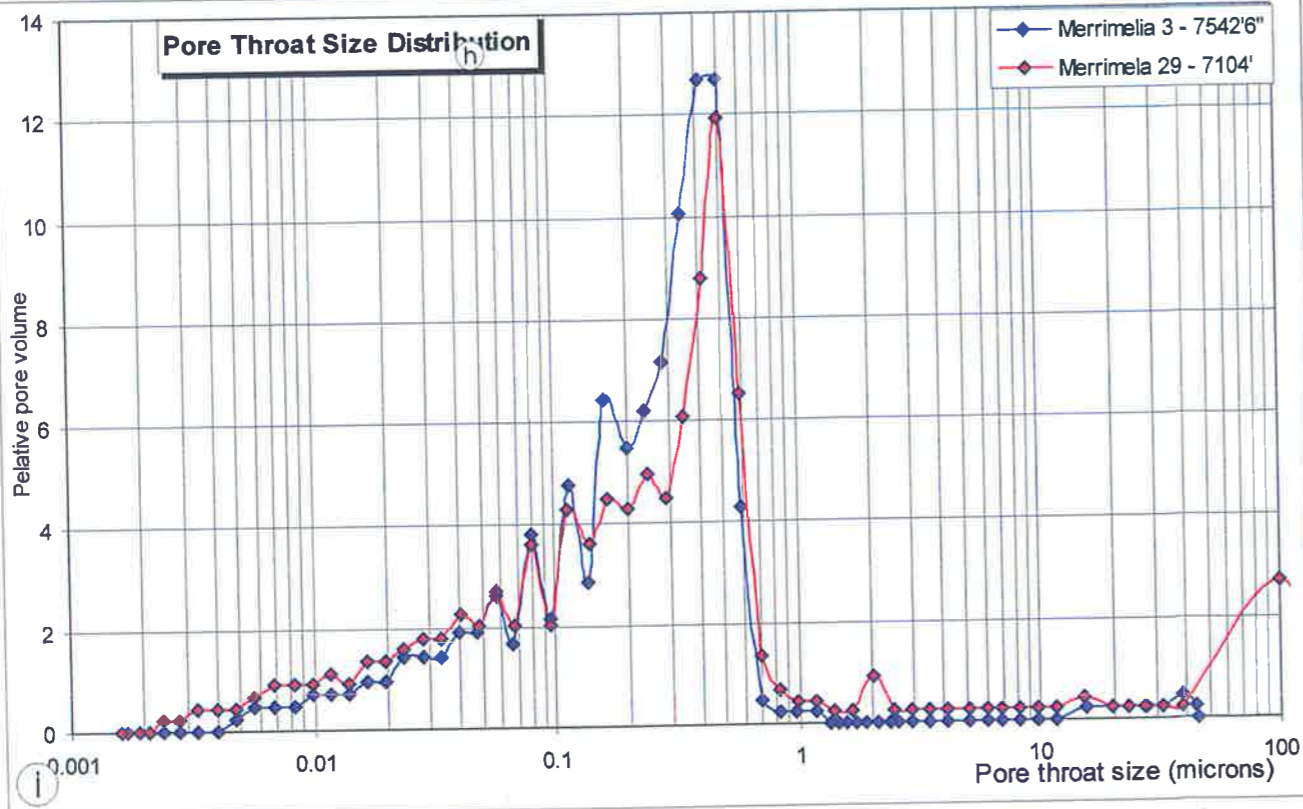
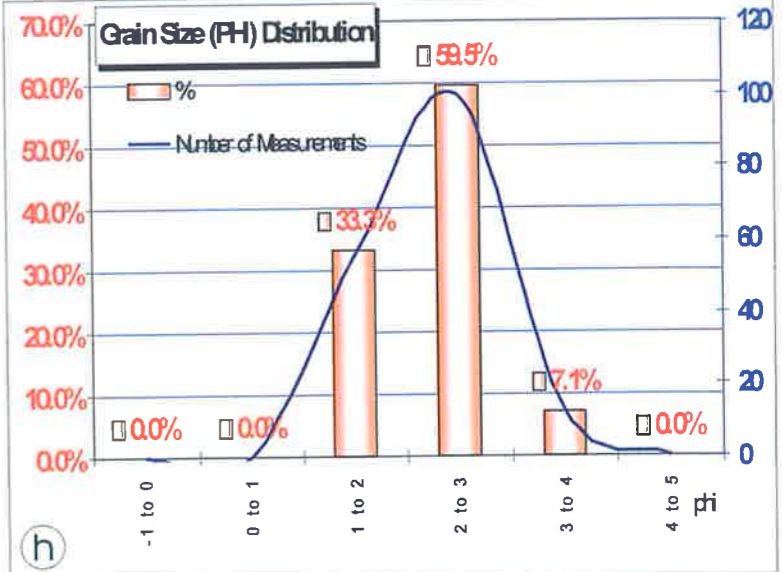
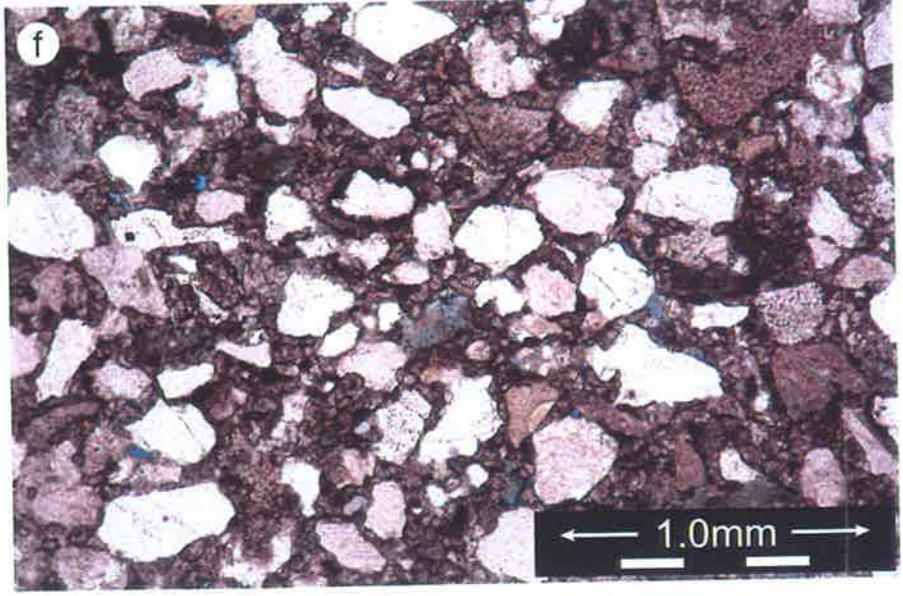
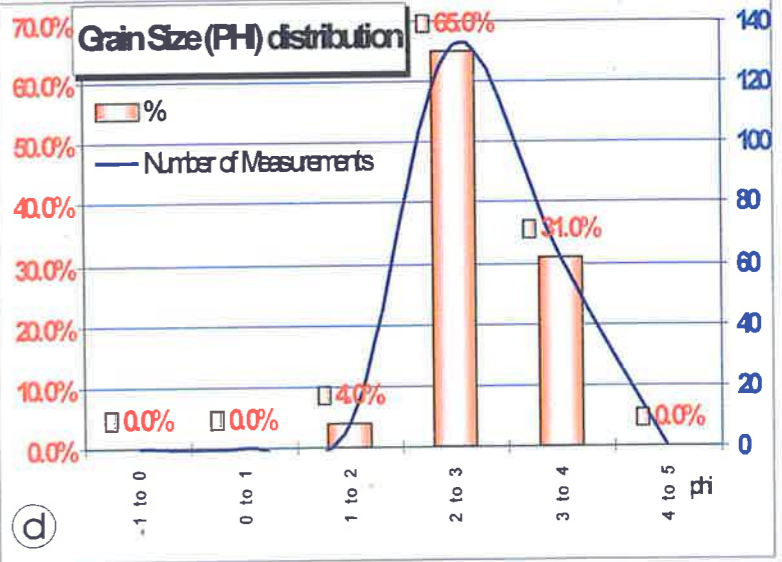
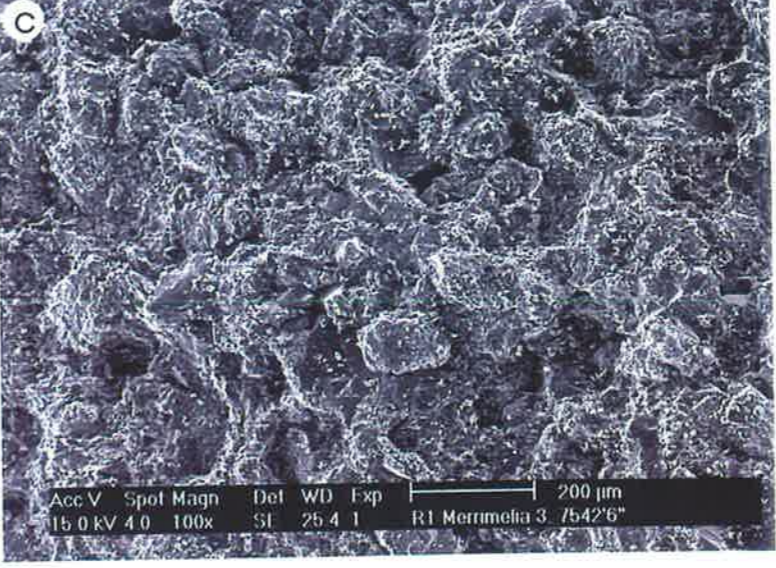
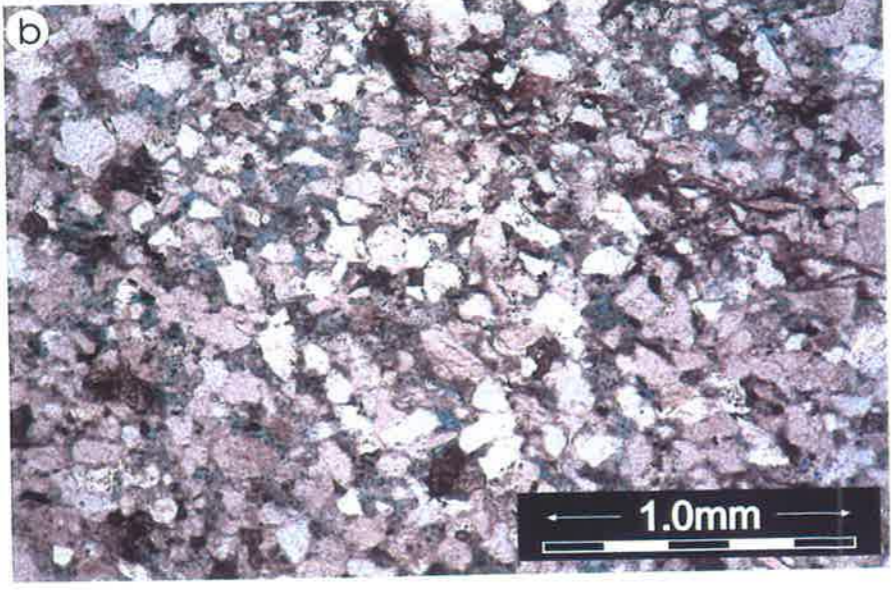


PLATE 2.7  
RF-5: FINE-GRAINED SANDS FROM TOP  
OF POINT BARS

## PLATE 2.8

### **Sample photographs, thin section and SEM photomicrographs, grain size distribution and mercury injection data of SF-1: Diagenetically-modified fluvial sandstones**

- a. Off white, fine-grained, sandstone with planar cross beds and silty wisps on foresets. In core, the rock seals an oil-impregnated interval below. Teloepa 2, 8186 ft 3 in.
- b. Thin section photomicrograph of diagenetically-modified sandstone (sublitharenite). Well-developed quartz overgrowth cement protects primary porosity from compaction. Kaolin fills the available pore spaces. Teloepa 2, 8186 ft 3 in, plane polarized light. Scale bar = 1 mm.
- c. Kaolin entirely surrounds and partially fills pores. The remnant primary pores are isolated. Teloepa 2, 8186 ft 3 in, plane polarized light. Scale bar = 0.5 mm.
- d. Overview SEM image of diagenetically-modified sandstone. The framework components are covered by clay cement, a process that significantly reduces porosity and permeability of this rock type. Teloepa 2, 8186 ft 3 in. Scale bar = 200 microns.
- e. Off white, very fine grained sandstone, with fine horizontal laminations and grey silty wisps. The rock seals an oil impregnated interval below. Merrimelia 15, 7114 ft 5 in.
- f. General overview of a lithic wacke. Kaolin precipitation almost completely obliterates porosity, drastically diminishing the permeability of this sample. The depositional detrital matrix facilitates compaction. Merrimelia 15, 7114 ft 5 in, plane polarized light. Scale bar = 1 mm.
- g. Grain size distribution suggests moderately well sorted (St. Dev. = 0.67), fine grained sand (PHI = 2-3), Teloepa 2, 8186 ft 3 in.

- h. Precipitation of kaolin in pore spaces and adjacent pore throats reduces the permeability giving a sealing attribute to this sample. Isolated pores of about 30 microns diameter are preserved between euhedral quartz overgrowths (bottom right). Telopea 2, 8186 ft 3 in. Scale bar = 100 microns.
  
- i. Pore throat distribution by MICP analysis displays excellent sorting. Pore throat sizes vary between 0.23 to 0.5 microns and correspond to the micropores created between kaolin booklets.
  
- j. Mercury injection capillary pressure curves showing Hg/air threshold pressures of 167 to 251 psi.

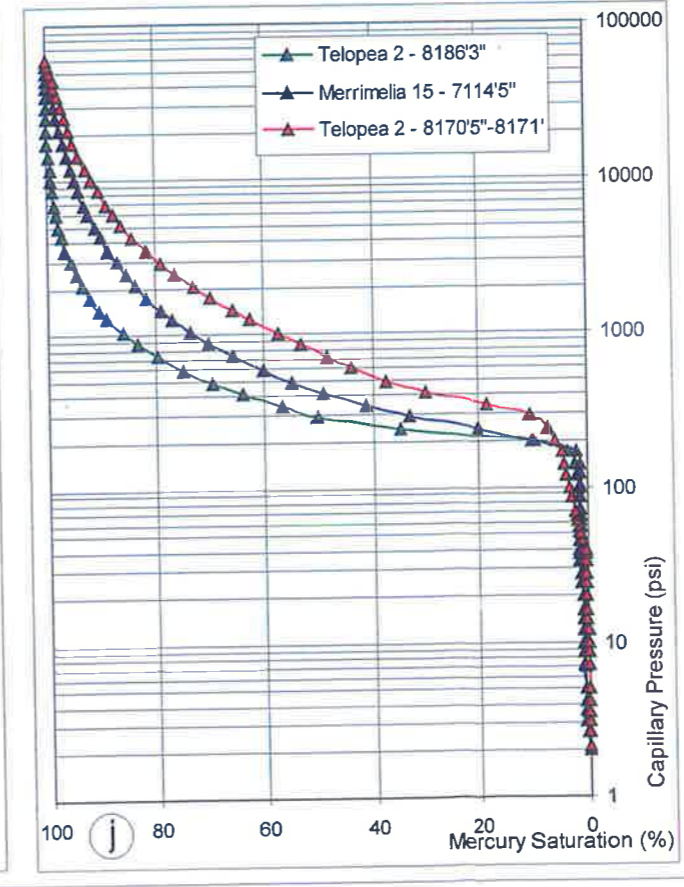
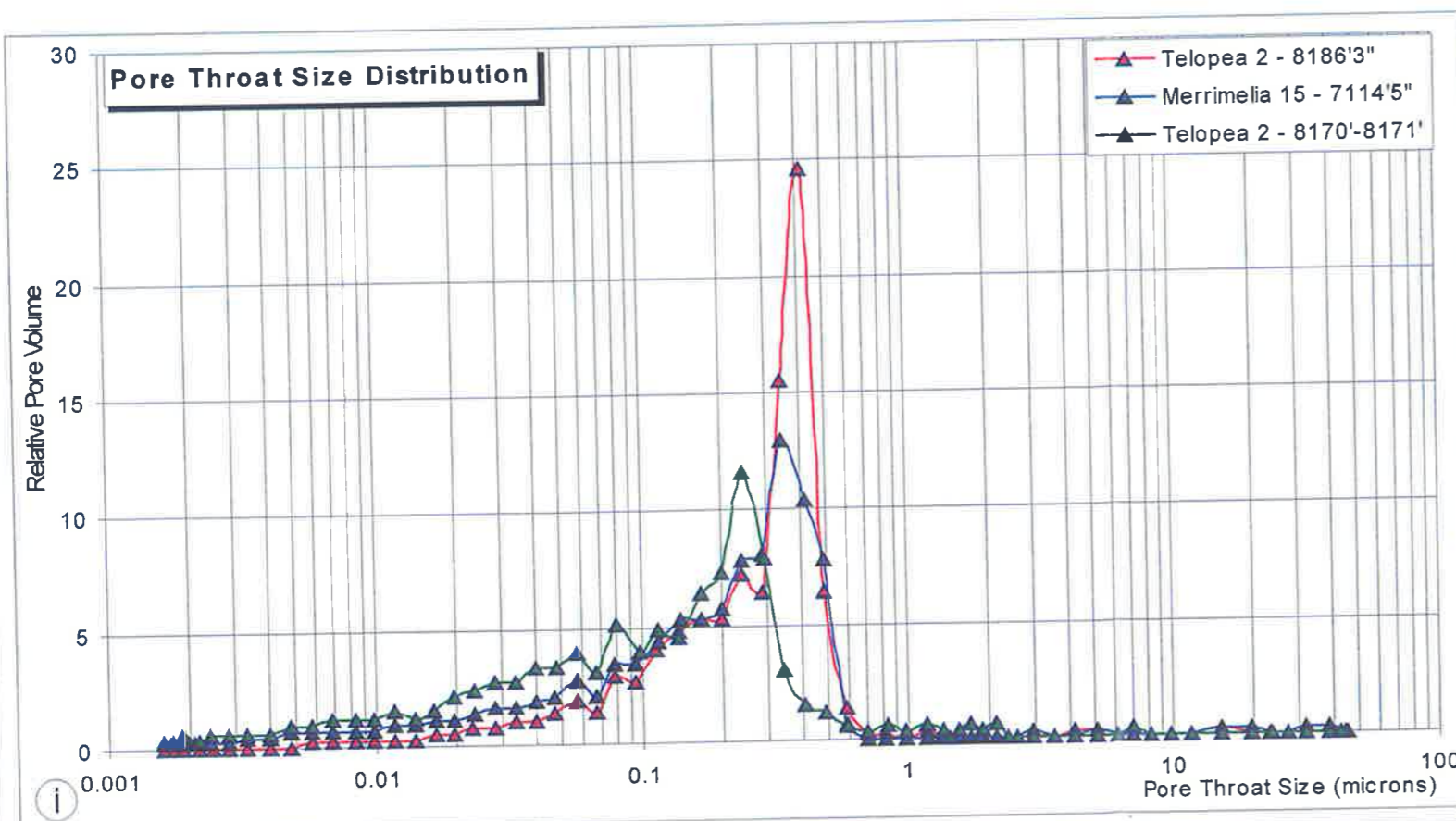
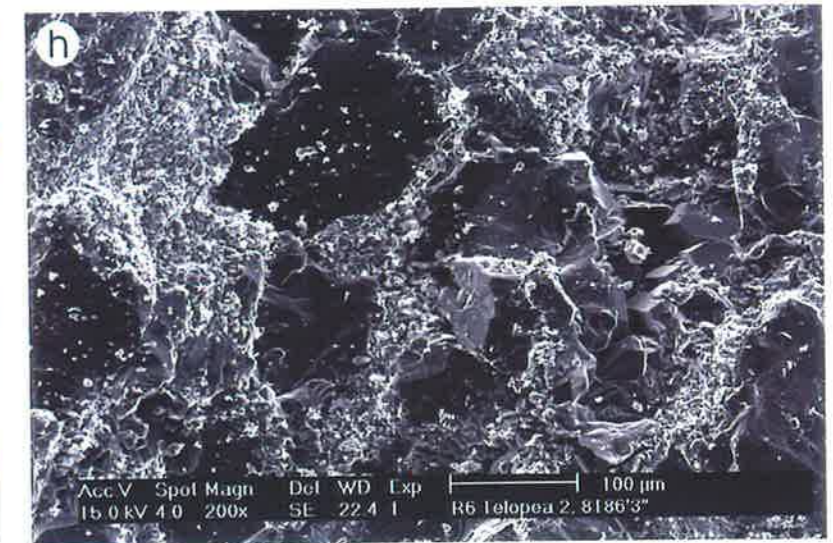
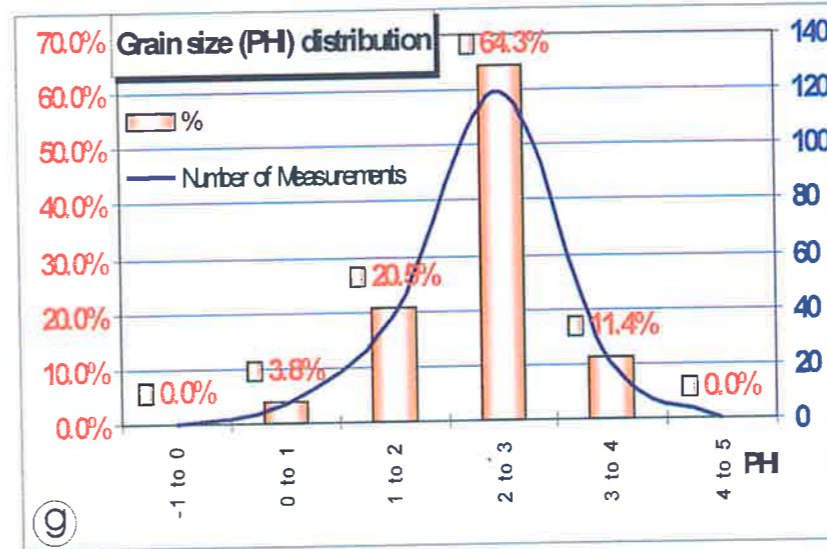
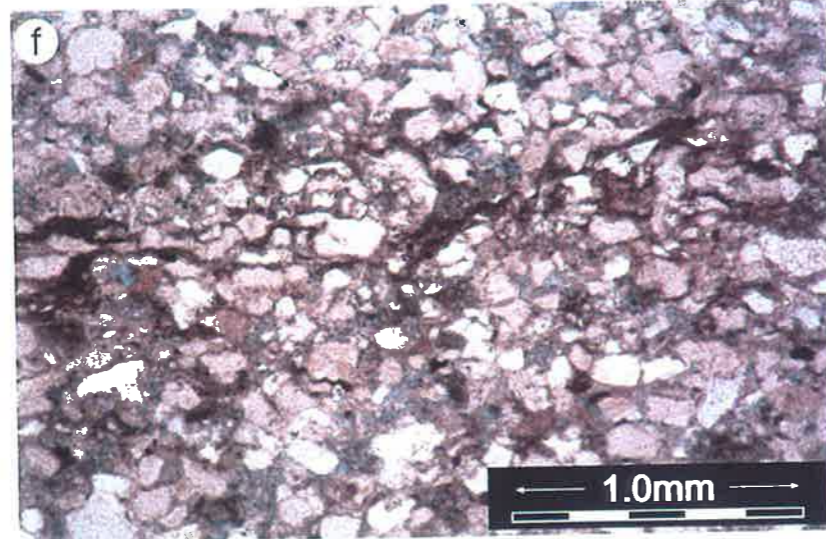
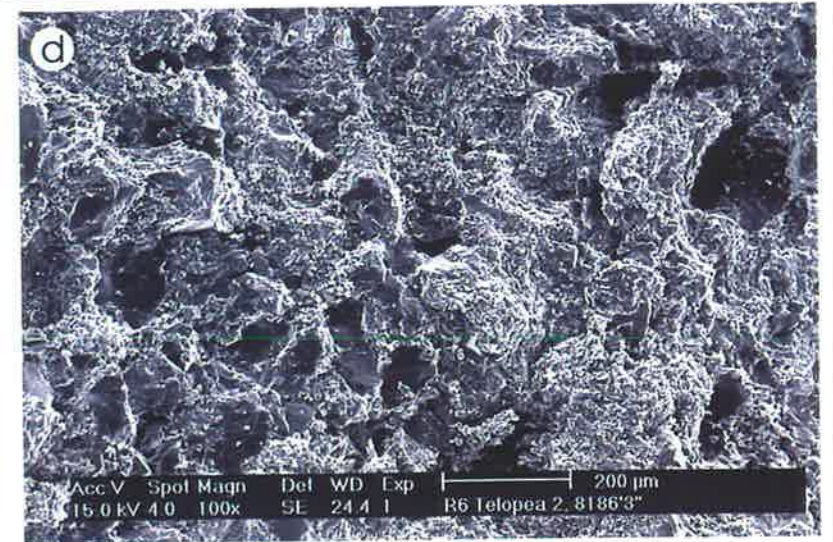
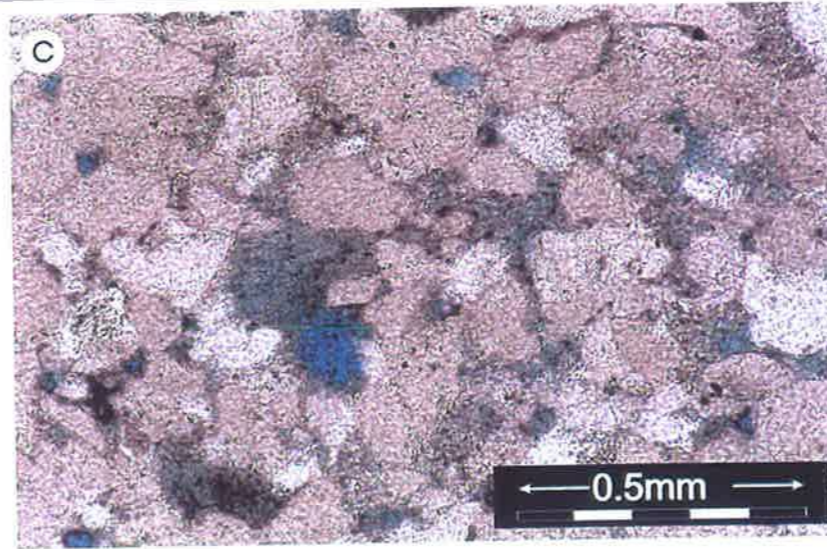
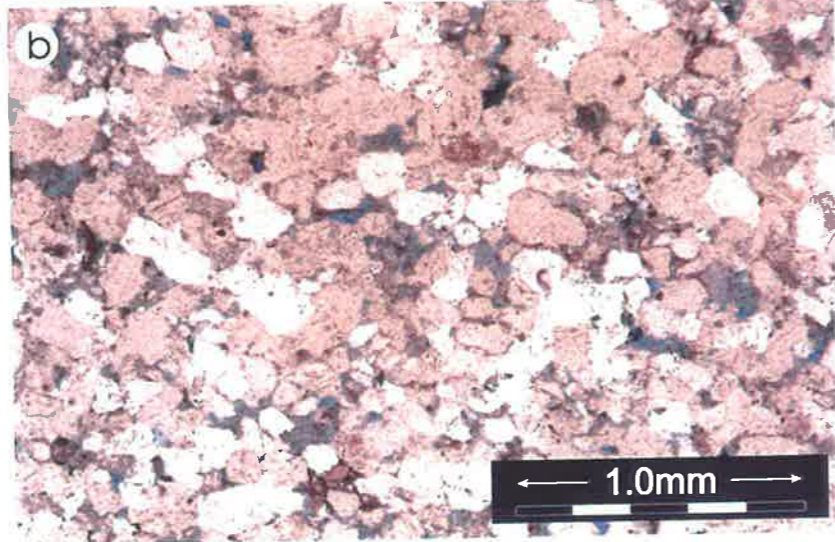


PLATE 2.8  
SF-1:  
DIAGENETICALLY-MODIFIED  
FLUVIAL SANDSTONES

## PLATE 2.9

### **Sample photographs, thin section and SEM photomicrographs, grain size distribution and mercury injection data of SF-2: Lacustrine mudstones**

- a. Fine grained sandstone; consist of alternating dark grey and beige, even laminae with small ripples. Beanbush 1, 8723 ft 3 in. Each subdivision of scale bar represents 1cm.
- b. Thin section photomicrograph of a sublithic wacke. The binding material of this sample is a matrix of detrital clays. No porosity is left. Beanbush 1, 8723 ft 3 in, plane polarized light. Scale bar = 1 mm.
- c. A low SEM magnification of a sublithic wacke deposited in a lacustrine environment. The rock shows no porosity with detrital clays occupying all the pore spaces. Beanbush 1, 8723 ft 3 in. Scale bar = 200 microns.
- d. Altered grain deformed to pseudo matrix. Beanbush 1, 8723 ft 3 in. Scale bar = 20 microns.
- e. The sample represents an alternation of clayey siltstones and silty claystones, with horizontal laminations and small ripples. Merrimelia 5, 7420 ft 9 in. Each scale bar subdivision represents 1cm.
- f. This thin section photomicrograph illustrates an alternation of clayey siltstone (central) and silty claystone laminae. Merrimelia 5, 7420 ft 9 in, plane polarized light, Scale bar = 1 mm.
- g. Framboidal pyrite associated with clayey siltstone intervals, in a lacustrine deposit. Merrimelia 5, 7420 ft 9 in, plane polarized light, Scale bar = 0.25mm.
- h. Pore throat distribution from MICP analysis displays good sorting. Pore throat sizes are very small and range between 0.002 and 0.015 microns.

- i. Mercury injection capillary pressure curves show high Hg/air threshold pressures: 2743 - 9231 psi.

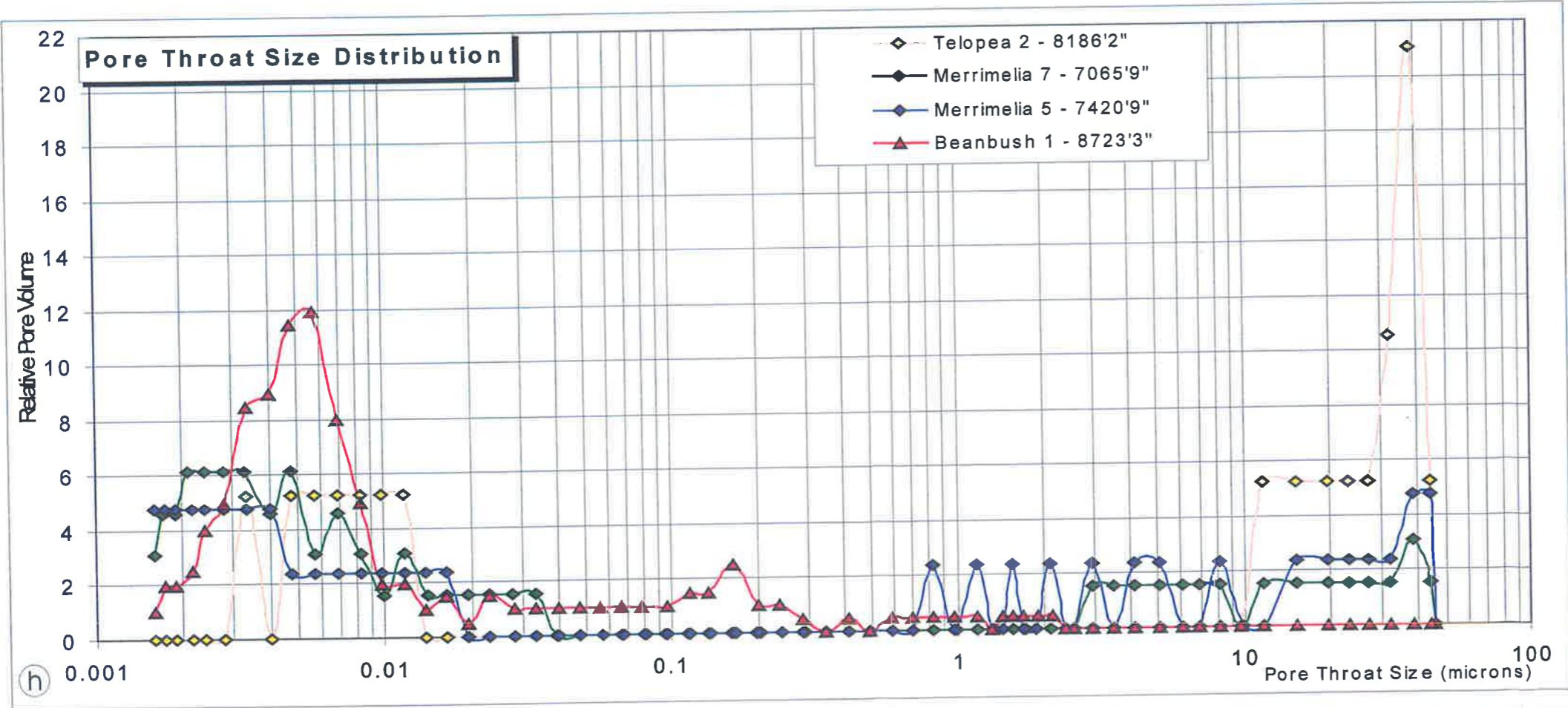
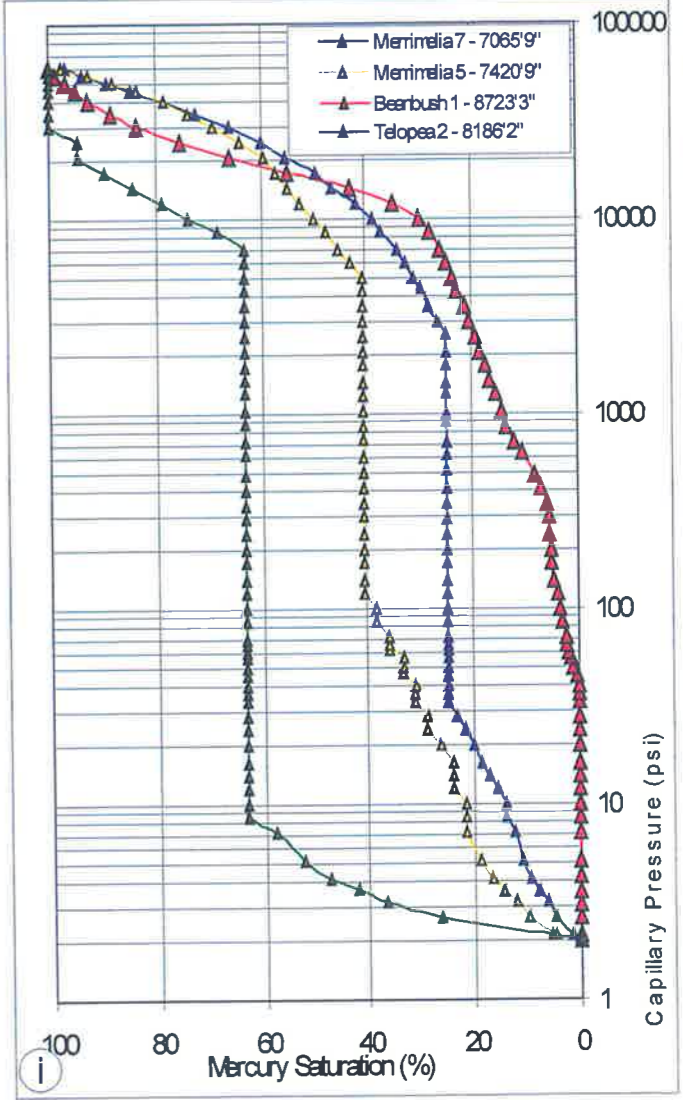
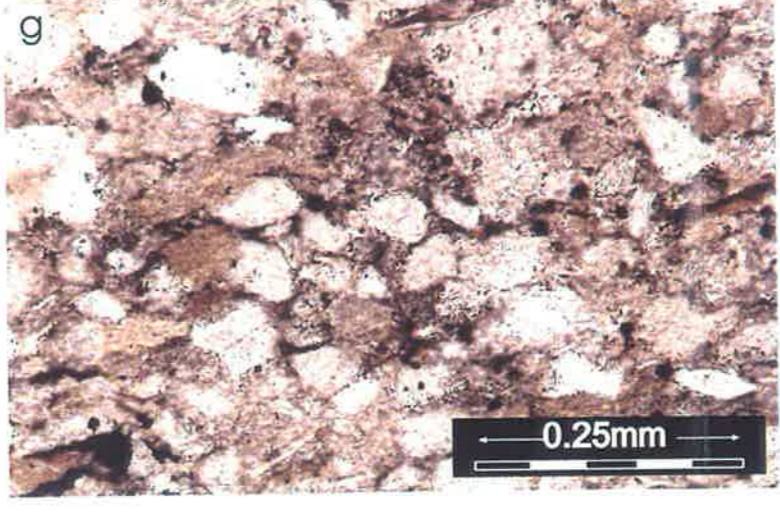
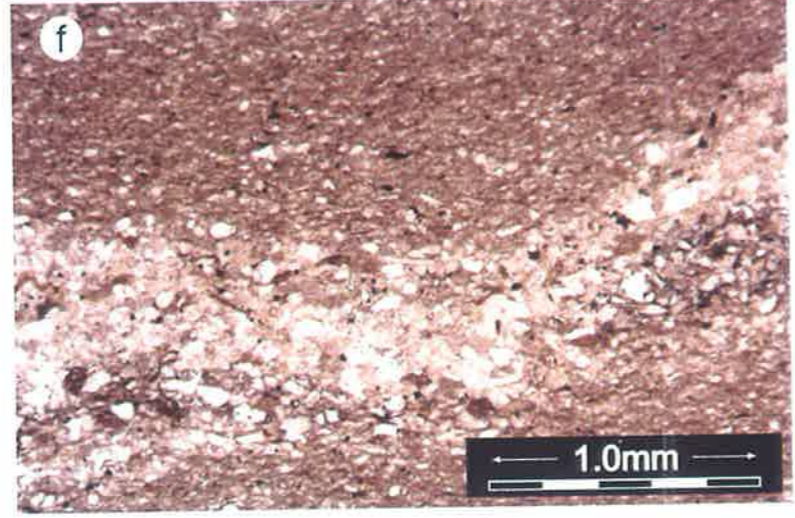
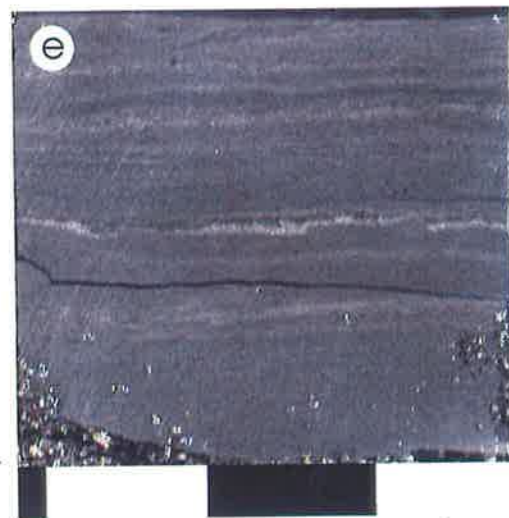
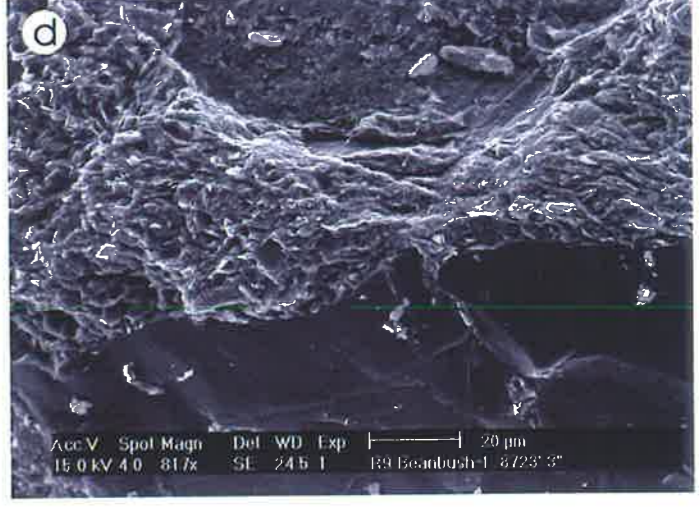
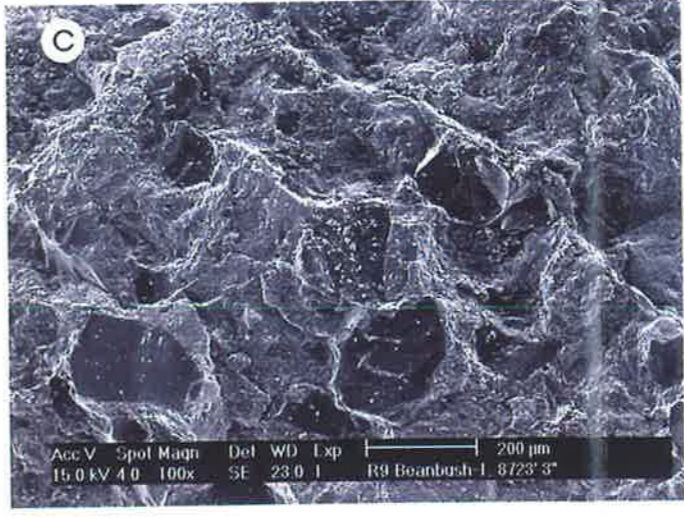
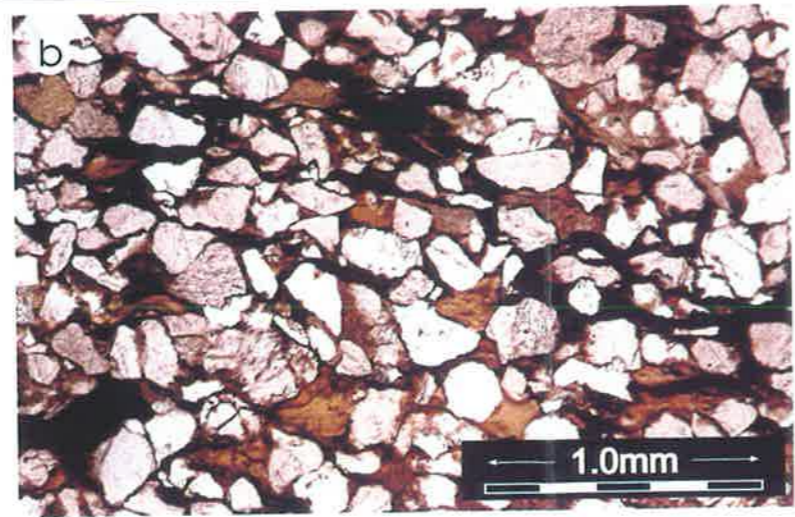


PLATE 2.9  
SF-2: LACUSTRINE  
MUDSTONES



## PLATE 2.10

### **Sample photographs, thin section and SEM photomicrographs, grain size distribution and mercury injection data of SF-3 Palaeosols**

- a. Medium grey siltstone with maroon siderite speckles and subvertical branching, Merrimelia 3, 7621 ft. Each scale bar subdivision represents 1 cm.
- b. Thin section photomicrograph of a sublithic wacke within a palaeosol deposit. Detrital clays tightly cement the framework components. Micritic siderite occurs as reddish to brown coloured blotches, replacing clays. Merrimelia 17, 7148 ft 4 in, plane polarized light. Scale bar = 1 mm.
- c. Clayey matrix in a palaeosol consists of detrital kaolin and illite. Merrimelia 17, 7148 ft 4 in, crossed polarized light. Scale bar = 0.25 mm.
- d. SEM photomicrograph of a palaeosol. Detrital clays cover the framework components, mainly quartz. Merrimelia 17, 7148 ft 4 in. Scale bar = 200 microns.
- e. Pale grey, destratified, fine-grained sandstone with dark grey mottles and siderite cement patches. The rock shows no porosity. Merrimelia 17, 7113 ft 8 1/2 in. Each scale bar subdivision represents 1 cm.
- f. Thin section photomicrograph of a sublithic wacke forming a palaeosol. The detrital clays are the main rock component. Merrimelia 17, 7113 ft 8 in, plane polarised light. Scale bar = 1 mm.
- g. SEM photomicrograph of a palaeosol. Abundant detrital clays cover the framework grains. Merrimelia 17, 7113 ft 8 in. Scale bar = 200 microns.
- h. SEM detail of platy clays, deformed under compaction. Merrimelia 17, 7148 ft 4 in. Scale bar = 20 microns.

- i. Pore throat distribution from MICP analysis displays good sorting. The majority of pore throats are very small and range between 0.002 and 0.01 microns.
- j. Mercury injection capillary pressure curves show Hg/air threshold pressures of 5484 - 7727 psi.
- k. Siderite spar replacing rootlets in palaeosols. Merrimelia 17, 7148 ft 4 in, crossed polarised light. Scale bar = 0.25 mm.

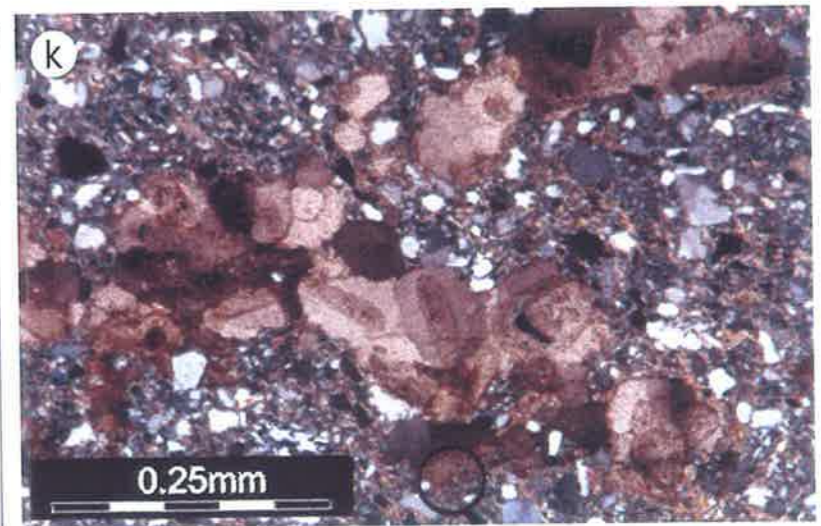
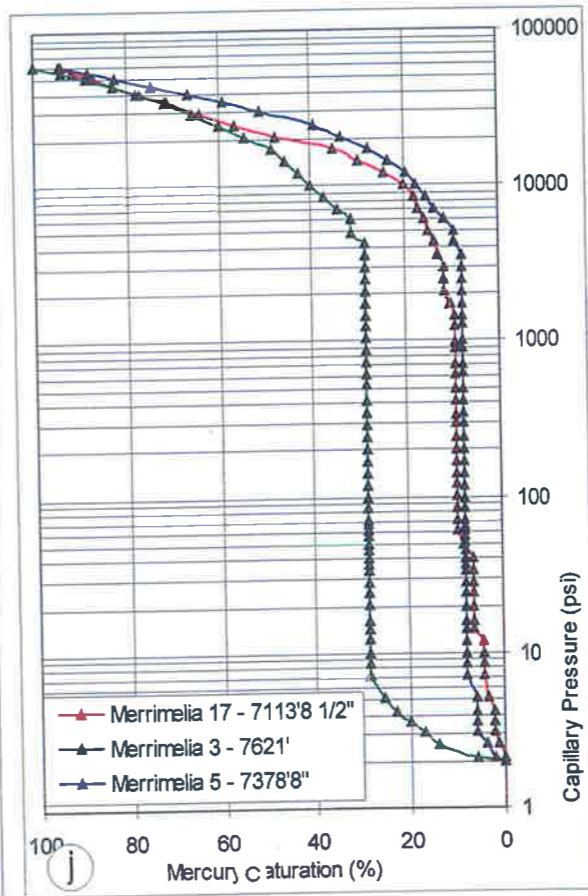
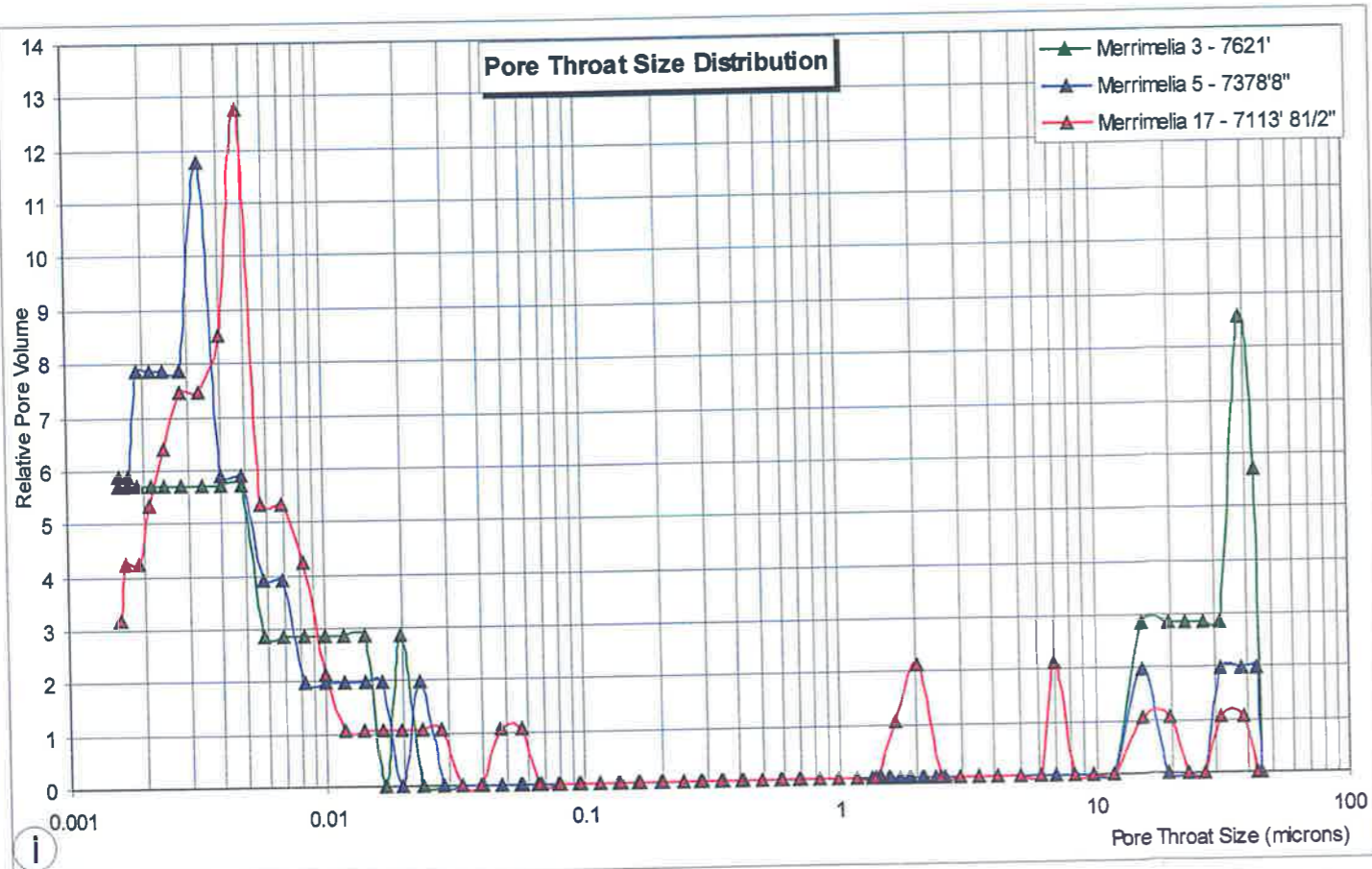
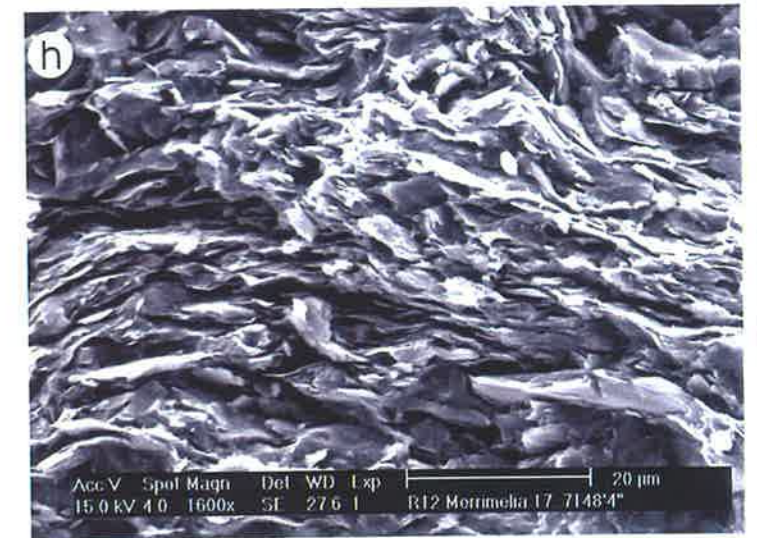
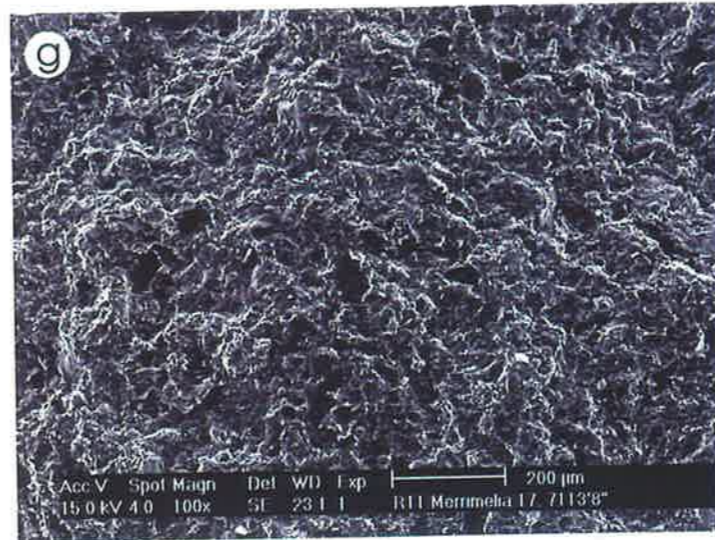
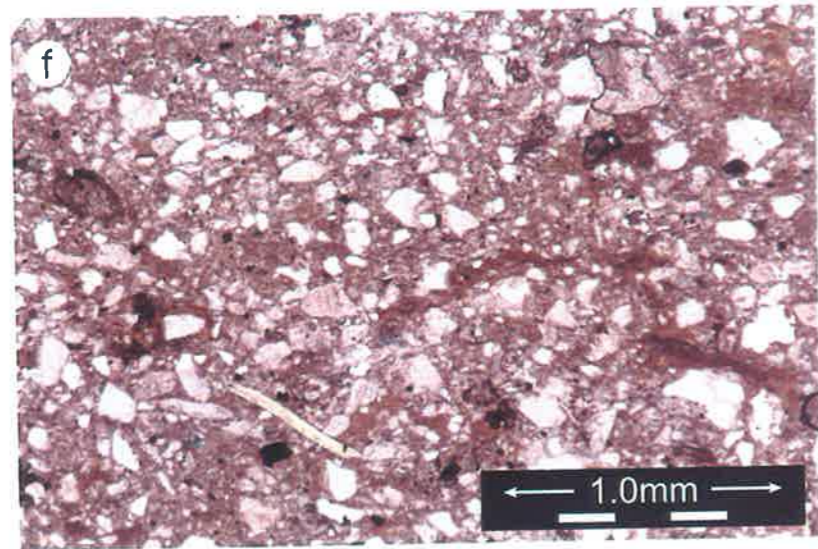
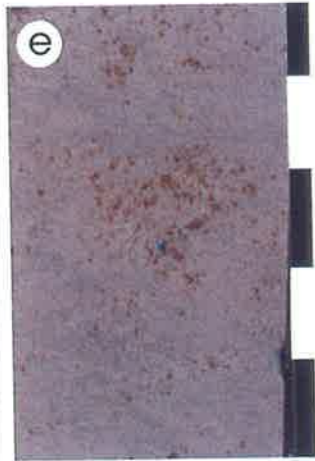
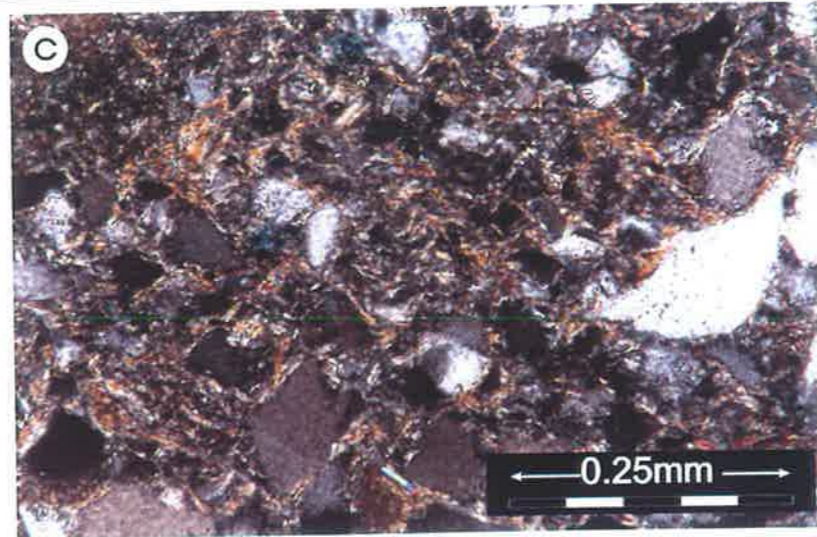
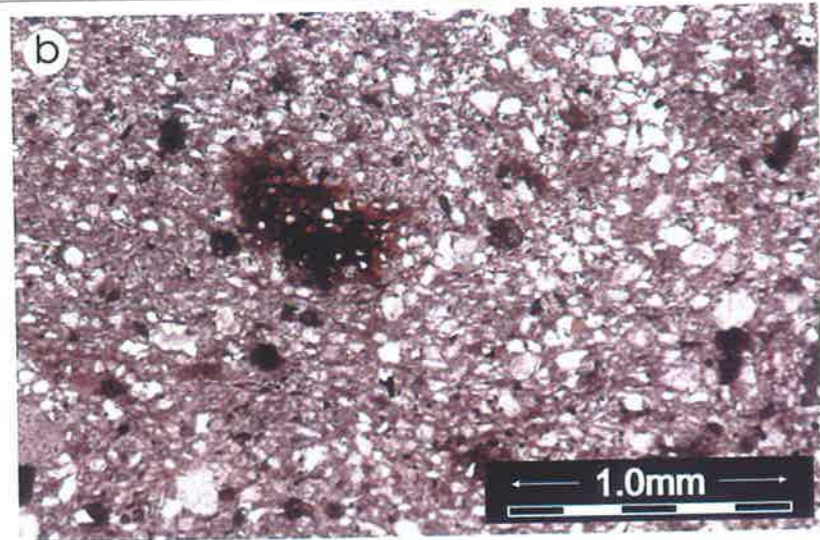


PLATE 2.10  
SF-3: PALAEOOLS

## PLATE 2.11

### **Sample photographs, thin section and SEM photomicrographs and mercury injection data of SF-4: Floodplain mudstones**

- a. Core photograph of a dark grey to black claystone with siltstone lenses deposited on a floodplain deposit. Beanbush 1, 8740 ft.
- b. Thin section photomicrograph of the above sample illustrates a silty claystone (bottom) in contact with a lens of clayey siltstone (above). The rock is tightly cemented and compacted with no porosity left. Characteristics for this sample are the pressure dissolution seams favoured by compaction and the presence of organic matter. Beanbush 1, 8740 ft 10 in, plane polarized light. Scale bar = 1 mm.
- c. Detail of depositional detrital clays and organic matter in a silty claystone. Beanbush 1, 8740 ft 10 in, plane polarized light. Scale bar = 0.25 mm.
- d. Low magnification SEM view of silty claystone. Detrital clays entirely fill the pore spaces of the rock and cover the framework components. Beanbush 1, 8740 ft 10 in. Scale bar = 200 microns.
- e. Homogeneous, dark grey to black silty claystone. Merrimelia 3, 7743 ft. Each subdivision of scale bar represents 1cm.
- f. This sample, a silty claystone, exhibits a predominance of the clay-sized material (detrital kaolin and illite) that surrounds the framework components, mainly quartz grains. Merrimelia 3, 7743 ft, plane polarized light. Scale bar = 1 mm.
- g. SEM photomicrograph of quartz grains tightly embedded in detrital clays. Practically no porosity is left. Beanbush 1, 8740 ft 10 in. Scale bar = 50 microns.

- h. Pore throat distribution determined by MICP analysis displays good sorting. Pore throat sizes are very small and range between 0.002 and 0.015 microns.
- i. Mercury injection capillary pressure curves illustrate Hg/air threshold pressures values between 3921 and 7725 psi.

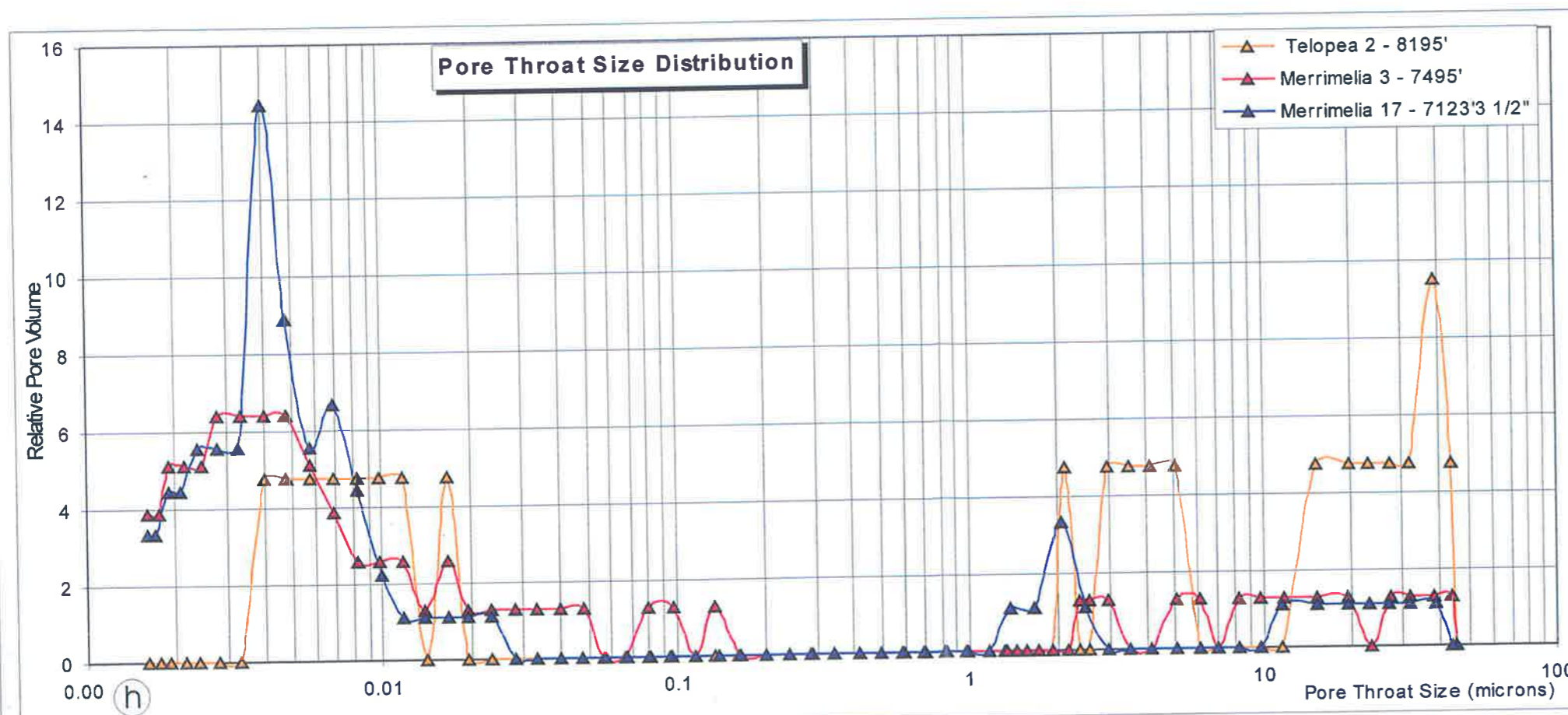
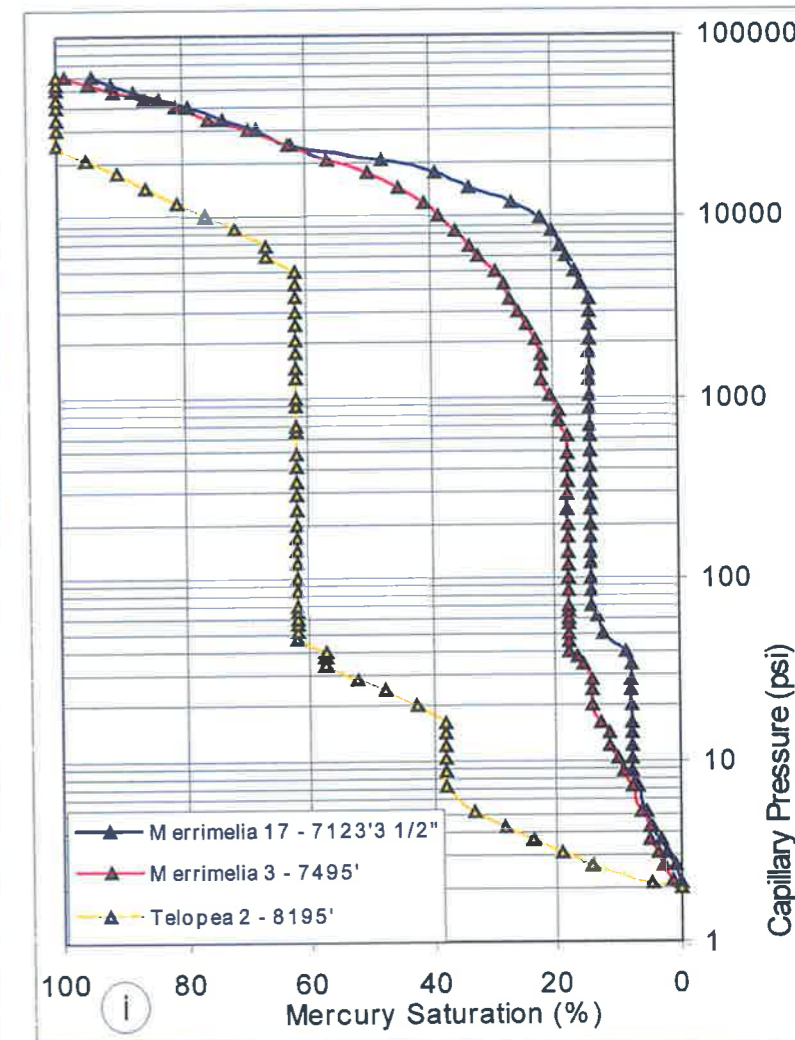
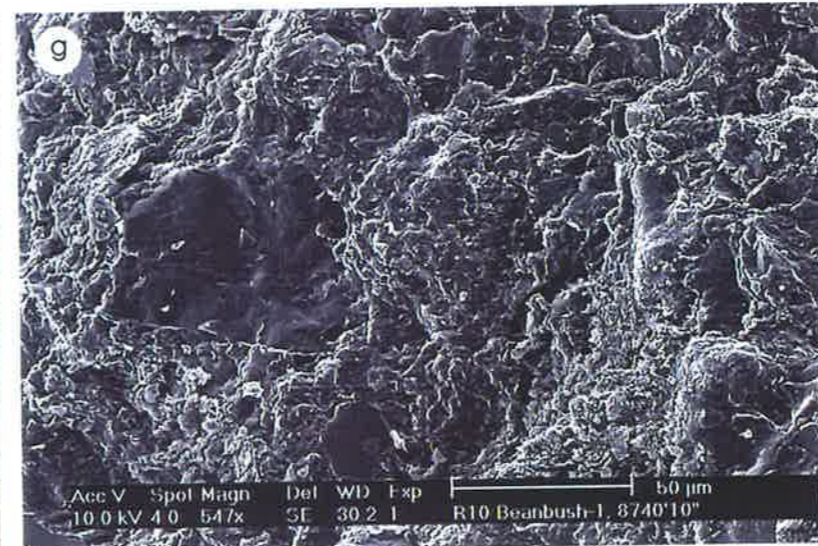
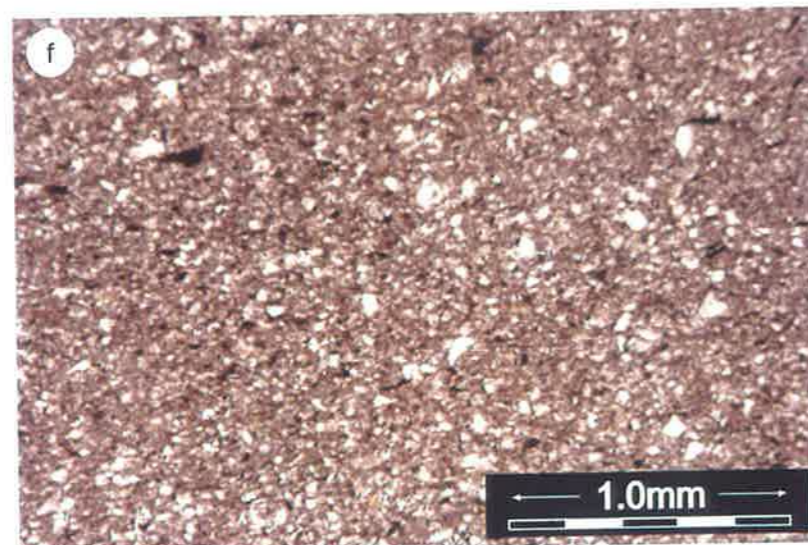
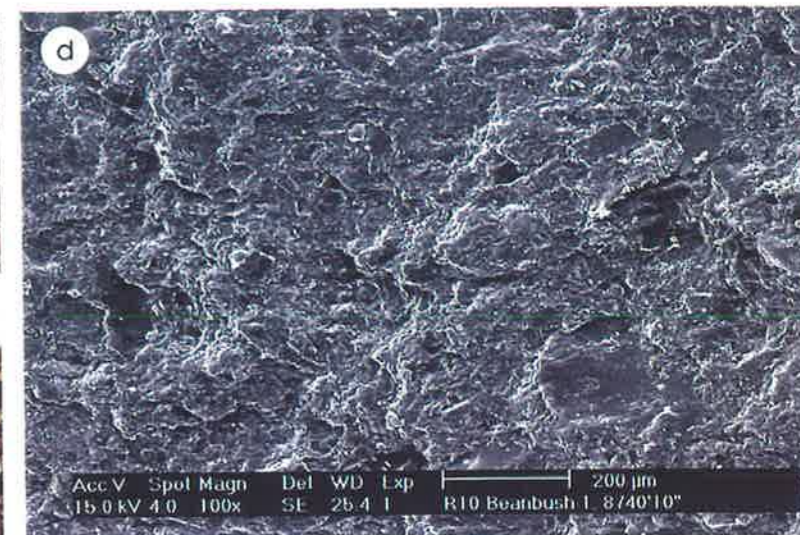
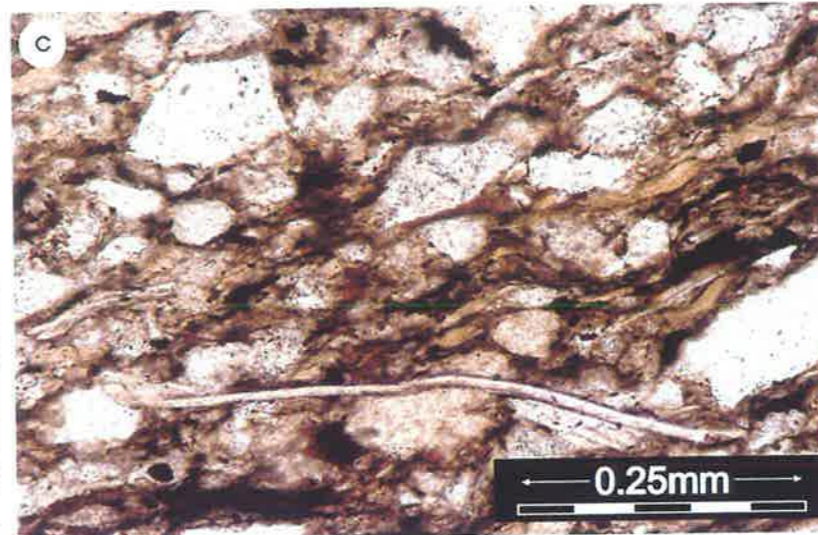
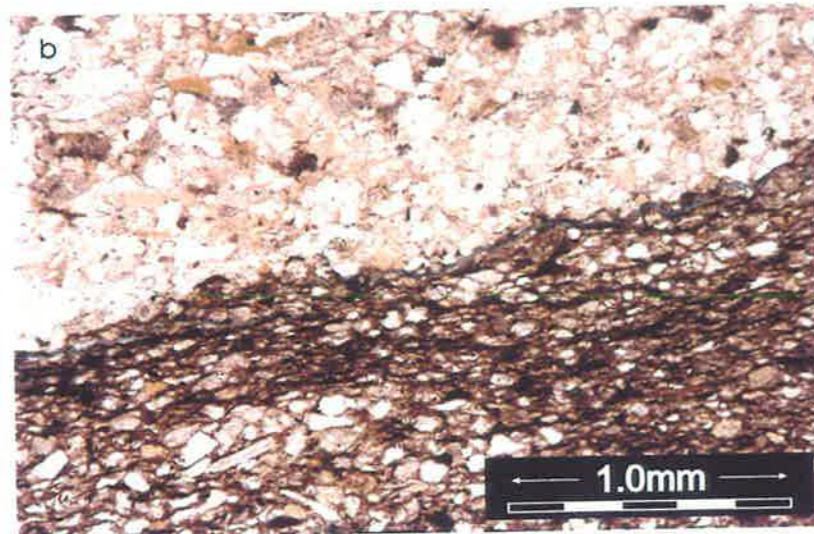


PLATE 2.11  
SF-4: FLOODPLAIN  
MUDSTONES

## CHAPTER THREE

### METHODOLOGY

#### 3.1 SEDIMENTOLOGICAL LOGGING

Detailed sedimentological description of cores was carried out by Alexander (1998-1999), prior to this study. Alexander's (1998-1999) interpretation of the Nappamerri Group as being deposited in a fluvial-meandering environment is used here. Several cores were examined and logged to calibrate previous work to this study. All cores were logged at the State Core Library of South Australia. The observed sedimentary structures and lithologies were interpreted for depositional facies within the fluvial environment in thirteen wells from Merrimelia, Telopea and Beanbush fields.

#### 3.2 SELECTION CRITERIA

A total of forty-seven samples were selected from core from the Nappamerri Group and Cuddapan Formation. The samples were selected from the Merrimelia, Telopea and Beanbush fields. Merrimelia field has widely spaced wells which penetrate hydrocarbon accumulations in the Callamurra, Paning and Wimma Members of the Arrabury Formation. Telopea field wells found oil accumulations in the Tinchoo Formation, while Beanbush was chosen for intersections of the Cuddapan Formation. All available depositional settings within the fluvial environment were sampled. They reflect major rock types and the range of differences within the rock types.

The analytical techniques employed in this study include: X-ray diffraction analysis, thin section description, scanning electron microscopy and mercury injection capillary pressure analysis. A list of the selected samples grouped by their depositional environment, together with the completed analyses is shown in Table 3.1.

#### 3.3 X-RAY DIFFRACTION (XRD) ANALYSIS

X-Ray diffraction analysis was used to determine the bulk mineralogy of forty-seven samples. The XRD traces of each sample are shown in Appendix 3.1. The use of

**SAMPLE SELECTION - SEALING LITHOLOGIES**

DEPOSITIONAL ENVIRONMENT	Formation	No	XRD	Depth	No	TH SECTIONS	Depth	No	SEM	Depth	No	MICP	Depth
<b>SF-1 DIAGENETICALLY-MODIFIED FLUVIAL SANDSTONES</b>	Tinchoo	1	Teloepa 2	8186'3"	1	Teloepa 2	8186'3"	1	Teloepa 2	8186'3"	1	Teloepa 2	8186'3"
	Paning	2	Merrimelia 15	7114'5"	2	Merrimelia 15	7114'5"				2	Merrimelia 15	7114'5"
	Tinchoo										3	Teloepa 2	8170'- 8171'
<b>SF-2 LACUSTRINE MUDSTONES</b>	Cuddapan	4	Beanbush 1	8723'3"	4	Beanbush 1	8723'3"	2	Beanbush 1	8723'3"	5	Beanbush 1	8723'3"
	Callamurra	5	Merrimelia 5	7420'9"	5	Merrimelia 5	7420'9"				6	Merrimelia 5	7420'9"
	Paning	6	Merrimelia 7	7065'9"							7	Merrimelia 7	7065'9"
	Tinchoo	7	Teloepa 2	8186'2"							8	Teloepa 2	8186'2"
<b>SF-3 PALAEOOLS</b>	Paning	8	Merrimelia 17	7113'8½"	6	Merrimelia 17	7113'	3	Merrimelia 17	7113'8½"	9	Merrimelia 17	7113'8½"
	Callamurra	9	Merrimelia 17	7148'4"	7	Merrimelia 17	7148'4"	4	Merrimelia 17	7148'4"			
	Wimma				8	Merrimelia 3	7321'6"						
	Callamurra	10	Merrimelia 3	7621'							10	Merrimelia 3	7621'
	Callamurra	11	Merrimelia 5	7378'8"							11	Merrimelia 5	7378'8"
	Callamurra	12	Merrimelia 29	7124'2"									
	Callamurra	13	Merrimelia 29	7128'41/2"									
	Callamurra	14	Merrimelia 29	7130'									
	Callamurra	15	Merrimelia 29	7148'81/2"									
	Tinchoo	16	Teloepa 2	8221'6"									
Paning	17	Merrimelia 7	7018'										
<b>SF-4 FLOODPLAIN MUDSTONES</b>	Cuddapan	18	Beanbush 1	8740'10"	9	Beanbush 1	8740'10"	5	Beanbush 1	8740'10"	12	Beanbush 1	8741'-8741'5"
	Paning	19	Merrimelia 17	7123'3½"							13	Merrimelia 17	7123'3½"
	Paning	20	Merrimelia 3	7495'							14	Merrimelia 3	7495'
	Callamurra	21	Merrimelia 3	7743'	10	Merrimelia 3	7743'						
	Tinchoo												
	Wimma	22	Merrimelia 3	7320'6"									
	Tinchoo	23	Teloepa 2	8195'							15	Teloepa 2	8195'
	Paning	24	Merrimelia 17	7100'									
Paning	25	Merrimelia 17	7138'										

Table 3.1 Sample selection and completed analyses. (a) sealing lithologies



**SAMPLE SELECTION - RESERVOIR LITHOLOGIES**

DEPOSITIONAL ENVIRONMENT	Formation	XRD	Depth	THIN SECTIONS	Depth	SEM	Depth	MICP	Depth				
<b>RF-1 GRAVELS AT THE BASE OF FLUVIAL CHANNELS</b>	Cuddapan	26	Beanbush 1	8735'2"	11	Beanbush 1	8735'2"	6	Beanbush 1	8735'2"	16	Beanbush 1	8735'2"
	Tinchoo	27	Teloepa 2	8188'	12	Teloepa 2	8188'	7	Teloepa 2	8188'	17	Teloepa 2	8188'
	Tinchoo	28	Teloepa 2	8189'	13	Teloepa 2	8189'						
<b>RF-2 FLUVIAL CHANNEL SANDS</b>	Tinchoo	29	Teloepa 2	8174'	14	Teloepa 2	8174'				18	Teloepa 2	8174'
	Paning	30	Merrimelia 29	7100'	15	Merrimelia 29	7100'	8	Merrimelia 29	7100'	19	Merrimelia 29	7100'
	Paning	31	Merrimelia 17	7156'									
	Paning	32	Merrimelia 17	7158'									
	Paning	33	Merrimelia 29	7080-7090'									
<b>RF-3 CHUTE SANDS</b>	Paning	34	Merrimelia 15	7120'½"	16	Merrimelia 15	7120'½"				20	Merrimelia 15	7120'½"
	Paning	35	Merrimelia 17	7078'2½"	17	Merrimelia 17	7078'2½"	9	Merrimelia 17	7078'2½"	21	Merrimelia 17	7078'2½"
<b>RF-4 CREVASSE SPLAY SANDS</b>	Paning	36	Merrimelia 7	7108'4"	18	Merrimelia 7	7108'4"	10	Merrimelia 7	7108'4"	22	Merrimelia 7	7108'4"
	Cuddapan	3	Beanbush 1	8716'	3	Beanbush 1	8716'				4	Beanbush 1	8716'
	Callamurra	37	Merrimelia 29	7136'	19	Merrimelia 29	7136'						
	Paning	38	Merrimelia 17	7105'	20	Merrimelia 17	7105'						
	Paning	39	Merrimelia 17	7094'									
	Paning	40	Merrimelia 17	7116'									
	Paning	41	Merrimelia 17	7129'									
	Paning	42	Merrimelia 17	7060-7070'									
	Paning	43	Merrimelia 17	7070-7080'									
<b>RF-5. FINE-GRAINED SANDS FROM TOP OF POINT BARS</b>	Paning	44	Merrimelia 7	7065'11"	21	Merrimelia 7	7065'11"	11	Merrimelia 7	7065'11"			
	Paning	45	Merrimelia 3	7542'6"	22	Merrimelia 3	7542'6"	12	Merrimelia 3	7542'6"	23	Merrimelia 3	7542'6"
	Paning	46	Merrimelia 29	7104'	23	Merrimelia 29	7104'				24	Merrimelia 29	7104'
	Paning	47	Merrimelia 29	7070-7080'									

Table 3.1 Sample selection and completed analyses. (b) reservoir lithologies

XRD for mineral identification is detailed by Hardy and Tucker (1988).

Representative samples for bulk analysis were cut from the edge of the same rock block used for thin section preparation. The sample was hand ground in a mortar and pestle and made into a slurry with distilled water. The slurry was placed on a glass slide and allowed to dry in air. The aim of the above process was to get a representative bulk sample with minimum separation of size fractions on the glass slide. The preparations were analyzed in a Philips 1050 PW diffractometer, using  $\text{Co K}\alpha$  radiation. The scans were collected from 3 to  $75^\circ 2\theta$  at a rate of  $2^\circ/\text{minute}$  in  $0.05^\circ$  steps.

The resulting scans were analysed using TRACES™ software. The main quartz peak in each trace was set to  $31.10^\circ 2\theta$ . Minerals were identified by displaying the positions and relative heights of peaks from the search-match database included in the software. Semi-quantitative results for mineral occurrences were achieved by ratioing a peak from the mineral of interest with the  $4.26 \text{ \AA}$  quartz peak. This peak was chosen to avoid interference from illite and to obtain an easy number to work with. The  $3.33 \text{ \AA}$  quartz peak is too big. The peaks chosen for quantification were illite  $10.1 \text{ \AA}$ , kaolin  $7.2 \text{ \AA}$ , and siderite  $2.79 \text{ \AA}$ . The ratio (kaolin to illite) quantifies the type of clay present, while the ratio kaolin plus illite to quartz identifies the total clay content of each sample (Pers. Comm. N. Lemon, 2000).

### 3.4 OPTICAL PETROGRAPHY

Twenty-seven thin sections without permanent cover slips were produced by Pontifex and Associates. The thin sections were cut perpendicular to the bedding, to a standard thickness of 0.3 cm, and impregnated with blue-dye epoxy resin to facilitate porosity recognition. Thin section descriptions are shown in Appendix 3.2.

Quantitative estimates of macroporosity, microporosity, pore size and grain size were accomplished using the color image analysis software VIDEOPRO 32 (Version 3.37).

An average of 180 grain size measurements per sample and 150 pore size measurements per sample, together with the associated scaling factor are presented in Appendices 3.3 and 3.4, respectively.

The grain size analysis was performed using the NCPGG program GRSORT. GRSORT was used to transform the grain size measurements from microns into the PHI scale and also to correct for grain sizes observed in randomly cut thin section into actual grain size that might be achieved by sieve analysis. GRSORT assumes that all grains are spherical. Although this might be a poor assumption, the mathematical and statistical results for nonspherical grains are very close to that of spherical grains (Pers. Comm. C. Dyt, 1999). The program equates first the grain size measurements from microns to PHI classes and then gives the corrected values of grain size in PHI range together with number of measurements and percentage of participation of each class (Appendix 3.5).

Thin section photomicrographs were taken to illustrate the diagenetic aspects and the porosity distribution. Both plane light and crossed polarized light were used at magnifications of x5, x10 and x20, using an Olympus BHSP petrological microscope.

### **3.5 SCANNING ELECTRON MICROSCOPY (SEM)**

Twelve representative samples were selected for SEM studies. An SEM sample consists of a small square block of rock (1 cm by 1 cm) with a fresh surface cut perpendicular to the bedding plane. The sample is attached to a metallic pin type stub and then is dried in a low temperature drying oven. A thin line of Silpaint provides the electrical ground from the sample to the plug. To obtain a clear image of an insulating material, the sample is coated with a combined coating of carbon plus gold.

A Philips XL20 scanning electron microscope was used to view the samples. The SEM image is formed by collecting the secondary electrons generated by the interaction of an internally generated primary electron beam with the sample. A magnification of x100 was employed in all samples to illustrate porosity distribution and higher magnifications to describe specific mineralogical aspects or diagenetic events. The spot size used was 4 or 5 and the accelerating voltage 15 kV or 10 kV.

The images display the actual three-dimensional grain relationships, details of intergranular pore structure and help identify smaller minerals. Selected images were digitally stored for later display.

### 3.6 MERCURY INJECTION CAPILLARY PRESSURE (MICP) TECHNIQUES

Mercury injection capillary pressure techniques were employed for seal capacity calculation. A total of 24 samples representing both sealing and reservoir lithologies were injected with mercury, using the Micromeritics Autopore 9410 mercury injection porosimeter at the National Centre for Petroleum Geology and Geophysics. The capillary pressure curves are presented in Appendix 3.6. The following information is compiled from the "Operative Instructions for the Micromeritics Autopore 9410 mercury injection porosimeter".

The Autopore 9410 machine is composed of two separate systems; one for low pressure runs and the second for the high pressure runs (Fig. 3.1 and Fig. 3.2). The cleaned and dried sample is weighed and placed in a sealed penetrometer. The penetrometer is sealed using a nylon nut and cover (Fig. 3.2 and Fig. 3.3). A light coating of Apiezon H high vacuum grease is applied to the rim of the penetrometer sample chamber and a metal sealing cap is placed on it. The sample is placed first in the low pressure system where the readings of pressure are taken from 2 psi up to 50 psi and then the sample is returned to atmospheric conditions. At that time the penetrometer is removed from the low pressure port and weighed. The high pressure run is then started. The high pressure system involves subjecting the sample to pressures from 45 psi to 60,000 psi and then back down to atmospheric pressure holding at each pressure for 20 seconds to allow the system to equilibrate. The pressure and volume data are continuously recorded digitally.

The mercury porosimeter technique is based on the principle that a non-reactive, non-wetting liquid will penetrate the pores of a sample only when a sufficient pressure is applied to force its entrance. The Washburn equation shows the relationship between the applied pressure and the pore size into which the mercury will intrude (Washburn, 1921).

$$P \cdot D = 4 \sigma \cos \theta$$

where:

$P$  = the applied pressure (dynes/cm<sup>2</sup>);

$D$  = diameter of pore throat (cm);

$\sigma$  = surface tension of mercury (480 dynes/cm);

$\theta$  = contact angle between mercury and pore wall (140°).

All pores are assumed right cylinders.

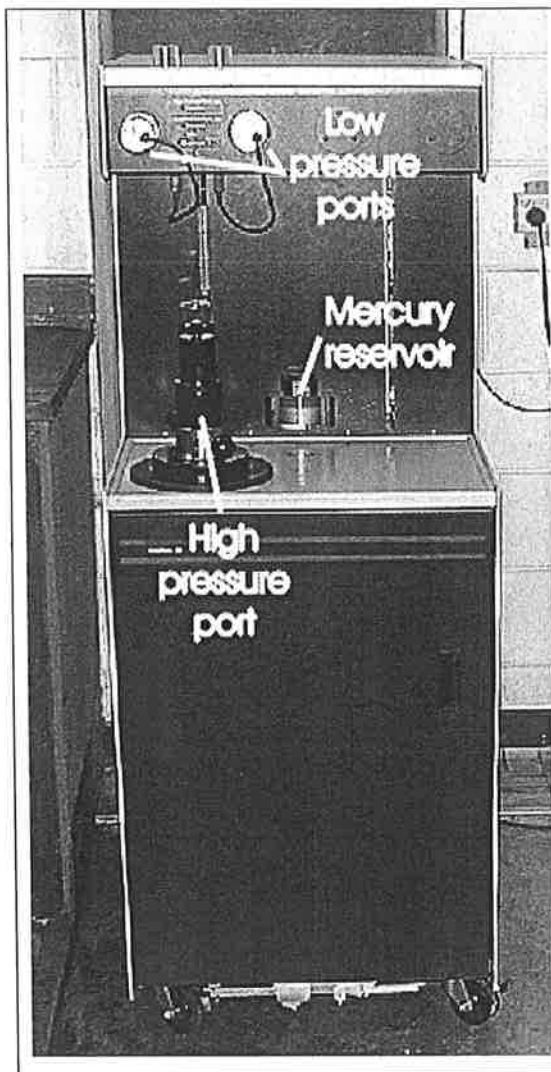


Figure 3.1 The Micromeritics Autopore 9410 mercury injection porosimeter

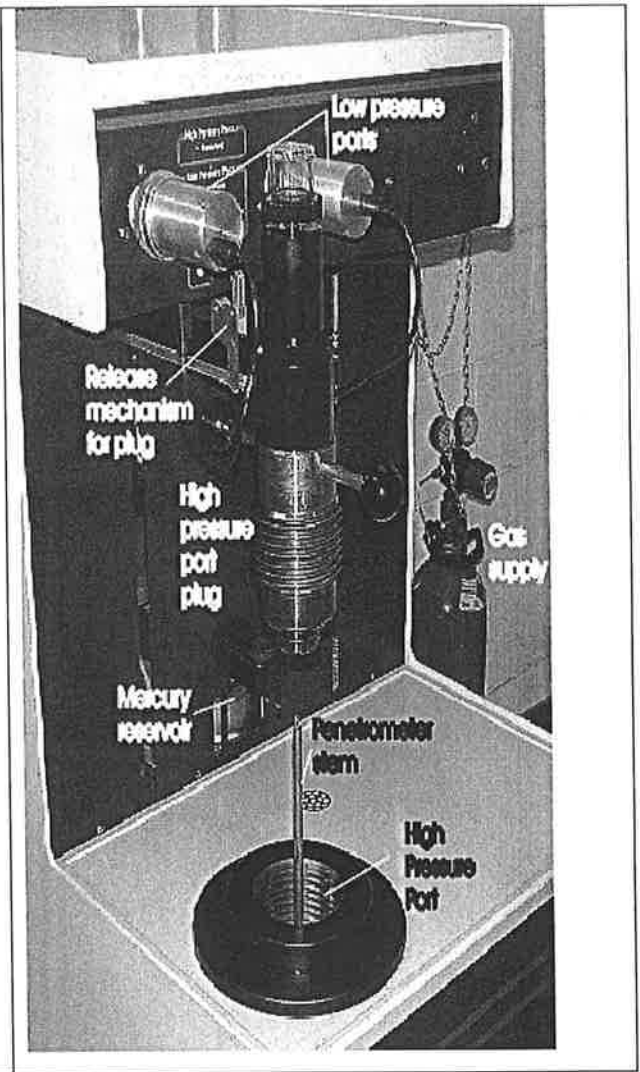


Figure 3.2 A closer view of the Micromeritics Autopore 9410 mercury injection porosimeter

As the pressure increases, mercury enters the rock pore system; first in the pores with the biggest pore throats and then in the pores with the smaller pore throats. The mercury injection curve represents the increasing saturation of mercury as a function of pressure. As mercury injection pressure is increased the instrument senses the intrusion of mercury by measuring the rock pore volume saturated by mercury.

From Darcy's equation

$$\frac{P_1 - P_2}{L} = \frac{\alpha \mu V}{g_c}$$

where:

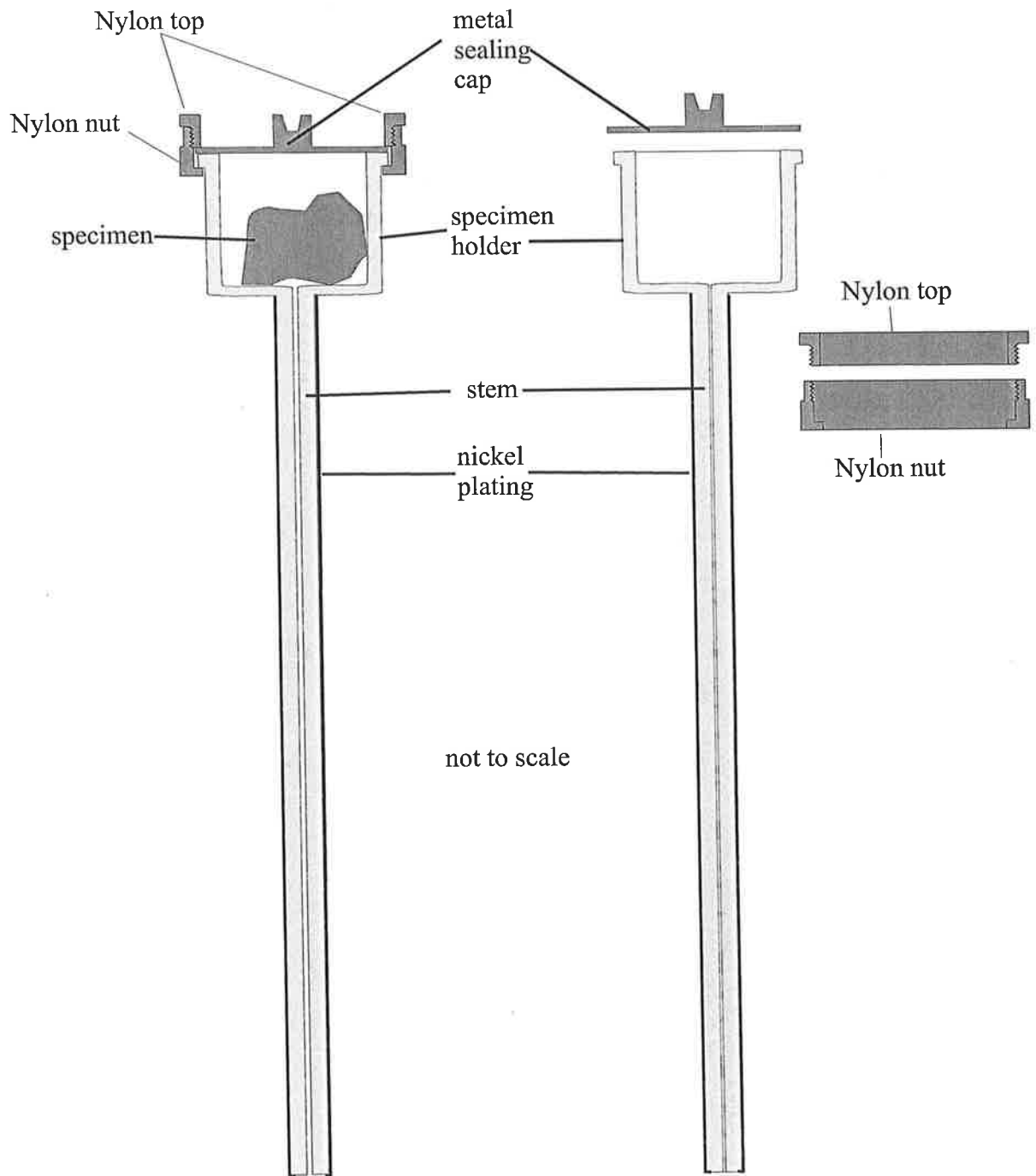


Figure 3.3 Schematic view of an assembled penetrometer and the component parts, using the nylon nut and cover (new style).

$P_1$  is the upstream pressure;  
 $P_2$  is the downstream pressure;  
 $L$  is the pore length;  
 $1/\alpha$  is the permeability coefficient;  
 $\mu$  is the fluid viscosity;  
 $V$  is the superficial velocity of fluid;  
 $g_c$  is a dimensional constant.

It can be seen that the velocity of flow in a viscous liquid such as mercury is proportional to the pressure drop and inversely proportional to the pore length. Therefore, for a specific limited flow velocity, the complete filling of a porous network is a function of time. The most accurate measurements are recorded when the mercury is allowed to fill all the available pores ("equilibration"). Incomplete filling of the pores leads to measurement of a lower pore volume and smaller pore throat size.

### **3.1 WIRE LINE LOG ANALYSIS AND MAPPING**

The analysis of wire-line logs was accomplished using Mincom Pty Ltd's Geolog software on a Sun workstation at the National Centre for Petroleum Geology and Geophysics (NCPGG). A total of twenty-five wells were analyzed for lithology discrimination, using gamma ray, density and sonic logs and correlated regarding depositional environment across Merrimelia field. Reservoir and non-reservoir sandstones were separated in one well, using litho-density (photoelectric factor) and natural gamma ray spectrometry (potassium concentration).

Maps of thickness and quality of the sealing intervals were produced using Petrosys software.

## CHAPTER FOUR

### SAMPLE PETROGRAPHY AND DIAGENETIC HISTORY

#### 4.1 INTRODUCTION

This chapter presents the petrographic/mineralogical composition, texture, and diagenesis of the Triassic sediments in the Cooper Basin. Depositional environment and post-depositional events affect the rock porosity and permeability and control reservoir or seal properties.

#### 4.2 PETROGRAPHIC OBSERVATIONS

##### 4.2.1 Texture

Grain size was measured for all reservoir and seal lithofacies in thin sections. Grain size distribution was described by statistical parameters such as average grain size, standard deviation, skewness and kurtosis. The samples were classified by their average grain size. Standard deviation or spread of values about the average was calculated to define the sorting of sediment. Skewness, the asymmetry of the grain size curve, was determined to evaluate whether finer (positive value) or coarser (negative value) than normal grain size distributions are present. Kurtosis shows the concentration or peakedness of a distribution. Very flat curves that represent poorly sorted sediments and bimodal frequency curves are considered platykurtic or flat. Peaked curves means very good sorting of the central part of the distribution and are called leptokurtic or spiky. A summary of commonly used descriptive terms of parameters is presented in Table 4.1.

The grain sizes range from pebble to clay-sized as a function of the depositional facies of each sample. The statistical parameters of the grain size distribution are summarised in Appendix 4.1. The average grain size and sorting are considered the key values. Skewness and kurtosis are subsidiary readings for sorting. Examples of grain size data and their statistical parameters for three reservoir lithofacies (fluvial channel sand RF-2, chute sand RF-3 and crevasse splay sand RF-4) are shown in the histograms from Fig. 4.1.



Sorting		Skewness		Kurtosis	
Very well sorted	< 0.35	Very positively skewed	+0.3 to +.01	Very platykurtic	< 0.67
Well sorted	0.35-0.50	Positively skewed	+0.1 to +0.3	platykurtic	0.67-0.90
Moderately well sorted	0.50-0.70	Symmetrical	+0.1 to -0.1	mesokurtic	0.90-1.11
Moderately sorted	0.70-1.00	Negatively skewed	-0.1 to -0.3	leptokurtic	1.11-1.50
Poorly sorted	1.00-2.00	Very negatively skewed	-0.3 to -0.1	Very leptokurtic	1.50-3.00
Very poorly sorted	2.00-4.00			Extremely leptokurtic	> 3.00
Extremely poorly sorted	> 4.00				

Table 4.1 Descriptive terms applied to parameter values (McManus, 1988).

In addition, visual estimates of particle size and sorting, using a comparison chart for sorting and sorting classes (Pettijohn *et al.*, 1972) were used for samples where grain size could not be measured in thin section (gravels, floodplain mudstones, fine-grained lacustrine sediments and palaeosols).

The texture of the analysed samples varies from very well sorted silts and clays (lacustrine mudstones SF-2, palaeosols SF-3 and floodplain mudstones SF-4), to poorly sorted pebble gravels (RF-1). The intermediate components consist of moderately sorted (St. Dev. = 0.71-0.73) fine (phi = 2-3) to medium grained (phi = 1-2) fluvial channel sands (RF-2), moderately well sorted (St. Dev. = (0.53-0.65) fine (phi = 2-3) to medium grained (phi = 1-2) chute sands (RF-3), moderately (St. Dev. = 0.73) to moderately well sorted (St. Dev. = 0.58-0.68) fine (phi = 2-3) or medium grained (phi = 1-2) crevasse splay sands (RF-4), moderately well sorted (St. Dev. = 0.53-0.58) fine grained (phi = 2-3) sands from top of point bars (RF-5) and of moderately well sorted (St. Dev. = 0.56-0.58) fine (phi = 2-3) to very fine (phi = 3-4) grained diagenetically modified sandstones (SF-1) and very fine (phi = 3-4) grained palaeosols (SF-3) .

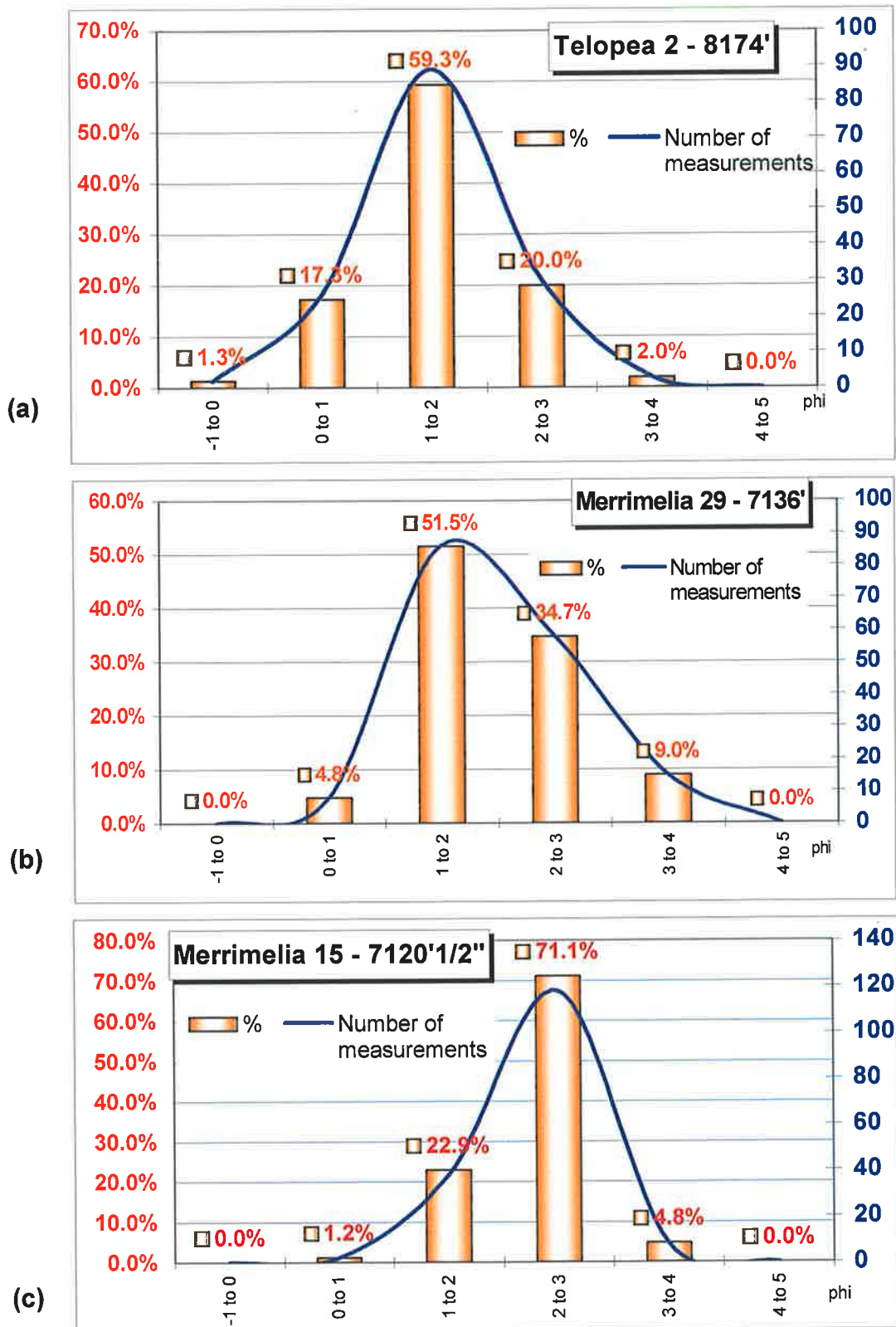


Figure 4.1 Examples of grain size distribution. a) medium sand, moderately sorted with symmetrical, very flat curve (RF-2), b) fine sand, moderately well sorted with negatively skewed, normal distribution (RF-3), c) medium sand, moderately sorted, with very flat, positively skewed curve (RF-4).

A visual comparison chart (Powers, 1982) was used to estimate roundness of grains. The great majority of samples show subangular to subrounded grain shapes.

The nature of grain to grain contacts is a key measure of compaction. Grain to grain relationships were determined visually and placed in a scale from “floating, tangential, straight, concave-convex to sutured”. Samples have a range of contacts; the most predominant ones are illustrated in Fig. 4.2. Note that the degree of compaction increases with grain size, and is lower in the fine-grained sediments, being dependant on depositional environment.

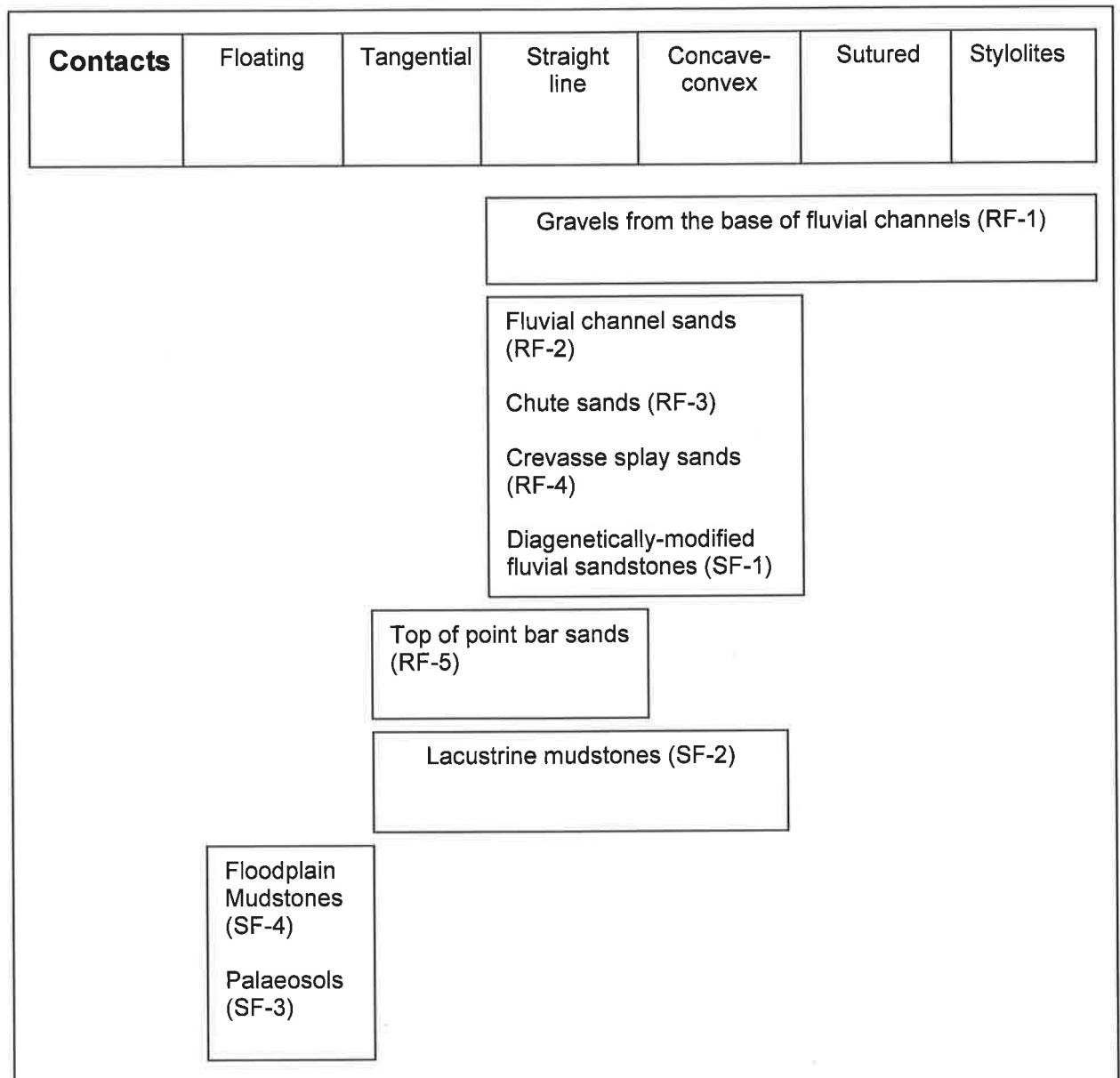


Figure 4.2. Grain to grain relationships. The low compaction indicators in the fine-grained sediments are in part a function of the presence of matrix.

## 4.2.2 Framework grain composition

The framework components of the rock were estimated visually in thin sections; the resulting values are summarized in Appendix 4.2.

Quartz is the main component within the studied samples, ranging from 15% to 67% of whole rock volume. Monocrystalline grains are far more common than polycrystalline ones. Some quartz grains, particularly those of a metamorphic or hydrothermal origin contain vacuoles, zircon, and acicular mineral inclusions and are partially affected by dissolution. Rock fragments make up 3% to 25% of the rock composition. They are represented by chert, mud chips and silt fragments and are affected by dissolution, alteration to clays or can be deformed during compaction. Feldspars are absent from the system, having been totally altered to clays, usually kaolin. Minor components such as heavy minerals (zircon, sphene, tourmaline), micas, together with organic matter participate from trace amounts to 15% of the rock composition. The percentage of framework components is illustrated in Fig. 4.3.

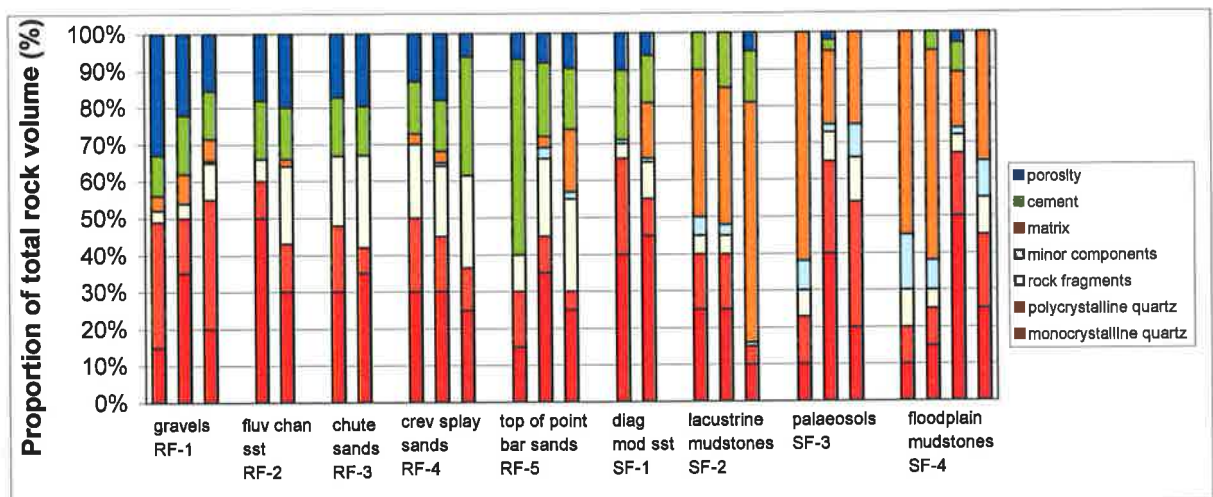


Figure 4.3 Constituents of the total rock composition as determined by visual estimation from thin sections of samples selected for MICP evaluation as listed in Table 3.1.

The sandstone facies plot on the Folk classification (Folk, 1968) as litharenite (fluvial channel sands RF-2, chute sands RF-3, crevasse splay sands RF-4, top of point bar sands RF-5) and sublitharenite (fluvial channel sands RF-2) or as lithic wackes (top of point bar sands RF-5, diagenetically-modified sandstones SF-1) and sublithic wackes (crevasse splay sands RF-4, diagenetically-modified sandstones SF-1, palaeosols SF-3) for samples with more than 10% matrix. The strong bias to the lithic

scale of the plot is a result of the alteration of feldspar to kaolin. No fresh feldspars have been observed in any of the reservoir units in the main Cooper Basin (Rezaee and Lemon, 1996; Schulz-Rojahn and Phillips, 1989) although there must have been feldspars in the mixed igneous, metamorphic sedimentary provenance. The Triassic Nappamerri Group is a continuation of the meandering stream fluvial sedimentation of the Permian Toolachee Formation with the same provenance and subject to the same diagenetic regime. The masses of kaolin observed in the Triassic sediments have, in all probability, been derived from feldspars. A series of samples collected from the southern limits of the Cooper Basin show the gradation from fresh feldspars to masses of kaolin in place of feldspars (Pers. Comm. N. Lemon, 2000). All framework constituents were recalculated to 100% and plotted on Quartz-Feldspar-Rock Fragments ternary diagram (Fig. 4.4).

In fine-grained sediments, the clay and silt-sized material was recalculated to 100% and plotted on a Clay-Sand-Silt ternary diagram (Fig. 4.5). According to Picard classification (1971), the fine-grained sediments are claystones (palaeosols SF-3, floodplain mudstones SF-4), silty claystones (lacustrine mudstones SF-2, floodplain mudstones SF-4) or clayey siltstones (lacustrine mudstones SF-2, floodplain mudstones SF-4).

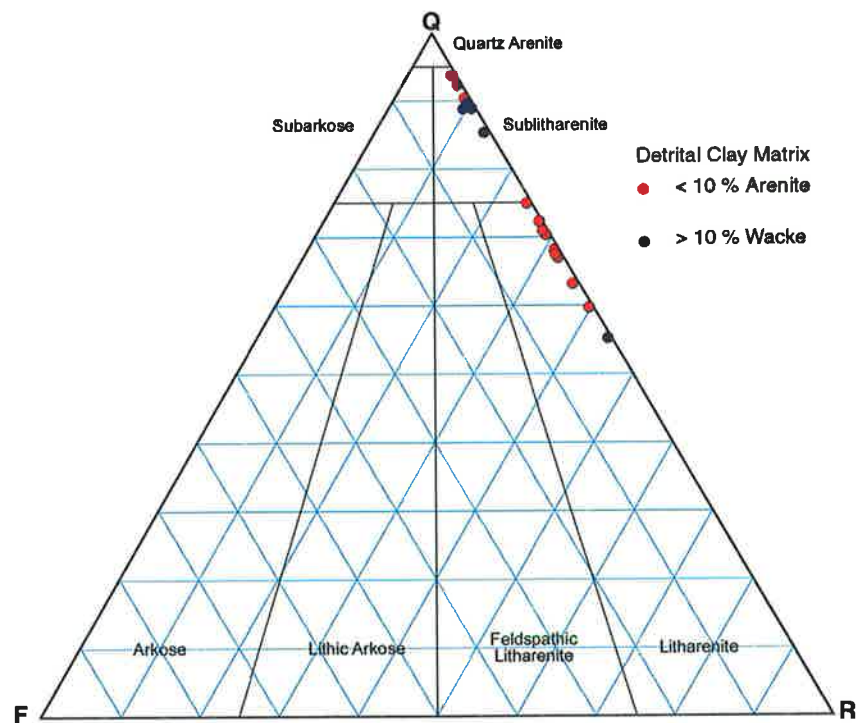


Figure 4.4 QFR ternary diagram showing the framework grain composition of the sandstone facies (Folk, 1968). The bias away from the feldspar pole is a function of the alteration of feldspar to clay.

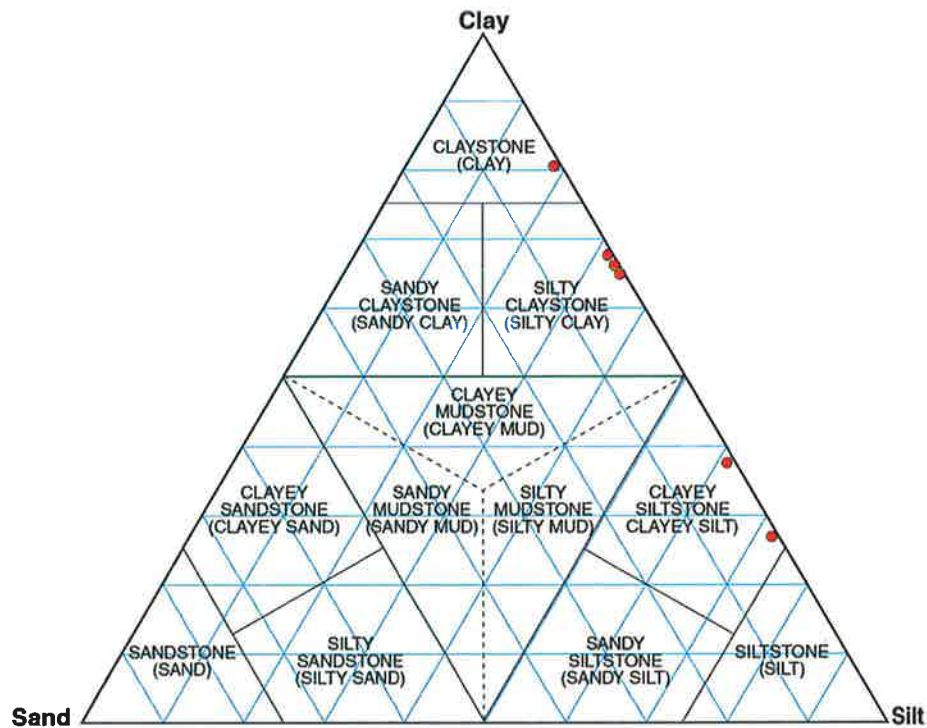


Figure 4.5 Textural classification of fine-grained rocks and sediments (Picard, 1971)

### 4.3 XRD RESULTS AND INTERPRETATION

The bulk X-Ray diffraction analyses indicate quartz, kaolin, illite and siderite as the major components for the studied samples (Fig. 4.6.a-d). Some traces show an elevated background inferring the presence of organic matter such as oil, kerogen or coaly matter.

The minerals were identified based on recognition of groups of peaks and their heights at known diffraction angles. The diffraction intensity of a mineral in a mixture is proportional to its concentration; therefore, measuring relative peak heights or area allows the estimate of the relative proportion of minerals in a sample (Hardy and Tucker, 1988). The relative proportion of minerals in a sample was estimated measuring peak areas, using Traces software for XRD data display (Appendix 4.3). Proportions of the major minerals at the rock constitution are illustrated in Fig. 4.7. There is an increase of quartz in coarser lithologies (RF-1 to RF-4) together with an increase in kaolin and illite relative to quartz in finer grained lithologies (SF-3 and SF-4). Siderite is most common in palaeosols (SF-3) and can be also found in crevasse splays (RF-4) and top of point bar sands (RF-5).

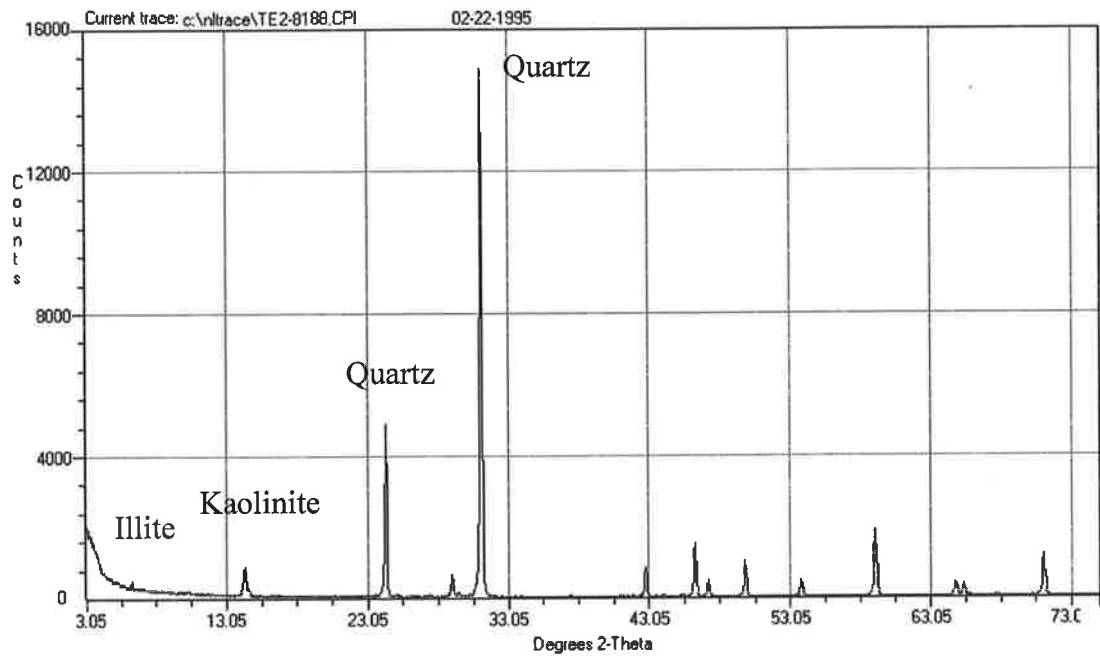


Figure 4.6.a Representative XRD peak pattern of clean quartz-rich gravel (RF-1), Telopea 2 – 8188 ft.

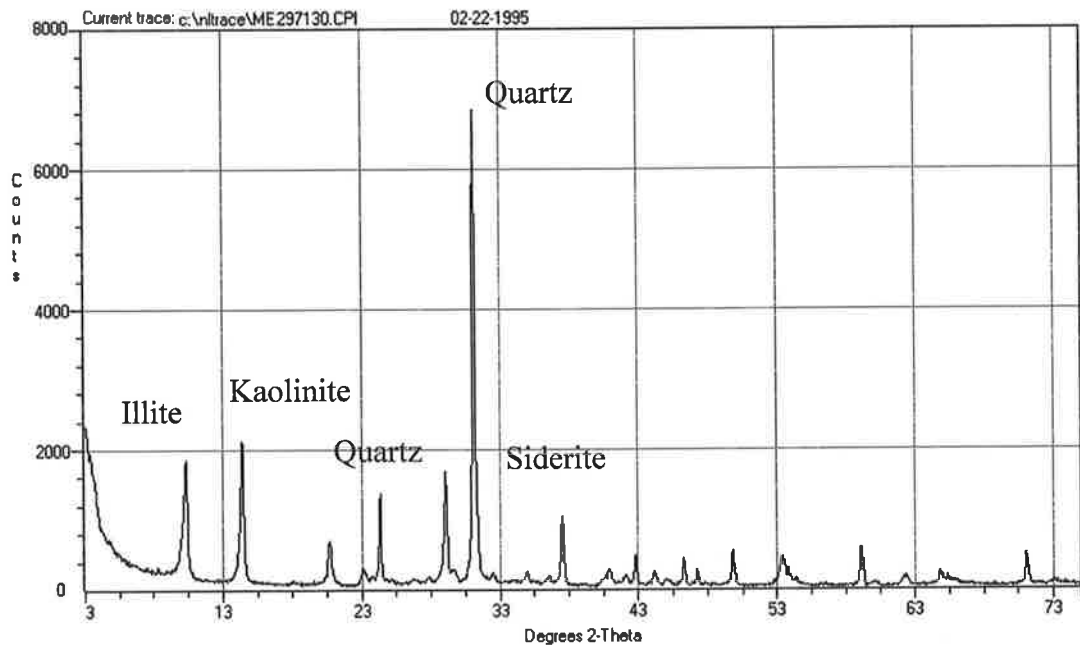


Figure 4.6.b Representative XRD peak pattern for a clay-rich palaeosol (SF-3), Merrimelia 29 – 7130 ft.

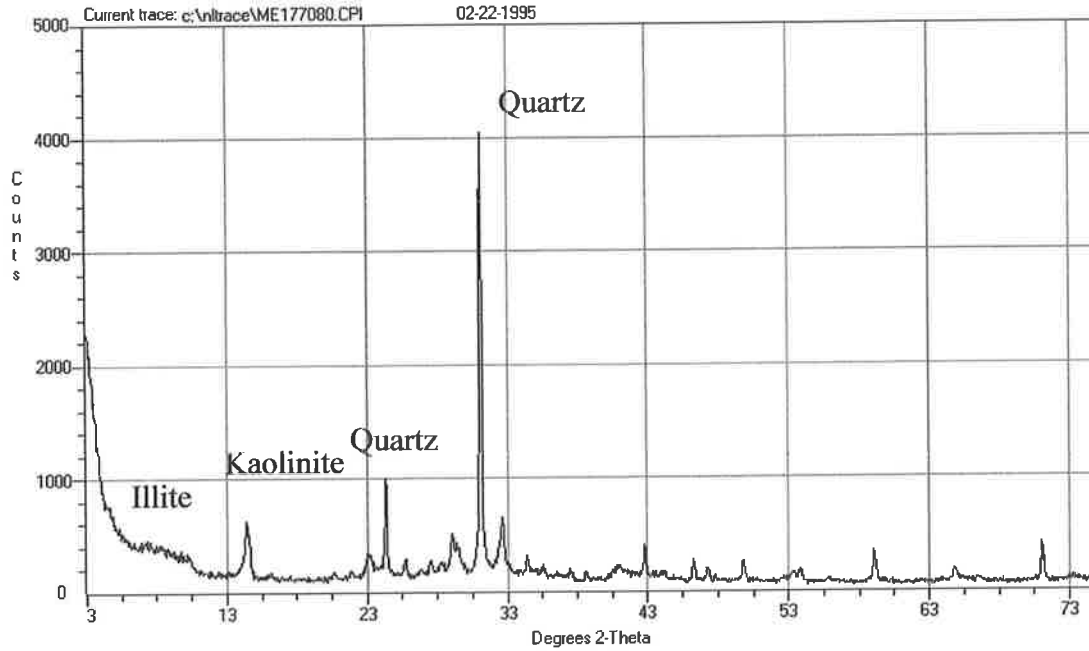


Figure 4.6.c Representative XRD peak pattern for a crevasse splay sand (RF-4) with a high background of organic material, Merrimelia 17 – 7080 ft.

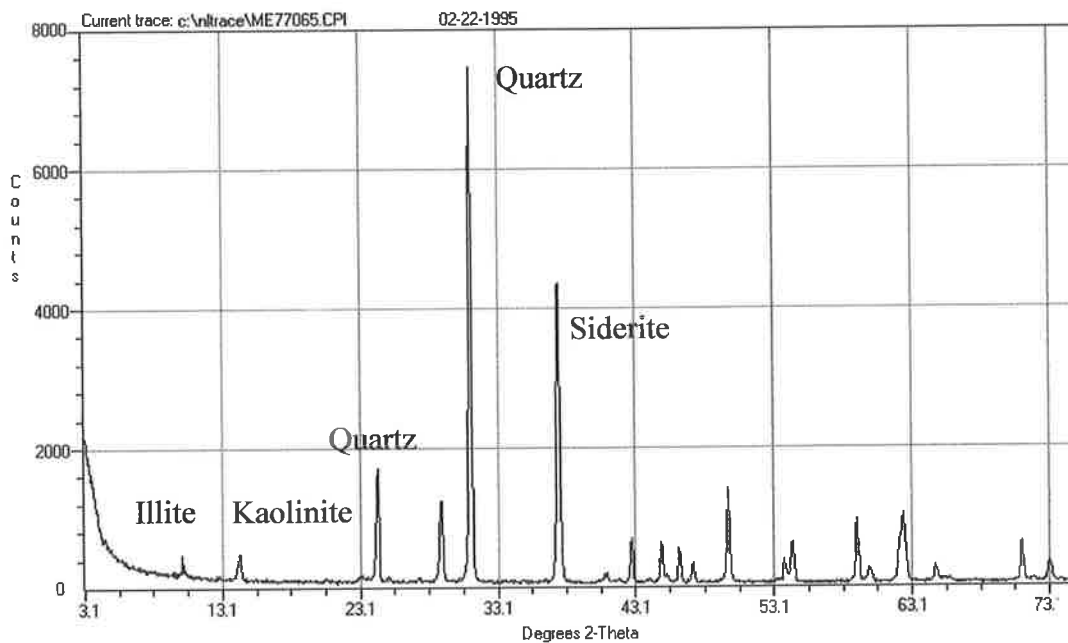


Figure 4.6.d Representative XRD peak pattern of siderite-cemented fine sand from the top of point bars (RF-5), Merrimelia 7 - 7065 ft 11 in.



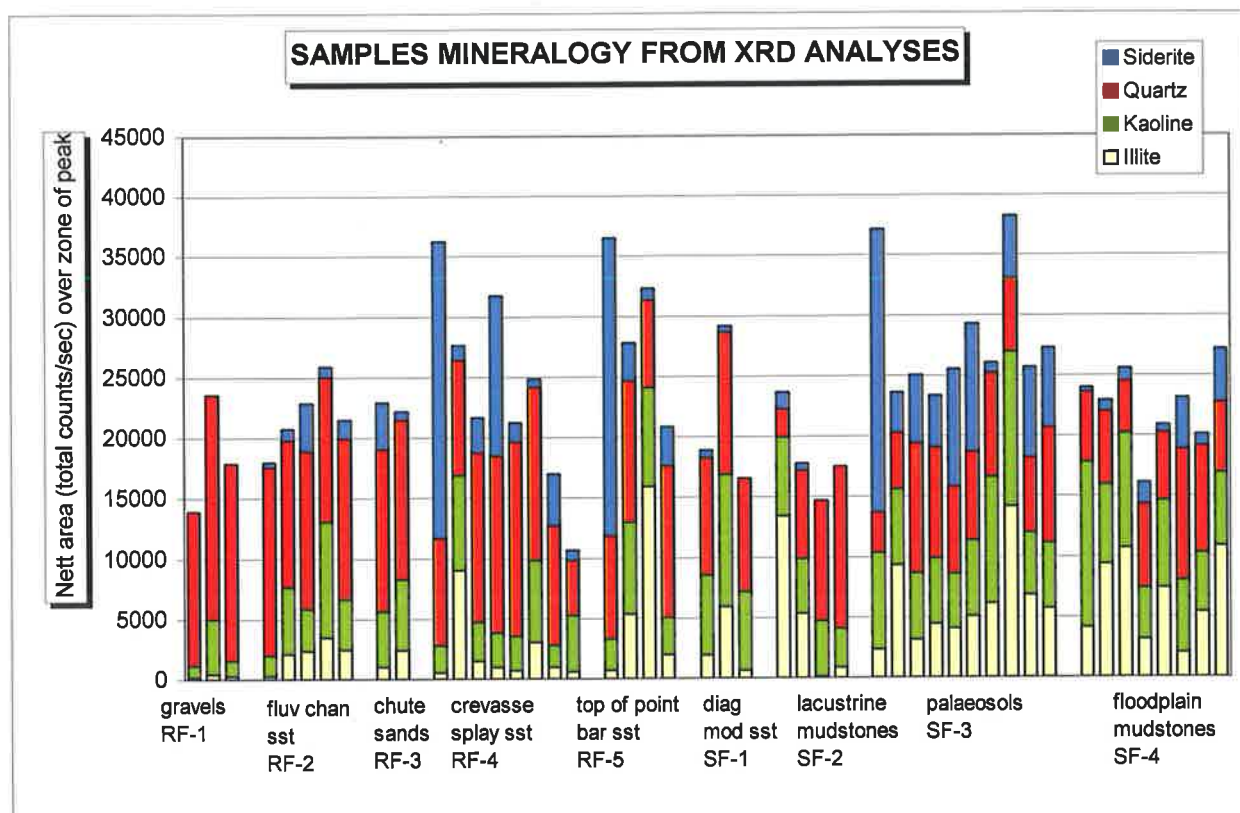


Figure 4.7 Indication of mineral composition from raw XRD peak area data. Variation in total counts is a function of smear thickness. Quartz is low because the  $4.27\text{\AA}^0$  peak was used. Bars indicate relative proportions between (see Table 3.1 for sample listing).

Reservoir/sealing quality was assessed by cross-plotting clay type (kaolin/illite ratio from XRD analyses) against total clay in the rock (kaolin + illite to represent total clay, valued over quartz from XRD analyses) (Fig. 4.8.a). The reservoir lithofacies samples plotted in an area in which clay content is less than quartz and kaolin is more than illite. The increase in both clay content and illite at the expense of kaolin diminishes the reservoir quality, while the sealing quality is enhanced by a predominance of clays. The quality of reservoir and sealing lithologies, separated on depositional lithofacies is illustrated in Fig. 4.8.b-c.

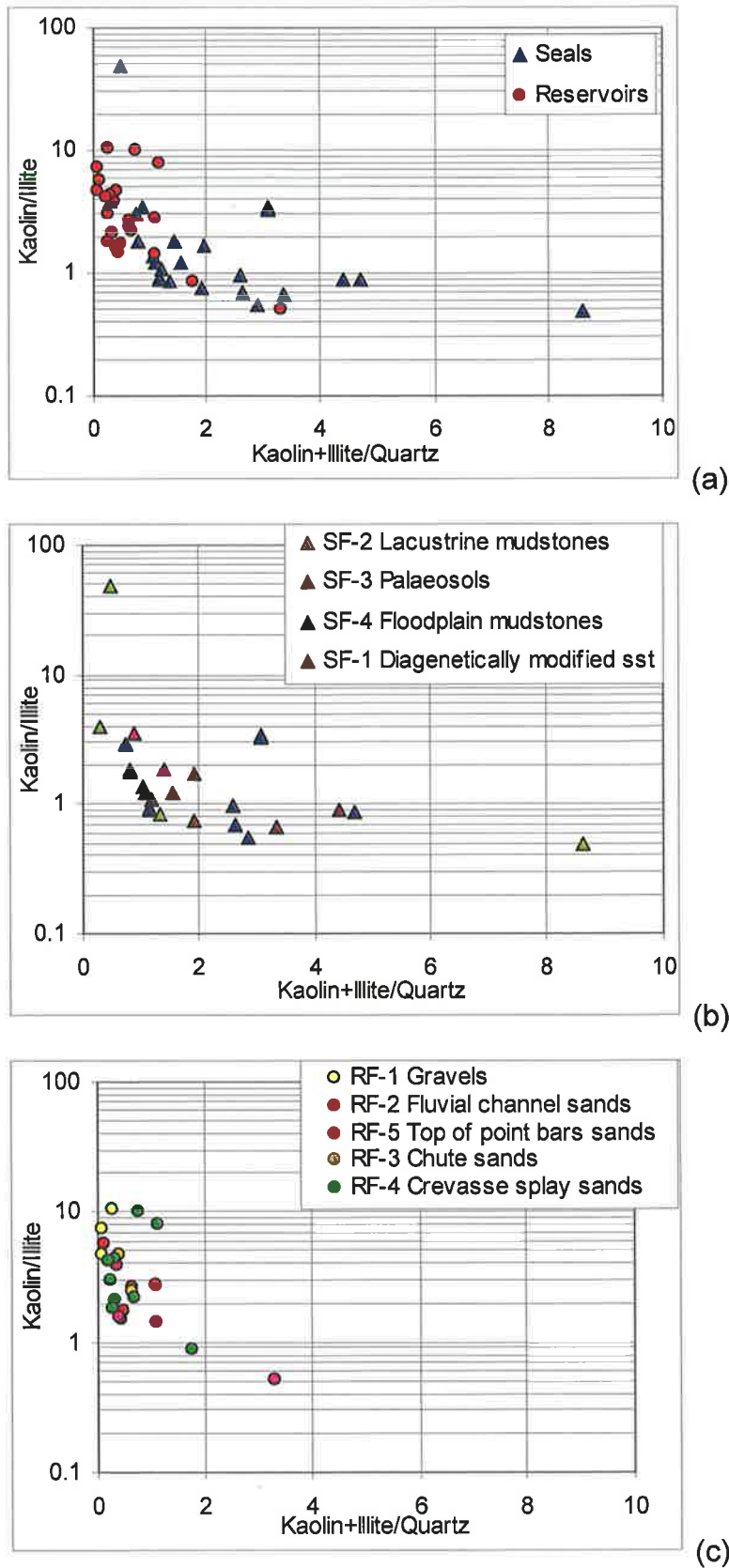


Figure 4.8 Cross-plots that illustrate (a) reservoir/seal quality (b) sealing lithofacies quality (c) reservoir lithofacies quality (values are derived from measurement of XRD peak areas).

Reservoir/sealing quality of the selected lithologies was also assessed by plotting core porosity and permeability versus the kaolin + illite, kaolin and illite content of the samples (Fig.4.9.a-f).

Porosity versus kaolin + illite (Fig.4.9.a). The plot shows a weak negative correlation that is difficult to interpret. The problem is resolved when the plots for individual clays are considered.

Permeability versus kaolin + illite (Fig.4.9.b). The plot shows a weak negative correlation. An increase in clay content sees a decrease in permeability.

Porosity versus kaolin (Fig.4.9.c). There is a weak to non-existent correlation. Kaolin is present in all samples, in the matrix, as masses after feldspar and partially filling the intergranular pore spaces. The style and distribution of the clay has only an indirect influence on porosity.

Permeability versus kaolin (Fig.4.9.d). This plot shows a good negative correlation. The more pore-filling kaolin present in a sample, the more tightly packed it will be. Pore-filling kaolin controls the open pathways through the rock, strongly influencing permeability.

Porosity versus illite (Fig.4.9.e). The plot shows a good correlation. Most of the illite in the samples is present as matrix clay, increasing in the finer grain sizes. As matrix partially or fully fills the pore spaces, the reason for the negative correlation is clear.

Permeability versus illite (Fig.4.9.f). At first glance, there is only a weak negative correlation. If the point RF-5 is considered as an outlier, the negative correlation between the rest of the samples is strong. This is to be expected as the platy illite in the matrix blocks any large pore throats.

SF-2, diagenetically-modified sandstones is the same as RF-5, fine-grained sands from the top of point bars but the distinction was made during sample collection because the top of the oil column could be seen in SF-2 facies in Telopea 2, 8186'3" and Merrimelia 15, 7114'5". The obvious seals were collected separately to see if they were any different from the same facies where there was no oil present to indicate their sealing/reservoir behaviour.

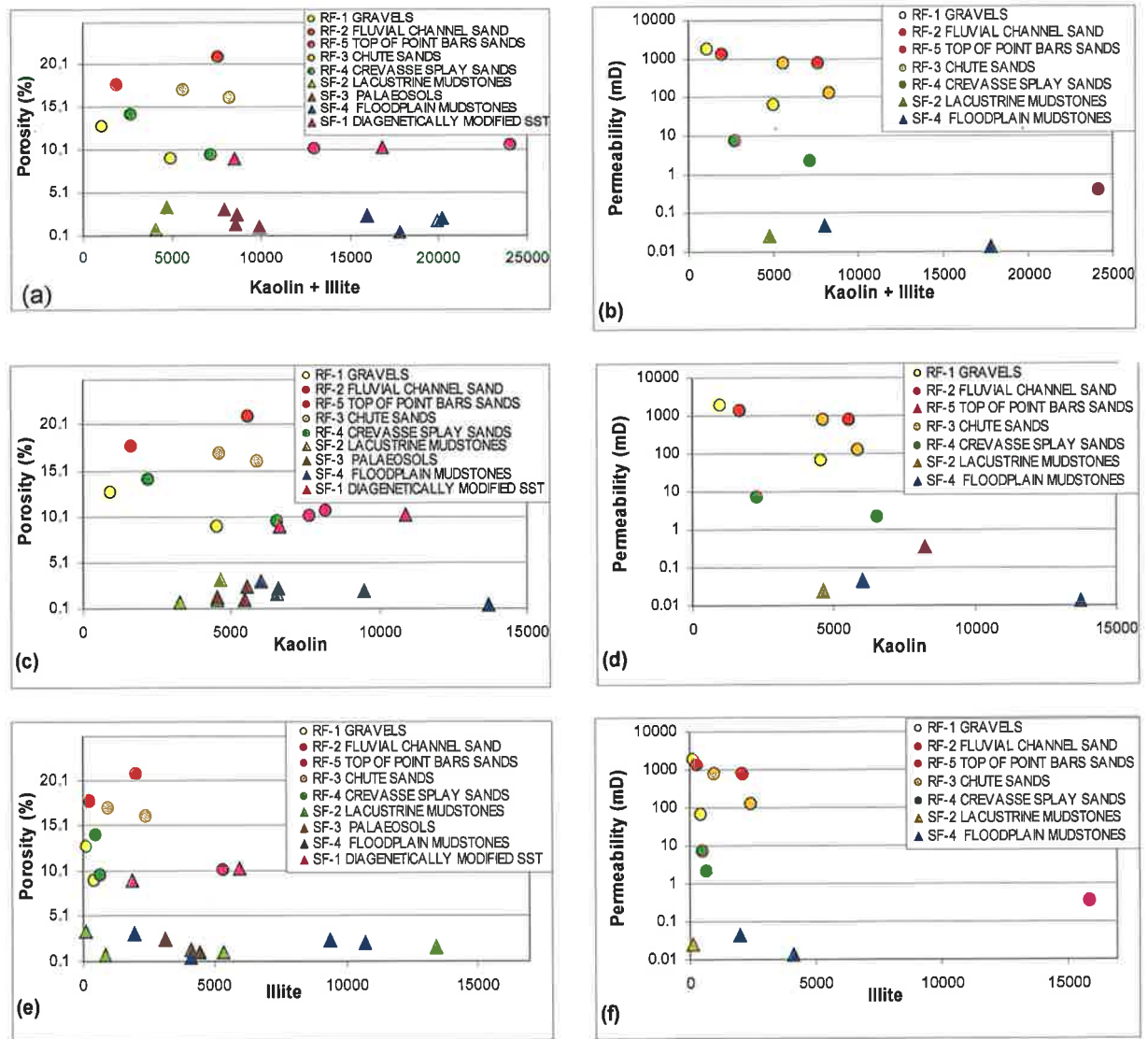


Figure 4.9 Cross-plots that illustrate reservoir/seal quality. (a) porosity versus kaolin + illite (b) permeability versus kaolin + illite (c) porosity versus kaolin (d) permeability versus kaolin (d) porosity versus illite (e) permeability versus illite (values are derived from measurement of XRD peak areas).

## 4.4 DIAGENETIC EVENTS

Mechanical and chemical compaction, cementation, dissolution and alteration are the diagenetic processes evidenced in the studied samples. Cementation and compaction have caused a reduction of the primary porosity and permeability while dissolution has contributed to an increase of porosity.

### 4.4.1 Compaction

Compaction is induced by the lithostatic pressure and is manifested as a reduction of primary porosity. Evidence of mechanical compaction includes plastic deformation of rock fragments (Plate 4.4.h), bent or distorted muscovite flakes (Plate 4.1.a), fractured grains and the large number of grain to grain contacts.

Chemical compaction is defined as the dissolution of framework grains under overburden pressure or tectonic forces and is illustrated by concave-convex and sutured grain contacts (Plate 4.1.b), pressure dissolution seams (Plate 4.1.d) and stylolites (Plate 4.1.c). The stylolites commonly develop against contacts with matrix. Mechanical compaction was observed in gravels (RF-1), fluvial channel sands (RF-2), and crevasse splay sands (RF-4); chemical compaction was observed in gravels (RF-1) and floodplain mudstones (SF-4).

### 4.4.2 Alteration

Alteration of feldspars is considered to be the source for quartz and kaolin cements, while illite is an alteration product of rock fragments.

### 4.4.3 Cementation

Quartz overgrowth, kaolin, illite, siderite and pyrite cements were observed in all reservoir facies and sealing facies SF-1. The proportion of each cement type was visually estimated in the thin sections (Appendix 4.2). The relative proportions of cements observed are illustrated in Fig. 4.10.

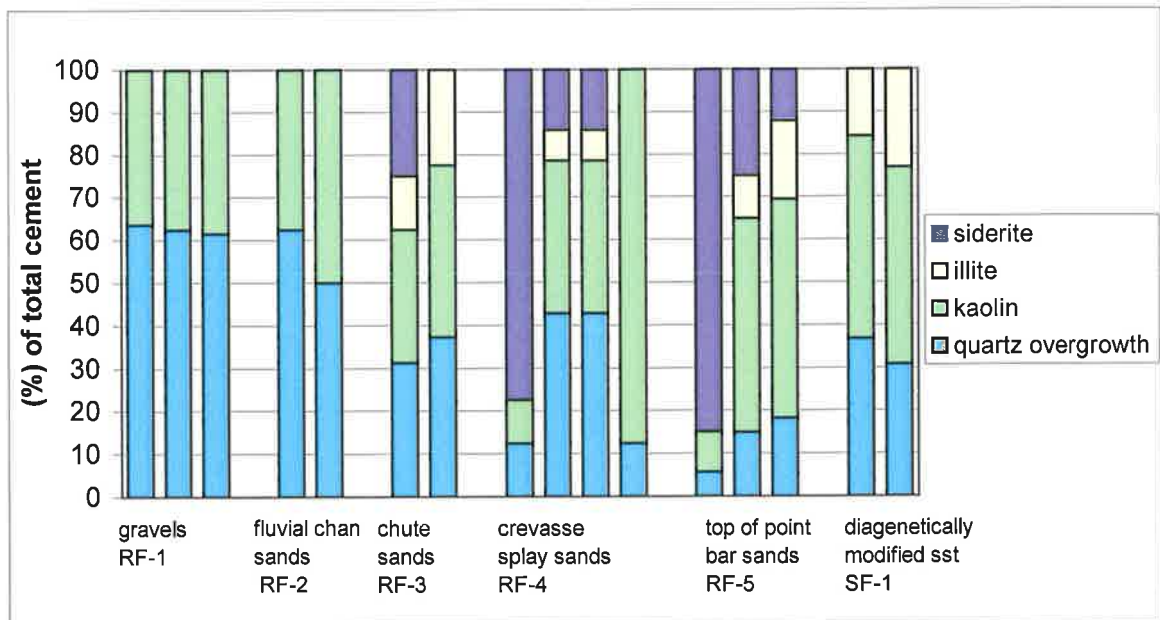


Figure 4.10 Relative proportions of cement types as determined by visual estimation in thin sections (see Table 3.1 for listing).

#### 4.4.3.1 Quartz

Authigenic quartz occurs as syntaxial overgrowths on detrital quartz grains. It can entirely or partially cover quartz grains. The overgrowths are recognizable by their prismatic euhedral crystal terminations (Plate 4.2.a - 4.2.d, 4.2.h), by dust or clay rims (Plate 4.2.a and 4.2.b) and by fluid inclusions on the contact with the detrital grains. The quartz overgrowths grow into primary and secondary pores, partially filling them (Plate 4.2.a and 4.2.b). This contributes to the partial preservation of the primary intergranular porosity between the euhedral crystal terminations by protecting the rock against compaction. Some quartz grains show only incipient overgrowths, which appear as small, closely spaced crystal prisms or druse (Plate 4.2.e). Quartz overgrowths are commonly intergrown with kaolin cement (Plate 4.2.g and 4.2.h). The overgrowths can be chemically etched resulting in V-shaped depressions (Plate 4.2.f).

Quartz overgrowth cement is predominant in gravels (RF-1) and fluvial channel sands (RF-2), comprising 7% to 10% of the total rock volume. In chute (RF-3), crevasse splay (RF-4) and top of point bar (RF-5) sands, authigenic quartz is subordinate to clay cement and represents less than 7% from the whole rock. Quartz cements are minor in the other sealing lithologies (Appendix 4.2).

#### 4.4.3.2. *Clay*

Clay minerals are both authigenic and allogenic (detrital). Authigenic clays are particularly evident under SEM, where they exhibit a euhedral habit. They have a narrow range of composition, evidenced by the relatively narrow, sharp peaks on XRD. Authigenic clays are mainly kaolin and subordinate illite.

Kaolin occurs as subhedral to euhedral booklets of various sizes, from 1-3 microns in fine sands to 30-40 microns in coarser sediments. The hexagonal kaolin booklets occur as stacks with a vermiform habit (Plate 4.3.a – 4.3.c). Kaolin occurs in three forms: 1) it fills the pore and pore throat spaces (Plate 4.3.d – 4.3.f), 2) covers the grains as clay films (Plate 4.3.g) or 3) replaces original grains such as feldspars, lithics or muscovite (Plate 4.3.h and Plate 4.4.e - 4.4.g). Kaolin can totally infill pore and pore throat spaces thereby altering the intergranular macroporosity to microporosity between kaolin booklets (Plate 4.3.d, and Plate 4.4.a – b, 4.4.d). Primary porosity can be incompletely filled with kaolin, in which case remnant pores are visible (Plate 4.3.e and 4.3.f, Plate 4.4.c). Kaolin may intergrow with quartz overgrowths or sit on overgrowths (Plate 4.4.a, 4.4.g and Plate 4.2.h).

Kaolin comprises 5% to 10% by the rock composition in fine-grained point bar sands (RF-5) and 4% to 8% in the other reservoir (RF-1 to RF-4) lithologies (Appendix 4.2).

Authigenic illite is a minor component in most samples, from a trace up to 3%. Illite occurs as fine fibres close to kaolin booklets and is associated with feldspars or rock fragment alteration. It bridges pores and pore throats, probably reducing permeability (Plate 4.4.g and 4.4.h).

The allogenic (syndepositional) clays can be mixed with silt-sized material (Plate 4.5.a). They comprise up to 17% in fine-grained point bar sands (RF-5), and 20% - 65% in floodplain (SF-4), lacustrine (SF-2) and palaeosols (SF-3) deposits (Plate 4.5.b - 4.5.d, 4.5.f - 4.5.g). Detrital clays are recognizable by their irregular, flake-like platy habit (Plate 4.5.e and 4.5.h).

#### 4.4.3.3 *Siderite*

Siderite cement is the only carbonate cement, occurring as micrite or spar. Micrite is seen in thin section as pore-filling cement, as isolated massive blotches in

palaeosols, SF-3 (Plate 4.6.g) or dispersed throughout the matrix, replacing the detrital clays and spar.

Sparry siderite occurs as euhedral rhombic cement crystals (Plate 4.7.a – 4.7.d), filling pores (Plate 4.6.a and 4.6.b) or as radial precipitates (Plate 4.6.e and 4.6.h) replacing rootlets in palaeosols (SF-3). It engulfs the quartz grains (Plate 4.7.c), the kaolin (Plate 4.6.f) and aggressively, replaces quartz grains or quartz overgrowth cements (Plate 4.6.a and 4.6.c – 4.6.d).

Siderite cement comprises 25% to 45% of the rock volume in crevasse splay (RF-4) or fine-grained point bar (RF-5) sands. It is common in palaeosols (SF-3) where is estimated at 10% to 15% of the rock volume (Appendix 4.2).

#### 4.4.3.4 *Pyrite*

Cubic pyrite occurs in trace amounts in fine point bar sands (RF-5), crevasse splay sands (RF-4) or lacustrine fine-grained sediments (SF-2). Pyrite was seen lining the margins of late siderite spar (Plate 4.8.e). This suggests that pyrite precipitation has occurred during the late stages of the diagenetic history. It is also locally disseminated through an organic-rich matrix, replacing the detrital clays or with a framboidal habit (Plate 4.8.f) when associated with organic-rich clayey siltstone (eg. lacustrine environments, SF-2). Pyrite has a golden yellow colour in reflected light.

## 4.5 HYDROCARBONS

Locally, oil stains or “dead” oil rim quartz overgrowths (Plate 4.8.a) and fill primary porosity (Plate 4.8.d). Hydrocarbons also fill the microporosity between the kaolin booklets (Plate 4.8.c) or the secondary pores resulting from dissolution of former grains (Plate 4.8.b).

## 4.6 DIAGENETIC HISTORY

The sequence of cement precipitation was determined by petrographic studies using thin sections and SEM.

- Two generations of siderite cement are present. The first, an early micritic siderite phase is dark brown in colour and appears as blotches in siltstones or coats detrital quartz grains in sand samples. The second phase is a clean siderite spar, which postdates quartz overgrowth cement. This siderite has



grown into the pore spaces, partially filling them, covering quartz grains and marginally replacing them. The late siderite commonly occurs as later precipitates on the micritic siderite (Plate 4.6.f). In this case, an irregular, serrated edge suggests dissolution of the primary phase prior to precipitation of the second phase.

- Kaolin and quartz overgrowths occur independently or intergrown.
- Pore-filling authigenic kaolin is enclosed and etched by the late sparry siderite (Plate 4.6.d and 4.6.f).
- Feldspars are absent and the abundance of authigenic kaolin suggests that kaolin was derived from feldspar alteration.
- Minor amounts of authigenic illite are present as alteration products or associated with kaolin.
- Pyrite replaces the late generation siderite and is associated with organic matter in siltstones and claystones, where it replaces the detrital clays. Framboidal pyrite is thought to occur early in the diagenetic history.

A combination of these observations determines some of the cement stratigraphy. The first of the cements were micritic siderite and framboidal pyrite. These were followed by the alteration of feldspars to supply ions for kaolin cementation and for quartz overgrowth. Late siderite spar postdates quartz and kaolin cements and is followed by illite as in situ alteration product of rock fragments. Crystalline pyrite cement represents the latest phase in the diagenetic history. Hydrocarbon migration occurred after quartz and kaolin precipitation.

#### **4.7 SUMMARY**

This chapter described the texture, the petrographic and mineralogical composition of the studied samples, the diagenetic events and their relative timing. Compaction occurred soon after deposition and is the first cause of porosity reduction. Quartz overgrowths also caused porosity loss, but at the same time preserved primary porosity between euhedral terminations. Kaolin was related to feldspar alteration. It transformed the primary porosity into microporosity between booklets, considerably diminishing the permeability. Dissolution of grains created oversized pores that enhanced primary porosity and permeability.

## PLATE 4.1

### Thin section photomicrographs of mechanical and chemical compaction

- a. Effect of mechanical compaction: muscovite flake bent between detrital quartz grains indicates compaction. Merrimelia 17, 7116 ft, crossed polarized light. Scale bar = 0.5 mm.
- b. Sutured contacts of quartz crystals indicate advanced compaction. Telopea 2, 8188 ft, crossed polarized light. Scale bar = 1 mm.
- c. Interconnecting network of stylolites with concentrations of insoluble material such as clays or organic matter. Quartz grains are truncated along the stylolite. Telopea 2, 8188 ft, plane polarized light. Scale bar = 1 mm.
- d. Pressure dissolution seams in a clayey siltstone with abundant organic matter. Beanbush 1, 8740 ft 10 in, plane polarized light. Scale bar = 1 mm.

# PLATE 4.1

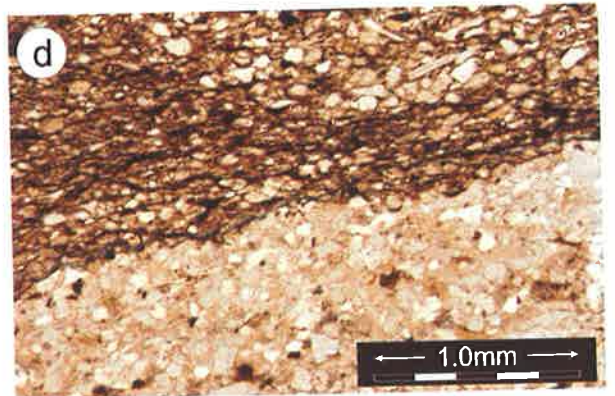
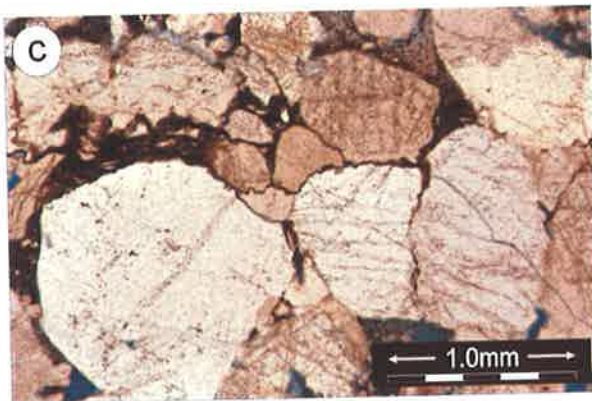
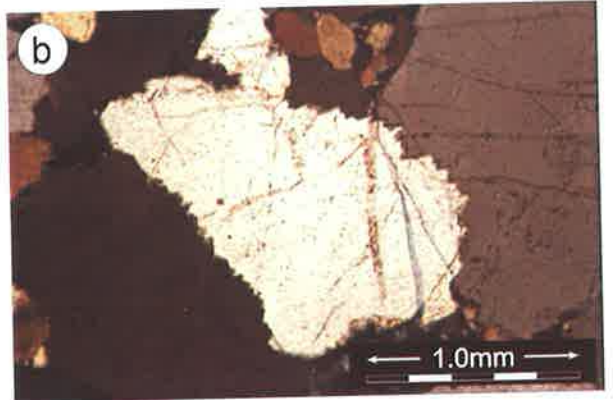
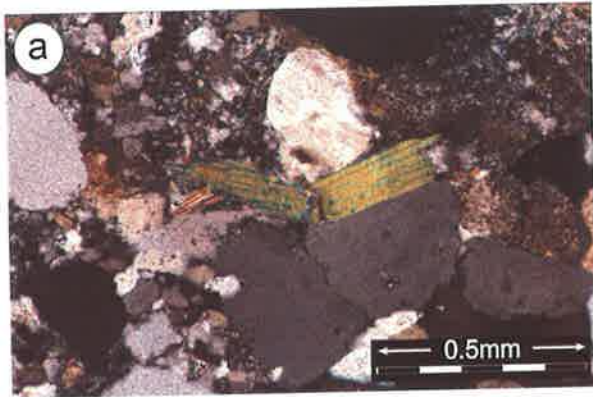


## PLATE 4.2

### Thin section and SEM photomicrographs of quartz cement

- a. Quartz overgrowth cement is outlined by dust rims and thick, euhedral faces. Oversized pores due to dissolution. Merrimelia 29, 7100 ft, plane polarized light. Scale bar = 0.5 mm.
- b. Euhedral faces of quartz overgrowth preserve the intergranular, primary porosity. The brown, pore-lining clays consist of kaolin and illite. Beanbush 1, 8735 ft 2 in, plane polarized light. Scale bar = 1 mm.
- c. Prismatic quartz overgrowths intergrown with kaolin. Merrimelia 7, 7065 ft 11 in. Scale bar = 20 microns.
- d. Euhedral terminations of quartz overgrowth and rhombohedral siderite engulfed by clay cement. Merrimelia 7, 7065 ft 11 in. Scale bar = 10 microns.
- e. Quartz cement developed as druse and euhedral quartz overgrowth growing into primary porosity. Pore size is 25  $\mu\text{m}$ . Merrimelia 3, 7542ft 6 in. Scale bar = 20 microns.
- f. Chemically etched V-shaped pits cover the surface of quartz overgrowth. Discrete prisms of quartz overgrowth show incomplete development. Pore size is 50 microns. Merrimelia 3, 7542ft 6 in. Scale bar = 20 microns.
- g. Jagged contact between kaolin booklets and quartz overgrowth cement. Merrimelia 7, 7065 ft 11 in. Scale bar = 20 microns.
- h. Kaolin booklets interfered with quartz overgrowth cement suggesting similar pore water chemistry and co-precipitation of both authigenic minerals. Merrimelia 17, 7078 ft 2 in. Scale bar = 20 microns.

# PLATE 4.2

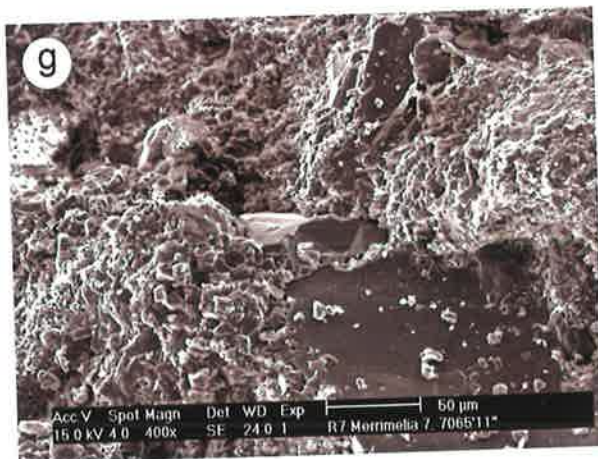
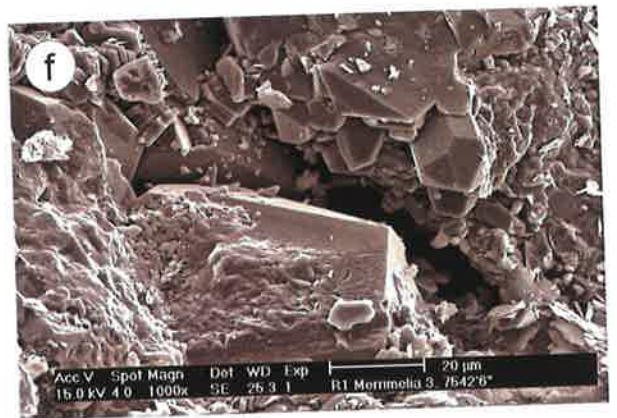
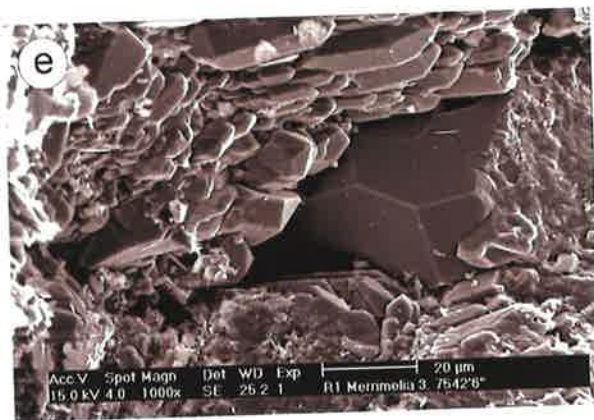
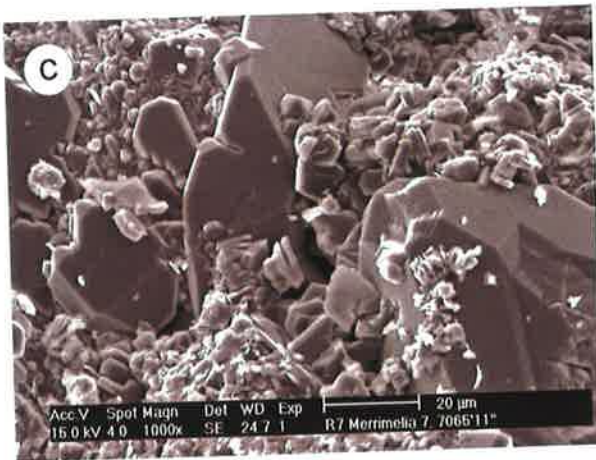
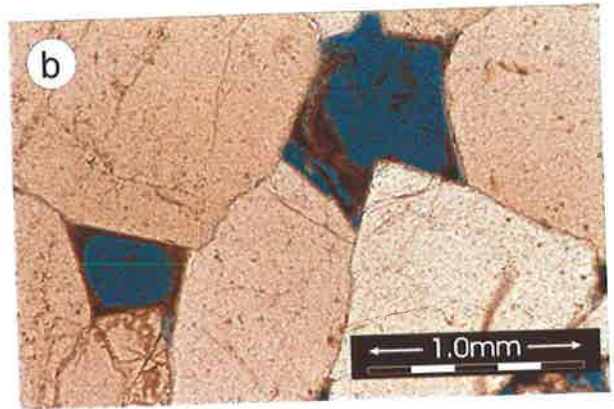
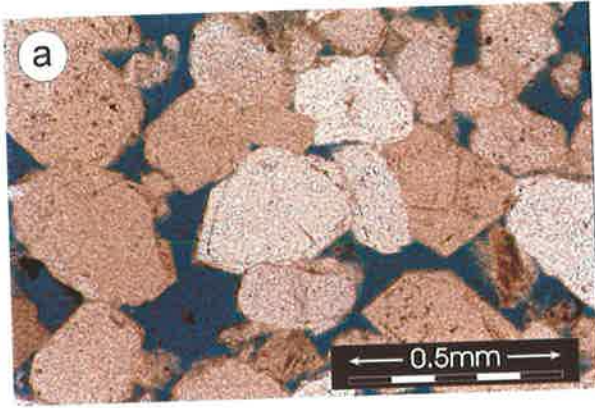


## PLATE 4.3

### SEM photomicrographs of kaolin cement

- a. Tight-packed kaolin creates minimum microporosity. Euhedral kaolin booklets of up to 30  $\mu\text{m}$ , grouped to a vermiform habit. Merrimelia 17, 7078 ft 2 in. Scale bar = 20 microns.
- b. Loose packed euhedral kaolin booklets create viable microporosity. Merrimelia 17, 7078 ft 2 in. Scale bar = 20 microns.
- c. Quartz overgrowth cement (lower left) intergrown with loose packed kaolin. Size of kaolin booklets is up to 20  $\mu\text{m}$  and size of micropores is up to 10  $\mu\text{m}$ . Telopea 2, 8188 ft. Scale bar = 20 microns.
- d. Precipitation of dense kaolin in pore spaces and adjacent throats reduces primary porosity and permeability. Pores of about 30  $\mu\text{m}$  sizes are preserved between euhedral quartz overgrowths (bottom right). Telopea 2, 8186 ft 3 in. Scale bar = 100 microns.
- e. Primary pores incompletely filled with blocky kaolin. The remnant pores are up to 15  $\mu\text{m}$  diameters. Merrimelia 3, 7542ft 6 in. Scale bar = 20 microns.
- f. Small vermiform kaolin booklets (3 to 4  $\mu\text{m}$ ) precipitate in the available spaces and bridge the pore spaces. The sizes of remaining pores are between 5 and 20  $\mu\text{m}$ . Telopea 2, 8186 ft 3 in. Scale bar = 20 microns.
- g. Kaolin platelets coating and partial filling the pores and pore throat spaces protected by quartz overgrowths. Beanbush 1, 8735 ft 2 in. Scale bar = 100 microns.
- h. Rock fragment altered to kaolin. Merrimelia 17, 7078 ft 2 in. Scale bar = 50 microns.

# PLATE 4.3

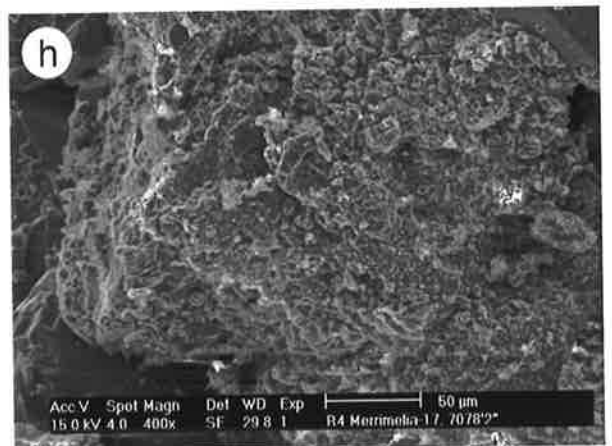
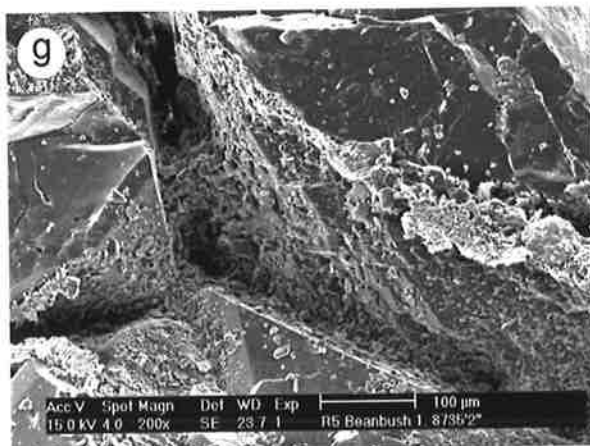
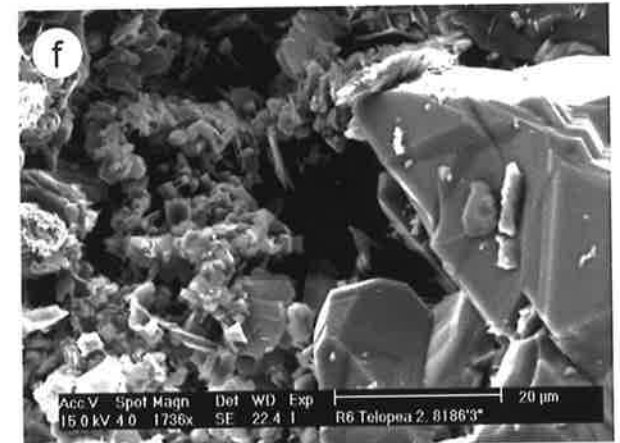
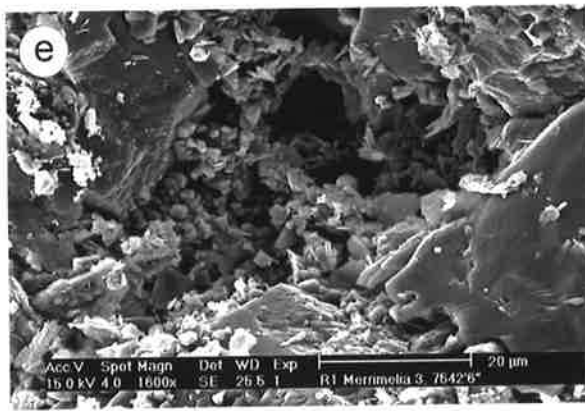
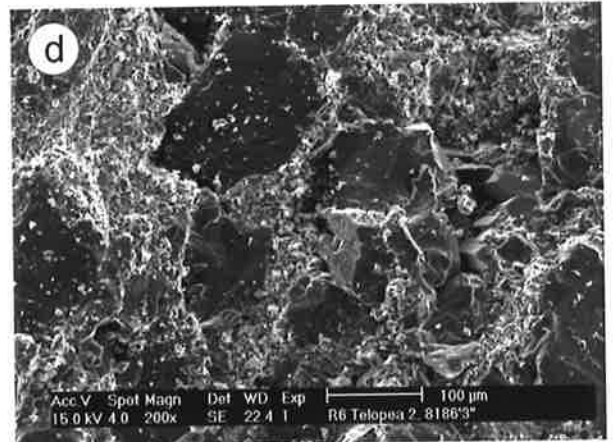
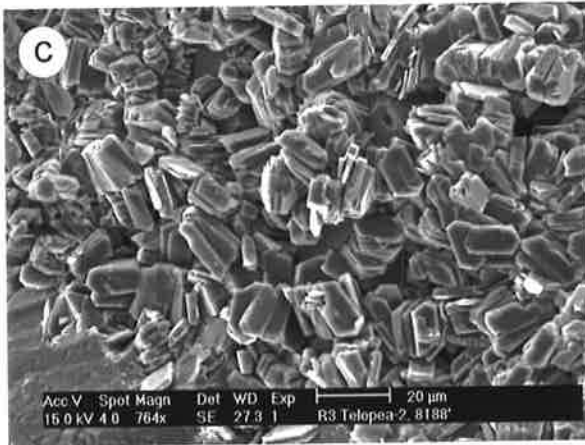


## PLATE 4.4

### Thin section photomicrographs of kaolin and illite

- a. Precipitation of vermicular kaolin in pore spaces and adjacent pore throats reduces macroporosity and permeability. Intergrown of kaolin with quartz overgrowth is evident from the jagged contacts. Beanbush 1, 8735 ft 2 in, crossed polarized light. Scale bar = 0.25 mm.
- b. Kaolin, completely fills the pore and throat spaces. Kaolin is intergrown with quartz overgrowths. Telopea 2, 8188 ft, crossed polarized light. Scale bar = 1 mm.
- c. Kaolin partially fills primary porosity (porosity shown with blue stained epoxy), pore throats and fractures. Beanbush 1, 8735 ft 2 in, plane polarized light. Scale bar = 1mm.
- d. Scattered microporosity in a kaolin-cemented interval. Beanbush 1, 8716 ft, plane polarized light. Scale bar = 0.5 mm.
- e. Kaolin precipitation as a result of former rock fragment dissolution. The dissolution phenomena are recognizable through the presence of molds of former particles, outlined by rims of clay. Sutured grain contacts. Telopea 2, 8174 ft, plane polarized light. Scale bar = 0.25 mm.
- f. Authigenic vermicular kaolin developed as an alteration product of a former muscovite grain. Beanbush 1, 8723 ft 3 in, crossed polarized light. Scale bar = 0.25 mm.
- g. Authigenic, fibrous illite, probably developed as an alteration product of a rock fragment (central left), kaolin intergrown with quartz overgrowth (right). Merrimelia 29, 7100 ft, crossed polarized light. Scale bar = 0.25 mm.
- h. Illite developed as alteration product of former grains deformed under compaction. Telopea 2, 8186 ft, crossed polarized light. Scale bar = 0.25mm.



# PLATE 4.4

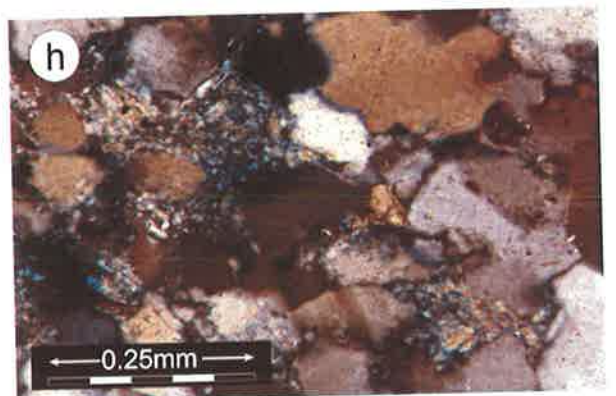
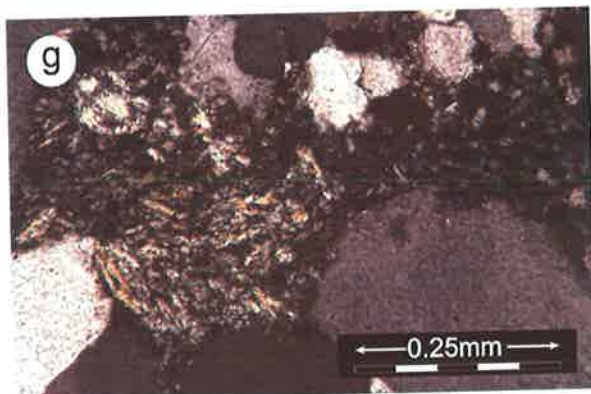
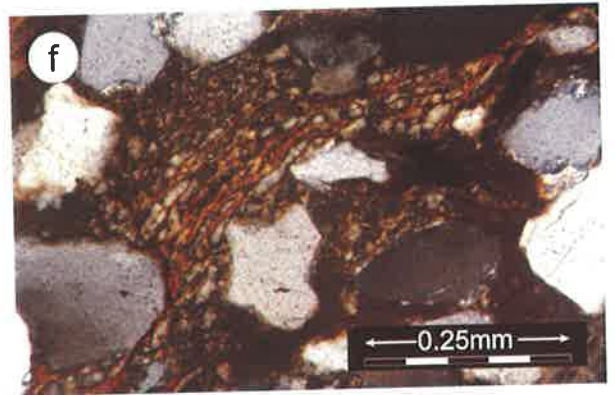
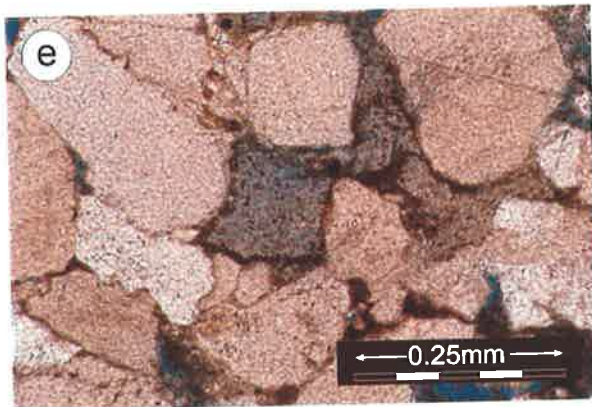
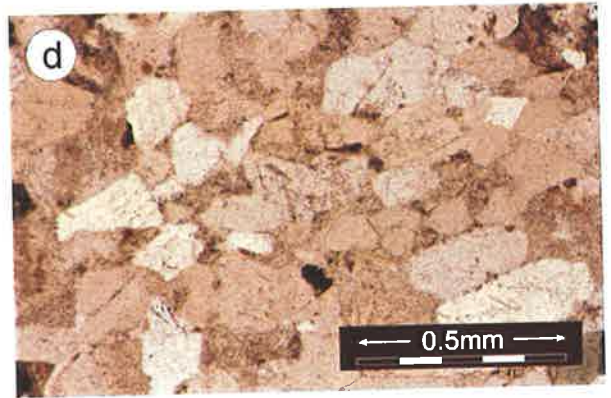
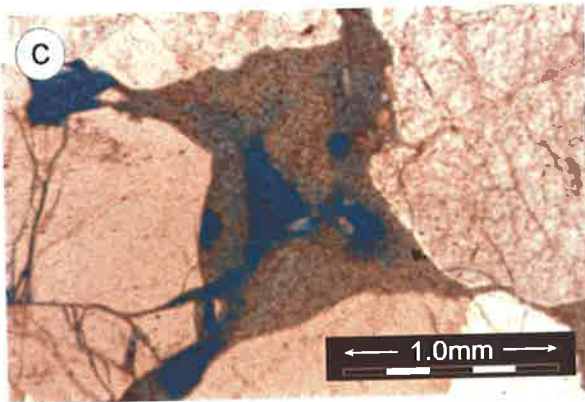
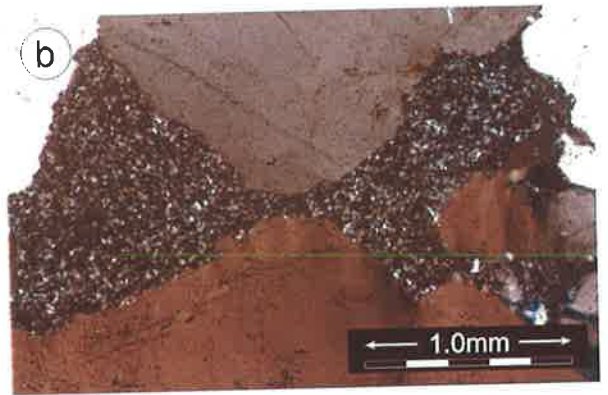
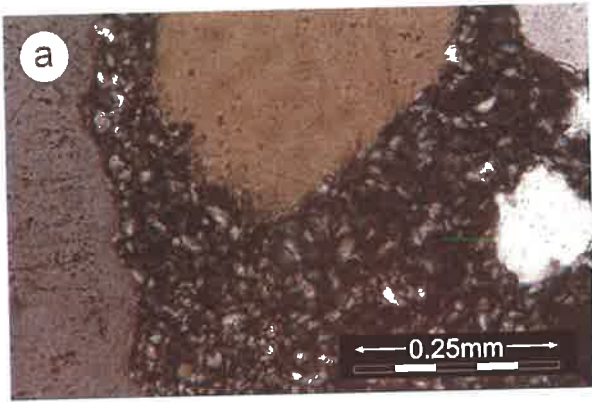


## PLATE 4.5

### Thin section and SEM photomicrographs of detrital clays

- a. Detrital, depositional matrix, constituted mainly from kaolin and subordinate, illite. Merrimelia 29, 7100 ft, plane polarized light. Scale bar = 0.25 mm.
- b. Clay cementation completely occludes porosity. Deformation of soft rock fragment and concave-convex to sutured contacts are evidence of compaction. The clays are aggressive on grain contours. Beanbush 1, 8716 ft, plane polarized light. Scale bar = 1 mm.
- c. Detrital clays as well as organic matter participate at the constitution of a silty claystone. Note the distorted mica. Beanbush 1, 8740 ft 11 in. Scale bar = 0.25 mm.
- d. Clayey matrix in a palaeosol, consisting in detrital kaolin and illite. Merrimelia 17, 7148 ft 4 in, crossed polarized light. Scale bar = 0.25 mm.
- e. Detrital clays with a platy crystal habit significantly reduce porosity and permeability in fine-grained litharenite. Merrimelia 3, 7542ft 6 in. Scale bar = 10 microns.
- f. Quartz grains tightly embedded in detrital clays, in a matrix-rich sample. Practically no porosity left. Beanbush 1, 8740 ft 10 in. Scale bar = 50 microns.
- g. Altered grain, deformed to pseudo matrix. Beanbush 1, 8723 ft 3 in. Scale bar = 20 microns.
- h. Irregular, flake-like, platy clays, deformed under compaction, occupy almost all the pore spaces in a palaeosol. Merrimelia 17, 7148 ft 4 in. Scale bar = 20 microns.

# PLATE 4.5

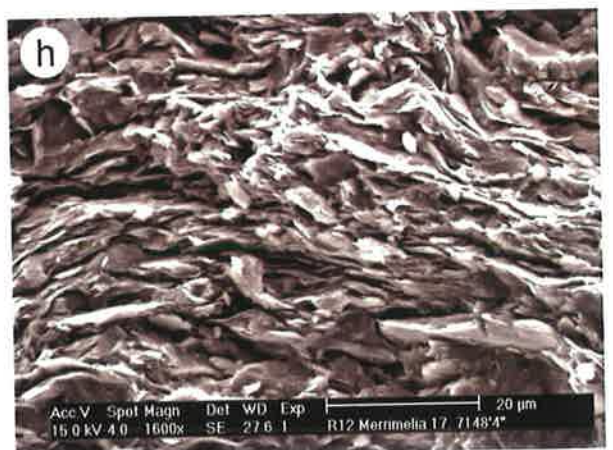
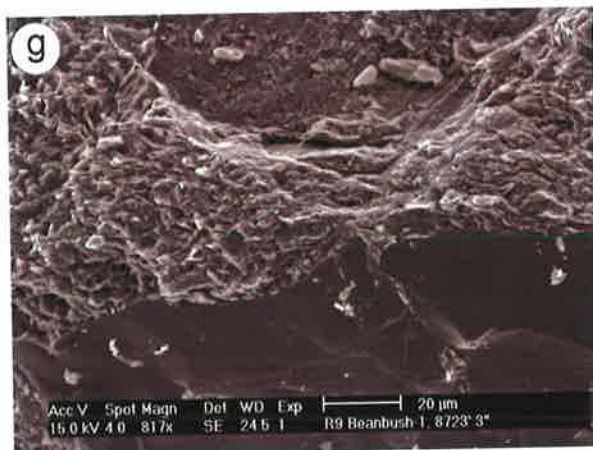
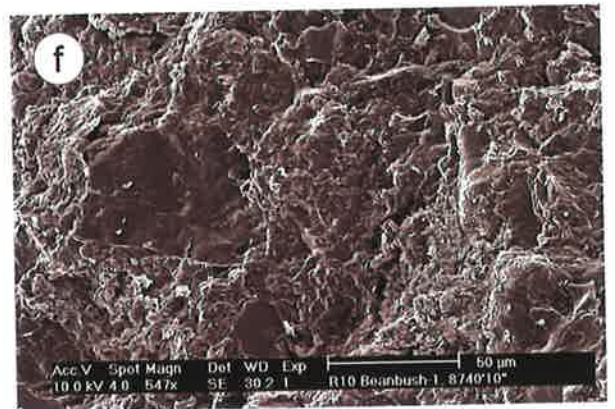
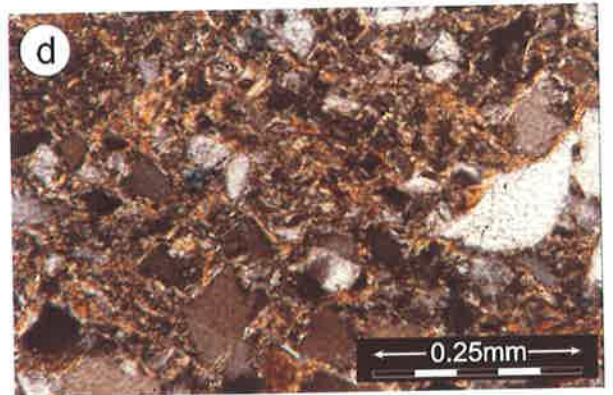
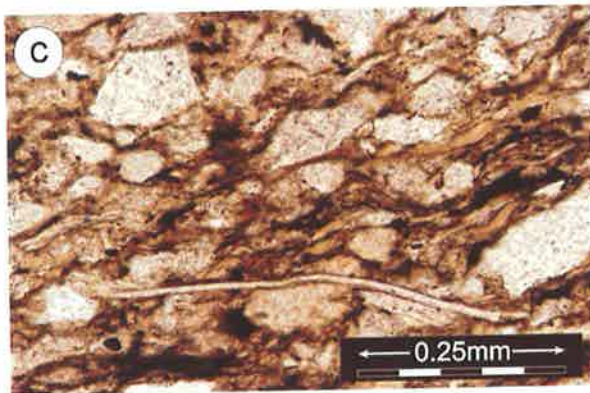
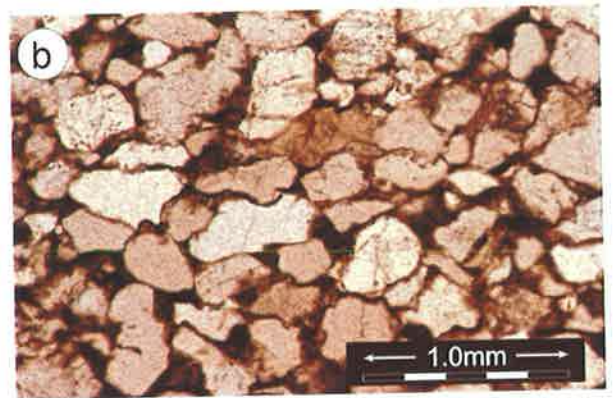
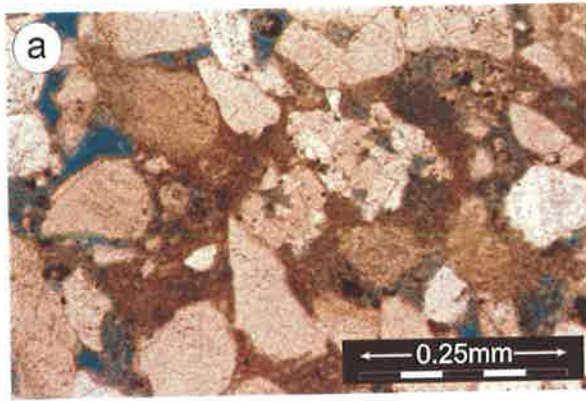


## PLATE 4.6

### Thin section photomicrographs of siderite cement

- a. Sparry siderite coats the framework grains. The siderite postdates quartz overgrowth cement, illustrated by dust rims and partially preserved euhedral faces (left) and aggressively etches grains. Loosely packed kaolin (bottom left). Merrimelia 7, 7108 ft 4 in, plane polarized light. Scale bar = 0.5 mm.
- b. Detail of rhombic, sparry siderite cement. Merrimelia 7, 7108 ft 4 in, plane polarized light. Scale bar = 0.25 mm.
- c. Siderite cemented fine-grained litharenite. Siderite, very aggressive on quartz grains grows as a micrite and spar phase. It postdates quartz overgrowth cement (recognizable by dust rims) and can replace kaolin. Merrimelia 7, 7065 ft 11 in, plane polarized light. Scale bar = 1 mm.
- d. Cement relationships in a crevasse splay litharenite. Dissolution of grains produces oversized pores with recognizable molds of former particles. Kaolin, as alteration product and quartz cement grows into the new pores created. Sparry siderite precipitates around partially preserved quartz overgrowth, marginally replacing it. Merrimelia 7, 7108 ft 4 in, plane polarized light. Scale bar = 0.5 mm.
- e. Sparry siderite crystals, replacing rootlets in a palaeosol. Merrimelia 17, 7148 ft 4 in, crossed polarized light. Scale bar = 1 mm.
- f. Diagenetic stratigraphy of four cement phases. Micritic siderite precipitates on existing grains. Kaolin precipitates in the pore spaces, and is surrounded by the siderite spar. Clean, sparry siderite postdates the micritic phase and marginally replaces it. Merrimelia 7, 7065 ft 11 in, crossed polarized light. Scale bar = 0.25 mm.

- g. Micritic siderite occurs as reddish to brown colored blotches, replacing the detrital clays. Merrimelia 17, 7148 ft 4 in, plane polarized light. Scale bar = 1 mm.
  
- h. Sparry siderite crystals precipitate in radial forms. Merrimelia 17, 7148 ft 4 in, plane polarized light. Scale bar = 1 mm.

# PLATE 4.6

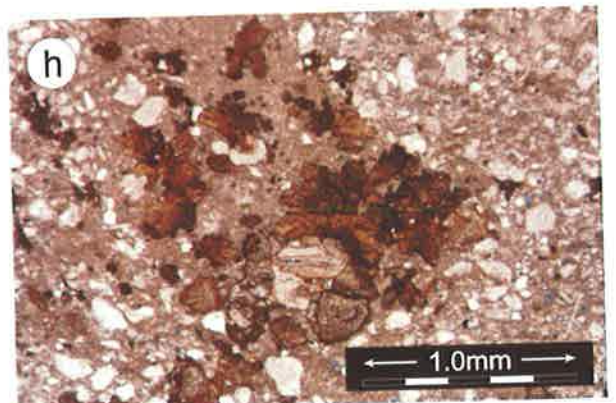
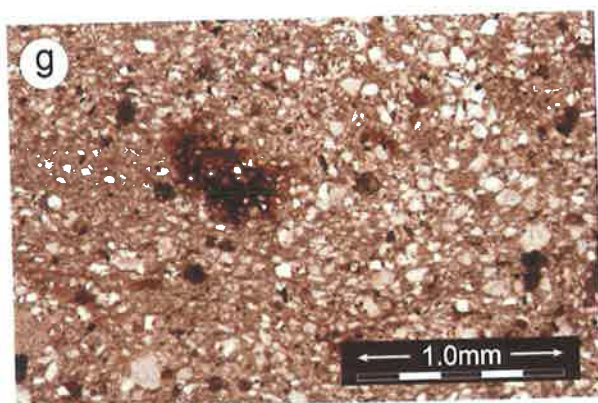
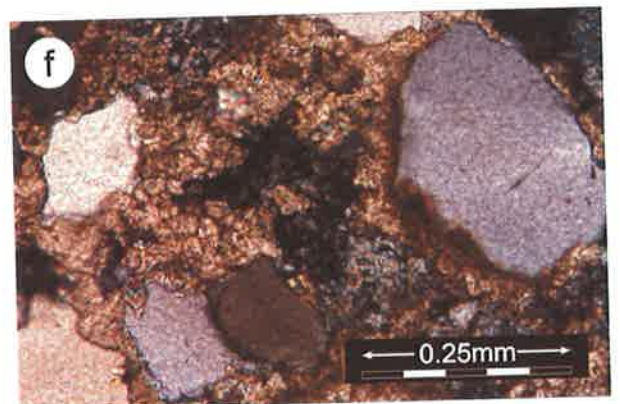
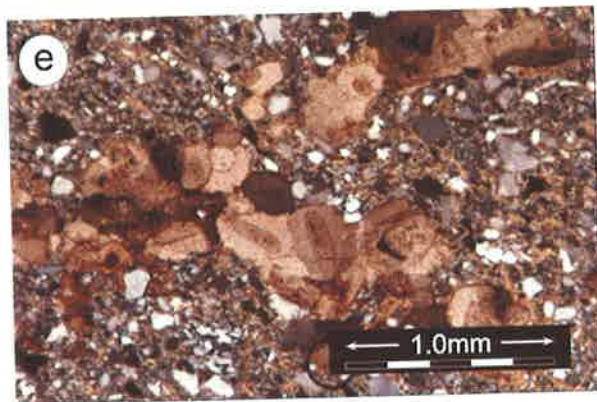
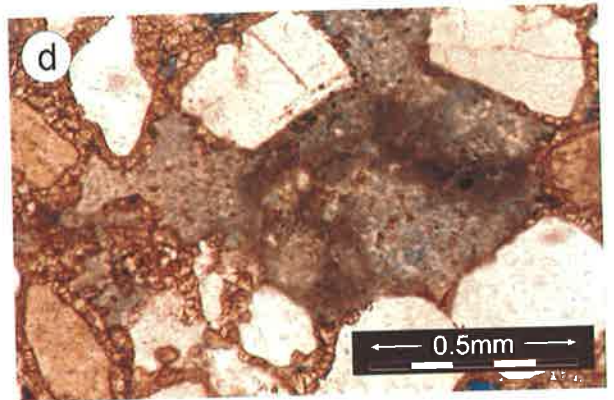
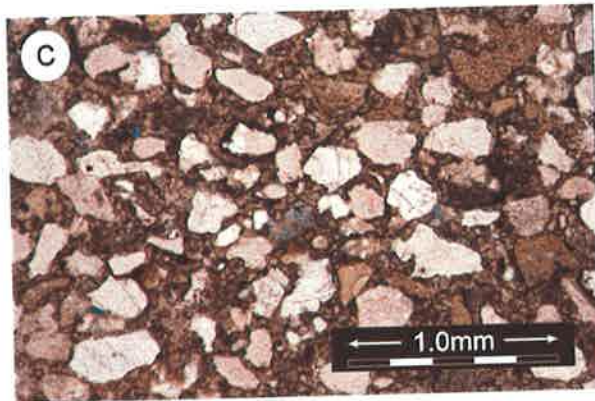
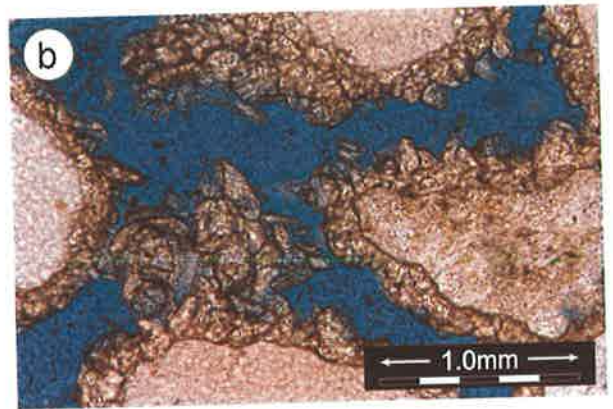
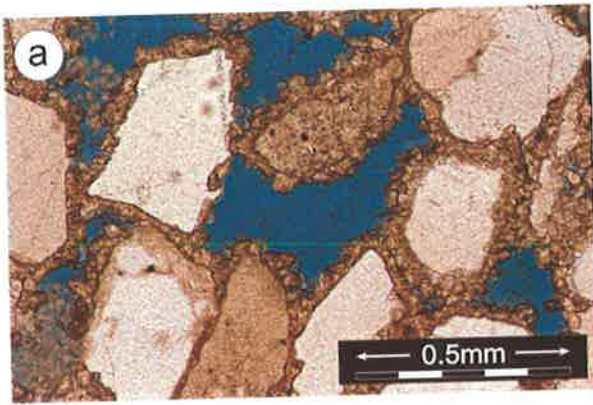


## PLATE 4.7

### SEM Photomicrographs of Siderite Cement

- a. Tight siderite-cemented section. Sparry crystals of rhombic siderite. Merrimelia 7, 7108 ft 4 in. Scale bar = 20 microns.
- b. Siderite growing on quartz overgrowth surface. Note the conservation of interconnected pores. Merrimelia 7, 7108 ft 4 in. Scale bar = 50 microns.
- c. Quartz overgrowth with prismatic terminations surrounded by rhombic siderite blades. Merrimelia 7, 7108 ft 4 in. Scale bar = 20 microns.
- d. Platy clays and siderite crystals. Source of clays appears to be the alteration of a precursor grain. Merrimelia 7, 7065 ft 11 in. Scale bar = 10 microns.

# PLATE 4.7

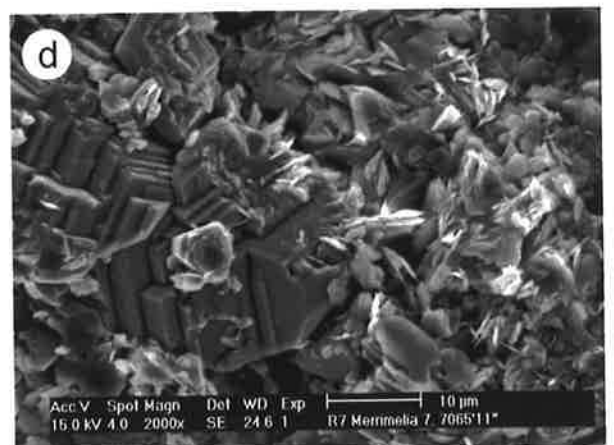
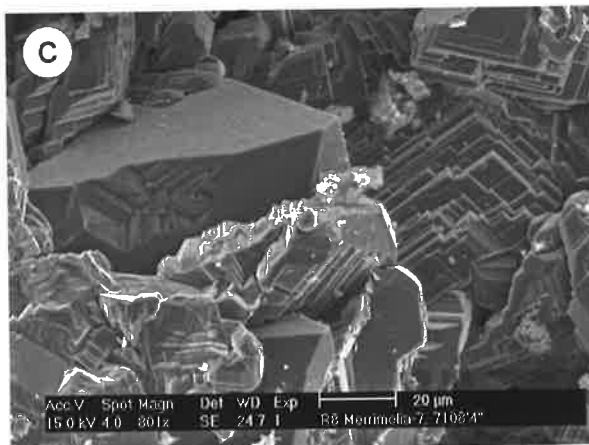
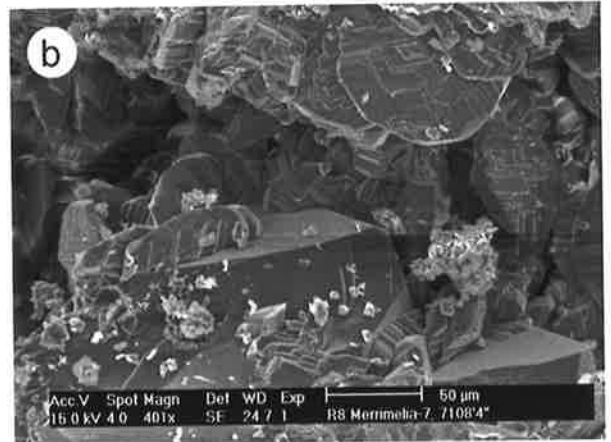
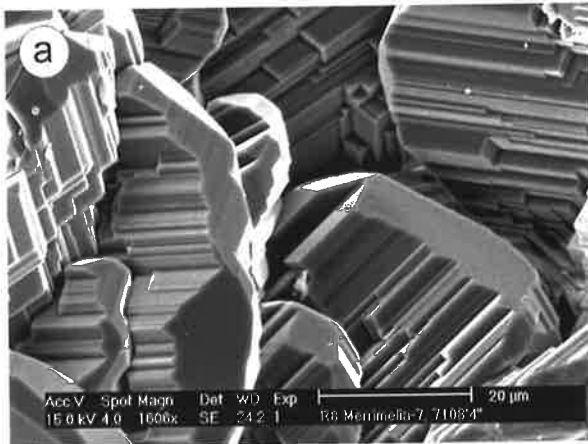


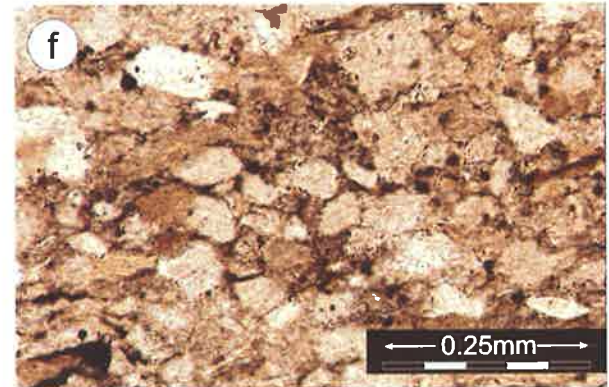
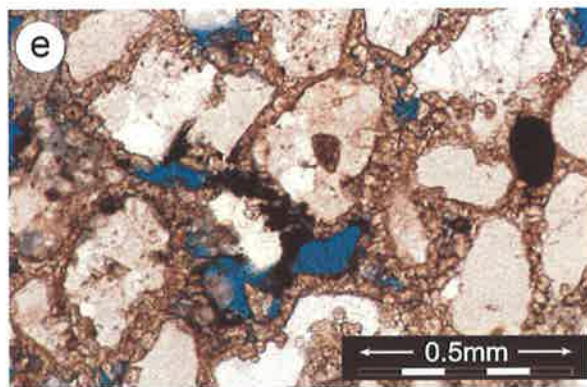
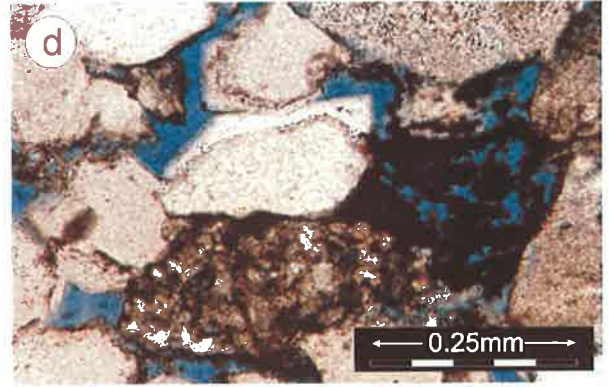
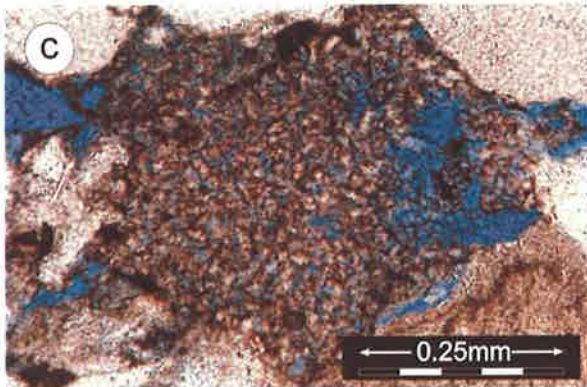
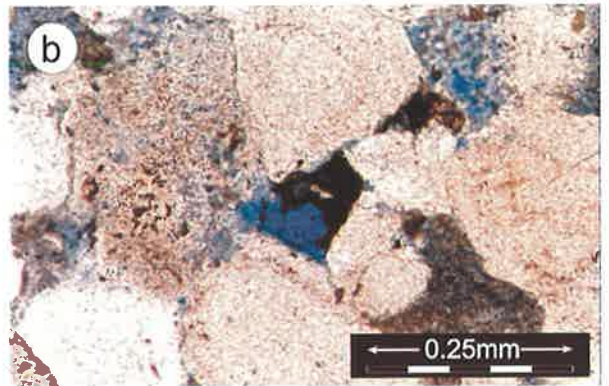
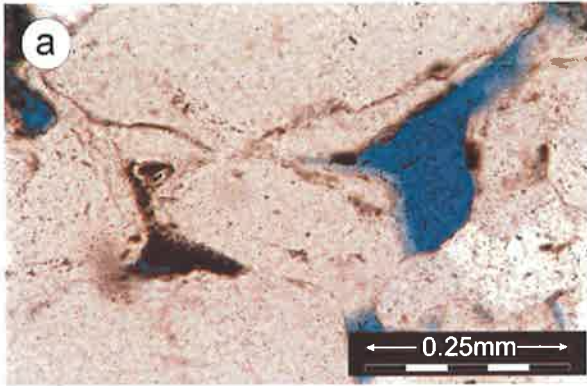


## PLATE 4.8

### Thin section photomicrographs of hydrocarbon occurrence and pyrite cement

- a. Residual oil in the pore spaces. Thick quartz overgrowth is identified by the presence of clay rims. Merrimelia 17, 7078 ft 2 ½ in, plane polarized light. Scale bar = 0.25 mm.
- b. Hydrocarbons fill the secondary pores resulted from dissolution. Thick quartz overgrowths are outlined by clays or dust rims. Merrimelia 17, 7078 ft 2 ½ in, plane polarized light. Scale bar = 0.25 mm.
- c. Hydrocarbons observed within kaolin booklets. Merrimelia 17, 7078 ft 2 ½ in, plane polarized light. Scale bar = 0.25 mm.
- d. Thin section photomicrograph of oil stains in the pore spaces. Merrimelia 29, 7104 ft, plane polarized light. Scale bar = 0.25 mm.
- e. Pyrite is the latest cement phase, after the sparry siderite. Merrimelia 7, 7108 ft 4 in, plane polarized light. Scale bar = 0.5 mm.
- f. Framboidal pyrite is associated with organic rich detrital matrix in a clayey siltstone deposited in a lacustrine environment. Merrimelia 5, 7420 ft 9 in, plane polarized light. Scale bar = 0.25 mm.

# PLATE 4.8



## CHAPTER FIVE

### RESERVOIR QUALITY

#### 5.1 INTRODUCTION

Reservoir quality is defined by its hydrocarbon storage capability and deliverability. The hydrocarbon storage capacity is determined by the effective porosity (the volume percentage of interconnected pores in a rock) and the size of the reservoir. The deliverability is a function of the permeability. The permeability (mD) of a rock is a property of porous media and measures the ability of a rock to transmit fluid in response to an applied pressure gradient (Grier and Marschall, 1993).

The Triassic sediments in the Cooper Basin contain both sealing and reservoir lithofacies. The sealing lithofacies 1 (SF-1) was observed sealing hydrocarbon accumulations even though it consists of sandstones situated at the top of point bars. This chapter discusses the nature of porosity and some of the factors that control porosity, pore geometry and permeability in the reservoir facies (RF-1 to RF-5). In addition, the factors that control the properties of sealing facies (SF-1) are detailed.

#### 5.2 POROSITY TYPES

Primary intergranular porosity, secondary porosity and microporosity have been identified within the studied samples. Different types of porosities were measured in thin sections, using Videopro 32 image analysis software. The results are presented in Appendix 4.2.

##### 5.2.1 Primary porosity

Primary intergranular porosity dominates quartz rich samples and is preserved between the euhedral terminations of quartz overgrowths (Plate 5.1.a - d and Plate 5.2.a). Primary porosity is well preserved in gravels (RF-1), where it ranges from 10% to 25% and in fluvial channel (RF-2) and chute sands (RF-3), where it varies from 7% to 12% (Appendix 4.2). Kaolin and siderite precipitation diminish the primary porosity

leaving just remnant pore spaces. SEM microscopy reveals primary pores of up to 400 microns in RF-1, up to 250 microns in RF-2, RF-3 and RF-4 but only up to 50 microns in RF-5.

### 5.2.2 Secondary porosity

Primary porosity is commonly associated with secondary porosity in the same sample (Plate 5.2.b and 5.2.f). Secondary porosity is recognizable from the presence of irregular, oversized and elongate pores (Plate 5.2.b and 5.2.c). It results from dissolution of unstable grains (Plate 5.2.d – 5.2.f) or from the dissolution of quartz grain margins (Plate 5.2.b). The amount of secondary porosity in gravels (RF-1), fluvial channel (RF-2) and chute (RF-3) sands is estimated as between 2% to 5% (Appendix 4.2).

### 5.2.3 Microporosity

Microporosity is associated with the presence of kaolin masses. Quantitative estimation of microporosity by image analysis shows values of up to 44% of the total kaolin filled area (Plate 5.2.g). The size of the micropores depends on the size of kaolin booklets and how tightly they are packed. SEM microscopy facilitates micropore measurements of 10 to 15 microns in gravels and chute sands and around 5 microns in diagenetically modified sandstones. Kaolin framework microporosity accounts for 4 to 8% of the rock volume in sands from top of point bars (RF-5) and diagenetically modified (SF-1) sandstones (Plate 5.2.h) and was estimated at 3% - 5% in the other reservoir lithology (Appendix 4.2).

## 5.3 FACTORS THAT CONTROL POROSITY

Thin section measurements of porosity (Appendix 4.2) show that fluvial channel, RF-2 and chute sands, RF-3 have the highest porosity (17% - 21%), followed by gravels, RF-1 (10% - 17%), crevasse splay sands, RF-4 (3% - 18%), and sands from top of point bars, RF-5 and SF-1 (6% - 10%). The various depositional facies show different proportions of the pore types. In RF-1 and RF-2, primary porosity dominates, while in RF-5 and SF-1, microporosity dominates (Fig.5.1).

Porosity is directly proportional (correlation coefficient  $r^2 = 0.83$ ) to the amount of quartz overgrowth cement (Fig. 5.2.a). This fact suggests the influence of rock

petrographic composition and diagenesis on porosity. Another relationship observed was that porosity is inversely proportional ( $r^2 = -0.71$ ) to the amount of matrix (Fig. 5.2.b). Also, a high percentage of rock fragments and kaolin correlate inversely with porosity, but the correlation coefficients are small. There is a linear relationship between thin section estimated porosity and core plug porosity, with a correlation coefficient  $r^2 = 0.75$  (Fig. 5.3).

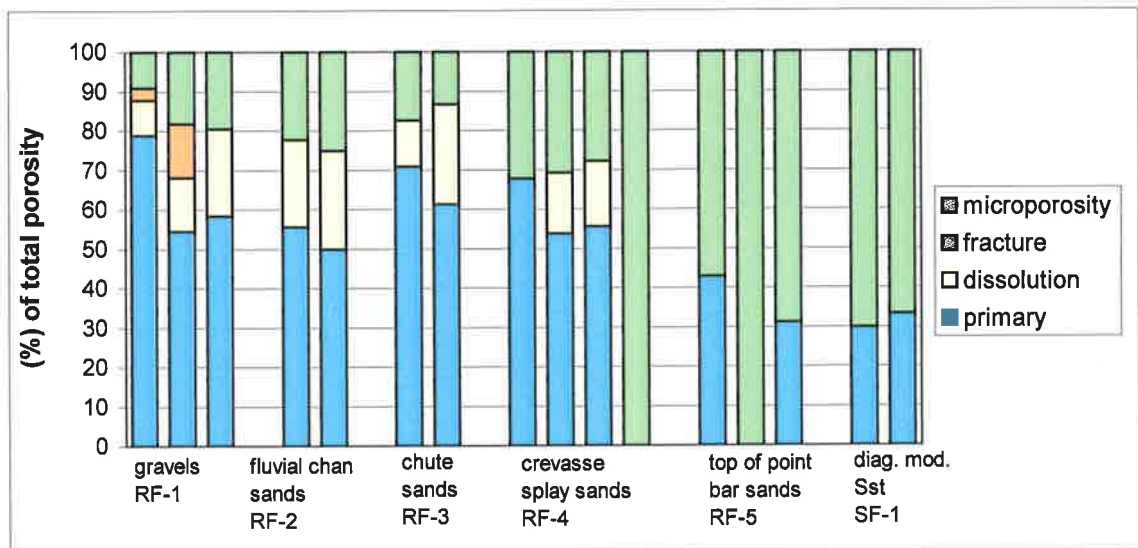


Figure 5.1 Relative proportions of porosity types as determined by visual estimation in thin sections.

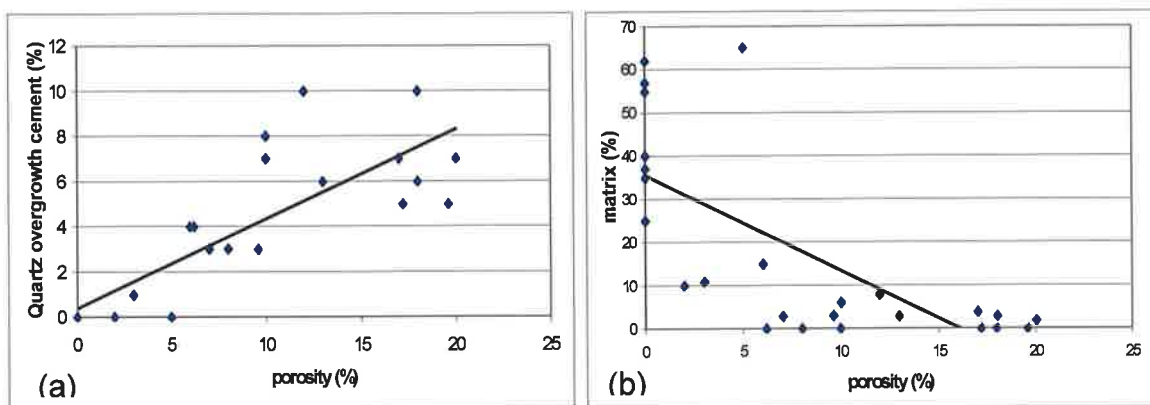


Figure 5.2 Relationship between (a) porosity and quartz overgrowth cement and (b) porosity and matrix.

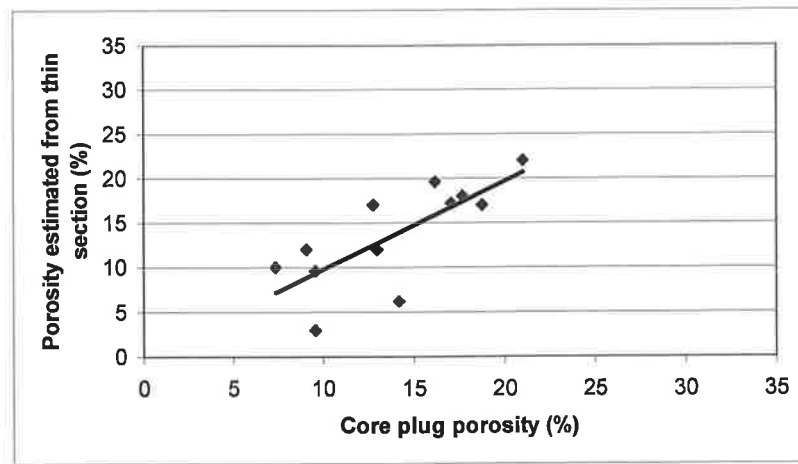


Figure 5.3 Relationship between core plug porosities and porosities measured in thin sections.

#### 5.4 FACTORS THAT CONTROL THE PORE SYSTEM GEOMETRY

Identified by their sedimentary environment, each lithofacies shows specific textural characteristics, petrographic composition, and diagenetic transformations. These are factors that control the pore geometry.

The textural characteristics such as grain size and sorting are reflected in pore and pore throat distribution.

RF-1 shows poorly sorted grain distribution. This is reflected in a poor sorting of pore (high standard deviations) and pore throat sizes. This group of rocks contains the biggest pores and pore throats, but their distribution is dispersed over wide range. This fact is reflected in a diminishing of porosity and permeability. Core measurements show smaller porosities values and equal or less permeabilities values than RF-2 and RF-3.

RF-2, RF-3 and RF-4 comprise moderately to moderately well sorted, fine to medium sands. In this case, even if the grain sizes are similar, the pore distribution of RF-2 and RF-3 has better sorting (low standard deviations) than RF-4. The majority of pore throats of RF-2 and RF-3 are grouped between 10 and 20 microns, while the pore throat distribution of RF-4 is much dispersed. This fact is reflected in higher porosity and permeability measurements of RF-2 and RF-3 samples than RF-4 samples. The fact that the textural characteristics do not influence the reservoir quality of these groups, demonstrates the importance of diagenesis on the pore system.

RF-5 and SF-1 samples are moderately well sorted, fine to very fine sands. The original pore distribution could not be determined due to the fact that kaolin fills the pore system. The pore throat sizes correspond to the kaolin framework microporosity. Macro-porosity of SF-2, SF-3 and SF-4 is 1-2%.

Primary rock fabric controls subsequent diagenesis, which in turn, controls the pore geometry.

Matrix-rich rocks are more affected by mechanical compaction. This results in the reduction of pore spaces. The presence of detrital clays in gravels favors compaction with appearance of stylolites, while in sealing lithofacies SF-2, SF-3 and SF-4 the clays easily compact, leading to the near-total loss of porosity.

Quartz overgrowths are better developed in rocks with a high proportion of quartz grains, such as RF-1 and RF-2. They diminish the pore spaces, but also help preserve the remaining primary porosity between the quartz overgrowth facies, by slowing compaction. Quartz cement development is also favoured by the dissolution of feldspar grains. In rocks having a high percentage of rock fragments (RF-3, RF-4 and RF-5), quartz overgrowths are less well developed.

Kaolin cementation can totally obstruct intergranular porosity and result in microporosity development (RF-4 and SF-1). Kaolin precipitation is favored by dissolution of feldspar grains or by matrix recrystallization. At the top of point bar successions fine-grained sands with a high amount of matrix are preferentially deposited. Kaolin and illite, the two minerals that give a sealing attribute to SF-1, form from recrystallization of the matrix. This shows the ultimate control of depositional environment on resulting pore geometry.

Siderite precipitation is favored by reducing conditions surrounding organic matter. This leaves iron in the +2 oxidation state suitable to be taken up into the carbonate crystal. Siderite precipitation contributes to porosity loss in RF-4, RF-5 and SF-3.

## **5.5 PERMEABILITY**

### **5.5.1 Factors that control permeability**

Permeability is defined as the capacity of a rock to deliver a liquid or gas. Observations in thin sections lead to a few conclusions about the factors that control permeability in the reservoir facies (RF-1 – RF-5) and sealing facies SF-1.

### *Grain size and sorting*

The coarser deposits (gravels RF-1, fluvial channel sands RF-2) have higher permeability than the fine-grained point bar sands RF-5 and SF-1. Sorting does not affect permeability as all studied samples, with the exception of RF-1 are moderately or moderately well sorted.

### *Rock composition*

A high proportion of soft rock fragments or detrital clays favors compaction that leads to occlusion of pore throats, therefore reducing the rock permeability. On the other hand, quartz-rich samples show good permeability.

### *Cementation*

Kaolin precipitation transforms primary porosity into microporosity (as can be seen in SF-1), rendering these rocks ineffective for oil migration. Fibrous illite though not very abundant, occurs in SF-1 obstructing pore throats, and therefore reducing permeability.

### *Porosity*

Permeability is not necessarily directly correlatable to porosity. The relationship between core plug porosity and horizontal permeability is poor with a low correlation coefficient  $r^2 = 0.53$  (Fig. 5.4)

### *Pore distribution*

The fluvial channel (RF-2) and chute sands (RF-3) show pore distribution with better sorting than gravels (RF-1). The permeability in gravels (RF-1) is low due to poor sorting of the pores.

### *Pore throat size distribution*

Of great importance in controlling permeability are the pore throat sizes and their arrangements. Mercury injection capillary pressure analyses permit a quantification of pore throat size distribution by plotting pore throat size versus relative pore volume (Appendix 3.6, Plates 2.4 – 2.11).



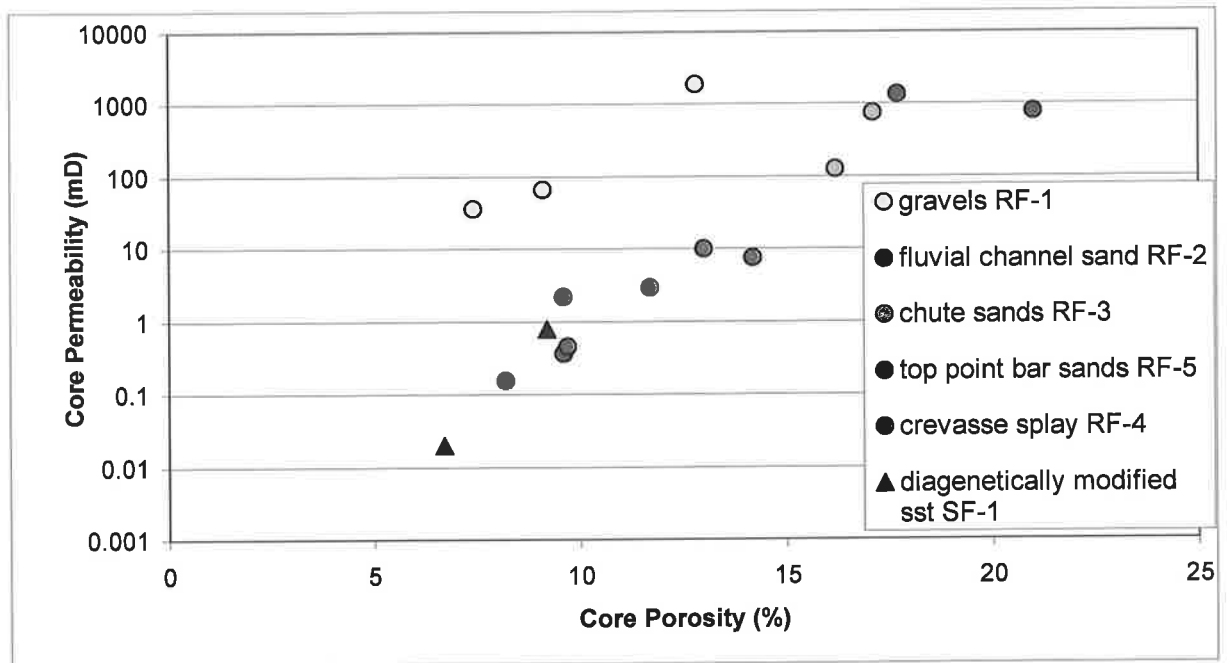


Figure 5.4 Semi-log cross plot of core porosity versus permeability.

### 5.5.2 Permeability evaluation from mercury injection capillary pressure curves

Washburn (1921) expressed the relationship between pore throat radius and capillary pressure.

$$(1) \quad P_c = -2 \gamma \cos \theta / r_c$$

where:

$P_c$  = Capillary pressure (dynes/cm<sup>2</sup>);

$\gamma$  = Mercury/air interfacial tension (dynes/cm);

$\theta$  = Contact angle of mercury in air;

$r_c$  = Radius of pore throat (microns).

If  $\gamma = 480$  dynes/cm and  $\theta = 140^\circ$ , then (1) becomes (2):

$$(2) \quad P_c = 107 / r_c$$

where:

$P_c$  = Capillary pressure (psi);

$r_c$  = Radius of pore throat (microns).

Swanson (1981) discovered that complete saturation of the interconnected pores

with a non-wetting phase corresponds to the apex of hyperbola of log-log mercury injection capillary pressure curves. He developed a relationship between permeability and capillary pressure data, based on sandstone and carbonate samples:

$$K_{\text{air}} = 339 (S_{\text{Hg}}/P_c)^{1.961}_{\text{apex}}$$

Where:

$K_{\text{air}}$  is air permeability (mD)

$S_{\text{Hg}}$  is the bulk volume mercury saturation (%)

$P_c$  is the capillary pressure (psi) corresponding to the apex of a hyperbola of a log-log mercury injection plot.

Swanson also showed a relationship between brine permeability at 1000 psi effective stress:

$$K_{\text{brine}} = 355 (S_{\text{Hg}}/P_c)^{2.005}_{\text{apex}}$$

Winland developed a relationship between porosity, air permeability and pore throat corresponding to 35% mercury saturation. The Winland equation, based on sandstones and carbonates samples with low permeability was used and published by Kolodzie (1980):

$$\text{Log } r_{35} = 0.732 + 0.588 \text{ Log } K_{\text{air}} - 0.864 \text{ Log } \phi$$

Pittman (1992) improved the equation published by Kolodzie, integrating more analyses of mercury injection, porosity and permeability done on sandstone samples. The result was a better approximation:

$$\text{Log } K = -1.221 + 1.415 \text{ Log } \phi + 1.512 \text{ Log } r_{25}$$

Where:

$K$  is the uncorrected air permeability (mD)

$\phi$  is porosity (%)

$r_{25}$  is the pore throat that correspond to 25% mercury saturation on the cumulative plot.

Permeability was calculated using the Swanson equations (Appendix 5.1) and the result plotted against horizontal core plug permeabilities. The cross plot of core

permeability versus permeability to air and to brine (Swanson) indicates a correlation coefficient  $r^2 = 0.91$  and  $r^2 = 0.89$ , respectively (Fig. 5.5.a). The Swanson method could not be applied to fine-grained lithologies as in this case, the capillary curves do not form a hyperbola on a log-log scale.

Permeabilities were calculated using Winland and Pittman equations (Appendix 5.1). These methods were successfully applied, especially if the conformance was not more than 35% or 25% mercury saturation. Cross plots of core plug permeability versus Winland permeability show a correlation coefficient  $r^2 = 0.798$  (Fig. 5.5.b) and cross plots of core plug permeability versus Pittman permeability show a correlation coefficient  $r^2 = 0.846$  (Fig. 5.5.c). Permeabilities calculated from Winland and Pittman equations show a correlation coefficient  $r^2 = 0.98$  (Fig. 5.5.d).

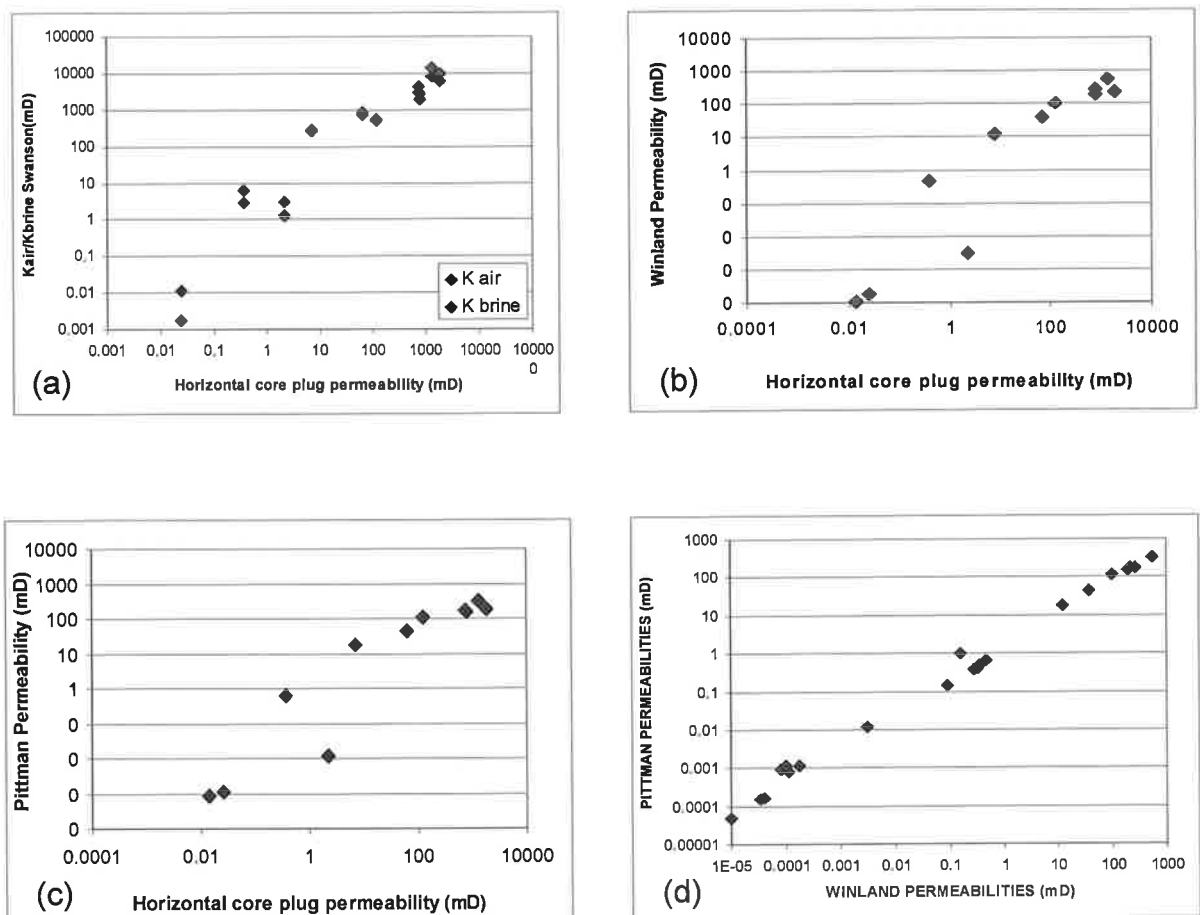


Figure 5.5 Relationship between horizontal core plug permeability and (a) Swanson permeability to air and brine, (b) Winland permeability, (c) Pittman permeability. (d) Correlation between Pittman and Winland permeabilities.

The absolute values of calculated permeabilities are different from the measured core permeabilities. Many errors can affect the credibility of the results.

- errors from the algorithms: the data base was designed for sandstones and carbonates and was applied to gravels, more or less clean sandstones, matrix-rich sands and even siltstones.
- errors from picking up the apex of the hyperbola of capillary pressure and mercury saturation curves; This error can be magnified by the logarithmic scale.
- core plug permeability measurements can have errors due to gas slippage (Klinkenberg error) – when the permeabilities are low.
- core plug permeabilities represent directional (horizontal) permeabilities, while the permeabilities calculated from capillary pressure data represent whole rock permeability where the non-wetting phase intrudes the sample from all sides.

## 5.6 SUMMARY

Reservoir quality in the sands of the Nappamerri Group is moderate to fair. Core porosity usually varies from 7% to 14% in RF-1, RF-4 and RF-5. Extreme porosity values reach 16% to 21% in RF-2 and RF-3. Permeability measured from core gives values of 66 to 1800 mD in sands with open pores RF-1, RF-2 and RF-3 but the values drop to 0.4 – 10 mD where kaolin platelets fill the primary pores, in RF-4, RF-5 and SF-1.

Primary and secondary macro-porosity and microporosity have been identified in the reservoir lithologies (RF-1 to RF-4), while primary porosity and microporosity were observed in RF-5 and SF-1. Different types of porosity develop preferentially in certain depositional environments. Primary porosity is well developed in coarser sandstones (RF-1 to RF-4), while microporosity forms in fine-grained sandstones at the top of point bars (RF-5, SF-1).

The most important factors for porosity preservation are the amount of matrix, which is a depositional factor and the quartz overgrowth cementation, a diagenetic factor. Gravels (RF-1) and fluvial channel sandstones (RF-2) have higher porosities due to a higher amount of quartz overgrowth cements that preserve porosity during compaction. Sandstones deposited at the top of point bars (RF-5, SF-1) or crevasse splays (RF-4) contain higher amounts of detrital clays and lower porosities.

Pore system geometry is controlled by diagenesis such as quartz, kaolin or siderite precipitation, compaction and dissolution. All these diagenetic events are determined by the primary composition of the rock. Composition and texture are ultimately controlled by the depositional environment of each lithofacies.

Rock composition, cementation and pore throat size distribution control permeability. Swanson (1981), Winland (Kolodzie, 1980) and Pittman (1992) developed equations to calculate permeability from mercury injection capillary curves. Comparison between permeabilities calculated using these equations and core measurements show different values. The correlation between sets of permeability values show high correlation coefficients.

**PLATE 5.1****SEM photomicrographs of primary porosity**

- a. Excellent preservation of the intergranular porosity between quartz overgrowths. Clays line some of the pores. Large pores, of 350 microns diameter have excellent interconnectivity. Beanbush 1, 8735 ft 2 in ( $\Phi = 12.8\%$ ,  $K = 1880\text{mD}$ ). Scale bar = 200 microns.
- b. Primary porosity preserved between clean, euhedral faces of quartz overgrowths. The pores show excellent interconnectivity. Telopea 2, 8188 ft. Scale bar = 100 microns.
- c. Tabular, open primary pores. Note the excellent pore interconnectivity. Clays occur around parts of some pores. Pore sizes are about 150 microns. Beanbush 1, 8735 ft 2 in. Scale bar = 500 microns.
- d. Primary porosity modified by clean quartz overgrowths and kaolin lining the pores. Large interconnected pore system. Telopea 2, 8188 ft. Scale bar = 100 microns.

# PLATE 5.1

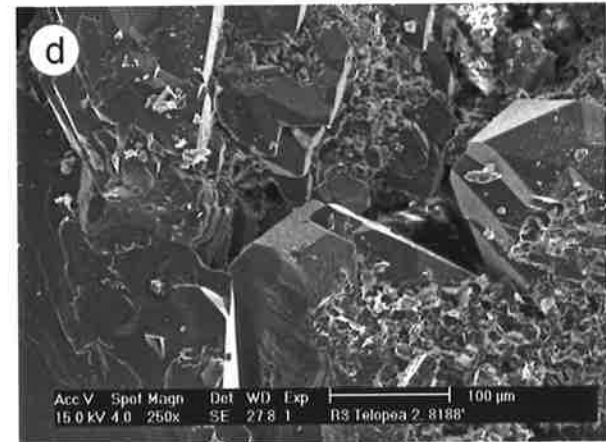
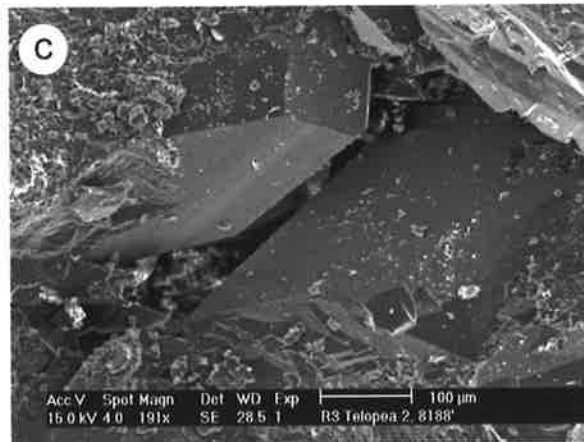
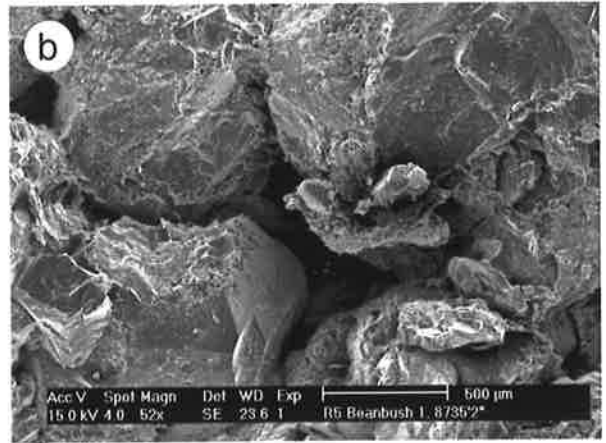
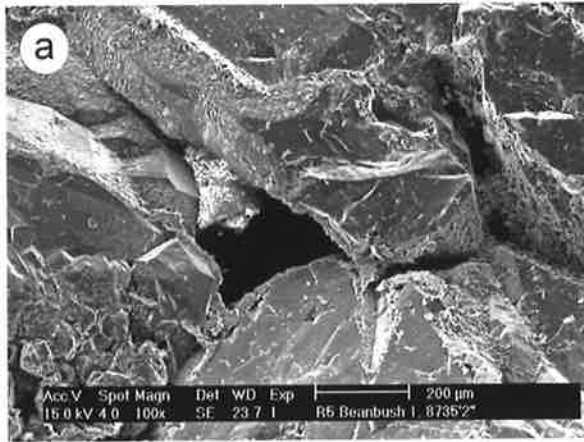
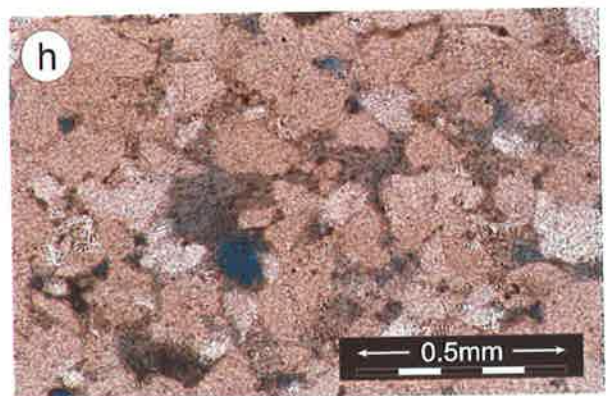
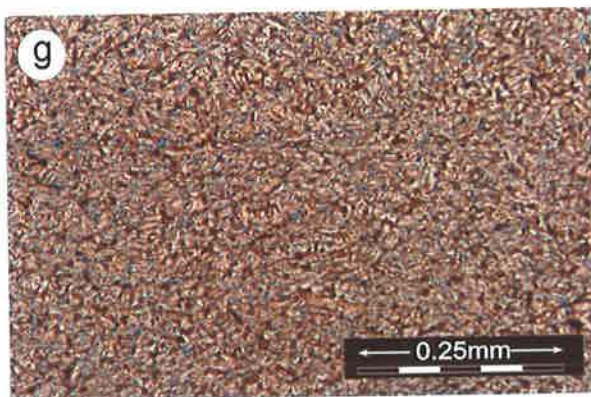
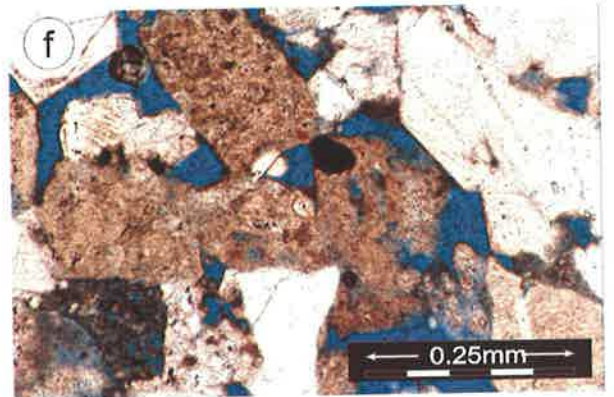
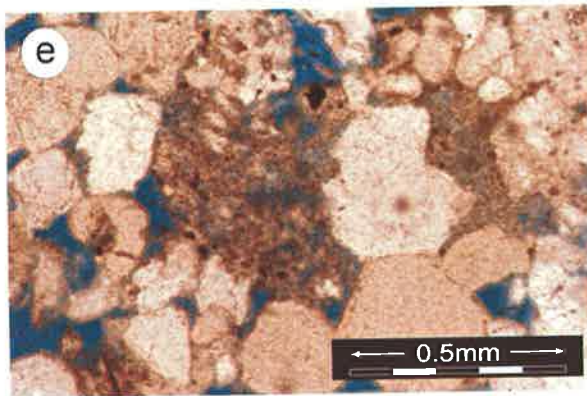
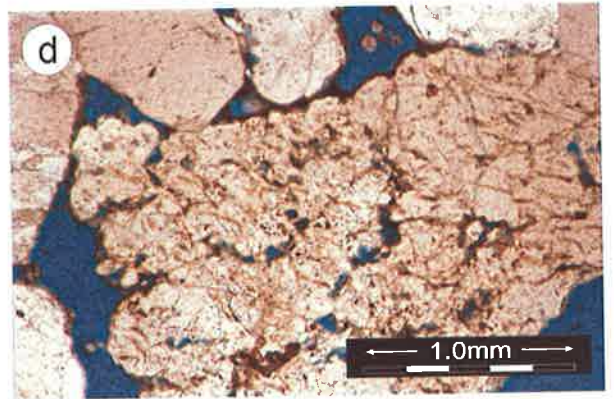
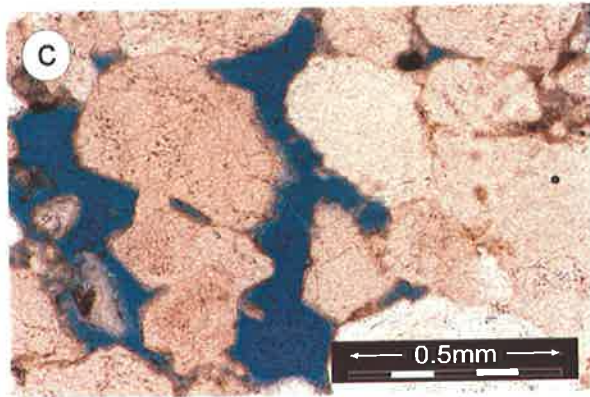
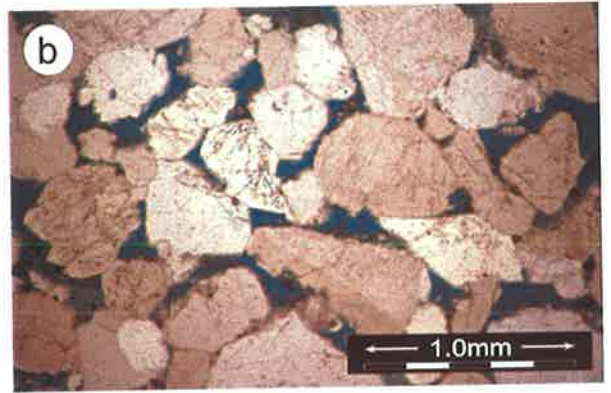
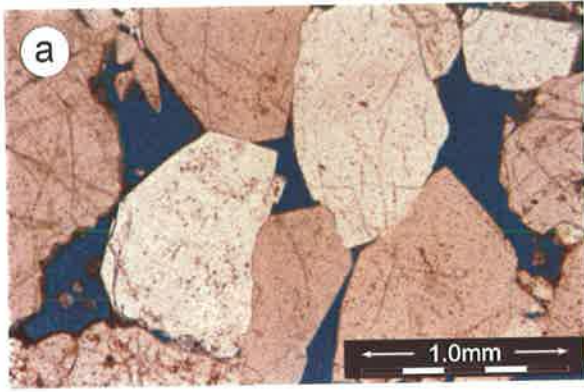


**PLATE 5.2****Thin section photomicrographs of primary porosity, secondary porosity and microporosity**

- a. Primary porosity preserved between well-developed quartz overgrowths. Beanbush 1, 8735 ft 2 in, plane polarized light. Scale bar = 1 mm.
- b. Intergranular porosity is enhanced by dissolution of quartz grains and overgrowth cement. Oversized pores result from dissolution. Teloepa 2, 8188 ft, plane polarized light. Scale bar = 1 mm.
- c. Oversized pores as a result of dissolution (left and central) and complete destruction of primary porosity as a result of quartz cementation (right). Teloepa 2, 8189 ft, plane polarized light. Scale bar = 0.5 mm.
- d. An incompletely leached polycrystalline quartz grain develops secondary porosity. Clays line the primary pores or the newly created micropores. Beanbush 1, 8735 ft 2 in, plane polarized light. Scale bar = 1 mm.
- e. Dissolution of quartz grains (left) and of rock fragments (central) creates secondary porosity. Merrimelia 29, 7100 ft, plane polarized light. Scale bar = 0.5 mm.
- f. Combination of primary pores preserved between thick quartz overgrowths and oversized pores, the result of dissolution. The quartz overgrowth is identified by the euhedral faces and dust rims. Clays line the pores. Merrimelia 17, 7078 ft 2 ½ in, plane polarized light. Scale bar = 0.25 mm.
- g. Coarsely crystalline kaolin booklets. Kaolin creates a microporosity that can account for up to 44 % of the total kaolin cemented areas when loosely packed. Beanbush 1, 8735 ft 2 in, plane polarized light. Scale bar = 0.25 mm.
- h. Clay cementation, mainly kaolin surrounds and fills the pores and pore throats making this sample a seal. The remnant pores are isolated, with no interconnectivity. Teloepa 2, 8186 ft 3 in, plane polarized light. Scale bar = 0.5 mm.



# PLATE 5.2



## CHAPTER SIX

# PETROPHYSICAL CONTROLS ON HYDROCARBON MIGRATION AND SEALING

### 6.1 INTRODUCTION

Primary migration is defined as the movement of hydrocarbons from the source rocks to carrier beds. "Secondary migration is the movement of hydrocarbons as a single continuous phase fluid through water-saturated rocks, faults or fractures and the concentration of the fluid in a trapped accumulation of oil and gas" (Schowalter, 1979). Buoyancy is the main driving force for the upward secondary migration of hydrocarbons and depends on the density difference between the wetting phase (water) and non-wetting phase (hydrocarbons). Buoyancy forces are affected by the existing hydrodynamic conditions from the subsurface. In the subsurface, hydrocarbons migrate through the pores of the rock. The main resistant force for secondary hydrocarbon migration through a water saturated porous rock is the capillary pressure (Schowalter, 1979). Capillary pressure opposes buoyancy. If the buoyancy pressure is less than the capillary pressure, then the hydrocarbons cannot migrate upwards and the rock is 100% water saturated. On the other hand, if the buoyancy is greater than capillary pressure, hydrocarbons can move upwards and the water saturation of the rock is less than 100%.

### 6.2 CAPILLARY PRESSURE

Leverett (1941) defined capillary pressure as the "pressure difference between the oil phase and the water phase across a curved oil-water interface".

As the wetting and non-wetting fluids have different densities, which results in different pressure gradients, the capillary pressure can be calculated:

$$P_C = P_{NW} - P_W = (\rho_{NW} - \rho_W)gh$$

Where:

$P_C$  = capillary pressure (psi);

$\rho_W$  = density of wetting phase ( $\text{g}/\text{cm}^3$ );

$\rho_{NW}$  = density of non-wetting phase ( $\text{g}/\text{cm}^3$ );

$g$  = gravity constant (0.433 psi/ft; 9.81 kPa/m);

$h$  = height above free water level (ft; m).

Physically, capillary pressure results from the interaction of cohesive forces (liquid-liquid; eg. interfacial tension) and adhesive forces (liquid-solid) that act within and between fluids and their bounding solids. The adhesive forces act in a narrow capillary tube placed in a wetting fluid by drawing the fluid into the tube above the original interface or free water level until adhesive and gravitational forces are balanced.

### 6.2.1 Displacement pressure

In the subsurface, the hydrocarbon filaments need to move through water-saturated porous rocks. The force required to displace water from cylindrical pores and force the oil filament through the pore was termed displacement pressure ( $P_d$ ) by Schowalter (1979). The factors that determine the magnitude of displacement pressure are interfacial tension, wettability and radius of capillary (Purcell, 1949).

$$P_d = \frac{2\sigma \cos \theta}{R_C}$$

Where:

$\sigma$  = interfacial tension between fluids and capillary tube (dynes/cm);

$\theta$  = contact angle (degrees);

$R_C$  = radius of the capillary (cm);

$P_d$  = Displacement pressure ( $\text{dynes}/\text{cm}^2$ ).

For water-saturated porous rocks, the displacement or breakthrough pressure is defined as the "minimum pressure required to establish a connected hydrocarbon filament through the pores of the rock" (Smith, 1966).

Determination of displacement pressure for a hydrocarbon-water-rock system facilitates the calculation of vertical hydrocarbon column that a rock can hold, therefore the sealing capacity for a cap rock seal.

### 6.2.2 Interfacial tension ( $\sigma$ )

Interfacial tension between two immiscible fluids is defined as the work required to enlarge the fluid interface by a unit area. Interfacial tension is the effect of the difference between the attraction of similar molecules within each fluid and the attraction of dissimilar molecules across the interface of the fluids (Schowalter, 1979). It is measured in dynes/centimeter.

Oil-water interfacial tension is a function of the chemical composition of the oil, amount and type of surface-active agents, types and quantities of gas in solution. Oil-brine interfacial tension decreases with increasing API gravity and temperature and is less affected by the pressure. The results of atmospheric oil or gas interfacial tension measurements at atmospheric conditions must be extrapolated at subsurface temperature and pressure.

Livingston (1938) estimated the interfacial tensions of 34 Texas crude oils and extrapolated the atmospheric conditions measurements to reservoir temperature using a nomograph that assumes decreases of 0.1 dynes/cm/<sup>0</sup>F temperature increase above 70<sup>0</sup>F. The subsurface oil-water interfacial tension ranges from 5 to 35 dynes/cm.

API Gravity	> 40	30 - 40	< 30
Interfacial tension (dynes/cm)	15	21	30

Cartmill (1976) suggested that the oil-water interfacial tension continue to decrease with temperature and pressure and become zero in which case the oil-water interfacial tension reduction is considered to be the cause for primary migration of oil.

Gas-water interfacial tension varies with the amount of surface-active agents in the water, the amount of heavy hydrocarbons in solution in the gas, temperature and pressure. Gas-water interfacial tension decreases with increasing temperature and pressure. The effects of temperature and pressure on methane-water systems were

combined in a nomograph to estimate the subsurface methane-water interfacial tension (Hough et al., 1951).

### 6.2.3 Wettability

Wettability is defined as the work required to separate a wetting fluid from a solid and is expressed by the contact angle of the water-oil interface against the solid pore wall, measured through the denser phase. Physically, wettability is a difference of forces that occur at the interface between three phases, one of which is a solid.

$$\cos \theta = \frac{\sigma_{os} - \sigma_{ws}}{\sigma_{ow}}$$

Where:

$\sigma_{os}$  = interfacial tension between oil and solid (dynes/cm);

$\sigma_{ws}$  = interfacial tension between water and solid (dynes/cm);

$\sigma_{ow}$  = interfacial tension between oil and water (dynes/cm);

$\theta$  = contact angle (deg).

When the adhesive forces are greater than cohesive forces, the liquid is said to be wetting and when cohesive forces are greater than adhesive forces, the liquid is nonwetting. In a rock-fluid system, if the contact angles vary between 0 and 90°, the rocks are considered to be water wet and if contact angles are greater than 90°, the rocks are considered oil-wet. Water-wet rocks will have a preference to imbibe water rather than oil, while oil-wet rocks will imbibe oil in preference to water. The general assumption is that most rocks are water wet; exceptions are oil reservoirs and rocks rich in organic matter such as source rocks; therefore, the wettability term in the displacement pressure equation can be considered as unity.

### 6.2.4 Radius of pore throats

The size of pore throats can be estimated from thin sections, scanning electron microscopy or from pore cast studies. In these cases, the three dimensional relationship of one pore to another cannot be determined. Furthermore, these techniques cannot be

used effectively on non-reservoir rocks, where the pore throats are too small to measure.

Mercury injection capillary pressure analyses estimate the distribution of the pore volume accessible by pore throats. In the air/mercury/solid system, where the interfacial tension is 485 dynes/cm and contact angle  $\theta$  is  $140^\circ$ , equation (1) becomes (2) (Washburn, 1921)

$$(1) \quad r_c = \frac{2\sigma \cos\theta}{P_d} \qquad (2) \quad r_c = \frac{107.6}{P_d}$$

Where:

$r_c$  = capillary radius (microns);

$P_d$  = displacement pressure (psi);

$\sigma$  = interfacial tension of the air/mercury system (dynes/cm).

### 6.2.5 Subsurface densities of fluids

Many factors influence the extrapolation of water and hydrocarbon densities to reservoir conditions. Pressure, temperature and amount and kinds of dissolved solids affect the subsurface water density. Oil or condensate subsurface density is dependent on composition of the oil and dissolved gasses, temperature and pressure. Subsurface oil density can be determined if the stock tank API gravity and the solution gas-oil ratio (in SCF/STB) are known. The factors that determine the subsurface gas density are shown by the following equation:

$$\rho_g = 1.485 \cdot 10^{-3} \frac{mp}{ZT}$$

Where:

$\rho_g$  = subsurface density of gas (g/cc);

$m$  = apparent average molecular weight;

$p$  = absolute subsurface pressure (lb/sq in);

$Z$  = compressibility factor;

$T$  = absolute subsurface temperature (Rankine).

### 6.3 SEAL CAPACITY CALCULATION

Seal capacity refers to the maximum column of hydrocarbons ( $H_{\max}$ ) that a rock type can hold back before it leaks. The maximum height of hydrocarbon column ( $H_{\max}$ ) is calculated using the following equation from Smith (1966):

$$H_{\max} = \frac{P_S - P_R}{(\rho_b - \rho_{hc}) \cdot 0.433} \quad (3)$$

Where:

$H_{\max}$  = the maximum height of hydrocarbon column a seal can hold before it leaks (ft);

$P_S$  = brine/hydrocarbon threshold pressure of the seal (psi);

$P_R$  = brine/ hydrocarbon threshold pressure of the reservoir (psi);

$\rho_b$  = brine density (g/cc);

$\rho_{hc}$  = hydrocarbon density (g/cc);

0.433 represents the gravity constant in psi/ft.

### 6.4 CONVERSION EQUATIONS FROM AIR / MERCURY LABORATORY DATA TO BRINE / HYDROCARBON RESERVOIR CONDITIONS

The capillary pressure, calculated in the laboratory using an air-mercury system must be converted to a brine-hydrocarbon system at subsurface conditions using the following equation (Purcell, 1949):

$$Pc_{b/hc} = Pc_{a/m} \cdot \frac{\sigma_{b/hc} \cos \theta_{b/hc}}{\sigma_{a/m} \cos \theta_{a/m}} \quad (4)$$

Where:

$Pc_{b/hc}$  = capillary pressure in the brine/hydrocarbon system (psi);

$Pc_{a/m}$  = capillary pressure in the air/mercury system (psi);

$\sigma_{b/hc}$  = interfacial tension for brine/ hydrocarbon system (dynes/cm);

$\sigma_{a/m}$  = interfacial tension for air/ mercury system (dynes/cm);

$\theta_{b/hc}$  = contact angle of the reservoir brine/hydrocarbon/solid system (deg);

$\theta_{a/m}$  = contact angle of the laboratory air/mercury/solid system (deg).

The interfacial tension of 480 dynes/cm and the contact angle of  $140^{\circ}$  are standard values for the air/mercury systems.

## **6.5 THRESHOLD PRESSURE**

### **6.5.1 Definition**

The threshold pressure ( $P_t$ ) is defined here as the pressure required to form a continuous filament of non wetting fluid through the largest connected pore throats of the rock. It is the pressure that determines the minimum buoyancy pressure needed for secondary migration. The pressure at which the mercury first enters the pore system of a rock, after the mercury has filled any surface irregularities (conformance) of the sample is termed the entry pressure.

### **6.5.2 Methods of estimating the threshold pressure from capillary pressure curves**

The threshold pressure is estimated from capillary pressure curves (Appendix 3.6). "It has been assumed that a continuous filament of nonwetting phase will occur somewhere on the capillary plateau" (Schowalter, 1979). The plateau represents a portion of the curve where the pressure difference between 10% and 50% mercury saturation is small and therefore threshold pressure can be estimated with precision. For seal lithologies, where the plateaus are steep or do not exist, the threshold pressure is determined as the critical non-wetting phase saturation needed to form a continuous non-wetting filament through the rock.

Schowalter (1979) conducted direct measurements of threshold pressure and critical saturation at breakthrough. He suggested that the saturation of non-wetting phase needed to establish a continuous filament across the length of the sample ranged from 4.5 to 17% of the rock pore volume, with an average of 10%. The extrapolation of capillary plateau method (Boult et al., 1993) is mainly applied to reservoir rocks, where the entry pressure and threshold pressure are approximately the same and therefore the capillary plateau is nearly flat. The threshold pressure is interpreted from a cumulative



plot by extrapolating the plateau interval to the line where the mercury saturation is 0%. A cumulative plot is acquired by plotting on a logarithmic scale the capillary pressure (psi) versus mercury saturation (%).

Thomas and Katz (1968) recommended the extrapolation of a line between the 30% and 5% mercury saturation back to the 0% line for threshold pressure determination.

With the incremental plot method (Boult et al., 1993) it can be determined where the apparent mercury displacement increases significantly. An incremental plot is acquired by plotting the capillary pressure on a logarithmic scale versus incremental pore volume (ml/g)

### 6.5.3 Determination of threshold pressure

For rocks with a well-defined capillary plateau (Fig.6.1), the capillary plateau extrapolation method was used to determine the threshold pressure. This correlated with the major inflection (ie significant intrusion) on the MICP plot (Boult, 1996). A tangent to the plateau was drawn and its intersection with the Y-axis (0% mercury saturation) represents the threshold pressure. Conformance is defined as apparent mercury intrusion due to sample surface irregularities that are not part of the pore volume (Sneider *et al.*, 1997). Conformance was less than 10% in all samples in this study (Fig. 6.1). This method was successfully applied to the sandstone samples (reservoir lithologies, RF-1 to RF-5 and diagenetically modified sandstones, SF-1).

MICP curves of fine-grained lithologies have steep slopes, and large conformance (many up to 30% and a few up to 63% mercury saturation). For potential sealing lithologies with a steep capillary plateau (Fig. 6.2), the inflection point (at which the curve becomes convex upwards) represents the threshold pressure (Katz and Thomson, 1987). In order to eliminate the effect of conformance, a horizontal line was drawn back to the Y-axis to determine the threshold pressure (Fig. 6.2). In all cases the estimated threshold pressures from the cumulative plots were compared to see whether they correspond to significant intrusions of mercury on the incremental plots (Appendix 3.6).

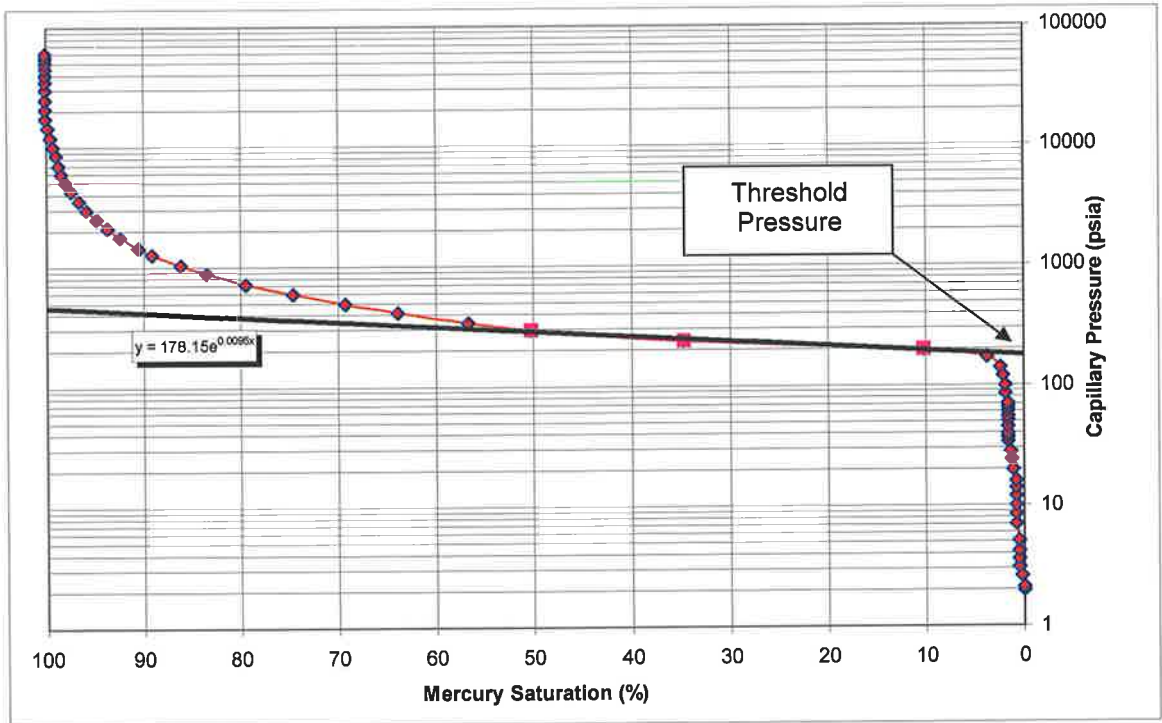


Figure 6.1 Mercury injection capillary pressure curve with a flat plateau (Telopea 2, 8186'3")

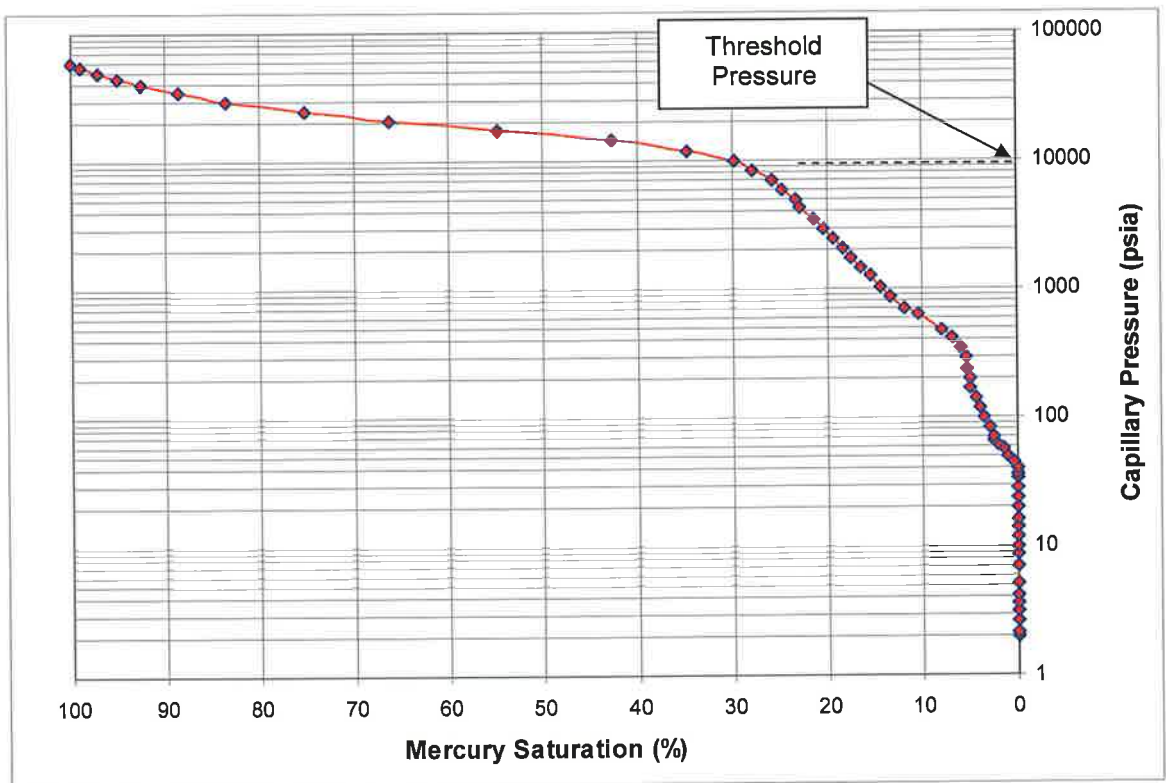


Figure.6.2 Mercury injection capillary pressure curve with a steep gradient (Beanbush 1, 8723'3")

The seal threshold pressure is the critical term in the seal capacity equation (3). The lacustrine mudstones (SF-2) have the highest air/mercury threshold pressure (9231 psi) followed by palaeosols (SF-3) and floodplain mudstones (SF-4) with air/mercury threshold pressure of 7725 psi and by diagenetically modified sandstones (SF-1) with air/mercury threshold pressure of 251 psi (Table 6.1).

The reservoir threshold pressure has a minor contribution to the seal capacity calculation. Gravels (RF-1), fluvial channel sands (RF-2), chute sands (RF-3), and some crevasse spaly sands (RF-4) have low air/mercury threshold pressure of less than 8.6 psi. The samples collected from distal crevasse spaly sands are tightly packed, clay cemented sandstones with small pore throat sizes. Their original porosity was lost due to compaction; therefore these samples have much higher air/mercury threshold pressure (1141.5 psi). The fine sands from the top of point bars (RF-5) are the same lithofacies as the diagenetically modified fluvial sandstones (SF-1). The distinction was made during sample collection because the top of the oil column could be seen in SF-1 in two wells: Telopea 2, 8186'3" and Merrimelia 15, 7114'5". No oil column was present in RF-5 samples to indicate their sealing/reservoir behaviour.

## **6.6 SUBSURFACE EXTRAPOLATION OF RESERVOIR FLUIDS DENSITY, INTERFACIAL TENSION AND WETTABILITY**

### **6.6.1 Subsurface oil density**

Subsurface oil densities were calculated using methodology of Tenny (Schowalter 1979), in which the surface gas-oil ratios (standard cubic feet/stock tank barrel) and stock tank API gravities from Merrimelia field wells were converted to subsurface values; this resulted in a subsurface oil density of 0.755 g/cm<sup>3</sup>.

### **6.6.2 Subsurface gas density**

Subsurface gas density was also determined from Tenny (Schowalter 1979). Input reservoir temperature = 210 – 266<sup>0</sup>F (99 - 130<sup>0</sup>C), pressure = 3125 – 3900 psi and average molecular weight = 22 – 33.75 mg/l were used. The gas samples from the Merrimelia and Beanbush wells were collected from drill stem tests at depths near the

<b>Facies</b>	<b>Air/Hg Threshold Pressure (psi)</b>	<b>Brine/Oil Threshold Pressure (psi) IT = 16, CA = 0</b>	<b>Brine/Gas Threshold Pressure (psi) IT = 30, CA = 0</b>
<b>Sealing facies</b>			
Diagenetically modified fluvial sandstones (SF-1)	167 – 251	7.2 – 11	14 – 21
Lacustrine mudstones (SF-2)	2743 - 9231	119 - 402	224 - 753
Palaeosols (SF-3)	5484 - 7727	239 - 336	447 - 630
Floodplain mudstones (SF-4)	3921 - 7725	171 - 336	320 - 630
<b>Reservoir facies</b>			
Gravels (RF-1)	2 - 5.4	0.1 - 0.2	0.2 - 0.4
Fluvial channel sands (RF-2)	3.5 - 6.1	0.2 - 0.3	0.3 - 0.5
Chute sands (RF-3)	3.9 - 5.5	0.2	0.3 - 0.4
Crevasse splay sands (RF-4)	8.6 – 1141.5	0.4 – 49.7	0.7 – 93.1
Fine sands from top point bar (RF-5)	135.8 - 155.8	5.9 - 6.8	11.1 - 12.7

Table 6.1 Range of air/mercury and brine/hydrocarbon threshold pressures for the identified sealing and reservoir facies, alternate interfacial tension (IT) 16 dynes/cm and 30 dynes/cm, with a 0° contact angle (CA).

samples analyzed in this study. The average molecular weight was calculated by multiplying the molecular volume (%) by the molecular weight (g/mole) of each gas component. The molecular volume of each gas component was determined from the gas chromatography analysis. This resulted in a gas subsurface density of 0.235 g/cm<sup>3</sup> (Appendix 6.2).

### 6.6.3 Subsurface brine density

Subsurface brine densities were similarly determined using the methods of Tenny (Schowalter 1979), in which reservoir temperature, pressure and total dissolved solids were input from drill stem test data. Total dissolved solids (milligrams/litre) of formation waters from Telopea, Beanbush and Merrimelia field wells were determined from

formation depths close to the MICP samples. The amount of total dissolved solids varies between 1822 and 8264 mg/l, characteristic of fresh waters. This resulted in a subsurface brine density of  $0.964 \text{ g/cm}^3$  (Appendix 6.3).

#### 6.6.4 Oil/water interfacial tension

The API gravities of oil from the Merrimelia and Telopea fields have values ranging from  $27.2^{\circ}\text{API}$  (low gravity crude oil) to  $57.4^{\circ}\text{API}$  (high gravity crude oil). The ambient oil-water interfacial tension estimates vary from 30 to 15 dynes/cm and extrapolating to reservoir temperature of  $210^{\circ}\text{F} - 266^{\circ}\text{F}$  ( $99 - 130^{\circ}\text{C}$ ), results in subsurface values of oil – water interfacial tension from less than 5 to 16 dynes/ cm (Livingston, 1938). As a sensitivity study, subsurface values of oil – water interfacial tension of 5, 16 and 21 dynes/ cm were used. Depending of the interfacial tension used in calculation, the maximum hydrocarbon column heights vary considerably (Fig. 6.3).

#### 6.6.5 Gas/water interfacial tension

Methane is the dominant component of the studied gas samples, with a molecular volume of 54.7% to 76.6%. (Beanbush and Merrimelia fields). The nomograph from Hough *et al.* (1951), in which reservoir temperature (210 to 266 deg F), and reservoir pressure (3125 to 3900 psi) were input from drill stem test data, was used in estimating the subsurface methane-water interfacial tension of 30 to 35 dynes/ cm.

Values of subsurface gas/water interfacial tension of 25, 30 and 35 dynes/cm were used to calculate hydrocarbon column heights as a measure of sensitivity to these values.

#### 6.6.6 Wettability

For seal capacity evaluation of the Triassic facies, the rocks were assumed to be strongly water-wet. Contact angles for brine/hydrocarbon/solid system of less than  $90^{\circ}$  were used (Vavra *et al.*, 1992). As a sensitivity case, hydrocarbon column height was calculated using contact angles of  $0^{\circ}$ ,  $15^{\circ}$  and  $20^{\circ}$  (Fig. 6.3). The results show that the calculated hydrocarbon column heights are only nominally affected by any variation of

contact angle in a water-wet system. Therefore, it is considered reliable to use a brine/hydrocarbon contact angle =  $0^{\circ}$  in  $H_{\max}$  calculations.

### 6.7 CALCULATION OF HYDROCARBON COLUMN HEIGHTS

The maximum height of the hydrocarbon column was calculated using equation (3). The following input parameters were used to calculate seal capacity in the Triassic rocks from the Cooper Basin.

Subsurface brine density =  $0.964 \text{ g/cm}^3$

Subsurface oil density =  $0.755 \text{ g/cm}^3$

Subsurface gas density =  $0.235 \text{ g/cm}^3$

Brine/oil interfacial tension (sensitivity cases) = 5, 16 and 21 dynes/cm<sup>2</sup>

Brine/gas interfacial tension (sensitivity cases) = 25, 30 and 35 dynes/cm<sup>2</sup>

Contact angle of brine/hydrocarbon/solid system =  $0^{\circ}, 15^{\circ}$  and  $20^{\circ}$  (water-wet rocks).

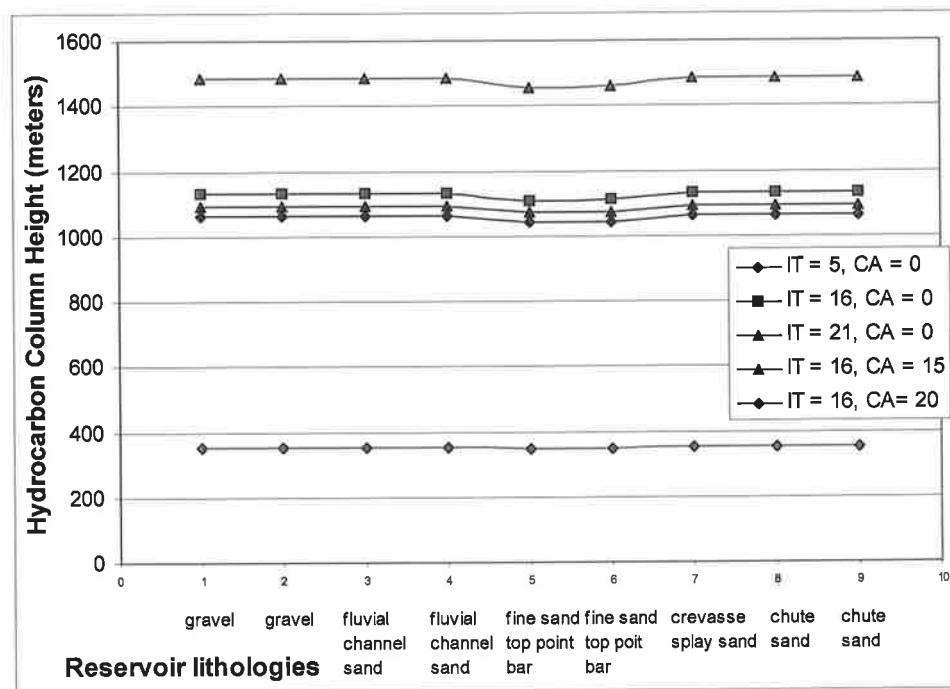


Figure 6.3 Sensitivity of hydrocarbon column height to interfacial tension (IT = 5, 16 and 21 dynes/cm) and contact angle (CA =  $0^{\circ}, 15^{\circ}$  and  $20^{\circ}$ ). Variations in

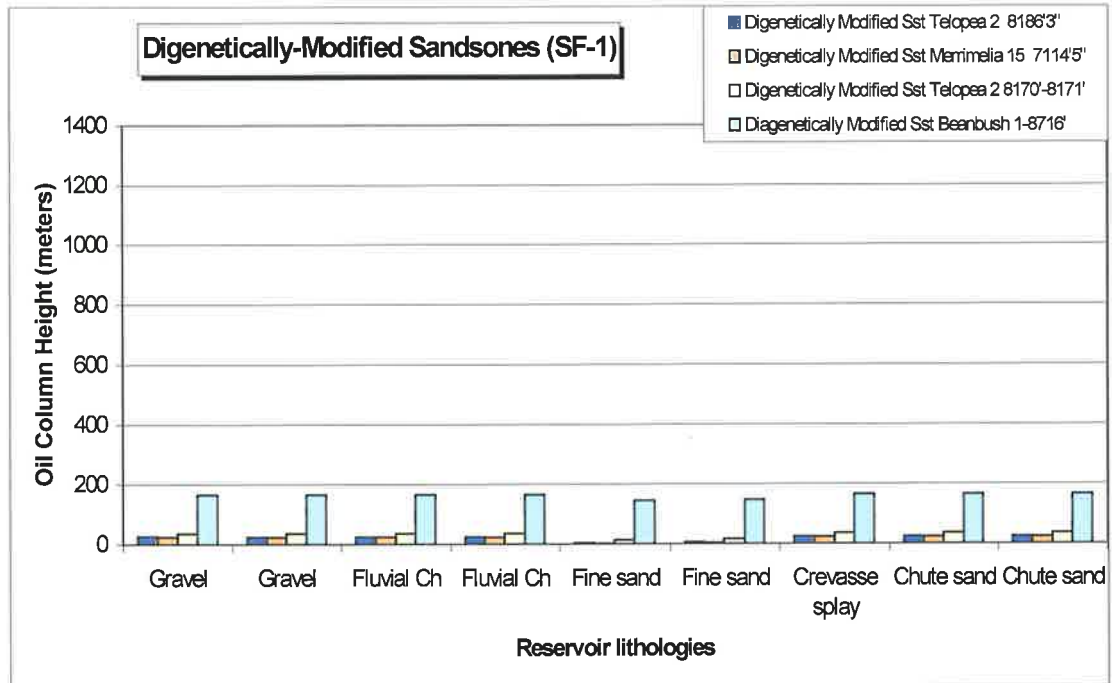
interfacial tension have a greater influence on column height than changes to the contact angle.

The hydrocarbon column heights held by the four sealing lithologies were calculated. Column heights were calculated in a range of reservoir lithologies (Fig. 6.4.a – d). The results showed that the maximum height of hydrocarbon column is mainly a function of the seal lithology (seal threshold pressure) and not of the reservoir lithology. For each sealing lithology, a minimum and maximum hydrocarbon column height was calculated. Variations in  $H_{\max}$  are due to differences in the individual sealing samples. Both oil/brine (interfacial tension used was 16 dynes/cm and contact angle used was  $0^{\circ}$ ) and gas/brine (interfacial tension used was 30 dynes/cm and contact angle used was  $0^{\circ}$ ) systems of reservoir were considered. The results are presented in Table 6.2.

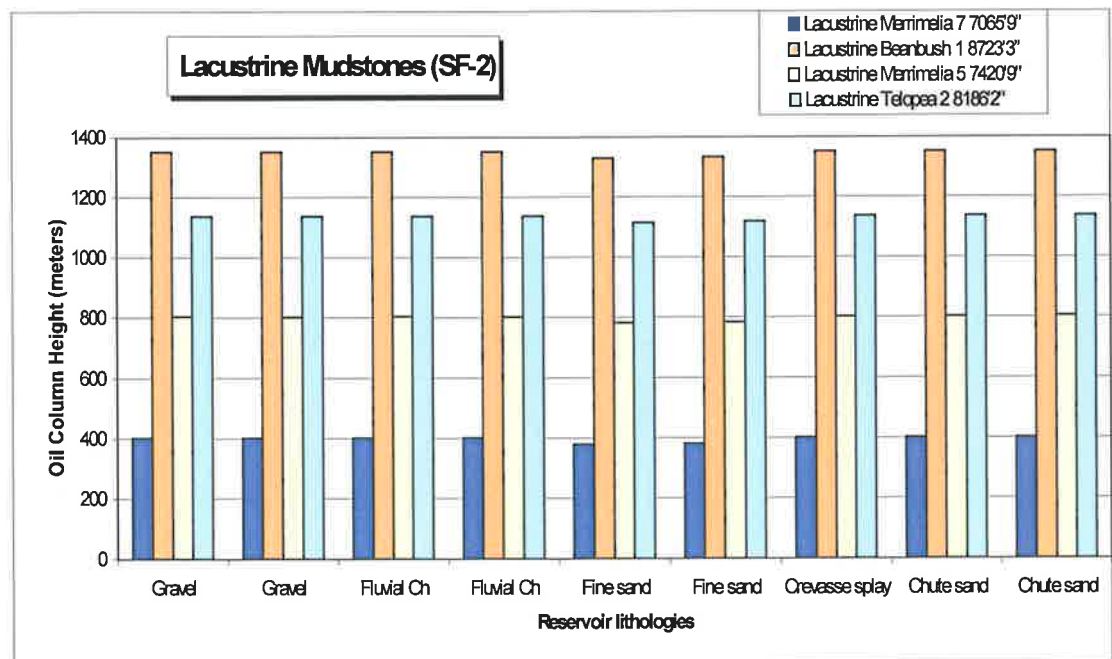
Facies	Seal Capacity			
	Hmax Oil (m) IT=16, CA=0	Hmax Oil (ft) IT=16, CA=0	Hmax Gas (m) IT=30, CA=0	Hmax Gas (ft) IT=30, CA=0
Diagenetically modified sst (SF-1)	2 - 37	7 - 121	1 - 20	3 - 66
Lacustrine mudstones (SF-2)	380 - 1353	1243 - 4439	204 - 727	669 - 2385
Palaeosols (SF-3)	781 - 1132	2562 - 3714	420 - 609	1378 - 1998
Floodplain mudstones (SF-4)	552 - 1132	1811 - 3714	297 - 608	947 - 1995

Table 6.2. Range of maximum hydrocarbon column heights as a function of seal lithologies, considering an oil/brine and gas/brine system of reservoir (hydrocarbon column height in meters and feet).

The highest seal capacity is held by SF-2 with maximum hydrocarbon column height of 1353 m (oil) and 727 m (gas) followed by SF-3 and SF-4 with maximum 1132 m oil and 609 m gas. The lowest seal capacity is associated with SF-1, with a maximum height of hydrocarbon column of 37 m oil and 20 m gas (Fig. 6.5.a and Fig. 6.5.b). The column bars represent the range between the minimum and maximum hydrocarbon columns held, using interfacial tension = 16 dynes/cm (oil) and 30 dynes/cm (gas). The lower values represent hydrocarbon column heights calculated using the lowest interfacial



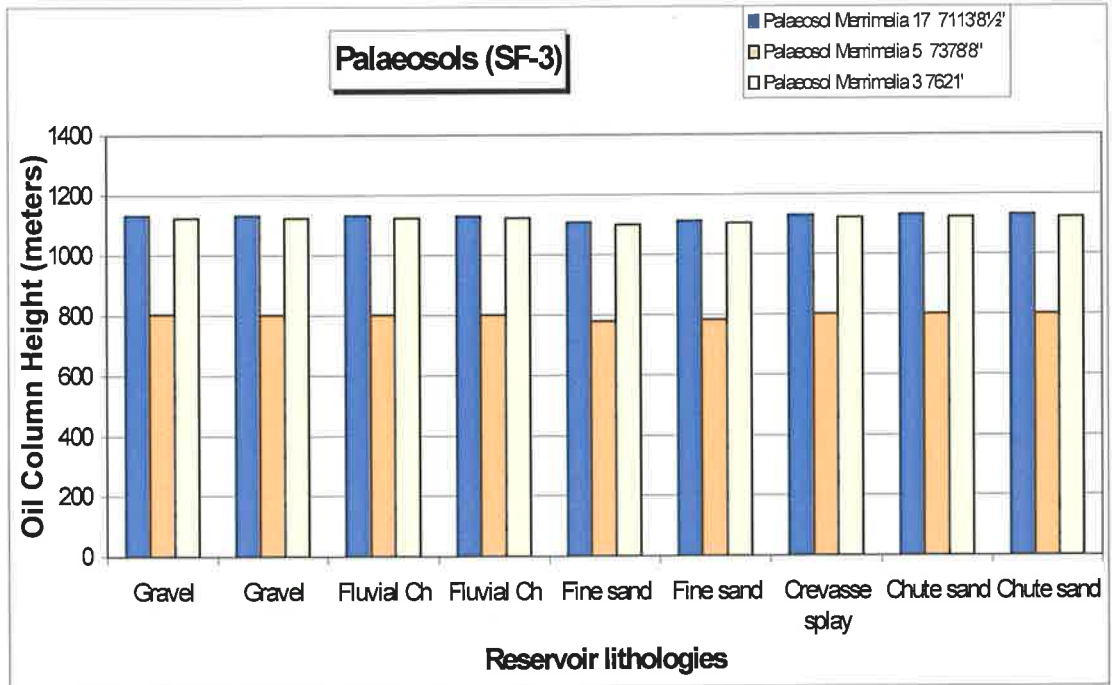
(a)



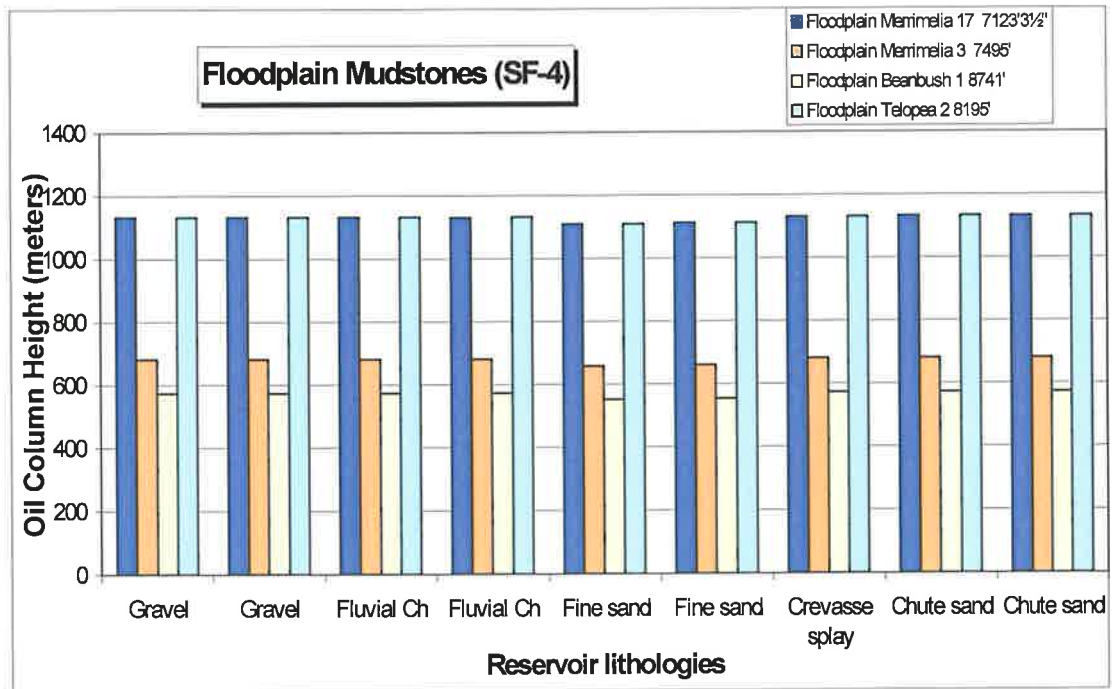
(b)

Figure 6.4 Calculated oil column heights held by (a) diagenetically-modified sandstones (SF-1) and (b) lacustrine mudstones (SF-2) versus various reservoir lithologies.





(c)



(d)

Figure 6.4 Calculated oil column heights held by (c) palaeosols (SF-3) and (d) floodplain mudstones (SF-4) versus various reservoir lithologies.

tension (5 dynes/cm for oil and 25 dynes/cm for gas), while the higher values represent hydrocarbon column heights calculated using the highest interfacial tension (21 dynes/cm for oil and 35 dynes/cm for gas). Seal capacity is directly proportional to interfacial tension; therefore the calculated oil and gas column heights are lower when low interfacial tension values are used and higher when high interfacial tension values are used.

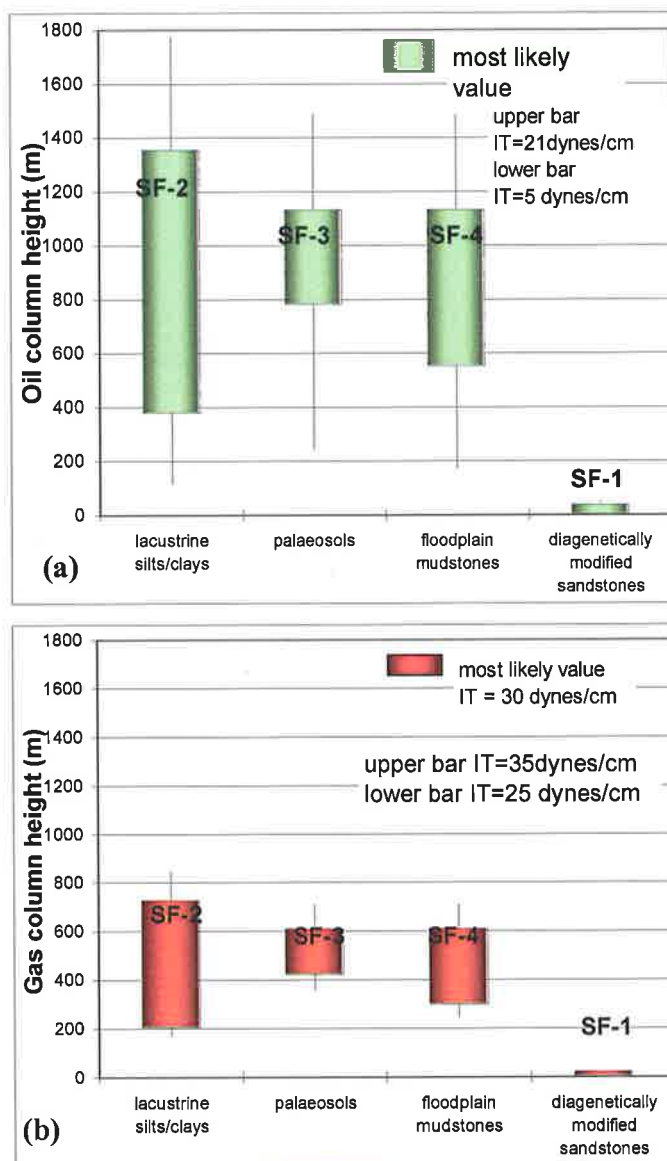


Figure 6.5 Seal capacity results. (a) Range of maximum oil column height held by each sealing lithology (including varying interfacial tensions). (b) Range of maximum gas column height held by each sealing lithology (including varying interfacial tensions).

## 6.8 SUMMARY

The seal capacities of the four sealing lithofacies identified within the Triassic sediments are ranked. The lacustrine fine-grained sediments have the best sealing capacity. They are followed by the palaeosols and fluvial mudstones holding back the same hydrocarbon column heights. The diagenetically-modified fluvial sandstones have the lowest seal capacity.

### **SF-2: Lacustrine mudstones**

380 – 1353m (oil); 204 – 727m (gas)

### **SF-3: Palaeosols**

781 – 1132m (oil); 420 – 609m (gas)

### **SF-4: Floodplain mudstones**

552 – 1132m (oil); 297 – 608m (gas)

### **SF-1: Diagenetically-modified fluvial sandstones**

2 – 37m (oil); 1 – 20m (gas)

## **CHAPTER SEVEN**

### **EVALUATION OF SEAL POTENTIAL**

#### **7.1 INTRODUCTION**

Evaluation of seal potential comprises calculation of the capacity of a rock to hold back hydrocarbons (seal capacity), determination of the rock thickness and lateral continuity (seal geometry) and evaluation of the rock mechanical properties (seal integrity). Seal potential was quantitatively assessed and sealing lithologies were ranked relatively using a methodology developed by Kaldi and Atkinson (1997).

The capacity of each sealing lithofacies was detailed in chapter six. Seal geometry was determined using the following methodologies: wire line log analyses, lithostratigraphic correlation and mapping of sealing intervals. Seal integrity was qualitatively assessed using petrographic criteria and rock mechanics studies from literature analogs.

#### **7.2 SEAL GEOMETRY**

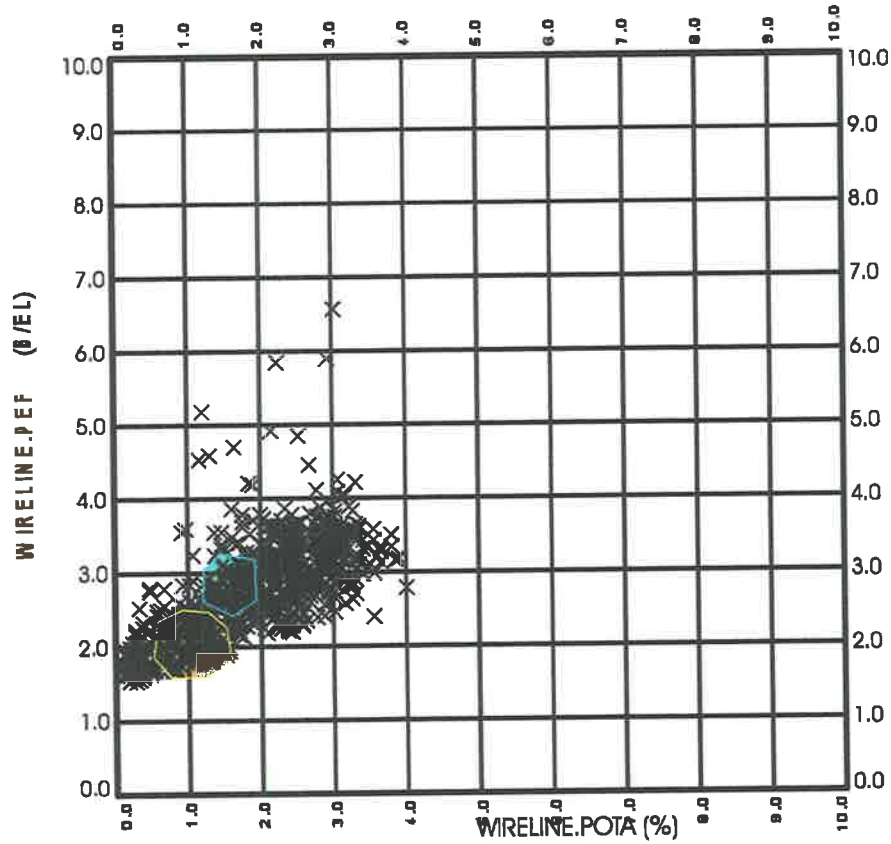
##### **7.2.1 Data availability**



Wireline logs from twenty-five wells that intersected the Nappamerri Group in the Merrimelia Field were interpreted for lithology discrimination. Cross-plots of gamma ray (GR) versus density (RHOB) logs or gamma ray (GR) versus sonic (DT) logs (where density logs were not available) were used to discriminate lithologies. In Merrimelia 15 PEF (photoelectric factor) and Pota (potassium % concentration) logs were available; therefore this well was further analyzed for kaolin cement identification.

##### **7.2.2 Mineral identification/lithology reconstruction from wireline logs**

Kaolin-cemented sandstones were identified in thin sections and on the litho-density (photoelectric factor) and natural gamma ray spectrometry logs (potassium %

**WIRELINE.PEF vs. WIRELINE.POTA Crossplot**  
**Well: MERRIMELIA-15**  
**2094.0 - 2222.9 METRES**



-  kaolin-cemented sandstones
-  sandstones without kaolin cement

**LEGEND**

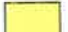




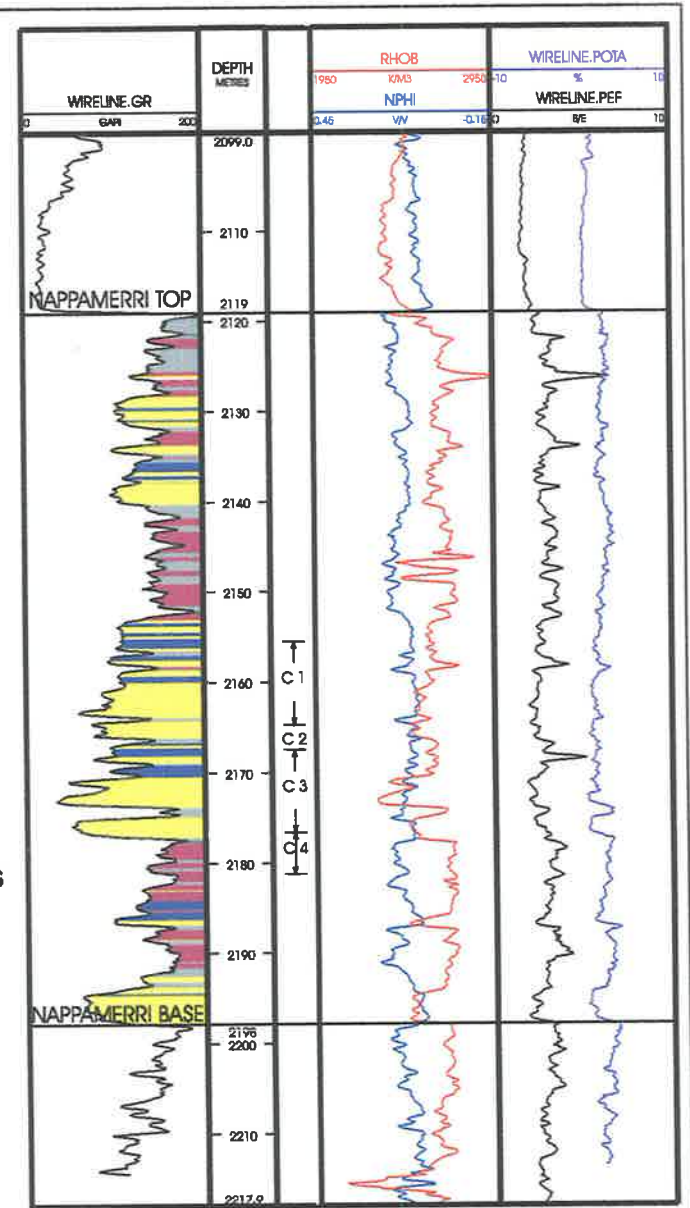
-  Fluvial sandstones
-  Palaeosols
-  Floodplain silts/shales
-  Lacustrine shales
-  Kaolin-cemented sandstones

Figure 7.1 Identification of kaolin-cemented sandstones from petrophysical cross-plots. Merrimelia 15



concentration) cross-plot. Results were extrapolated over the entire Nappamerri Group (Fig.7.1).

Gamma ray and density logs were cross-plotted to discriminate lithologies. Gamma ray values of 120 to 130 API were chosen to separate sands from silts and gamma ray values of 160 to 180 API were chosen to discriminate between silts and shales (Fig.7.2); the cut-off values vary little from log to log. Where density logs were not available, GR cut-off 130 API was used to discriminate sands from silts and shales (Fig.7.3).

Palaeosols comprise mainly silts with a significant amount of siderite. The high density of siderite ( $3.89 \text{ g/cm}^3$ ) results in the palaeosols having a high density log reading. Gamma ray versus density cross plots were calibrated using existing cores; as a result, the palaeosol facies were characterized with GR in the range of 130-180 API and  $\text{RHOB} > 2.7 \text{ g/cm}^3$  (Fig. 7.2). The cut-off values were calibrated against the logs of cored intervals for consistency with interpreted lithologies. Palaeosols were identified where no cores were available by calibrating existing cores with wireline logs and the results extrapolated beyond the available cores.

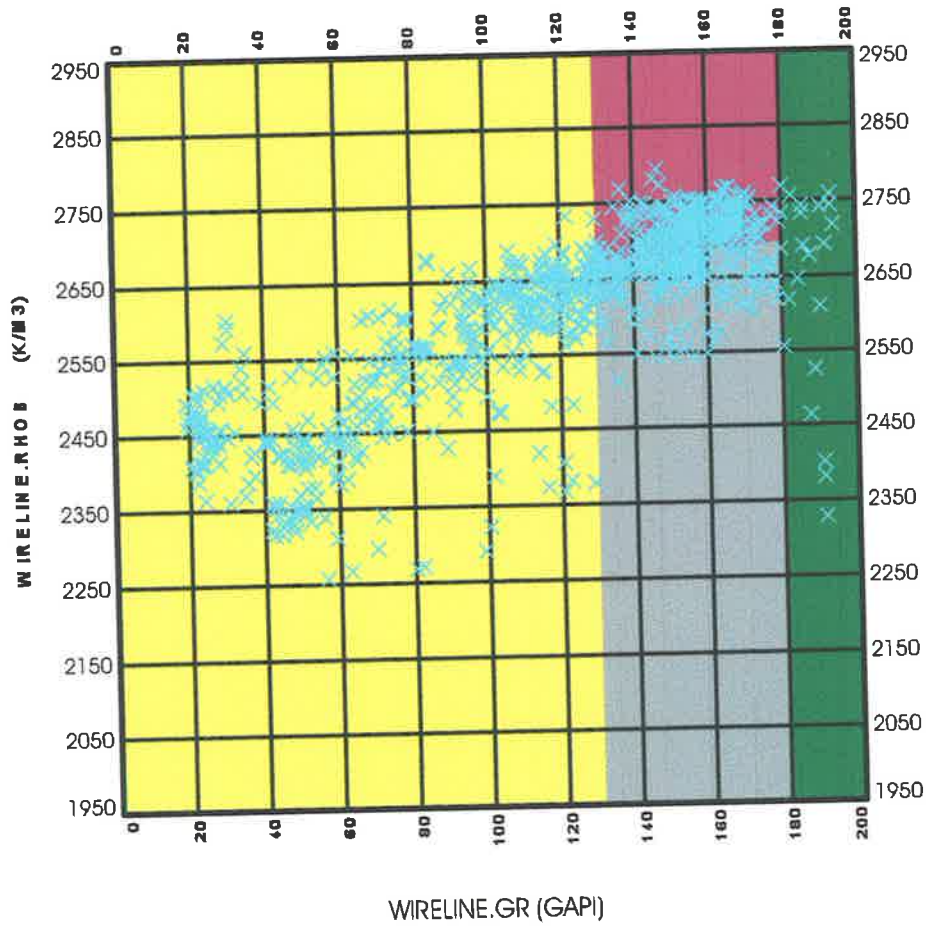
### 7.2.3 Correlation and mapping

Four lithostratigraphic cross-sections of Merrimelia Field are presented in Figs. 7.4 to 7.7). Nappamerri Group tops are taken from the PEPS Database (Appendix 7.1). PEPS-SA (Petroleum Exploration and Production System - South Australia) is a pc-based comprehensive relational database containing a wide range of technical data relevant to the petroleum industry (Petroleum Group, 2003).

Two major sand-rich "reservoir" successions and two sand-poor sealing intervals (Sealing interval 1 and Sealing interval 2) were correlated throughout the studied interval. The reservoir successions comprise stacked fluvial point bar deposits. The sealing intervals consist of floodplain mudstones and palaeosols.

Lithofacies assignments are based on log motifs and petrophysical cross-plots and displayed as gamma ray logs on the cross-section (Fig. 7.4 to 7.7). The floodplain mudstones and palaeosols have similar sealing capacities (Chapter six); therefore these two lithologies were combined for geometry estimation purpose. Their thicknesses were

WIRELINE.RHOB vs. WIRELINE.GR Crossplot  
 Well: MERRIMELIA-29  
 2092.8 - 2229.3 METRES



LEGEND

- Fluvial sandstones
- Palaeosols
- Floodplain silts/shales
- Lacustrine shales

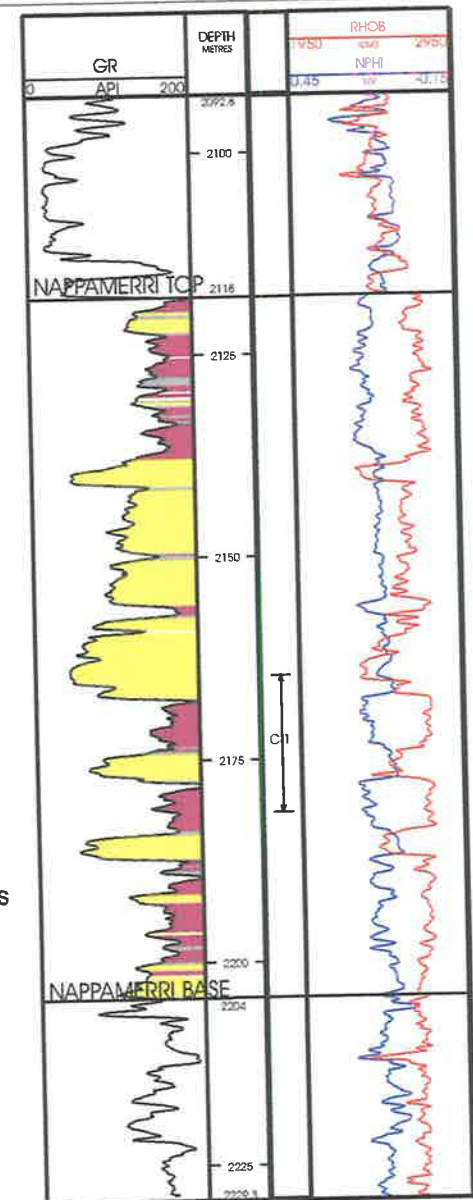
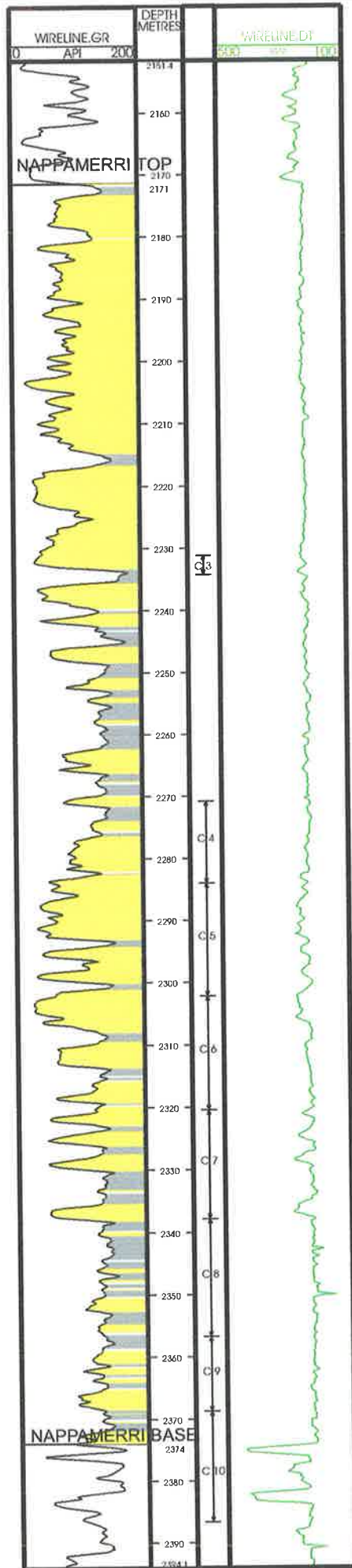


Figure 7.2 Lithology reconstruction from petrophysical cross-plots. Merrimelia 29



### LEGEND

- Fluvial sandstones
- Floodplain silts/shales

Figure 7.3 Separation of sands from silts and shales using a GR cut-off value of 130 API. Merrimelia 3



WELL	SHALE THICKNESS (M)			SHALE/TOTAL THICKNESS RATIO (%)		
	Seal Int 1	Seal Int 2	Napp Group	Seal Int 1	Seal Int 2	Napp Group
Merrimelia 1	17.25	18.5	50	53.1	35.6	35
Merrimelia 2	13	16.5	41.5	67.2	42.3	25.9
Merrimelia 4	29	23	57	61.7	54.1	42.8
Merrimelia 5	28.75	32.75	71.5	82.1	79.9	56.3
Merrimelia 6	11	8.5	24	71.6	43.6	26.9
Merrimelia 7	23	11.5	45	59.7	37.7	36
Merrimelia 8	7.25	27.75	38.75	85.3	77.9	56.9
Merrimelia 9	21.75	13.5	41.25	59.2	96.4	42.5
Merrimelia 10	13	14.75	31.25	64.2	100	45.95
Merrimelia 11	19	23.75	45	73.8	84.1	54.2
Merrimelia 12	0	25.75	39	0	85.8	54.2
Merrimelia 13	30.5	25.25	67	70.1	73.7	53.6
Merrimelia 14	29	21	54	69	68.3	45.4
Merrimelia 15	14.25	25.5	42.25	85.1	75	53.5
Merrimelia 17	29.5	6.75	52.75	66.3	38.6	42.2
Merrimelia 18	31.25	25.5	74.5	93.3	42.5	50
Merrimelia 20	28.5	33	77.25	70.8	84.1	58.5
Merrimelia 22	37.25	19.25	63.5	76.8	46.6	43.8
Merrimelia 23	12.5	16.75	34.7	92.6	77	59.7
Merrimelia 25	30.25	29	71.5	70.3	70.7	54.2
Merrimelia 29	24.5	17.75	45	75.4	88.75	52.3
Merrimelia 30	16.75	28.75	52.75	99.7	77.7	62.05
Merrimelia 31	7.75	20.5	30.25	86.1	69.5	48.8
Merrimelia 32	8.5	17	38.75	97.1	64.2	48.4

Table 7.1 Cumulative shale thickness (m) and shale/total thickness ratios (%) of the Sealing Intervals 1, 2 and the the Nappamerri Group.

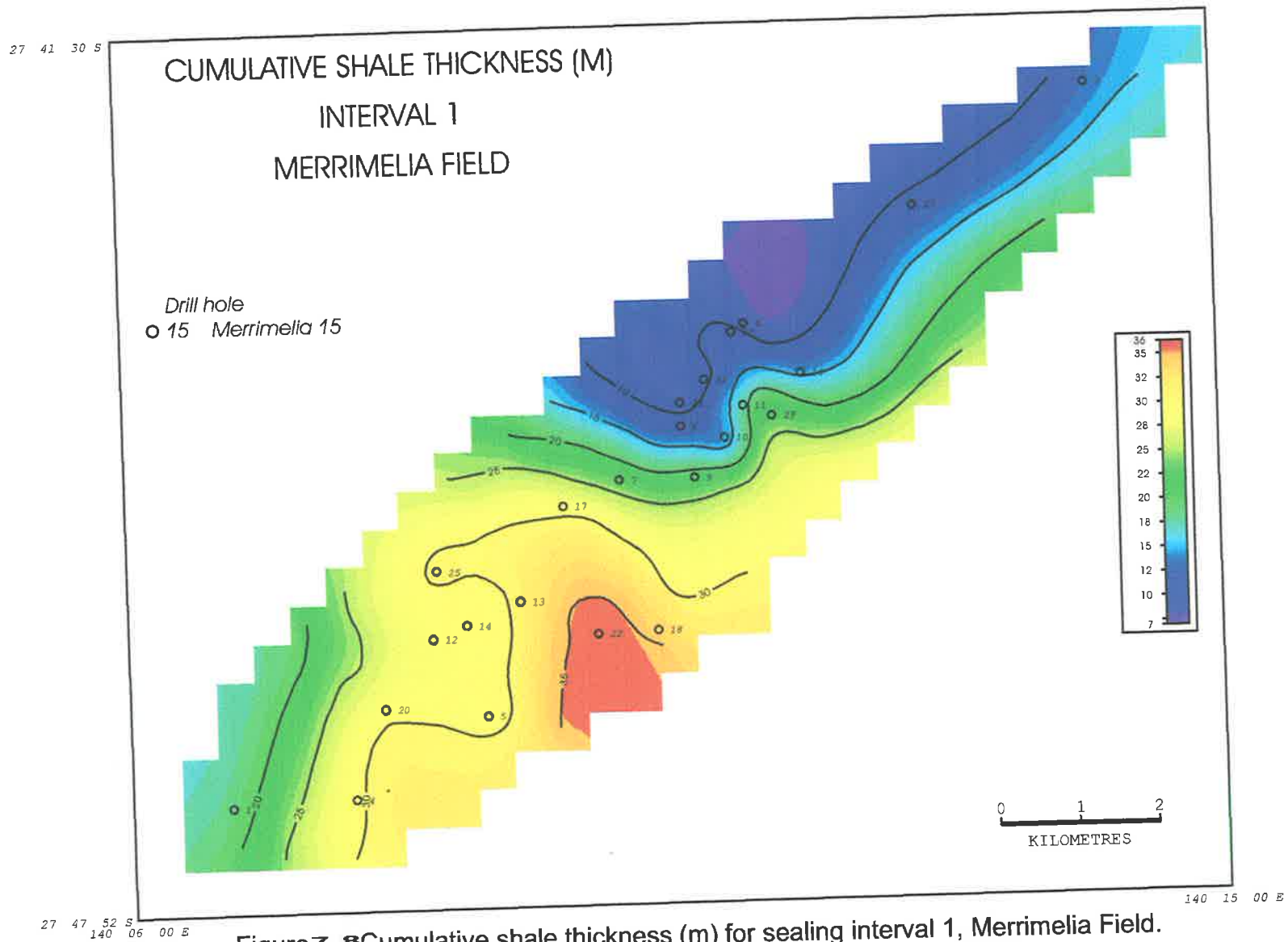


Figure 7.8 Cumulative shale thickness (m) for sealing interval 1, Merrimelia Field. The northern end of this field shows much less shale than the south and east.

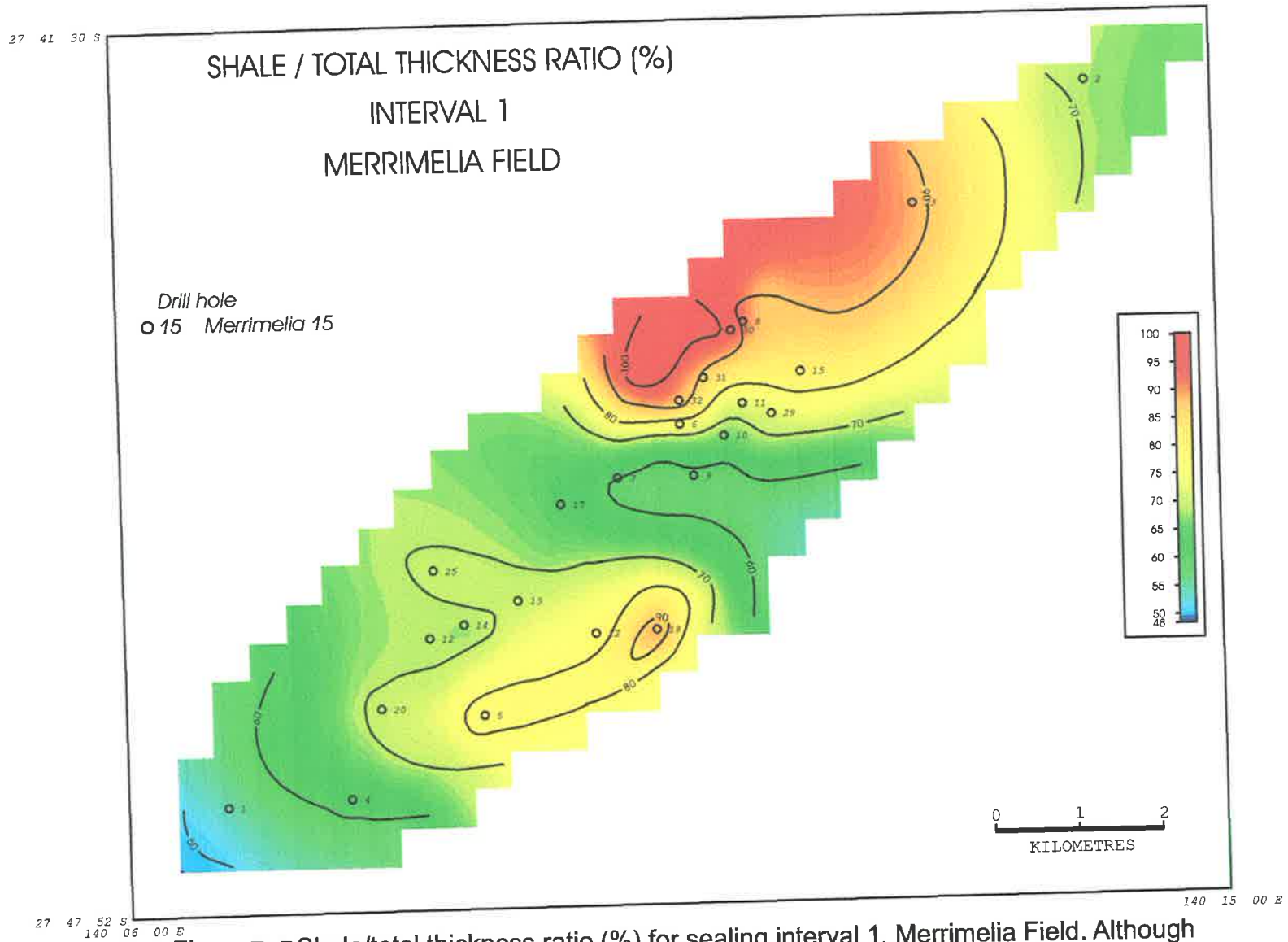


Figure 7. Shale/total thickness ratio (%) for sealing interval 1, Merrimelia Field. Although sealing interval 1 is thin in the northern part of the field, the shale content is very high.

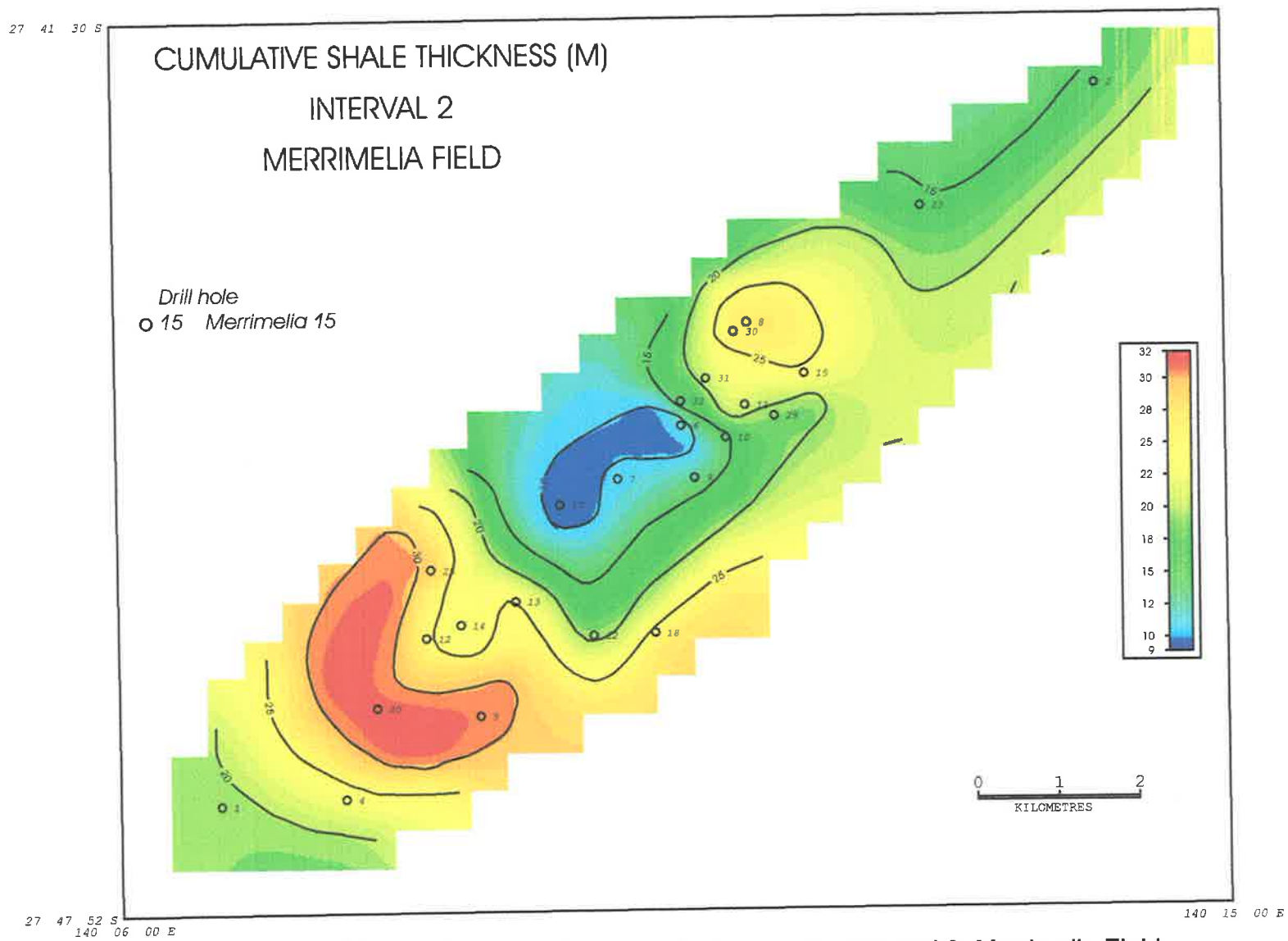
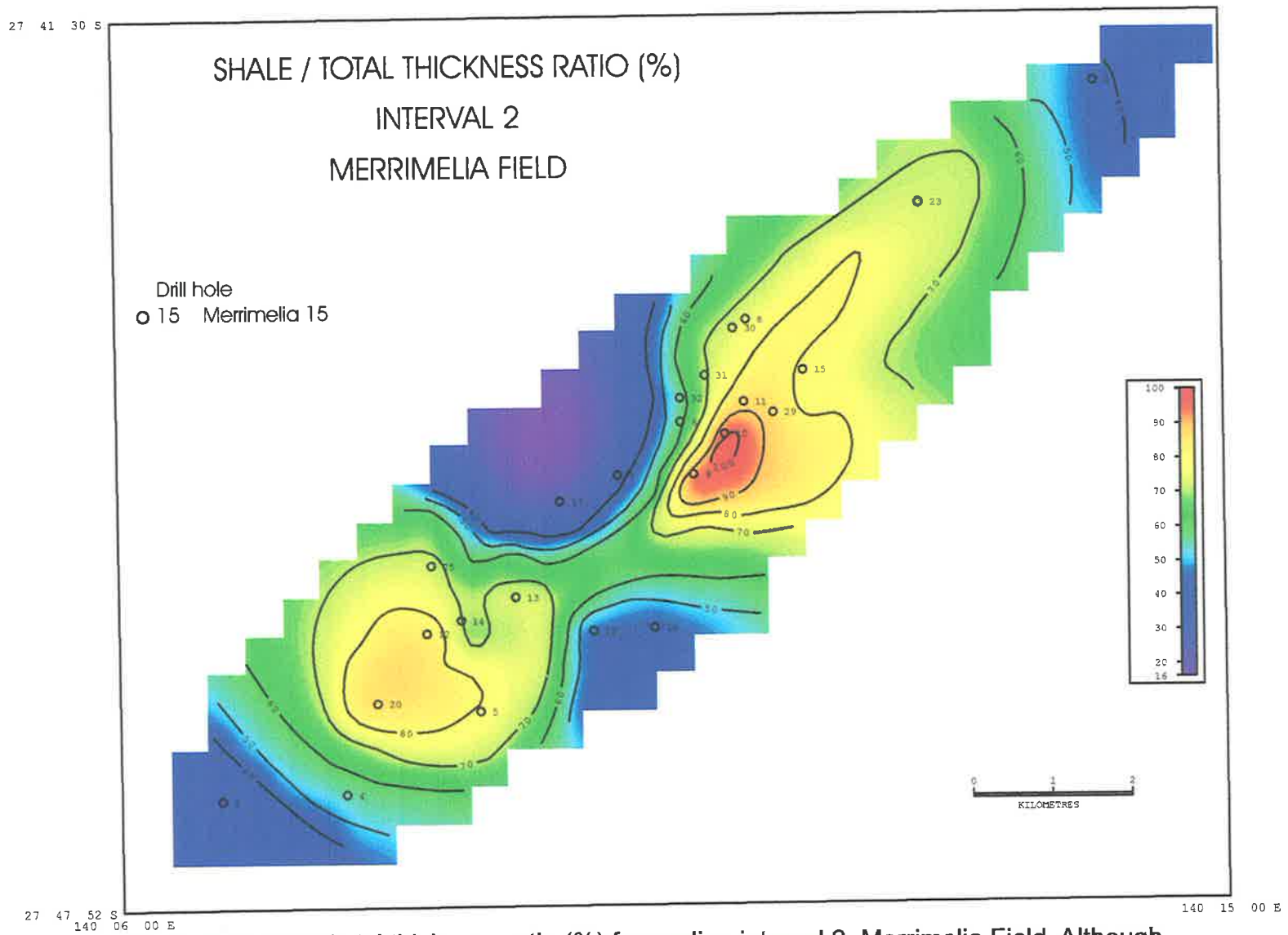


Figure 7.10 Cumulative shale thickness (m) for sealing interval 2, Merrimelia Field. The southern end of this field shows more shale than the central and northern part.



**Figure 7-11** Shale/total thickness ratio (%) for sealing interval 2, Merrimelia Field. Although sealing interval 2 is thin in the central and northern part of the field, the shale content is very high.

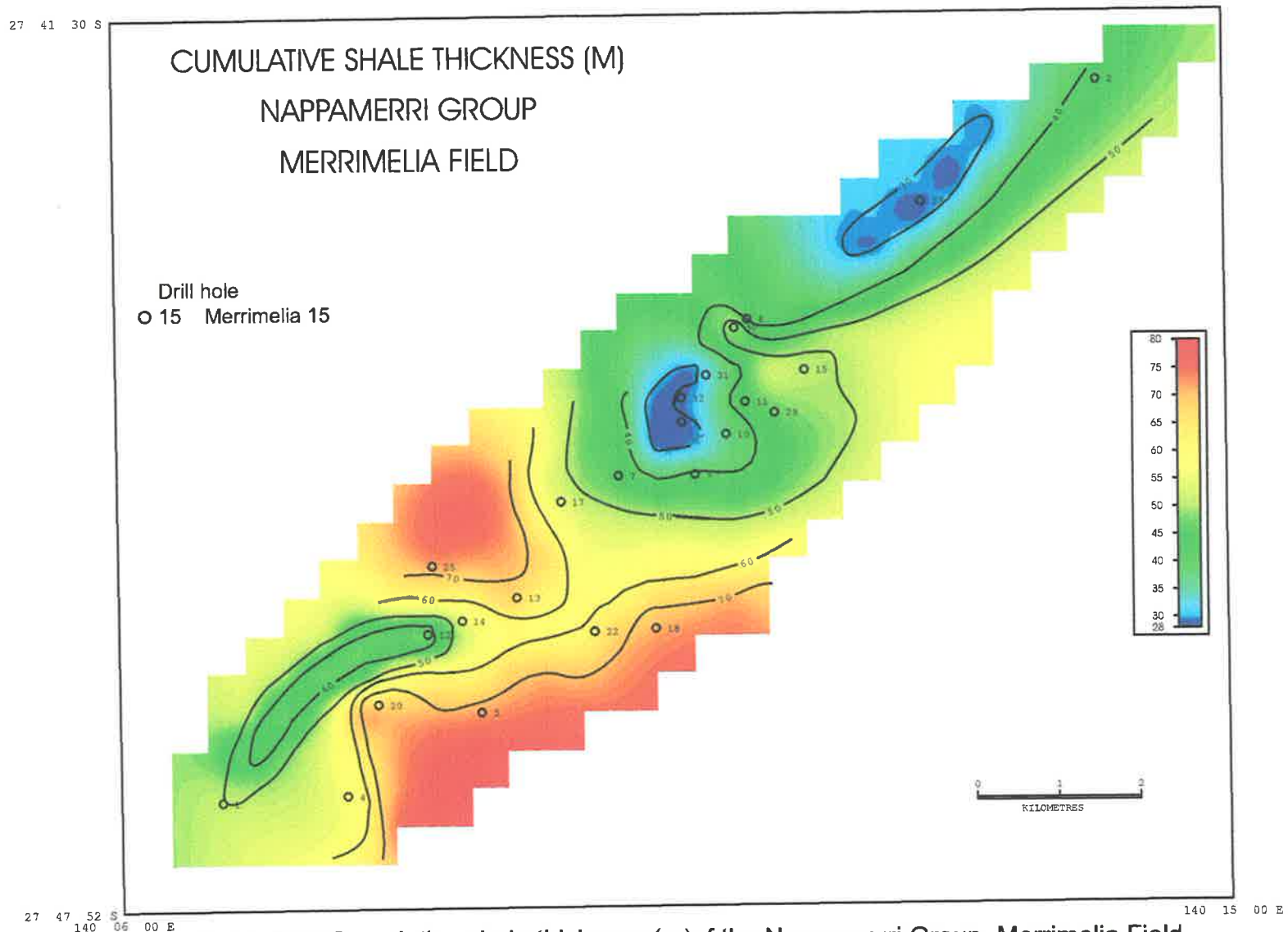


Figure 7.12 Cumulative shale thickness (m) of the Nappamerri Group, Merrimelia Field. The southern end of this field shows more shale than the northern part.

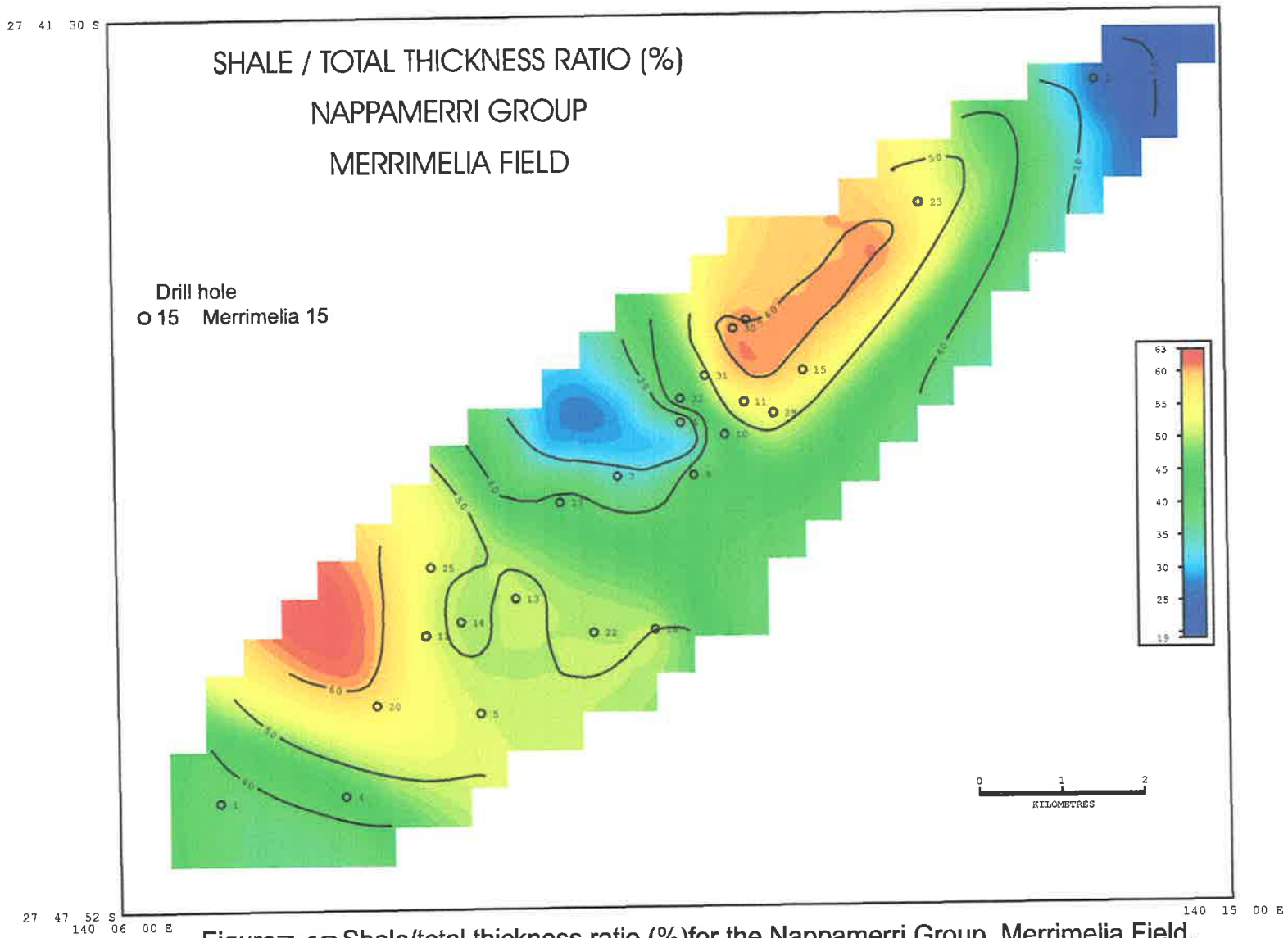


Figure 7.13 Shale/total thickness ratio (%) for the Nappamerri Group, Merrimelia Field. The shale content is low because of two sandy units within the Nappamerri Group.

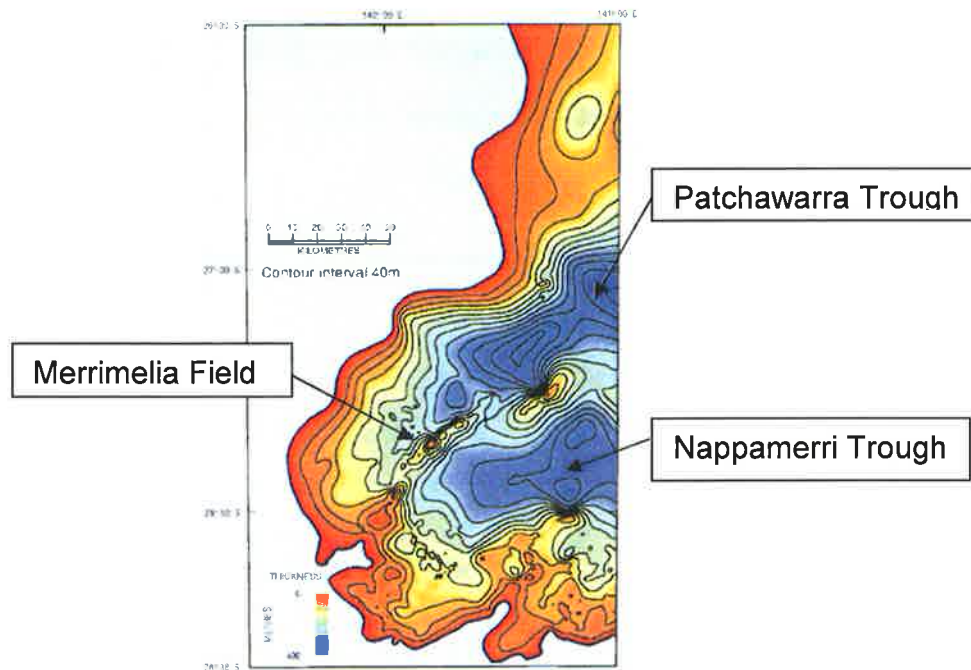


Figure 7.14 Isopach map of the Nappamerri Group (Alexander et al., 1998), showing the thickening of Nappamerri Group toward adjacent troughs (Nappamerri and Patchawarra Trough).

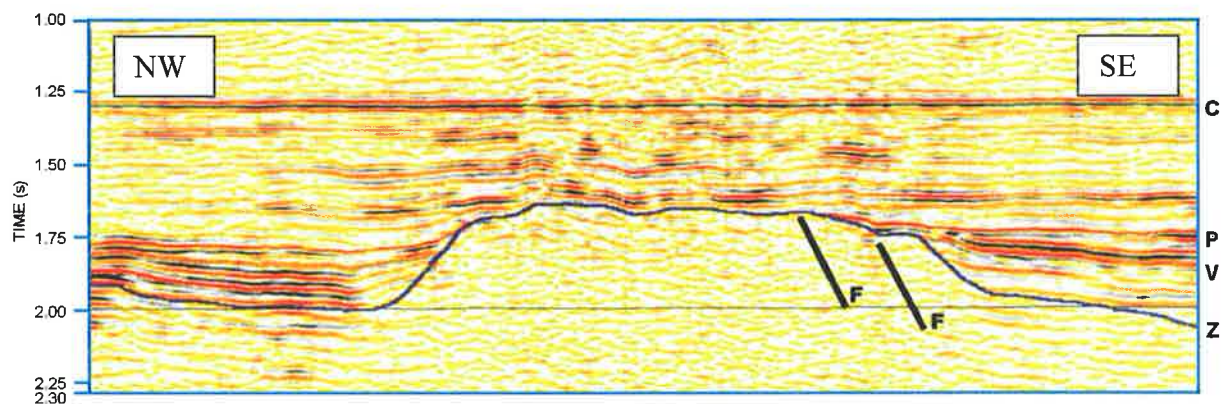


Figure 7.15 Merrimelia Ridge and adjacent troughs, with the C seismic horizon (Early Cretaceous as datum near top of the Cadna-Owie Formation) (Gravestock, and Jensen-Schmidt, 1998), showing Merrimelia Ridge dipping toward southeast; Nappamerri Group is situated above the P seismic horizon (Late Permian, near top of the Toolachee Formation). F = fault.



measured and results grouped to represent the shale thickness of Sealing Interval 1, Sealing Interval 2 and the whole Nappamerri Group (Table 7.1). Maps of seal thickness and seal thickness to total thickness ratios were produced to assess the thickness, quality and lateral distribution of sealing intervals (Figs. 7.8 to 7.13). The interpretation was biased to match the structural regional trend that shows the thickening of Nappamerri Group towards Nappamerri and Patchawarra Troughs (Fig. 7.14) and the eastward dipping trend of the Merrimelia Ridge (Fig. 7.15).

#### **7.2.4 Thickness and areal extent of SF-1 Diagenetically-modified sandstones**

Sandstones with kaolin cement preferentially develop at the top of point bar successions. Their spatial distribution is unpredictable and laterally limited by the point bar dimensions. The thickness and vertical occurrence of the kaolin-cemented layers were evaluated by extrapolating the area identified in photoelectric factor and potassium concentration cross-plot as kaolin cemented sandstones throughout Nappamerri Group. The thickness of SF-1 is generally less than 1m (Fig.7.1) and is confined to the top of point bars.

#### **7.2.5 Thickness and areal extent of SF-2 Lacustrine mudstones**

Lacustrine sediments are deposited in abandoned channels, also named ox-bow lakes and in shallow lakes on the floodplain. Such deposits, as revealed from cores and from wireline logs, are thin, around 1m and locally up to 1.5 m. This lithofacies could not be correlated from well to well. Hence, it is probably not areally extensive (ie. Merrimelia 22, Fig. 7.7).

#### **7.2.6 Thickness and areal extent of SF-3 and SF-4 Palaeosols and Floodplain mudstones**

Two structural trends were observed over the Merrimelia Field:

- The shale thickness of the sealing intervals is greater towards structurally lower areas: to the southeast into the Patchawarra Trough and to the northwest into the Nappamerri Trough (Fig. 7.8, Fig. 7.10 and Fig. 7.12).

In the northeastern part of Merrimelia structure, the Nappamerri Group sits unconformably on the basement (Pre-Permian, Innamincka Formation) or on a thin interval of Merrimelia Formation, which make up the crest of the Merrimelia Ridge. In the southwestern part of Merrimelia Field, the eastern flank of Patchawarra Trough, the Nappamerri Group is conformable on the Toolache Formation (Fig. 7.4). The lithostratigraphic correlations from Fig. 7.4 and Fig. 7.5 show a thickening of the sealing intervals, particularly of the Sealing Interval 2 (Sealing Interval 1 was eroded), towards the southwest (Patchawarra Trough). The sealing intervals are thinner in wells situated on the Merrimelia Ridge (Fig. 7.6) than those located towards Patchawarra Trough (Fig. 7.7). Also, the lithostratigraphic correlation from Fig. 8.6 shows that the sealing intervals are thicker towards the east (Nappamerri Trough) than on the Merrimelia Ridge.

Upflank, in crestal areas, where the subsidence is lower, the units are thinner and the fluvial sequences are mainly stacked point bar sands (Fig. 7.16). Downflank, where local subsidence is slightly greater, there is an increase of floodplain mudstones. Isolated channels or crevasse splay sands are also present, but there is a decrease in sand body interconnection. It is concluded that downflank, the sealing intervals are thicker than on the crestal areas. In the lower areas, sand bodies are isolated, conferring good sealing quality to the study intervals as suggested by Stuart *et al* (1988).

- Sealing intervals contain more shale on crestal areas (Merrimelia Ridge) than in the lower areas (Fig. 7.9, 7.11 and 7.13).

Comparison of the shale/total thickness ratio maps with the equivalent interval isopach maps shows that over the crest of the structure, high shale ratios occur in thinner intervals. This suggests that the main channel system followed paleotopographic lows and avoided the highs within the basin.

Based on two-dimensional, theoretical simulation studies of meandering channel belts, sandstone bodies are essentially isolated if they represent less than 50% of the succession (Fielding & Crane, 1987; Allen, 1978). The degree of connectedness grows very rapidly as the proportion of sand bodies increase above 50% (Fig. 7.17).

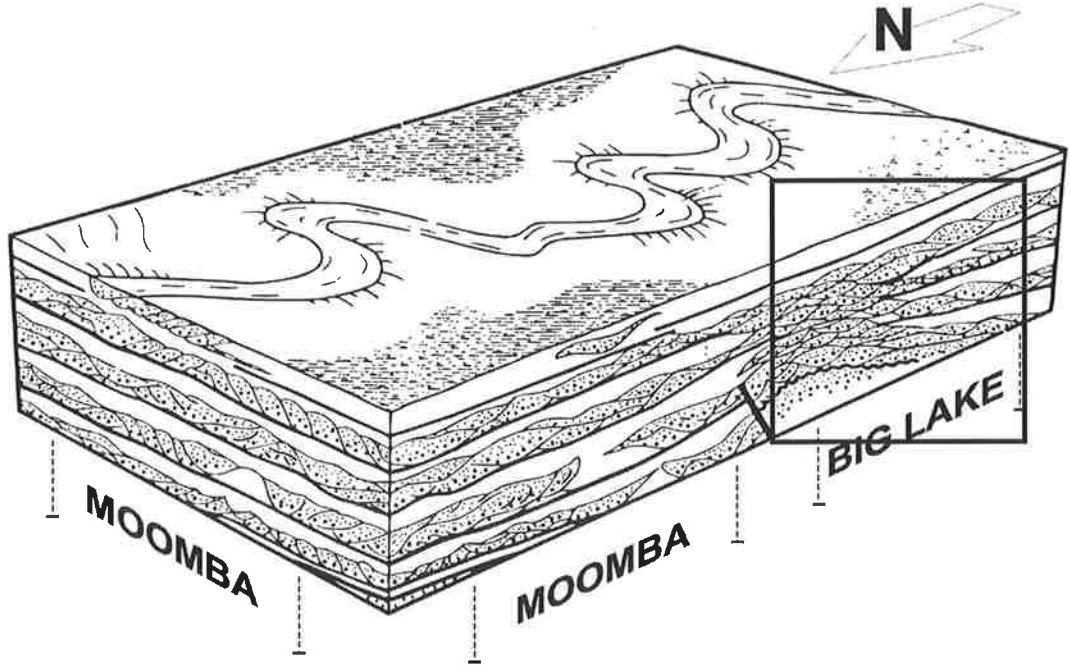


Figure 7.16 Schematic palaeogeographic representation of Big Lake and Moomba areas (Stuart *et al.*, 1988).

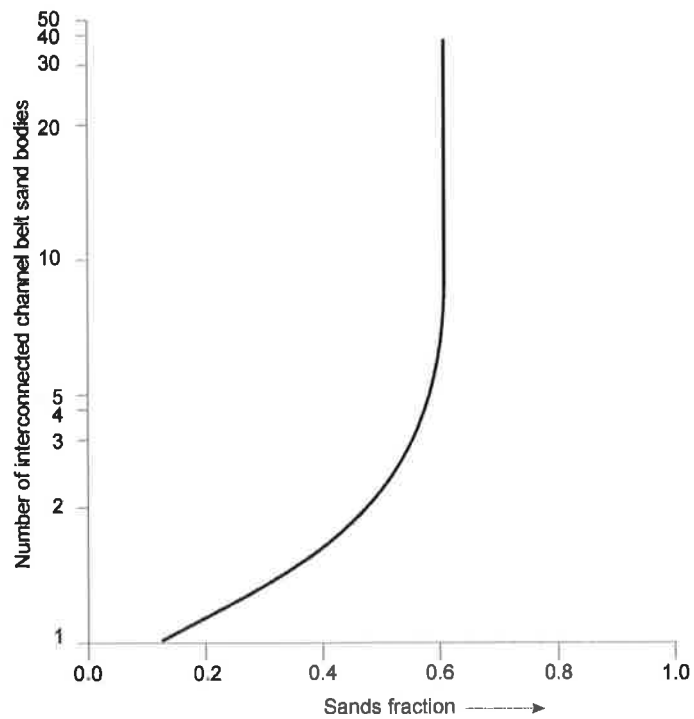


Figure 7.17 Sandstone body interconnection as a function of the net sands fraction of the sequence (Crane, 1982).

Cox and Knackstedt (1999), using percolation theory, have numerically modeled the relative proportions of isolated, dangling and backbone elements for simulated growth of simple fault networks. Their results indicate that the critical strain required to reach the percolation threshold is substantially lower in a three-dimensional percolation model than in a two-dimensional model. If extrapolated in terms of sand body intersection, the above conclusion provides a higher probability of connection in 3D than in the 2D example. Therefore, the 50% sand percentage required for sand body connectivity in 2D can be lowered in a 3D model.

It can be concluded that more than 50% shale/total thickness ratio (less than 50% sand) means a low probability of sand-body interconnectivity, therefore good sealing properties. In shale over total thickness ratio maps more than 50% is considered as a cut-off for seal effectiveness. Applying this to the study area:

- Shale/total thickness ratios of Sealing Interval 1 vary from 50% to 100% over the entire Merrimelia Field, with relatively higher values on crestal areas, to the west of the Merrimelia Ridge, than in lower areas, on the eastern flank of Patchawarra Trough (Fig. 7.9). At that time, many flooding events deposited floodplain mudstones, which, during sub-areal exposure, developed pedogenetic features. Sand deposition consists of isolated fluvial channels or crevasse splays.
- During the time of Sealing Interval 2 deposition, shale to total thickness ratios of 50 to 100% are found in only two restricted areas: on the Merrimelia Ridge and in the Patchawarra Trough, with relatively higher values on crestal areas (Fig. 7.11). Where the meander belt approaches the central Merrimelia Field, it is characterised by less than 50% shale/total thickness ratios.
- Within the Nappamerri Group, areas with more than 50% shale/total thickness ratios areas are located in the northwestern part of Merrimelia Ridge and towards Patchawara Trough (Fig. 7.13).

If a lower cut-off for sand body interconnection is considered (eg. 30%), shale/total thickness ratio for an effective seal becomes 70%. In this case, the areas where Sealing Interval 1 and Sealing Interval 2 become effective are smaller and restricted to the Merrimelia Ridge and Patchawarra Trough. This study only considers the area near the

Merrimelia Field. A different distribution of sealing and reservoir facies might be expected in areas that were subsiding more rapidly during sedimentation.

### 7.3 SEAL INTEGRITY

Rock mechanical properties of sealing lithologies were qualitatively evaluated using the petrographic criteria and the diagram (Fig. 7.18) for seal integrity (Brown, in Kaldi, 2000).

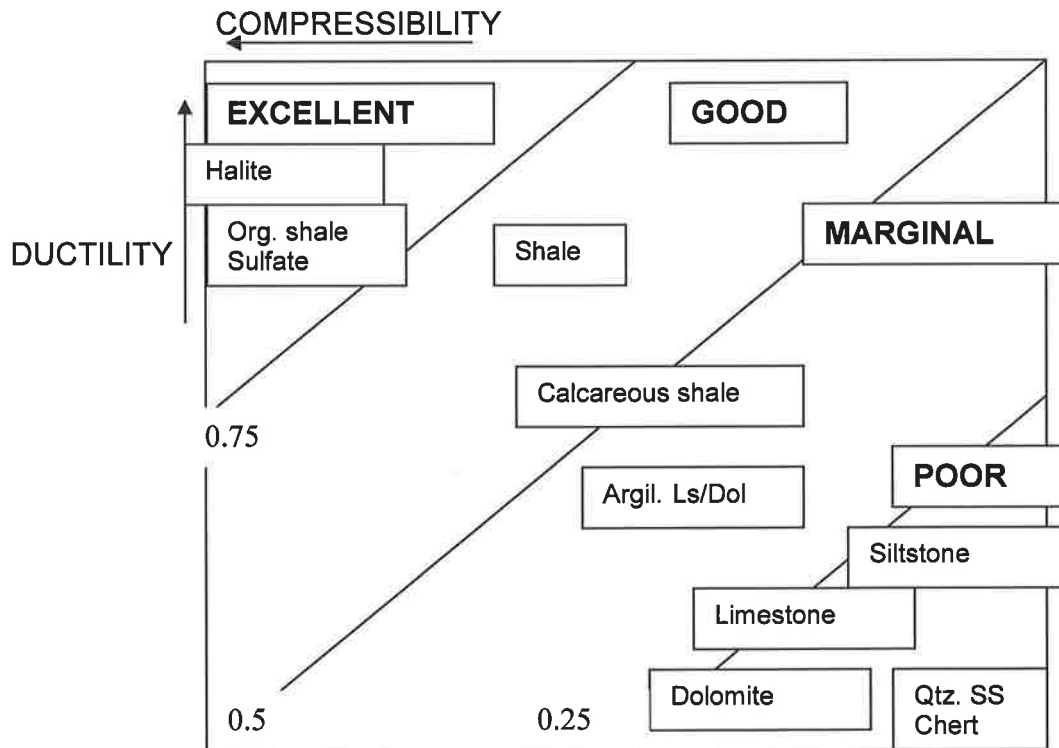


Figure 7.18 Seal integrity (after Brown, in Kaldi, 2000).

The SF-1 lithofacies, the kaolin cemented sublithic to lithic sandstones fall into the quartz-rich end member of Brown's classification. No fractures were visible in cores or thin sections. This lithofacies was assessed as having "poor" seal integrity. The SF-2 lithofacies (lacustrine mudstones) comprise silty claystones and clayey siltstones; these are generally rocks with high clay content. No fractures were observed within this lithofacies. SF-2 is thus considered having "good" seal integrity. The palaeosols (SF-3) and floodplain mudstones (SF-4) lithofacies are silty claystones, clayey siltstones or muddy lithic sandstones. The clay content is very high in palaeosols that are characterised by the presence of carbonates, usually siderite. Water escape structures

and rootlets disturb the depositional bedding and micro-fractures were observed in palaeosols in thin sections. The seal integrity of SF-3 and SF-4 is considered to be "marginal".

## 7.4 SEAL POTENTIAL. RISK ASSESSMENT

Seal potential was assessed quantitatively. The quality of each sealing attribute was represented by a value between zero and one. The final seal potential was calculated by cross multiplying the individual parameters of capacity, geometry and integrity. The sealing lithologies were ranked relatively using the methodology developed by Kaldi and Atkinson (1997).

### 7.4.1 Seal capacity

The highest seal capacity is in SF-2, lacustrine mudstones (up to 1353 m of oil or 727 m of gas). The next highest column could be held by SF-3 and SF-4, the palaeosols and floodplain mudstones (up to 1132 m of oil or 608 m of gas). SF-4, the diagenetically modified fluvial sandstones hold the lowest hydrocarbon column, up to 37 m of oil or 20 m of gas. SF-2, SF-3 and SF-4 have seal capacities that exceed any published accounts of empirical hydrocarbon columns in the Cooper Basin. On this basis, a probability for seal capacity for SF-2, SF-3 and SF-4 is set equal to 1. A relatively lower probability (0.5) is assigned as the adequacy of seal capacity of SF-1.

The hydrocarbon column heights present in the Merrimelia Field wells (Fig. 7.19 and Fig. 7.20) are actually smaller than measured seal capacities. Empirical observations indicate that the palaeosols and floodplain mudstones hold only up to 13 m oil column and 14 m gas column (Fig. 7.20), while the lacustrine facies hold approximately 3 m oil column. In Telopea Field, log evaluation suggests 9 m of net oil pay is sealed by diagenetically modified sandstones. The reason for this may be attributed to tertiary hydrocarbon migration path variations, subtle structural spill points or subseismic structural permeability (fracture) leakage.

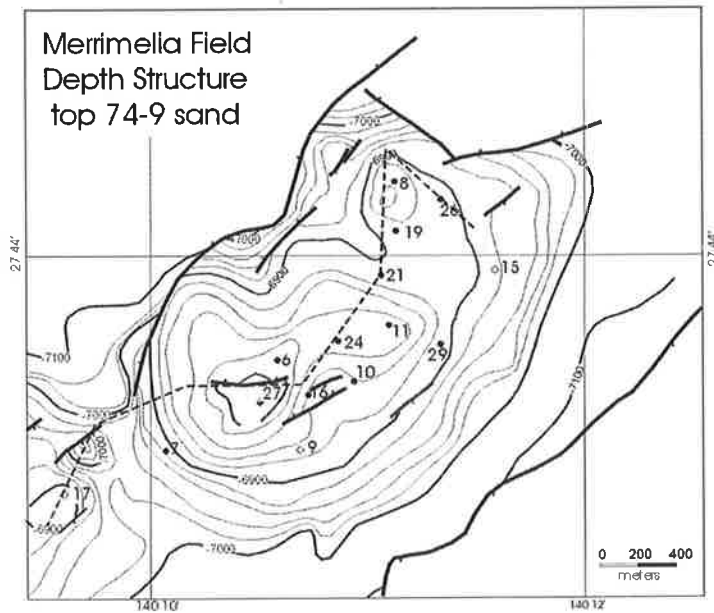


Figure 7.19 Merrimelia Field Depth Structure Top 74-9 Sand, Mid Nappamerri Formation (Siffleet, 1992).

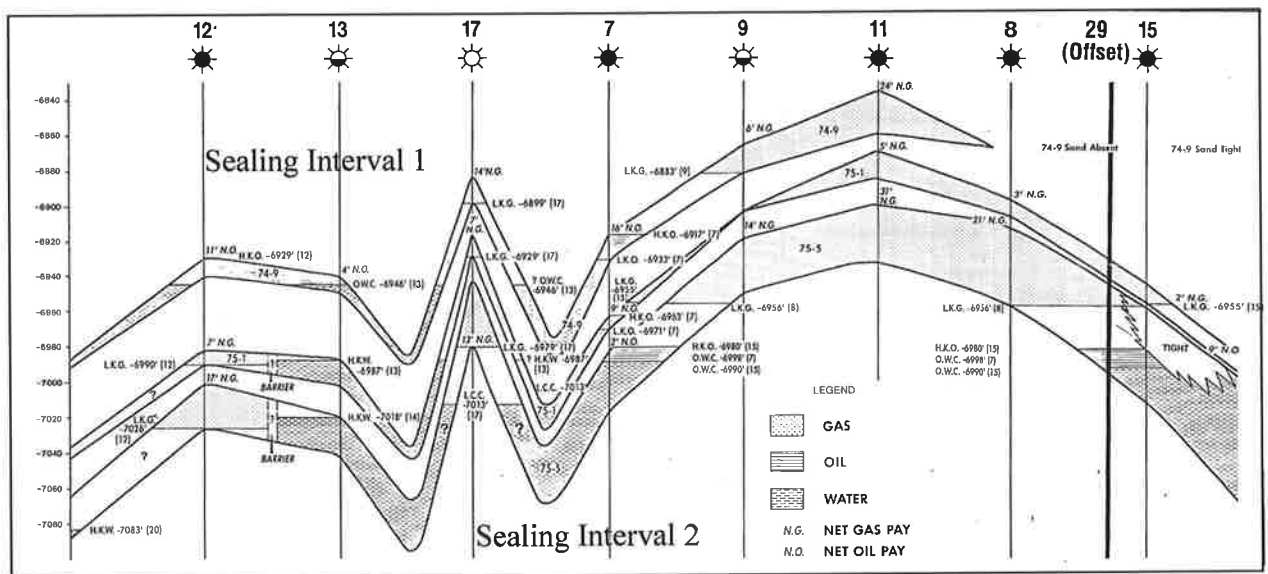


Figure 7.20 Schematic cross section through Merrimelia Field, showing main sealing intervals and hydrocarbon distribution, modified after Burgess, 1990. Location of cross section is marked on Fig. 7.19.

### 7.4.2 Seal geometry

A minimum 15 m cumulative shale thickness having greater than 50% shale/total thickness ratio is needed for any seal to be effective in this area. Fifteen meters was chosen as this is the seismically resolvable thickness below which the displacement of small-scale faults cannot reliably be observed. Resolution is a function of the speed of the seismic wave and its frequency. High frequency gives the best resolution but the high frequency energy input is most readily attenuated with depth. Similarly, the speed of the waveform increases with depth. Consequently resolution diminishes with depth. The wells in Merrimellia field penetrate the sealing intervals between 2100 and 2200 m. The velocity of the seismic wave through the rocks at this depth is about 4000 m/s. If 30 Hz frequency of the seismic wave is considered, then resolution can not exceed 33 m. 15 m resolution might be expected by thin bed tuning.

For both conditions to be achieved, the shale/total thickness ratio maps (Figs. 7.9, 7.11 and 7.13) were superimposed on the thickness maps (Figs. 7.8, 7.10 and 7.12). Shale thickness of Sealing Interval 1 is equal to or greater than 15 m over an area representing 66% of the Merrimelia Field. Shale thickness of Sealing Interval 2 is equal to or greater than 15 m in 75% of the Merrimelia Field, while shale thickness of Nappamerri Group is more than 15 m over 100% of the Merrimelia Field.

If more than 50% shale/total thickness is considered the cut-off for seal effectiveness, then, Sealing Interval 1 is effective over the entire Merrimelia structure, while Sealing Interval 2 only over 66% of the structure. The Nappamerri Group has more than 50% shale/total thickness ratios over an area that represents half of the Merrimelia structural closure. SF-3 and SF-4 are ranked for seal geometry as follows:

	Thickness	Areal extent (Seal area/Structure area)
Sealing Interval 1	0.66	1
Sealing Interval 2	0.75	0.66
Nappamerri Group	1	0.5

Kaolin-cemented sandstones (SF-1) have an unpredictable distribution, being developed only at the top of point bars. Their presence, extent and continuity in such deposits depends of many factors such as: the presence of silica and aluminum-rich solutions to



precipitate kaolin, the preservation of those layers from erosion and the number and vertical or lateral interconnectivity of the point bar successions (Fig. 7.21). Therefore, the probability that SF-1 will have an adequate areal extent is low (approximately 0.1). The probability that SF-1 will have an adequate (eg. effective) thickness is likewise low (0.1).

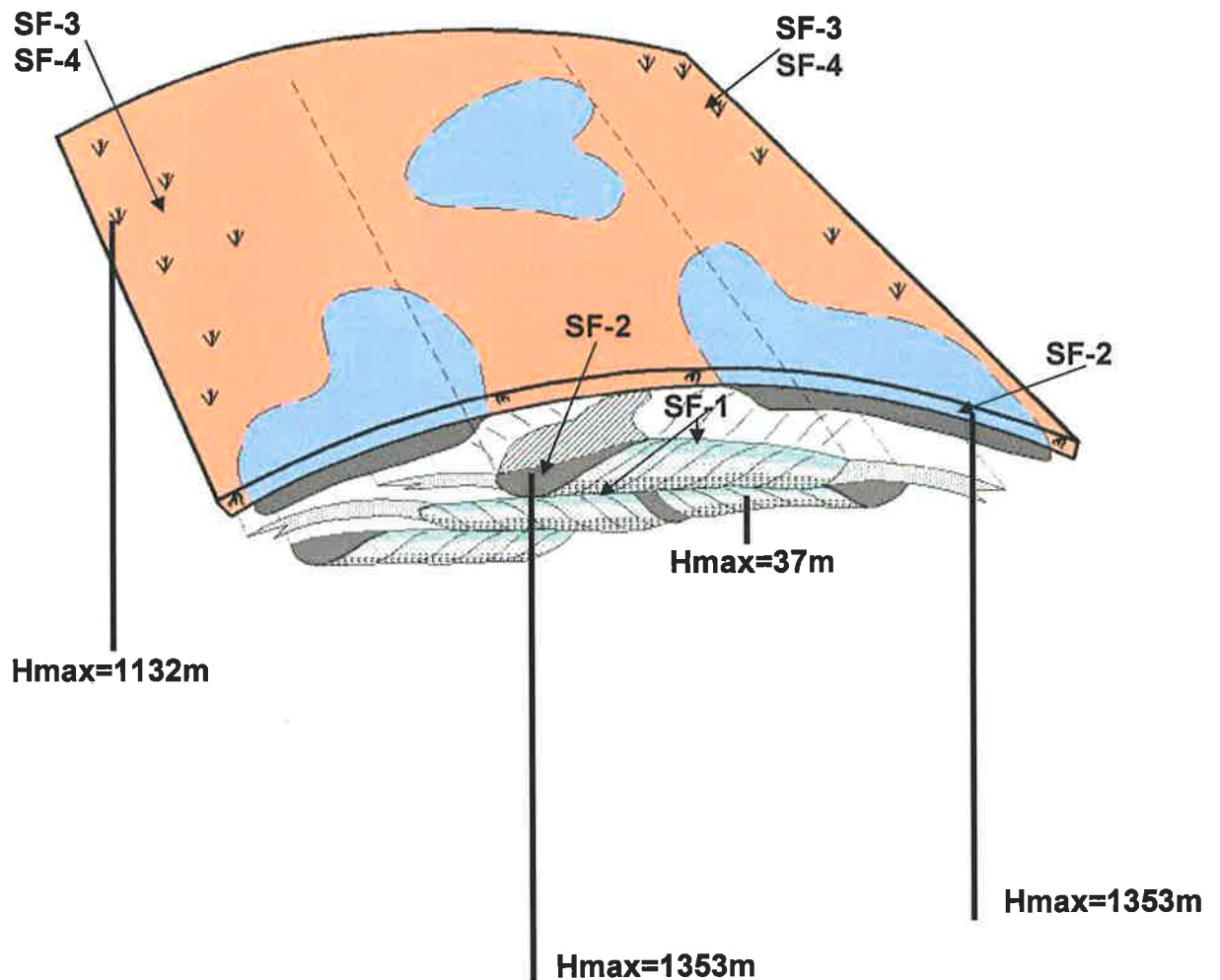


Figure 7.21 Schematic illustration of the sealing facies geometry and their relative seal capacity (not to scale). SF-1 extent is from approximate 100m to less than 1Km. SF-2 extent is less than 1Km. SF-3 and SF-4 extent is from approximate 500m to more than 10Km.

SF-2 has a restricted distribution occurring in isolated floodplain and channel abandonment lakes deposits (Fig. 7.21). Consequently, SF-2 is assigned values of 0.1 for thickness and 0.2 for lateral extent.

### 7.4.3 Seal integrity

The qualitative evaluation of seal integrity was estimated as follows:

SF-1: poor integrity 0.2

SF-2: good integrity 0.6

SF-3 and SF-4: marginal integrity 0.4

## 7.5 SEAL POTENTIAL RANKING

The relative potential of identified seals was derived as the serial product of components: seal capacity x seal integrity x seal thickness x seal areal extent (Fig. 7.22).

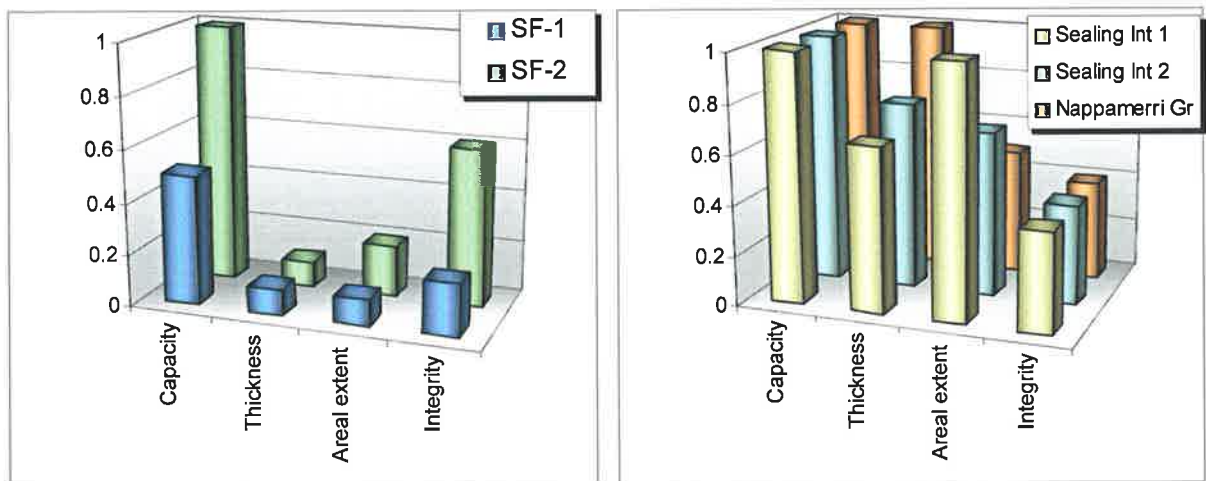


Figure 7.22 (a) The relative seal potential of diagenetically modified sandstones (SF-1) and lacustrine silts and clays (SF-2). (b) The relative seal potential of palaeosols (SF-3) and floodplain mudstones (SF-4).

The best sealing potential is assigned to SF-3 and SF-4:

Sealing Interval 1	$1 \times 0.66 \times 1 \times 0.4 = 0.264$	(ie. likelihood of sealing = 26%)
Sealing Interval 2	$1 \times 0.75 \times 0.66 \times 0.4 = 0.198$	(ie. likelihood of sealing = 20%)
Nappamerri Group	$1 \times 1 \times 0.5 \times 0.4 = 0.2$	(ie. likelihood of sealing = 20%)

The sealing potential of SF-2 is considerably less than SF-3 and SF-4:

$$1 \times 0.1 \times 0.2 \times 0.6 = 0.012 \quad (\text{ie. likelihood of sealing} = 1.2\%)$$

SF-1 has the lowest sealing potential of all the facies investigated:

$$0.5 \times 0.1 \times 0.1 \times 0.2 = 0.001 \quad (\text{ie. likelihood of sealing} = 0.1\%)$$

## 7.6 SUMMARY

The thickness and lateral extent of sealing lithologies were evaluated. Shale thickness in sealing intervals 1 and 2, representing palaeosols (SF-3) and floodplain mudstones (SF-4) is greater towards the structurally lower areas. The shale content in these intervals is higher on the crest of the Merrimelia Ridge. A greater than 50% shale/total thickness ratio extends over the entire Merrimelia Field for Sealing Interval 1. For Sealing Interval 2 and the Nappamerri Group as a whole, a ratio of more than 50% occurs only in two restricted areas: the Merrimelia Ridge and the eastern flank of the Patchawarra Trough. The thickness of diagenetically modified sandstones (SF-1) is less than 1 m and its areal distribution is unpredictable. The lacustrine facies (SF-2) is less than 1.5 m thick and is only locally developed. The distribution of shale thickness and its quality depends on the width of the fluvial system which is in turn controlled by the structure, sediment supply and rate of accommodation.

The seal potential of the four lithofacies identified in the study area was ranked and the best seal potential exists within SF-3 and SF-4. These lithofacies, grouped as two sealing intervals, are thick (7 to 36 m cumulative shale thickness), extend over most of the Merrimelia Field and have high measured seal capacities (1132 m for oil or 609 m for gas). Although SF-2 has the highest seal capacity (1353 m for oil and 727 m for gas) and homogeneity, it has a lower seal potential due to its low thickness (1.5 m) and

localized extent. SF-1 has the lowest seal potential. This lithofacies is thin (1 m), has unpredictable distribution, poor rock mechanical properties and the lowest seal capacity (37 m for oil and 20 m for gas). The rock mechanical properties were not measured in this study, but are inferred from other studies (Stearns and Friedman, 1972).

## CHAPTER EIGHT

### CONCLUSIONS

This study describes the main reservoir and sealing lithologies from the Triassic strata (Nappamerri Group and Cuddapan Formation) in the Cooper Basin, focusing mainly on the seal potential. A total of forty-seven samples were selected from Merrimelia, Telopea and Beanbush Fields. The methodology used comprises lithofacies analysis, X-ray diffraction analysis, thin section petrography, scanning electron microscopy, mercury injection capillary pressure analysis, wireline logs analysis, lithostratigraphic correlation, mapping and risk analysis.

Based on lithofacies identification and position in the sedimentary sequence, four depositional facies of sealing rocks (SF-1 to SF-4) and five depositional facies of reservoir rocks (RF-1 to RF-5) are identified. They are: SF-1, diagenetically-modified sandstones; SF-2, lacustrine mudstones; SF-3 palaeosols; SF-4, floodplain mudstones; RF-1, gravels; RF-2, fluvial channel sands; RF-3, chute sands; RF-4, crevasse splay sands and RF-5, fine-grained sands from the top of point bars.

The texture, petrographic and mineralogical composition of each sedimentary environment together with the diagenetic events and their relative timing were described. Primary porosity, secondary porosity and microporosity are recognized in the reservoir lithologies. The most important factors for porosity preservation are the amount of matrix, and the quartz overgrowth cementation. Rock composition, cementation and pore throat size distribution control permeability. Pore throat size and distribution were used in evaluating the sealing/reservoir rock properties.

Depositional environment and post-depositional diagenesis are the main factors that determine the quality of the seals and reservoirs. Depositional environment is reflected in the texture and composition of a rock. The petrographic composition and the nature of fluids that circulate through the rock pore system influence its diagenesis. Diagenesis includes cementation, mineral alteration and compaction. These control pore and pore throat sizes and their interconnectivity.

Seal capacity was evaluated by calculating the maximum hydrocarbon column height that a lithology can support. Mercury injection capillary pressure analyses were obtained by measuring the pressure needed to inject mercury into the rock pore throats, using a Micromeritics Autopore 9410 mercury injection porosimeter. The threshold pressure was determined from mercury injection capillary pressure curves. The best seal capacity was found in the lacustrine mudstones (SF-2) that can hold a maximum hydrocarbon column height of 1353m for oil or 727m for gas. The second best seal capacity was found in palaeosols (SF-3) and floodplain mudstones (SF-4) that can hold a maximum of 1132m oil and 608m gas. The diagenetically modified fluvial sandstone (SF-1) had the lowest seal capacity with a maximum hydrocarbon column height of 37m oil or 20m gas.

Seal geometry comprises thickness and areal extent of the seal. Seal geometry was determined from lithostratigraphic correlation of the sealing lithofacies and by comparison with depositional analogs from the literature. Having the same seal capacity and integrity, the palaeosols (SF-3) and the floodplain mudstones (SF-4) were grouped in two intervals: Sealing Interval 1 and Sealing Interval 2. The thickness and areal extent of these two sealing intervals were analysed in Merrimelia Field. Shale thickness in sealing intervals 1 and 2 varies between 7 and 36m and is greater towards the structurally lower areas. The shale content in these intervals is higher on the crest of the Merrimelia Ridge. A greater than 50% shale/total thickness ratio extends over the entire Merrimelia Field for Sealing Interval 1. For Sealing Interval 2 a ratio of more than 50% occurs only in two restricted areas: the Merrimelia Ridge and the eastern flank of the Patchawarra Trough. The thickness of diagenetically modified sandstones (SF-1) is less than 1 m and its areal distribution is unpredictable. The lacustrine facies (SF-2) is less than 1.5 m thick and is only locally developed.

Seal integrity was evaluated from rock mechanics studies from literature analogs and the petrographic analysis. SF-2 was assessed as having good seal integrity, followed by SF-3 and SF-4 with marginal seal integrity and SF-1 with poor seal integrity.

The sealing potential of each of the sealing lithologies was derived as a product of the three individual components: seal capacity x seal geometry x seal integrity. The seal potential of the four lithofacies identified in the study area was ranked and the

best seal potential exists within SF-3 and SF-4. These lithofacies, grouped as two sealing intervals, are thick (7 to 36 m cumulative shale thickness), extend over most of the Merrimelia Field and have high measured seal capacities (1132 m for oil or 609 m for gas). Although SF-2 has the highest seal capacity (1353 m for oil and 727 m for gas) and homogeneity, it has a lower seal potential due to its low thickness (1.5 m) and localized extent. SF-1 has the lowest seal potential. This lithofacies is thin (1 m), has unpredictable distribution, poor rock mechanical properties and the lowest seal capacity (37 m for oil and 20 m for gas).

In terms of hydrocarbon exploration, the seal study has shown two things:

- The palaeosol (SF-3) and floodplain (SF-4) facies can effectively seal a hydrocarbon accumulation. On the scale of a local structure, these facies are laterally extensive enough to provide a local seal. This is proven by the number of gas and oil pockets on the Merrimelia Ridge exploited by exploration companies.
- The lateral distribution of the sealing facies over a broad area is likely to be discontinuous. Convoluted migration pathways exist through the entire formation. Proof of this exists in the occurrence of oil and gas at all levels in the Nappamerri Group, even though the formation itself has very little source rocks. Further proof is provided by the occurrence of oil and gas in formations above the Nappamerri Group. These hydrocarbons were derived in part from the Permian below.

The project aimed to evaluate the seal potential of the poorly studied Nappamerri Group, also called the “regional seal“, in the Cooper Basin. The project was designed to address a market failure identified by Petroleum Group, PIRSA: the regional seal characteristics and facies of the Nappamerri Group have not been previously studied in detail.

This study has shown that the Nappamerri Group contains a variety of lithofacies with different seal potentials and can no longer be regarded as a simple regional seal, but must be treated as a series of discrete intraformational seals.

More understanding of the seal potential of this unit will enable better risking of current prospects and plays as well as identification of potential new play types and prospects.

---

**REFERENCES**

Alexander, E.M., Gravestock, D.I., Cubitt, C., Chaney, A., 1998. Lithostratigraphy and environments of deposition. *In: Gravestock, D.I., Hibburt, J.E. and Drexel, J.F. (Eds.), Petroleum Geology of South Australia. Volume 4, Cooper Basin*, p. 69 - 115.

Alexander, E., 1989. Core logs description. (unpublished).

Allen, G.P. and Lang, S., 2000. Siliciclastic Reservoir Sedimentology, *Course Notes prepared for the National Centre for Petroleum Geology and Geophysics, University of Adelaide*, chapter 3, p. 14 - 32.

Allen, J.R.L., 1978. Studies in fluvial sedimentation: an exploratory quantitative model for the architecture of avulsion-controlled alluvial sites. *Sedimentary Geology*, v. 21, p. 129 - 147.

Apak, S.N., Stuart, W.J. and Lemon, N. M., 1993. Structural-stratigraphic development of the Gidgealpa-Merrimelia-Innaminka Trend with implication for petroleum trap styles, Cooper Basin, Australia. *Australian Petroleum Exploration Association Journal*, v. 33, p. 94 - 104.

Apak, S.N., Stuart, W.J., Lemon, N. M., and Wood G., 1997. Structural evolution of the Permian-Triassic Cooper Basin, Australia: relation to hydrocarbon trap styles. *AAPG Bulletin*, 81(4): 533 - 554.

Atkinson C.D., 1986. Tectonic control on alluvial sedimentation as revealed by an ancient catena in the Capella Formation (Eocene) of northern Spain. *In: Wright, V.P. (Ed.) Palaeosols: their recognition and interpretation*. Blackwell Scientific, Oxford, p. 139 - 179.

Battersby, D.G., 1976. Cooper Basin oil and gas fields. *Australasian Institute of Mining and Metallurgy*, Monograph 7, p. 321 - 370.

Boult, P.J., Theologu, P.N. and East, R., 1993, End of grant report, Energy Research and Development Corporation, Project number 1541, Quantification of Hydrocarbon migration and entrapment, unpublished, 75 p.



- Boult, P.J., 1996. An investigation of reservoir/seal couplets in the Eromanga Basin; implications for petroleum entrapment and production. Development of secondary migration and seal potential theory and investigation techniques. *University of South Australia. Ph.D. thesis* (unpublished).
- Boult, P.J., Theologu, P.N., Foden, J., 1997. Capillary seals within the Eromanga Basin, Australia: implications for exploration and production. *In: Surdam, R.C. (Ed.), Seals, traps and the petroleum system. AAPG Memoir, v. 67, p. 143 - 167.*
- Bowering, O.J.W., 1982. Hydrodynamics and hydrocarbon migration-a model for the Eromanga Basin. *APEA Journal, 22: 227 - 236.*
- Brown, T.M. and Kraus, M.J., 1987. Integration of channel and floodplain suites, I. Development of sequence and lateral relations of alluvial palaeosols. *J. Sediment. Petrol. 57: 587 - 601.*
- Burgess, L., 1990. Merrimelia Field Schematic cross section through Merrimelia 12, 13, 17, 7, 9, 11, 8&15 Mid Nappamerri Formation. *In: Allen, P., 1993. Merrimelia 29 Well Completion Report, Santos Limited* (unpublished).
- Cartmill, J.K., 1976. Obscure nature of petroleum migration and entrapment: *AAPG Bulletin, v. 60, p. 1520 - 1530.*
- Channon, G.J., Wood, G.R., 1989. Stratigraphy and hydrocarbon prospectivity of Triassic sediments in the Northern Cooper Basin, South Australia. *South Australia. Department of Primary Industries and Resources. Confidential Envelope, 8126* (unpublished).
- Cox, S.F. and Knackstedt, 1999. Ore genesis in fracture controlled hydrothermal systems: percolation theory approaches. *PACRIM, p. 639 - 642.*
- Crane, R.C., 1982. A computer model for the architecture of avulsion-controlled alluvial suites: Unpublished Ph.D. Dissertation, University of Reading, 548 p.
- Dunlop, E.C., Browne, N.V., Tadiar, E.F., 1992. Depletion of gas reservoirs by molecular diffusion - a case study. *APEA Journal, 32, p. 369 - 390.*

Fielding, C.R., Crane, R.C., 1987. An application of statistical modelling to the prediction of hydrocarbon recovery factors in fluvial reservoir sequences. *Recent Developments in fluvial sedimentology. Contribution from the Third International Fluvial Sedimentology Conference*, p. 321 - 327.

Folk, R.L., 1968. Petrology of sedimentary rocks: Austin, Texas, Hemphill's Book Store, p. 170.

Foster, C.B., 1982. Spore-pollen assemblages of the Bowen Basin, Queensland (Australia): their relationship to the Permian/Triassic boundary. *Review of Palaeobotany and Palynology*, v. 36, p. 165 - 183.

Galloway W.E. and Hobday, D.K., 1983. Terrigenous clastic depositional systems: applications to petroleum, coal, and uranium exploration, 383 p. (Springer-Verlag, New York, Inc.).

Gravestock, D.I., Alexander, E.M., Morton, J.G.G and Sun, X., 1998. Reservoirs and Seals. In: Gravestock, D.I., Hibburt, J.E. and Drexel, J.F. (Eds.), *Petroleum Geology of South Australia. Volume 4, Cooper Basin*, p. 157 - 179.

Gravestock, D.I. and Jensen-Schmidt, B., 1998. Structural Setting. In: Gravestock, D.I., Hibburt, J.E. and Drexel, J.F. (Eds.), *Petroleum Geology of South Australia. Volume 4, Cooper Basin*, p. 47 - 67.

Gravestock, D.I. and Morton, J.G.G., 1994. Geology of the Della Field, a perspective on the history of the Cooper Basin. *APEA Journal*, 24: 266 - 277.

Gray, R.J. and Roberts, D.C., 1984. A seismic model of faults in the Cooper Basin. *Australian Petroleum Exploration Association Journal*, v. 24, p. 421 - 428.

Grier, S.P. and Marschall, D.M., 1993, Reservoir Quality. In: Morton-Thompson, D. and Woods, A.M. (Eds.), *Development Geology Reference Manual, AAPG Methods in Exploration Series, No.10*, p. 275-277.

Grund, R., 1966. The glaciogene sediments of Coopers Creek Basin. Unpublished. B.Sc. (Hons.) thesis, University of Adelaide, Australia, 197 p.

Hamlin, H.S., Dutton, S.P., Seggie, R.J. and Tyler, N., 1996. Depositional controls on reservoir properties in a braid-delta sandstone, Tirrawarra oil field, South Australia. *AAPG Bulletin*, 80(2): 139-156.

Hardy, R. and Tucker, M., 1988. X-ray powder diffraction of sediments. *In*: Tucker, M. (Ed), *Techniques in Sedimentology*. Blackwell Scientific Publications. p. 191 - 228.

Heath, R., McIntyre, S. and Gibbins, N., 1989. A Permian origin for Jurassic reservoired oil in the Eromanga Basin. *In*: O'Neil, B.J. (Ed.), *The Cooper and Eromanga Basins, Australia*. Proceedings of the Cooper and Eromanga Basins Conference, Adelaide, 1989. Petroleum Exploration Society of Australia, Society of Petroleum Engineers, Australian Society of Exploration Geophysicists (SA Branches), p. 405 - 416.

Hillis, R.R., Sandiford, M., Coblenz, D.D. and Zhou, S., 1997. Modelling the contemporary stress field and its implications for hydrocarbon exploration. *Exploration Geophysics*, 28 (1, 2): 88 - 93.

Hollingsworth, R.J.S., 1989. The exploration history and status of the Cooper and Eromanga Basins. *In*: O'Neil, B.J. (Ed.), *The Cooper and Eromanga Basins, Australia*. Proceedings of the Cooper and Eromanga Basins Conference, Adelaide, 1989. Petroleum Exploration Society of Australia, Society of Petroleum Engineers, Australian Society of Exploration Geophysicists (SA Branches), p. 3 -13.

Hough, E.W., M.J. Rzasa and B.B. Wood, 1951. Interfacial tensions of reservoir pressures and temperatures, apparatus and the water-methane system. *AIME Petroleum Transactions*, vol. 192, p 57 – 60.

Kaldi, J.G., 2000. Assessing reservoir quality and seal potential. Short course notes, *AAPG International Convention* Bali, Indonesia.

Kaldi, J.G. and Atkinson, C.D., 1993. Seal potential of the Talang Akar Formation, BZZ area, offshore NW Java, Indonesia. Proceedings. Indonesian Petrol. Assoc. 22<sup>nd</sup> Ann. Conv., Jakarta, Indonesia, vol.1, p. 373-394.

Kaldi, J.G. and Atkinson, C.D., 1997. Evaluating seal potential: Example from the Talang Akar Formation, offshore northwest Java, Indonesia: *In: R.C. Surdam (Ed.), Seals, traps, and the petroleum system: AAPG Memoir 67*, p. 85 - 101.

Kantsler, A.J., Prudence, T.J.C., Cook, A.C. and Zwigulis, M., 1983. Hydrocarbon habitat of the Cooper/Eromanga Basin, Australia. *Australian Petroleum Exploration Association Journal*, v. 23, p. 373 - 389.

Katz, A.J. and Thompson, A.H., 1987. Prediction of rock electrical conductivity from mercury injection measurements. *Journal of Geophysical Research*, vol. 92, p. 599 - 607.

Kolodzie, S. Jr., 1980. Analysis of pore throat size and use of the Waxman-Smiths equation to determine OOIP in Spindle Field, Colorado. *Society of Petroleum Engineers, 55<sup>th</sup> Annual Fall Technical Conference*, Paper 9382, 10 p.

Kraus, M.J., 1987. Integration of channel and floodplain suites, II. Vertical relations of alluvial palaeosols. *J. Sedim. Petrol.* 57: 602 - 612.

Kraus, M.J., 1992. Mesozoic and tertiary palaeosols. *In: Martini, I.P., Chersworth, W (Eds.), Weathering, soils and palaeosols.* Elsevier, Amsterdam, p. 525 - 542 (Development in earth surface processes, no 2).

Kuang, K.S., 1985. History and style of Cooper - Eromanga Basin structures. *Exploration Geophysics*, 16: 245 - 248.

Leverett, M.C., 1941, Capillary behavior in porous solids: *AIME Petroleum Trans.*, v. 142, p. 152 - 169.

Livingston, H. K., 1938. Subsurface and interfacial tension of oil-water systems in Texas oil sands. *AIME Technical Paper 1001*.

Martin, C.A., 1967. The Gidgealpa and Merrimelia Formation in the Cooper's Creek Basin. *Australian Oil and Gas Journal*, v.14, p. 29 -35.

McManus, J., 1988. Grain size determination and interpretation. *In: Tucker, M. (Ed), Techniques in Sedimentology*. Blackwell Scientific Publications. p. 63 - 85.

Miall, A.D., 1978. Lithofacies types and vertical profile models in braided river deposits: a summary. *In: Miall, A.D. (Ed.) Fluvial sedimentology. Can. Soc. Petrol. Geol. Mem 5: 597 - 604.*

Miall, A.D., 1996. *The Geology of Fluvial Deposits. Sedimentary Facies, Basin Analysis and Petroleum Geology, Springer-Verlag Berlin Heidelberg.*

Michaelsen, B.H. and McKirdy, D.M., 1989. Organic facies and petroleum geochemistry of the lacustrine Murta Member (Mooga Formation) in the Eromanga Basin, Australia. *In: O'Neil, B.J. (Ed.), The Cooper and Eromanga Basins, Australia. Proceedings of the Cooper and Eromanga Basins Conference, Adelaide, 1989. Petroleum Exploration Society of Australia, Society of Petroleum Engineers, Australian Society of Exploration Geophysicists (SA Branches), p. 541 - 558.*

Papalia, N., 1969. The Nappamerri Formation: *APEA Journal*, v. 9, p. 108 - 110.

Petroleum Group, 2003. Petroleum exploration and development in South Australia. 15<sup>th</sup> edn. *South Australia. Department of Primary Industries and Resources. Petroleum Exploration Data Package, 4.* Edited and designed by PIRSA Publishing Services March 2003.

Pettijohn, F.J., Potter, P.E. and Siever, R., 1972. Comparison chart for sorting and sorting classes. *Sand and sandstone: New York, Springer-Verlag.*

Picard, M. D., 1971. Classification of fine-grained sedimentary rocks: *Jour. Sed. Petrology*, v. 41, p. 179 - 195.

Pittman, E.D., 1992. Relation of porosity and permeability to various parameters derived from mercury injection-capillary pressure curves for sandstones. *AAPG Bulletin*, v. 76, p. 191 - 198.

Powell, C. McA. and Veevers, J.J., 1987. Namurian uplift in Australia and South America triggered the main Gondwanan glaciation. *Nature*, 326: 177 - 179.

Powers, M.C., 1982. Comparison chart for estimating roundness and sphericity. AGI Data Sheet 18. American Geological Institute.

Powis, G.D., 1989. Revision of Triassic stratigraphy at the Cooper Basin to Eromanga Basin transition. *In: O'Neil, B.J. (Ed.), The Cooper and Eromanga Basins, Australia*. Proceedings of the Cooper and Eromanga Basins Conference, Adelaide, 1989. Petroleum Society of Australia, Society of Petroleum Engineers. Australian Society of Exploration Geophysicists (SA Branches), p. 265 - 277.

Purcell, W.R., 1949, Capillary pressure - their measurements using mercury and the calculation of permeability therefrom: *AIME Petroleum Trans.*, v. 186, p. 39 - 48.

Rezaee, M. and Lemon, N.M., 1996. Controls on pore geometry in the Tirrawarra Sandstone reservoir, Cooper Basin, Australia. *PESA Journal*, 24:116-138.

Schlumberger, 1977. Log Interpretation Charts. p. 4 - 29.

Schulz-Rojahn, J.P. and Phillips, S.E., 1989. Diagenetic alteration of Permian reservoir sandstones in the Nappamerri Trough and adjacent areas, southern Cooper Basin. *In: O'Neil, B.J. (Ed.), The Cooper and Eromanga Basins, Australia*. Proceedings of the Cooper and Eromanga Basins Conference, Adelaide, 1989. Petroleum Exploration Society of Australia, Society of Petroleum Engineers, Australian Society of Exploration Geophysicists (SA Branches), pp.629-645.

Schowalter, T.T., 1979. Mechanics of secondary hydrocarbon migration and entrapment: *AAPG Bulletin*, v. 63, No. 5, p. 723 - 760.

Seggie, R.J., Lansom, P.B., Hamlin, H.S. and Johnson, G.A., 1994. The Tirrawarra oil field: field revitalisation through reservoir description and characterisation. *APEA Journal*, 34 (1): 33-54.

Siffleet, P., 1992. Merrimelia Field Depth Structure Top 74-9 Sand. Mid Nappamerri Formation. *In: Allen, P., 1993. Merrimelia 29 Well Completion Report, Santos Limited* (unpublished).

Smith, D.A., 1966. Theoretical consideration of sealing and non-sealing faults: *AAPG Bulletin*, v. 50, p. 363 - 374.

Sneider, R.M., 1987. Practical petrophysics for exploration and development. *AAPG Education Department Short Course Notes*.

Sneider R.M., Sneider J.S., Bolger G.W. & Neasham J.W., 1997. Comparison of seal capacity determinations: conventional cores vs. cuttings. *In: Surdam R.C. (Ed.) Seals, traps and the petroleum system, AAPG Memoir, 67, 1-12.*

Solomon, C.J., 1992. The application of capillary pressure in determining the seal capacity of Eromanga Basin cap-rocks: *University of Adelaide, M Sc thesis (unpublished)*.

Sprigg, R.C., 1958. Petroleum prospects of western parts of the Great Australian Artesian Basin. *AAPG Bulletin*, 42 (10): 2465 - 2491.

Stanmore, P.J., 1989. Case study of stratigraphic and fault traps in the Cooper Basin, Australia. *In: O'Neil, B.J. (Ed.), The Cooper and Eromanga Basins, Australia. Proceedings of the Cooper and Eromanga Basins Conference, Adelaide, 1989. Petroleum Society of Australia, Society of Petroleum Engineers. Australian Society of Exploration Geophysicists (SA Branches), pp. 361 - 369.*

Stearns, D.W. and Friedman, M., 1972. Reservoirs in fractured rocks. *In: King, R.E. (Ed.), Stratigraphic oil and gas fields – classification, exploration methods and case histories. AAPG Memoir, v.10, p. 82-106.*

Stuart, W.J., 1976. The genesis of Permian and lower Triassic reservoir sandstones during phases of southern Cooper Basin development. *APEA Journal*, 16: 37 - 47.

Stuart, W.J., Kennedy, S. and Thomas, A.D., 1988. The influence of structural growth and other factors on the configuration of fluvial sandstones, Permian Cooper Basin. *APEA Journal*, p. 255 - 265.

Sun, X., 1997. Structural style of the Warburton Basin and control in the Cooper and Eromanga Basins, South Australia. *Exploration Geophysics*, 28 (4): 333 - 339.

- Swanson, B.F., 1981. A simple correlation between permeabilities and mercury capillary pressures: *Journal of Petroleum Technology*, v. 33, p. 2498 - 2504.
- Theriault, P. and Desrochers, A., 1993. Carboniferous calcretes in the Canadian Arctic. *Sedimentology* 40: 449 - 466.
- Thomas, L.K. and Katz, D.L., 1968. Threshold pressure phenomena in porous media. *SPE Journal*, p. 174 - 184.
- Thornton, R.C.N., 1979. Regional stratigraphic analysis of the Gidgealpa Group, southern Cooper Basin, Australia. South Australia. *Geological Survey. Bulletin*, 49.
- Vavra, C.L., Kaldi, J.G. and Sneider, R.M., 1992. Geological applications of capillary pressure: A review. *AAPG Bulletin*, Vol. 76, p. 840 - 850.
- Veevers, J.J., 1984. Phanerozoic Earth history of Australia. *Oxford Geological Sciences Series*, 2.
- Veevers J.J., Conaghan, P.J. and Shaw, S.E., 1994. Turning point in Pangean environmental history of the Permo-Triassic (P-Tr) boundary. *In: Klein, G. de V. (Ed.), Pangea: paleoclimate, tectonics and sedimentation during accretion, zenith and breakup of a supercontinent. Geological Society of America. Special Paper*, 288: 187 - 196.
- Walker, R.G. and Douglas, J.C., 1984. Sandy Fluvial Systems. *In: Walker, R.G. (Ed.), Facies Models, Second Edition. Geoscience Canada, Reprint Series 1*, p. 71 - 89.
- Washburn, E.W., 1921, Note on a method of determining the distribution of pore sizes in a porous material: *Proceedings of the National Academy of Science*, v. 7, p. 115 - 116.
- Williams, B.P.J., 1982. Facies analysis of Gidgealpa Group reservoir rocks, southern Cooper Basin, South Australia. *Report for South Australian Oil and Gas Corporation Pty Ltd (unpublished)*.



- Williams, B.P.J. and Wild, E.K., 1984. The Tirrawarra Sandstone and Merrimelia Formation of the southern Cooper Basin, South Australia - the sedimentation and evolution of a glaciofluvial system. *APEA Journal*, 24 (1): 377 - 392.
- Williams, B.P.J., 1984. Reservoir geometry and alluvial architecture of the Toolachee Formation, Moomba Field, south Cooper Basin. In: 7<sup>th</sup> Australian Geological Convention, Sydney, 1984. *Geological Society of Australia. Abstracts*, 12: 552 - 553.
- Williams, B.P.J., Wild, E.K. and Suttill, R.J., 1985. Paraglacial aeolianites: potential new hydrocarbon reservoirs, Gidgealpa Group, southern Cooper Basin. *Australian Petroleum Exploration Association Journal*, v. 25, p. 291 - 310.
- Williams, B.P.J., 1995. Core workshop – 'non-marine deposystems'. *Sagasco Resources Ltd* (unpublished).
- Wiltshire, M.J., 1982. Late Triassic and Early Jurassic sedimentation in the Great Artesian Basin. In: Moore, P.S. and Mount, T.J. (Compilers), *Eromanga Basin Symposium, Adelaide, 1982. Summary papers*. Petroleum Exploration Society of Australia, Geological Society of Australia, Geological Society of Australia (SA Branches), pp.58 - 67.
- Wilson, M. D., 1993. Evaluating diagenetically complex reservoirs. In: Morton-Thompson, D. and Woods, A.M. (Eds.), *Development Geology Reference Manual, AAPG Methods in Exploration Series, No.10*, p. 314-320.
- Wopfner, H., 1985. Some thoughts on the post-orogenic development of northeastern South Australia and adjoining regions. In: Lindsay, J.M. (Ed.), *Stratigraphy, palaeontology, malacology-papers in honor of Dr Nell Ludbrook. South Australia. Department of Mines and Energy. Special Publication*, 5: 365 - 372.
- Wright, V.P., 1990. Estimating rates of calcrete formation and sediment accretion in ancient alluvial deposits. *Geol. Mag.* 127: 273 - 276.
- Youngs, B.C. and Boothby, P.G., 1982. The middle Permian-middle Triassic rocks of the southwestern Cooper Basin. In: Moore, P.S. and Mount, T.J. (Compilers), *Eromanga Basin Symposium, Adelaide, 1982. Summary Papers*. Petroleum

---

Exploration Society of Australia, Geological Society of Australia (SA Branches), p. 76 - 78.

Youngs, B.C. and Boothby, P.G., 1985. The Nappamerri Formation in the Cooper Basin, South Australia and southwest Queensland. *In*: Lindsay, J.M. (Ed.), Stratigraphy, palaeontology, malacology – papers in honour of Dr Nell Ludbrook. South Australia. *Department of Mines and Energy. Special Publication*, v. 5, p. 373 - 387.